Three-dimensional quantitative analysis of bone microvasculature in synchrotron micro-CT imaging

Hao Xu

N°d'ordre NNT: 2021LYSEI019

THESE de DOCTORAT DE L'UNIVERSITE DE LYON
opérée au sein de
L'Institut National des Sciences Appliquées de Lyon

Ecole Doctorale 160
Électronique, Électrotechnique, Automatique

Spécialité/ discipline de doctorat : Traitement du Signal et de l'Image

Soutenue publiquement le 26/03/2021, par :
Hao Xu

Three-dimensional quantitative analysis of bone microvasculature in synchrotron micro-CT imaging

---

Devant le jury composé de :

Présidente (Lafage-Proust Marie Hélène)

Rousseau David	Professeur, Univ Angers	Rapporteur
Redenbach Claudia	Professeur, Tech Univ Kaiserslautern	Rapporteur
Lafage-Proust Marie Hélène	Professeur, Univ J M Saint-Etienne	Examinateur
Grimal Quentin	Professeur, Univ Sorbonne	Examinateur
Peyrin Françoise	Directeur de recherche, INSA-LYON	Directrice de thèse
Langer Max	Chargé de recherche, CNRS	Co-directeur de thèse

Département FEDORA – INSA Lyon - Ecoles Doctorales – Quinquennal 2016-2020

SIGLE	ECOLE DOCTORALE	NOM ET COORDONNEES DU RESPONSABLE
CHIMIE	**CHIMIE DE LYON** **http://www.edchimie-lyon.fr** Sec. : Renée EL MELHEM Bât. Blaise PASCAL, 3e étage **secretariat@edchimie-lyon.fr** INSA : R. GOURDON	**M. Stéphane DANIELE** Institut de recherches sur la catalyse et l'environnement de Lyon IRCELYON-UMR 5256, Équipe CDFA 2 Avenue Albert EINSTEIN 69 626 Villeurbanne CEDEX **directeur@edchimie-lyon.fr**
E.E.A.	**ÉLECTRONIQUE, ÉLECTROTECHNIQUE, AUTOMATIQUE** **http://edeea.ec-lyon.fr** Sec. : M.C. HAVGOUDOUKIAN **ecole-doctorale.eea@ec-lyon.fr**	**M. Gérard SCORLETTI** École Centrale de Lyon 36 Avenue Guy DE COLLONGUE 69 134 Écully Tél : 04.72.18.60.97 Fax 04.78.43.37.17 **gerard.scorletti@ec-lyon.fr**
E2M2	**ÉVOLUTION, ÉCOSYSTÈME, MICROBIOLOGIE, MODÉLISATION** **http://e2m2.universite-lyon.fr** Sec. : Sylvie ROBERJOT Bât. Atrium, UCB Lyon 1 Tél : 04.72.44.83.62 INSA : H. CHARLES **secretariat.e2m2@univ-lyon1.fr**	**M. Philippe NORMAND** UMR 5557 Lab. d'Ecologie Microbienne Université Claude Bernard Lyon 1 Bâtiment Mendel 43, boulevard du 11 Novembre 1918 69 622 Villeurbanne CEDEX **philippe.normand@univ-lyon1.fr**
EDISS	**INTERDISCIPLINAIRE SCIENCES-SANTÉ** **http://www.ediss-lyon.fr** Sec. : Sylvie ROBERJOT Bât. Atrium, UCB Lyon 1 Tél : 04.72.44.83.62 INSA : M. LAGARDE **secretariat.ediss@univ-lyon1.fr**	**Mme Sylvie RICARD-BLUM** Institut de Chimie et Biochimie Moléculaires et Supramoléculaires (ICBMS) - UMR 5246 CNRS - Université Lyon 1 Bâtiment Curien - 3ème étage Nord 43 Boulevard du 11 novembre 1918, 69622 Villeurbanne Cedex Tel : +33(0)4 72 44 82 32 **sylvie.ricard-blum@univ-lyon1.fr**
INFOMATHS	**INFORMATIQUE ET MATHÉMATIQUES** **http://edinfomaths.universite-lyon.fr** Sec. : Renée EL MELHEM Bât. Blaise PASCAL, 3e étage Tél : 04.72.43.80.46 **infomaths@univ-lyon1.fr**	**M. Hamamache KHEDDOUCI** Bât. Nautibus 43, Boulevard du 11 novembre 1918 69 622 Villeurbanne Cedex France Tel : 04.72.44.83.69 **hamamache.kheddouci@univ-lyon1.f**
Matériaux	**MATÉRIAUX DE LYON** **http://ed34.universite-lyon.fr** Sec. : Stéphanie CAUVIN Tél : 04.72.43.71.70 Bât. Direction **ed.materiaux@insa-lyon.fr**	**M. Jean-Yves BUFFIÈRE** INSA de Lyon MATEIS - Bât. Saint-Exupéry 7 Avenue Jean CAPELLE 69 621 Villeurbanne CEDEX Tél : 04.72.43.71.70 Fax : 04.72.43.85.28 **jean-yves.buffiere@insa-lyon.fr**
MEGA	**MÉCANIQUE, ÉNERGÉTIQUE, GÉNIE CIVIL, ACOUSTIQUE** **http://edmega.universite-lyon.fr** Sec. : Stéphanie CAUVIN Tél : 04.72.43.71.70 Bât. Direction **mega@insa-lyon.fr**	**M. Jocelyn BONJOUR** INSA de Lyon Laboratoire CETHIL Bâtiment Sadi-Carnot 9, rue de la Physique 69 621 Villeurbanne CEDEX **jocelyn.bonjour@insa-lyon.fr**
ScSo	**ScSo*** **http://ed483.univ-lyon2.fr** Sec. : Véronique GUICHARD INSA : J.Y. TOUSSAINT Tél : 04.78.69.72.76 **veronique.cervantes@univ-lyon2.fr**	**M. Christian MONTES** Université Lyon 2 86 Rue Pasteur 69 365 Lyon CEDEX 07 **christian.montes@univ-lyon2.fr**

*ScSo : Histoire, Géographie, Aménagement, Urbanisme, Archéologie, Science politique, Sociologie, Anthropologie

ACKNOWLEDGMENT

I would like to present my deep gratitude toward everyone who gave me continuous help and supports during my PhD thesis.

First and foremost, I'm profoundly indebted to my advisors Dr. Françoise Peyrin and Dr. Max Langer for their patient guidance, many of insightful discussion and suggestion. Actually, I was a beginner in the field of medical image processing at the first year of my PhD, since my previous research background was more about optics. Thus, they gave me much more time to learn the basic knowledge and explained to me many basic definitions and principles in this field. On the other hand, although I was not able to speak fluent English, they always listened to me patiently and tried to help me to find solutions and overcome challenges. In addition, they not only let me know deeper about my PhD subject, but also taught me how to think in a scientific way. Therefore, I learnt a lot from our regular weekly meeting and appreciated a free research environment they provided to me.

I express my thanks to the jury members of this thesis. Particularly, I thank Dr. Françoise Peyrin and Dr. Max Langer for giving me many valuable comments and corrections during the redaction process of this thesis. Also, deep gratitude goes to Dr. David Rousseau and Dr. Claudia Redenbach for conscientiously reading this thesis and writing the constructive reports. At the same time, I thank Dr. Marie Hélène Lafage-Proust and Dr. Quentin Grimal for their insightful suggestions in terms of the biological interpretation.

I acknowledge all the members in the Tomoradio team and CREATIS lab for giving me their help. In particular, I thank Cécile Olivier for data acquisition in ESRF and the following technical supports. I also express my gratitude to Pierre-jean Gouttenoire for assistance in computer programming. Additionally, my gratitude goes to Marie-Hèlène Lafage-Proust and Bernard Roche from the SAINBIOSE Lab (INSERM U1059, Université de Lyon), Lamia Bouazza and Philippe Clezardin from the Lyos, Lyon (INSERM UMR 1033, Université de Lyon) for the animal protocol and sample preparation.

Last but not least, my sincere thanks go to my parents and all friends around me for their supports. I also would like to express my deepest gratitude to my beloved Zhu Meng for her company in this wonderful journey.

CONTENTS

ABSTRACT

Breast cancer is common and dangerous in women worldwide, and the major mortality is caused by bone metastases. Breast cancer bone metastases cannot only bring about bone destructions but also facilitate the formation of undesirable vascularization. There is a large body of evidence that angiogenesis is a rate-limiting step in the growth of metastatic bone tumors, making it a relevant target for therapeutic intervention. Therefore, the tools for the evaluation of anti-angiogenic drugs need to be developed.

Three-dimensional (3D) X-ray microcomputed tomography (μCT) is a tool of choice to image bone, and can also be used to visualize the vascular architecture with a contrast agent. However, these studies required to decalcify the bone. Therefore, μCT was only used to image and analyze either bone microstructure or vascular architecture separately, and did not permit a complete analysis of the relationships between the bone and vessels. Synchrotron radiation microcomputed tomography (SR-μCT) has a significant advantage of yielding high spatial resolution images with a high signal-to-noise ratio, compared to standard μCT, due to the high photon flux of the synchrotron source. SR-μCT has been applied to the quantitative analysis of bone up to the micrometer scale. In addition, SR-μCT coupled with a contrast agent permitted to visualize simultaneously the 3D bone microstructures and vascular networks in preclinical studies.

Segmentation is an important step in image analysis. Previously, the bone and vessels of rats, simultaneously imaged using SR-μCT with a contrast agent, have been segmented automatically using 3D region growing method. To make more models of pathologies available, it would be desirable to image mice. However, this transition is not straightforward. As opposed to in rat bone, vessels may appear to be in contact with the bone surface in mice. This precludes the correct segmentations of bone and vessels using 3D region growing.

In this thesis, we proposed an algorithm based on marker-controlled watershed in conjunction with the monogenic signal phase asymmetry. The marker-controlled watershed was used to separate vessels appearing to be touching the bone surface, without the need for post-segmentation merging of regions. An important step of the algorithm is to generate the marker image to initialize the watershed algorithm. Here, we used three classes of markers: bone, vessels and background, which were generated using hysteresis thresholding and morphological filters, with the aim to achieve coverage of all connected components in each class and no false positives. The other essential step is to generate a control surface, in which the "flooding" of the watershed algorithm happens from the markers to find boundaries between different compartments. Here, we proposed the use of 3D monogenic signal phase asymmetry to improve the edge detections at the bone and vessel interfaces, in which the contrast is relatively weak compared to the bone-background and the vessel-background interfaces, leading to weaker gradient magnitude at these edges. The monogenic signal phase has the property of invariance to signal intensity. The phase asymmetry can therefore quantify whether the image is locally edge-like or line-like independently of the intensity of the structure.

To evaluate the accuracy and robustness of the proposed method, a series of synthetic volumes were generated to mimic the real vessel, bone and background structures. Different contrasts between various compartments, different noise levels, as well as the segmentation of thin structure were considered. In this study, we generated 259 synthetic volumes for four kinds of models. The multi-class compartments were segmented using the proposed method. The overall segmentation quality was evaluated using the Matthews correlation coefficient (MCC) by comparing to the ground truth. Finally, we studied the impacts of contrasts and noise levels on segmentations, and investigated the segmentation capability of thin structure under a various levels of noise. The simulation study indicates that the algorithm is performant in other multi-class segmentation problems.

We reported the application of the proposed method to the real datasets. The female mice were injected with breast cancer tumor cells, and the preventive treatments were performed with anti-angiogenic drugs. 3D SR-μCT was used to image the bone vasculatures on tibia of mice, with contrast agent. Next, the acquired 3D datasets of mouse bone were segmented into vessels, bone and background compartments using the proposed marker-controlled watershed algorithm and the monogenic signal phase asymmetry. The segmentation quality was evaluated using the Dice coefficient and the Matthews correlation coefficient (MCC) by comparing to the manual segmentations on representative small volumes. The results indicate that segmentation quality with the proposed method is much improved compared to hysteresis thresholding or gradient based watershed segmentations.

To characterize bone and vasculatures, several quantitative parameters were extracted. Finally, statistical analysis was performed to study the influence of anti-angiogenesis drugs on bone and vessels, in the context of breast cancer bone metastases.

RÉSUMÉ ÉTENDU

CONTEXTE

Chapitre 1: Introduction

Contexte

Le cancer du sein est le cancer le plus fréquemment diagnostiqué chez les femmes dans le monde entier (Bray et al., 2018). En termes de mortalité, on compte environ 508 000 décès par an dans le monde (Tulotta et al., 2019). La morbidité et la mortalité les plus importantes sont causées par les métastases osseuses, qui entraînent généralement des lésions ostéolytiques. Environ 70 % des patientes atteintes d'un cancer du sein atteignent la phase avancée où les tumeurs se métastasent aux os (Akhtari et al., 2008). Une fois les métastases localisées dans l'os, les traitements existants ne sont pas en mesure de guérir la maladie, et le taux de survie médian est d'environ 24 à 65 mois (Lote, Walløe and Bjersand, 1986; Nutter et al., 2014; Catarina et al., 2017).

Les métastases osseuses du cancer du sein provoquent non seulement des destructions osseuses, mais entrainent également la formation d'une vascularisation indésirable. L'angiogenèse tumorale est une prolifération nécessaire d'un réseau de vaisseaux sanguins qui fournit des nutriments et de l'oxygène et élimine les déchets (Nyangoga et al., 2011). En outre, il existe un grand nombre de preuves que les traitements anti-angiogéniques pourraient limiter la croissance des tumeurs osseuses métastatiques, ce qui en fait une cible pertinente pour une intervention thérapeutique (Ebos and Kerbel, 2011). Il est donc nécessaire de développer les outils d'évaluation des médicaments anti-angiogéniques.

La micro-tomographie (µCT) est un outil de choix pour obtenir des images tri-dimensionnelles de la micro-architecture de l'os trabéculaire (Kuhn et al., 1990) ainsi que de l'os cortical et de son réseau haversien (Cooper et al., 2003; Bousson et al., 2004). En outre, la µCT peut être utilisée pour visualiser l'architecture vasculaire avec un agent de contraste (Moore et al., 2003; Zhang et al., 2005). Cependant, dans le cas du tissu osseux, il est généralement nécessaire de décalcifier l'os. Par conséquent, la µCT associée à un agent de contraste a permis d'imager et d'analyser la microstructure osseuse et l'architecture vasculaire séparément, sans permettre une analyse complète des relations entre l'os et les vaisseaux.

La micro-tomographie par rayonnement synchrotron (SR-µCT) a l'avantage de produire des images à haute résolution spatiale avec un rapport signal/bruit élevé, par rapport à la µCT standard, en raison du flux de photons élevé des sources synchrotron par rapport aux sources de rayons X standards (Salomé et al., 1999). La SR-µCT a été appliquée à l'analyse quantitative de l'os trabéculaire humain jusqu'à des échelles inférieures au micromètre (Peyrin et al., 1998a; Larrue et al., 2011). En outre, la SR-µCT couplée à l'utilisation d'un agent de contraste a permis de visualiser simultanément les microstructures osseuses 3D et les réseaux vasculaires chez la souris (Schneider et al., 2009) ou le rat (Prisby et al., 2011). Des visualisations simultanées de la microstructure osseuse et des vaisseaux sanguins ont

également été démontrées à l'aide de la micro-tomographie par rayonnement synchrotron à contraste de phase (SR-PCT) sans agent de contraste dans un modèle de souris (Núñez et al., 2017). Toutefois, dans cette étude, le champ de vue était limité en raison de la petite taille des pixels utilisés, et les vaisseaux ont été segmentés à la main en raison du faible contraste des vaisseaux, ce qui limite les applications de ce protocole à de grands ensembles de données.

La segmentation est une étape importante dans l'analyse des images. Peu de méthodes ont à ce jour été proposées pour la segmentation simultanée des structures osseuses et vasculaires. Dans le travail de (Schneider et al., 2009), les auteurs ont utilisé une méthode de segmentation automatique à l'aide d'un seuillage global sur des images de souris par SR-µCT avec agent de contraste. Auparavant, notre groupe a proposé une méthode pour imager et analyser simultanément les os et les vaisseaux en 3D de rats en utilisant la SR-µCT avec agent de contraste (Langer et al., 2010; Prisby et al., 2011). Un protocole d'analyse automatique des images, basé sur le seuillage par hystérésis et le filtrage morphologique, a été conçu pour segmenter les différents compartiments osseux et les vaisseaux.

Pour disposer de plus de modèles de pathologies, il serait souhaitable d'imager des souris. Cependant, l'application de la méthode proposé précédemment chez la souris ne s'est pas révélée suffisante. Contrairement aux os de rats, les vaisseaux peuvent sembler être en contact avec la surface de l'os chez la souris, ce qui compromet une segmentation correcte de l'os et des vaisseaux en utilisant ce protocole.

Dans le cadre de cette thèse, nous disposions d'images d'os et de vaisseaux du tibia de souris ont été simultanément imagés simultanément à l'aide de SR-µCT avec agent de contraste, dans le contexte d'une étude sur le traitement de métastases osseuses dans un modèle animal de cancer du sein. L'objectif était de proposer un protocole automatique pour segmenter les deux classes, os et vaisseaux, de le valider, et de l'appliquer à la série d'images SR-µCT.

Après une étude bibliographique, nous nous sommes orientés vers une méthode basée sur les bassins versants contrôlés par des marqueurs. Cette méthode a été utilisé pour séparer les vaisseaux qui semblent toucher la surface de l'os, sans qu'il soit nécessaire de fusionner les régions après la segmentation. Une étape importante de l'algorithme consiste à générer l'image du marqueur pour initialiser l'algorithme du bassin versant. Ici, nous avons utilisé trois classes de marqueurs : l'os, les vaisseaux et le fond, qui ont été générés à l'aide de seuils d'hystérésis et de filtres morphologiques, dans le but d'obtenir une couverture de tous les composants connectés dans chaque classe et d'éviter les faux positifs. L'autre étape essentielle consiste à générer une surface de contrôle, dans laquelle l'inondation de l'algorithme du bassin versant se produit à partir des marqueurs pour trouver des limites entre les différents compartiments. Pour cette étape, nous avons introduit l'utilisation du signal monogénique 3D pour améliorer les détections de bord aux interfaces os et vaisseaux, dans lesquelles le contraste est relativement faible par rapport aux interfaces os - fond et vaisseaux - fond, ce qui entraîne une amplitude de gradient plus faible à ces bords. Plus précisément, nous avons exploité l'asymétrie de phase du signal monogénique. La phase de signal monogénique a la propriété d'être invariante par rapport à l'intensité du signal. L'asymétrie de phase peut donc quantifier si l'image est localement en forme de bord ou de ligne indépendamment de l'intensité de la structure.

Pour ce qui est de l'évaluation de la méthode, nous avons envisagé différents critères de qualité, donc le classique coefficient de Dice et proposé d'utiliser le coefficient de corrélation de Matthews (MCC). D'une part, cette évaluation a été réalisée à partir de segmentations manuelles sur des petits volumes représentatifs. D'autre part, la précision et la robustesse de la méthode proposée ont été évaluées sur une série de volumes synthétiques générés pour imiter les structures réelles des vaisseaux, des os et du fond. Différents contrastes entre divers compartiments, différents niveaux de bruit, ainsi que la segmentation de la structure mince ont été pris en compte. Les résultats indiquent que l'algorithme est performant et pourrait être exploité dans d'autres problèmes de segmentation multi-classes.

La méthode a ensuite été appliquée aux 70 volumes expérimentaux disponibles répartis dans différents groupes. Finalement une analyse quantitative a été réalisée en calculant différents paramètres pour caractériser les microstructures et les vaisseaux sanguins des os. En outre, une analyse statistique des différents groupes a été effectuée à l'aide de tests appropriés.

Organisation du manuscrit

Cette thèse est divisée en deux grandes parties : le contexte et les contributions.

(1) Partie contexte : cette partie comprend 4 chapitres pour présenter les connaissances et l'état de l'art.

Dans le chapitre 1, nous présentons brièvement le contexte général, l'objectif et l'organisation du manuscrit.

Dans le chapitre 2, nous décrivons les connaissances de base sur les structures osseuses et les fonctions du système vasculaire. En outre, nous passons en revue les techniques existantes d'imagerie de l'os et des vaisseaux.

Dans le chapitre 3, nous introduisons les méthodes génériques de segmentation d'images biomédicales et passons en revue l'état de l'art des techniques de segmentation de l'os et des vaisseaux à partir d'image µCT.

Dans le chapitre 4, nous présentons les méthodes d'évaluation existantes de la qualité de la segmentation.

(2) Partie contribution : nous présentons les contributions, concluons cette thèse et suggérons des perspectives.

Dans le chapitre 5, nous décrivons le nouveau protocole de segmentation de l'os et des vaisseaux proposé à partir des images SR-µCT. En outre, nous introduisons les critères d'évaluation de la qualité de la segmentation pour un compartiment unique et des classes multiples.

Le chapitre 6 est consacré à une évaluation poussée de la méthode proposée sur simulations. Une série de volumes synthétiques sont générés pour simuler les vaisseaux et les os réels. Nous considérons différents contrastes entre les différents compartiments, différents niveaux de bruit, ainsi que la segmentation de la structure mince. La série de volumes synthétiques multi-classes est segmentée en utilisant la méthode proposée et nous présentons les résultats sur les critères quantitatifs de segmentation.

Dans le chapitre 7, nous présentons l'application de la méthode proposée à l'ensemble de données réelles sur les os et les vaisseaux de souris, acquises par SR-µCT avec agent de

contraste. La préparation des échantillons et l'acquisition des images sont décrites. Nous décrivons également les différents prétraitements qui ont été nécessaires pour appliquer cette méthode aux données expérimentales sur les images. Enfin, des paramètres quantitatifs sont extraits de chaque structure et une analyse statistique des différents groupes est effectuée.

Dans le chapitre 8, nous concluons cette thèse et suggérons les perspectives des travaux futurs.

Chapitre 2: Os et vaisseaux

Introduction

Compte tenu du contexte de la thèse qui porte sur l'imagerie des structures vasculaires dans l'os, nous introduisons quelques connaissances de base sur l'os et les fonctions des vaisseaux. Nous passons également en revue les techniques existantes d'imagerie de l'os et des vaisseaux.

Structures osseuses

L'os est un organe important chez les animaux vertébrés. Il est composé de plusieurs types de tissus, tels que le tissu osseux, le cartilage, le tissu conjonctif dense, l'épithélium, le tissu adipeux et le tissu nerveux. Au niveau macroscopique, la structure des os longs se compose de la diaphyse, de l'épiphyse, de la métaphyse, du cartilage articulaire, du périoste, de la cavité médullaire et de l'endoste (Tortora and Derrickson, 2018).

Au niveau microscopique, on peut distinguer deux types d'os : l'os cortical et l'os trabéculaire. L'os cortical forme l'enveloppe externe de l'os et constitue la majeure partie de la diaphyse (Tortora and Derrickson, 2018). De plus, l'os cortical est dense et présente une porosité de l'ordre de 6 % (Fratzl and Weinkamer, 2007; Eliaz and Metoki, 2017). L'os trabéculaire est situé à l'intérieur de l'os et constitue le noyau des épiphyses et de la métaphyse. Il est organisé en un réseau complexe de travées osseuses, typiquement en forme de plaques ou de tubes (Tortora and Derrickson, 2018).

Vascularisation dans l'os

Les vaisseaux sanguins sont essentiels à la santé de chaque tissu car ils peuvent transporter l'oxygène, les nutriments et les molécules inflammatoires, ainsi qu'éliminer le dioxyde de carbone et les déchets (Tse, 2018). Les vaisseaux sanguins sont particulièrement abondants dans certaines parties des os, comme le tibia mature. Les vaisseaux entrent dans la diaphyse par de nombreux canaux de l'os cortical, et se divisent en branches alimentant la partie interne de l'os cortical, l'os trabéculaire, la moelle osseuse rouge (Tortora and Derrickson, 2018).

L'angiogenèse est la formation de nouveaux vaisseaux sanguins et peut être un signe distinctif du cancer (Welti et al., 2013). Par exemple, l'angiogenèse joue un rôle important dans le développement du cancer du sein (Bachelier et al., 2014). Il existe un grand nombre de preuves que l'angiogenèse est une cible thérapeutique anticancéreuse. Par conséquent, de nombreux agents anti-angiogéniques ciblent le VEGF ou ses récepteurs comme médicaments anticancéreux potentiels (Ebos and Kerbel, 2011).

Imagerie du tissu osseux et du système vasculaire

L'imagerie histologique est un outil de recherche bien établi pour étudier la pathogenèse. Elle est couplée à la microscopie optique et nécessite souvent la préparation d'échantillons tels que des coupes et des colorations (An and Martin, 2003; Kulak and Dempster, 2010). L'imagerie histologique a été utilisée pour obtenir des images de l'os de souris (Zhao et al., 2007; Bachelier et al., 2014), et pour visualiser la vascularisation osseuse avec un agent de contraste (Roche et al., 2012). Cependant, l'imagerie histologique fournit des coupes 2D et manque d'informations architecturales en 3D pour évaluer les aspects structurels des pathologies.

La radiographie est une technique d'imagerie rapide par projection, non invasive et *in vivo*. Elle utilise une source de rayons X qui irradie l'objet, et fournit une image d'atténuation qui dépend de la densité et de la composition structurelle de l'objet (Shelledy and Peters, 2014). Par exemple, le tissu osseux est visible sur une image radiographique (Zhao et al., 2007; Bachelier et al., 2014). Bien que la radiographie puisse surveiller les lésions ostéolytiques, elle ne permet de les détecter qu'à un stade tardif, lorsque la destruction osseuse est en cours. De plus, l'image radiographique 2D de l'os ne donne pas accès à une information 3D que projetée.

La microscopie confocal à balayage laser (LCSM) est une technique de microscopie optique à haute résolution (0,2 µm à 0,5 µm). La LCSM permet d'obtenir des reconstructions 3D d'un objet en assemblant une série de tranches 2D à différentes profondeurs dans l'échantillon (Ross and Pawlina, 2006). Cette technique a, par exemple, été utilisée pour imager la vascularité par immunocoloration, dans un échantillon de biopsie de moelle osseuse humaine (Lundberg et al., 2000) ou pour imager les microvascularisation des os de souris par coloration immunofluorescente, après décalcification (Ubellacker et al., 2017; Allocca et al., 2019; Haider et al., 2020). Le LCSM est un outil d'imagerie puissant dans les sciences de la vie, mais il possède un spectre limité de molécules qui peuvent être visualisées, en fonction de la disponibilité des sondes. En outre, le LCSM est limité par le champ de vue et la profondeur de pénétration dans les tissus, notamment dans l'os.

La micro-tomographie (µCT) est un outil de choix pour obtenir des images de la micro-architecture de l'os trabéculaire (Kuhn et al., 1990) ainsi que de l'os cortical et de son réseau haversien (Cooper et al., 2003; Bousson et al., 2004). En outre, la µCT peut être utilisée pour visualiser l'architecture vasculaire avec un agent de contraste (Moore et al., 2003; Zhang et al., 2005). Cependant, ces études nécessitent la décalcification de l'os. Par conséquent, la µCT n'a été utilisée que pour imager et analyser la microstructure osseuse et l'architecture vasculaire séparément, ce qui ne permet pas une analyse complète des relations entre l'os et les vaisseaux.

La micro-tomographie par rayonnement synchrotron (SR-µCT) présente l'avantage de produire des images à haute résolution spatiale avec un rapport signal/bruit élevé, par rapport à la µCT standard, en raison du flux de photons élevé des sources synchrotron (Salomé et al., 1999). La SR-µCT a été appliquée à l'analyse quantitative de l'os trabéculaire humain jusqu'à des échelles inférieures au micromètre (Peyrin et al., 1998a; Larrue et al., 2011). En outre, la SR-µCT couplée à l'utilisation d'un agent de contraste a permis de visualiser simultanément les microstructures osseuses 3D et les réseaux vasculaires chez la souris (Schneider et al., 2009) ou le rat (Prisby et al., 2011). La faisabilité de visualiser simultanément la microstructure osseuse calcifiée et les vaisseaux sanguins a également été démontrée à l'aide de la micro-tomographie par rayonnement synchrotron à contraste de phase (SR-PCT) sans agent de contraste dans un modèle de souris (Núñez et al., 2017). Toutefois, dans cette étude, le champ de vue était limité en raison de la petite taille des pixels utilisés, et les vaisseaux ont été segmentés à la main en raison du contraste de phase relativement faible dans les vaisseaux, ce qui limite les applications du protocole à de grands ensembles de données.

Chapitre 3: Techniques de segmentation d'images biomédicales

Introduction

La segmentation est une étape importante dans l'analyse des images. Dans cette thèse, nous visons à proposer un protocole automatique pour segmenter l'os et les vaisseaux du tibia de souris, imagé à l'aide de SR-µCT avec un agent de contraste. Il est donc nécessaire de présenter l'état de l'art des techniques de segmentation pour la séparation des os et des vaisseaux sur les images de µCT.

Techniques de segmentation

La segmentation manuelle exige des experts qu'ils délimitent le contour ou spécifient chaque unité (pixel ou voxel) de l'objet d'intérêt, coupe par coupe ou en 3D. Elle est utilisée dans bon nombre d'études comme par exemple celle de (Núñez et al., 2017) pour segmenter les vaisseaux dans les images SR-PCT. La segmentation manuelle intègre les connaissances préalables des experts et son résultat est généralement utilisé comme une vérité terrain pour évaluer la précision des techniques de segmentation automatique (Preim and Botha, 2013; Starmans et al., 2020). Toutefois, pour les images 3D ou les grands ensembles de données, la segmentation manuelle peut être très fastidieuse, laborieuse et longue. L'autre inconvénient de la segmentation manuelle est qu'elle est sujette à la variabilité intra et inter-observateurs (Starmans et al., 2020).

La méthode de seuillage global est la technique de segmentation de base et la plus utilisée. Dans cette méthode, un niveau de seuil est fixé sur les niveaux de gris de l'image pour séparer un objet du fond sur l'image originale (Leszczyński et al., 2016). Dans le contexte qui nous intéresse, le seuillage global a été utilisé pour segmenter les microstructures osseuses chez le rat (Hsu et al., 2013; Coutel et al., 2018; Sharma et al., 2018), et chez la souris (Mehadji, Ahmed and Berteau, 2019; Oliviero et al., 2019). En outre, cette méthode a également été appliquée pour segmenter l'os et la vascularisation sur une image µCT. (Schneider et al., 2009; Zeitoun et al., 2019). Malgré la facilité de mise en œuvre du seuillage global, cette méthode suppose un histogramme bimodal et la qualité de la segmentation est facilement réduite par le durcissement du faisceau, les artefacts, les effets de volume partiel et le bruit sur l'image.

La croissance de région est également une méthode très populaire dans le domaine de la segmentation d'images. Elle démarre à partir des germes initiaux et agrège les pixels (ou voxels) adjacents selon un critère prédéfini (Erdt, Steger and Sakas, 2012). La croissance de région a été utilisée pour segmenter les vaisseaux et les os à partir d'images SR-µCT, dans un modèle de rat (Langer et al., 2010; Prisby et al., 2011) et dans un modèle de souris (Roche et al., 2012). Cependant, chez le tibia de la souris, les vaisseaux peuvent sembler être en contact avec la surface de l'os sur l'image SR-µCT, ce qui empêche les segmentations correctes de l'os et des vaisseaux en utilisant cette méthode.

Les techniques de segmentation basées sur des modèles sont des approches puissantes pour effectuer des tâches de segmentation en utilisant des connaissances préalables sur l'emplacement, la taille et la forme de l'objet (McInerney and Terzopoulos, 1996; Preim and Botha, 2013). La technique des contours actifs (Tassani, Korfiatis and Matsopoulos, 2014; Korfiatis, Tassani and Matsopoulos, 2017) et la technique basée sur l'atlas (Newton,

Junginger and Maerz, 2020), qui appartient à la famille des méthodes basées sur des modèles, ont été par exemple utilisées pour segmenter l'os sur une image µCT.

Chapitre 4: Évaluation de la qualité de la segmentation

Introduction

Après la segmentation de l'image, il est important d'évaluer si la qualité de la segmentation est suffisamment élevée pour l'étape ultérieure de l'analyse de l'image. L'évaluation de la qualité de la segmentation est souvent effectuée en comparant le résultat de la segmentation avec une image de référence (Mohan and Subashini, 2019; Wang, Wang and Zhu, 2020). Les mesures d'évaluation les plus couramment utilisées comprennent les méthodes de comparaison basées sur le recouvrement et les méthodes de comparaison basées sur la distance.

Méthodes de comparaison basées sur le recouvrement

Un certain nombre de mesures d'évaluation pour une segmentation en deux classes ont été proposées : sensibilité (également appelée taux de vrais positifs), spécificité (également appelée sélectivité ou taux de vrais négatifs), précision (ou valeur prédictive positive), exactitude, indice de Jaccard, coefficient de Dice (également appelé F1score ou coefficient de similarité de Dice), coefficient de corrélation de Matthews (MCC).

La segmentation et l'évaluation d'images multi-classes ont également été largement étudiées dans le domaine de l'analyse d'images. Dans cette thèse, dans l'étude de l'analyse des microstructures des os et des vaisseaux basée sur l'image SR-μCT, trois classes d'os, de vaisseaux et de fond doivent être segmentées et évaluées (Langer et al., 2010; Núñez et al., 2017).

La précision est l'une des mesures d'évaluation globale les plus couramment utilisées. Sa définition peut être simplement étendue à des segmentations multi-classes, puisqu'elle considère toutes les classes de la segmentation correcte parmi le nombre total d'éléments d'image. Le coefficient de Dice, peut également être étendu pour une évaluation multi-classes en utilisant la procédure de moyenne, basée sur la mesure à deux classes (Chicco and Jurman, 2020). Le MCC a été étendu pour évaluer la qualité de la segmentation multi-classe (Gorodkin, 2004).

CONTRIBUTION

Chapitre 5: Approches de segmentation de l'image et évaluation de la qualité

Introduction

Pour analyser quantitativement les os et les vaisseaux, une méthode de segmentation de l'image robuste est indispensable. De nombreuses approches ont été développées pour segmenter les os et les vaisseaux dans les études précliniques. En général, la méthode par seuillage global reste la plus couramment utilisée en pratique (Schneider et al., 2009) mais sa qualité est facilement réduite par les artefacts qui peuvent être présents dans l'image tomographique (durcissement du faisceau, volume partiel, bruit…). La croissance de région est une autre technique courante utilisée pour segmenter les os et les vaisseaux. Contrairement au seuillage global, cette méthode prend en compte la connectivité des régions composant la structure et a donné de bons résultats dans des travaux antérieurs sur la vascularisation osseuses de rats à partir d'images SR-µCT (Langer et al., 2010; Prisby et al., 2011).

Toutefois ces méthodes se révèlent insuffisantes pour la segmentation des structures osseuses et vasculaires dans des images SR-µCT de souris et de nouvelles méthodes doivent être recherchées.

Pour relever ce défi, nous avons développé un algorithme de segmentation par bassins versants contrôlés par marqueurs en conjonction avec l'asymétrie de phase du signal monogénique.

Bassin versant contrôlé par marqueur

Méthode des bassins versants contrôlée par des marqueurs inonde "l'eau" à partir de marqueurs initialement identifiés sur une surface de contrôle, puis segmente une image en plusieurs objets en détectant des "bassins" et des "lignes de crête" lorsque les différentes sources d'eau fusionnent. Cette méthode peut éliminer les effets causés par des minima régionaux non souhaités. En outre, cette approche permet de gagner du temps en réduisant le nombre d'itérations et simplifie la fusion des segments résultants (Beucher and Meyer, 1990; Gonzalez and Woods, 2017).

Génération de marqueurs

Une étape importante de la méthode proposée consiste à générer des marqueurs pour initialiser l'algorithme du bassin versant. Nous avons ici trois classes de marqueurs : les os, les vaisseaux et le fond, qui ont été générés à l'aide de seuils d'hystérésis et de filtres morphologiques. L'objectif est d'obtenir une couverture de tous les composants connectés dans chaque classe et d'éviter les faux positifs. La procédure de génération des marqueurs est illustrée sur la une coupe d'os de souris dans l'image SR-µCT dans la Fig. 1. L'image finale du marqueur a été générée en ajoutant le marqueur de fond, le marqueur de vaisseau et le marqueur d'os, en bleu, rouge et vert, respectivement.

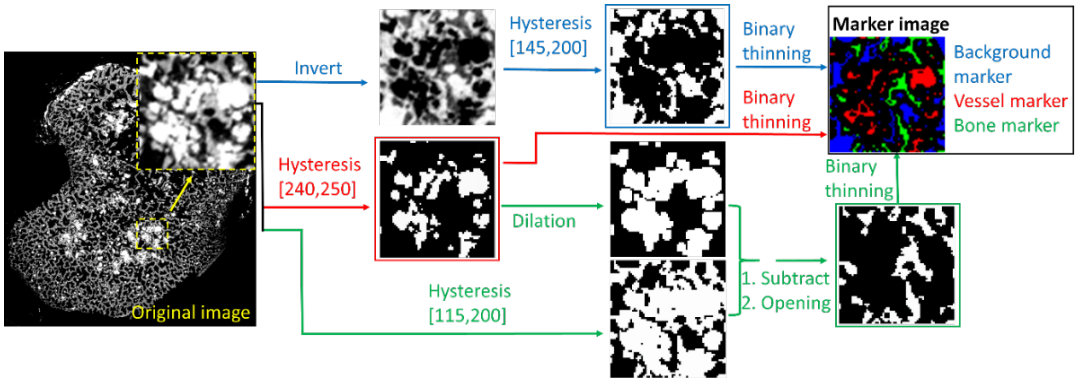

Fig. 1 Procédure de génération de l'image du marqueur. Les marqueurs du fond, des vaisseaux et des os sont donnés par des flèches bleues, rouges et vertes, respectivement.

Génération de surfaces de contrôle

L'autre étape essentielle de l'algorithme des bassins versants contrôlés par des marqueurs est la génération d'une surface de contrôle. Classiquement, l'amplitude du gradient est utilisée comme surface de contrôle, en relation avec les changements d'intensité dans l'image originale (Bhabatosh, 2011). Cependant, dans notre cas, le contraste aux interfaces entre les os et les vaisseaux est relativement faible par rapport aux interfaces os - fond et vaisseaux - fond, ce qui entraîne une plus faible amplitude du gradient à ces interfaces.

Pour pallier ce problème, nous proposons d'exploiter l'asymétrie de phase du signal monogénique 3D comme surface de contrôle pour améliorer la détection des bords aux interfaces à faible contraste. La phase locale du signal monogénique a la propriété d'être invariante par rapport à l'intensité du signal, et l'asymétrie de phase peut être utilisée pour quantifier si le signal est localement de type front ou ligne. L'objectif étant de détecter les interfaces entre différentes structures, nous n'avons utilisé que les structures en forme de bord comme surface de contrôle (Felsberg and Sommer, 2001; Bridge, 2017).

Les surfaces de contrôle générées sont illustrées à la Fig. 2. La Fig. 2 (a) montre un zoom sur une tranche 2D du volume original 3D. La flèche rouge montre l'interface de contraste relativement faible entre l'os et le vaisseau. La surface de contrôle a été générée en utilisant les méthodes de détection des bords en 3D. Par exemple, la Fig. 2 (b) montre le gradient d'image de l'image originale comme surface de contrôle. La limite à faible contraste entre l'os et le vaisseau ne peut pas être bien détectée comme la flèche rouge. La Fig. 2 (c) montre l'asymétrie de phase (multi-échelle $\lambda = 6, 7, 8$) du signal monogénique 3D comme surface de contrôle. Même si la méthode de l'asymétrie de phase permet de détecter certains bords parasites dans des zones homogènes, ceux-ci sont toujours couverts par un marqueur dans les zones solides. Par conséquent, ils n'influencent pas les résultats de la segmentation. En comparant les surfaces de contrôle utilisant l'asymétrie de phase Fig. 2 (c) à l'utilisation du gradient d'image Fig. 2 (b), on constate des améliorations substantielles dans la détection des bords d'interface à faible contraste, comme le montre la flèche rouge.

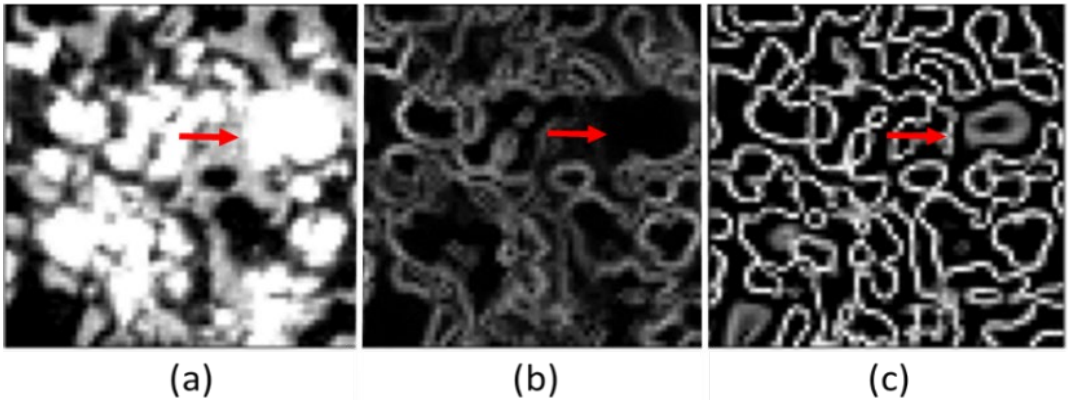

Fig. 2 Illustration des surfaces de contrôle générées. (a) Image originale. (b) Surface de contrôle générée en calculant l'amplitude du gradient. (c) Surface de contrôle générée en utilisant l'asymétrie de phase multi-échelle du signal monogénique 3D. Toutes les images sont des tranches 2D des volumes 3D.

Segmentation manuelle

Après la segmentation de l'image, il est très important d'évaluer si la qualité de la segmentation est suffisamment élevée pour l'étape ultérieure de l'analyse quantitative. Dans cette étude, nous avons segmenté manuellement deux volumes représentatifs comme images de référence. Ici, nous avons utilisé l'outil 3D Magic Wand du logiciel VGStudio Max (Volume Graphics GmbH, Heidelberg, Allemagne) pour créer les sélections d'un objet. Ces deux petits volumes (64×64×64 voxels) ont été sélectionnés à partir d'une image 3D pour représenter une structure simple et complexe. Les Fig. 3 et 4 montrent les résultats de la segmentation manuelle pour les structures simples et complexes, respectivement.

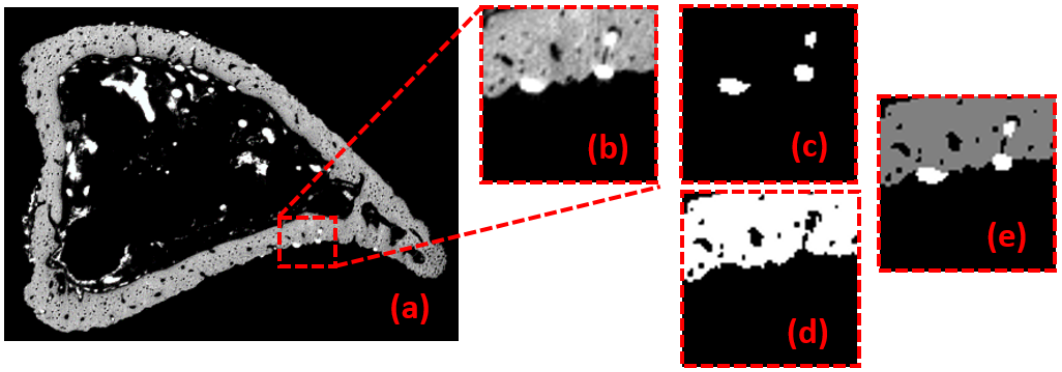

Fig. 3 Illustration de la segmentation manuelle pour une structure simple. (a) L'ensemble de l'image originale. (b) La petite image originale représentative. (c) La segmentation manuelle du navire. (d) La segmentation manuelle de l'os. (e) L'image composite des segmentations manuelles comprenant à la fois les compartiments des vaisseaux (blanc) et des os (gris). Toutes les images sont des coupes en 2D sélectionnées dans les volumes en 3D.

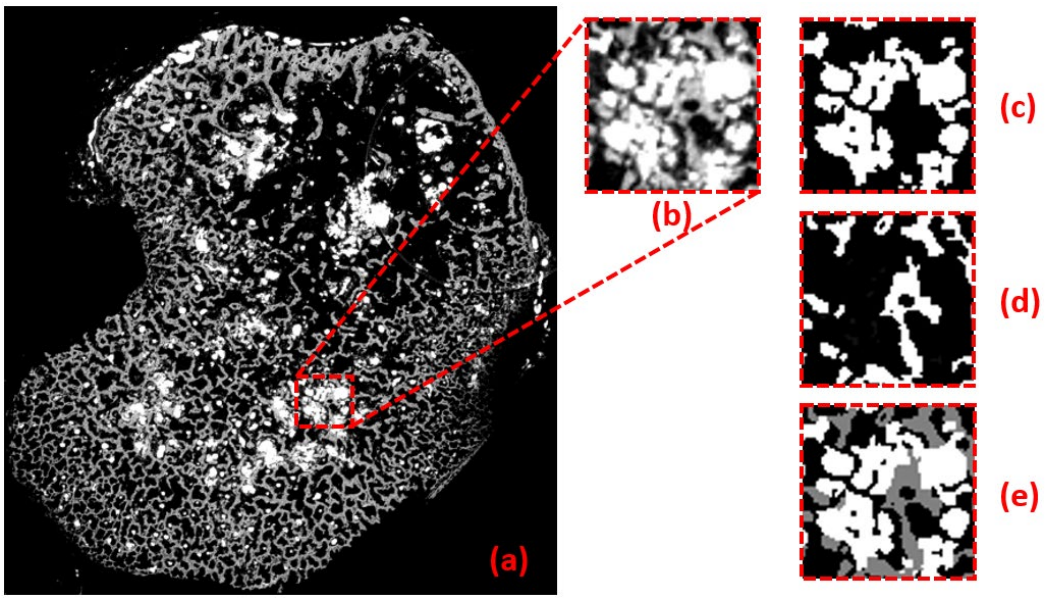

Fig. 4 Illustration de la segmentation manuelle pour une structure complexe. (a) L'ensemble de l'image originale. (b) La petite image originale représentative. (c) La segmentation manuelle du navire. (d) La segmentation manuelle de l'os. (e) L'image composite des segmentations manuelles comprenant à la fois les compartiments des vaisseaux (blanc) et des os (gris). Toutes les images sont des coupes en 2D sélectionnées dans les volumes en 3D.

Évaluation

Enfin, la qualité de la segmentation de chaque compartiment (os, vaisseau ou fond) a été validée à l'aide du coefficient de Dice, et la qualité globale de la segmentation a été évaluée à l'aide du coefficient de corrélation de Matthews (MCC), par comparaison avec la segmentation manuelle.

Chapitre 6: Évaluation de l'approche de segmentation sur les données synthétiques

Introduction

Afin d'évaluer la précision et la robustesse de l'approche proposée, ainsi que sa généralisation à d'autres applications, nous avons fait une étude sur divers volumes synthétiques 3D. Tout d'abord, nous avons généré des volumes synthétiques en 3D pour imiter les ensembles de données réels. Ici, nous avons considéré la validation de la segmentation de la structure mince, les différents contrastes entre les différentes classes, ainsi que les différents niveaux de bruit. Ensuite, les volumes synthétiques multi-classes créés ont été segmentés en utilisant la méthode proposée (bassin versant contrôlé par marqueur proposé en conjonction avec l'asymétrie de phase du signal monogénique). La qualité globale de la segmentation a été évaluée à l'aide du coefficient de corrélation de Matthews (MCC) en la comparant à la vérité de terrain. Enfin, nous avons étudié l'impact des contrastes et des niveaux de bruit sur les segmentations, et étudié la capacité de segmentation d'une structure mince sous différents niveaux de bruit.

Génération de 3D modèles synthétiques

Les objectifs de la conception de modèles synthétiques 3D sont d'imiter les types de structures que l'on peut trouver pour les vaisseaux, les os et le fond dans nos données expérimentales. Dans cette étude, quatre types de modèles synthétiques 3D (images 3D 8 bits avec 256×256×150 voxels) ont été créés, comme le montre la Fig. 5. Le modèle-1 a été conçu pour simuler la structure 3D des vaisseaux (niveau de gris 255) et la porosité des os (niveau de gris 0) de différentes épaisseurs, qui étaient entourés par l'os (niveau de gris 128), comme le montre la Fig. 5 (a). Le modèle-2 simulait que les vaisseaux (niveau de gris 255) étaient en contact avec la surface de l'os (niveau de gris 128) et le fond (niveau de gris 0) en même temps, comme le montre la Fig. 5 (b). Le modèle-3 a été conçu pour simuler une structure isolée dans l'ensemble de données du monde réel, comme le montre la Fig. 5 (c). Le modèle-4 décrit une situation dans laquelle un vaisseau (niveau de gris 255) traverse une porosité osseuse variable (niveau de gris 0), comme le montre la Fig. 5 (d). Le cylindre mince au centre du vaisseau simulé, et la structure entourant ce cylindre était la structure osseuse synthétique (niveau de gris 128).

Pour étudier l'impact des contrastes sur la segmentation, dans les modèles-1, 2 et 4, les niveaux de gris des cylindres, qui simulent les structures osseuses dans les données réelles, ont été fixés à une intensité croissante à partir de 48 à 208 (les contrastes définis de 48 à 208 se référant au fond). Dans le modèle-3, le niveau de gris de la structure du sablier augmentait à partir de l'intensité de 48 à 255 (contraste défini 48 à 255 se référant au fond).

De plus, pour explorer l'influence du bruit sur la segmentation, différents niveaux de bruit gaussien ont été ajoutés sur les fantômes synthétiques 3D. Le niveau de bruit a été défini par l'écart-type du bruit gaussien, passant de 10 à 70.

Nous avons ainsi généré 259 volumes synthétiques pour quatre modèles.

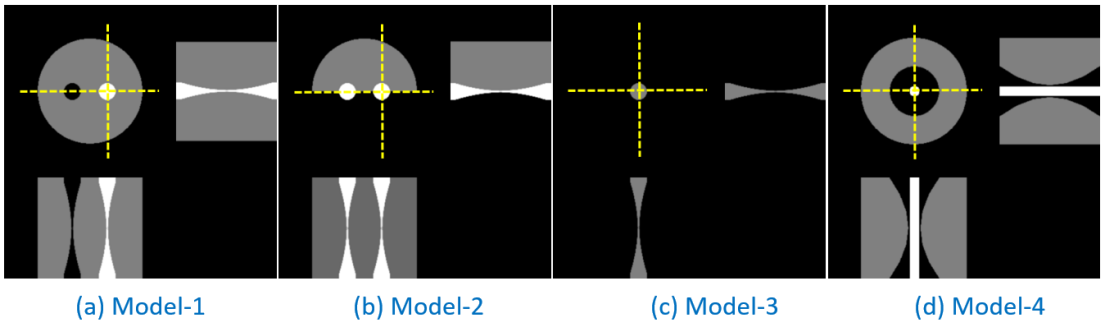

Fig. 5 Trois tranches orthogonales dans les modèles synthétiques 3D : (a) Le modèle-1 représente la structure des vaisseaux (niveau de gris 255) et la porosité des os (niveau de gris 0) de différentes épaisseurs, qui sont entourés par l'os (niveau de gris 128). (b) Le modèle-2 simule que les vaisseaux sont en contact avec la surface de l'os et le fond en même temps. (c) Le modèle-3 représente une structure isolée dans l'ensemble de données du monde réel. (d) Le modèle-4 décrit la situation dans laquelle un vaisseau passe à travers une porosité osseuse variable.

Résultats

Des compartiments multi-classes de chaque volume synthétique ont été segmentés en utilisant la méthode proposée. Nous montrons 9 exemples de segmentations pour chaque modèle, obtenus à partir du volume d'intérêt (VOI) du volume synthétique, sous les différents contrastes et niveaux de bruit, comme le montre la Fig. 6. Toutes les coupes 2D ont été sélectionnées à partir des volumes 3D. Les Fig. 6 (a), (b), (c) et (d) représentent respectivement le modèle-1, le modèle-2, le modèle-3 et le modèle-4. Dans chaque modèle, des segmentations ont été obtenues à partir des volumes synthétiques avec des contrastes de 48, 128 et 208 (ou 255) ainsi que des niveaux de bruit de 10, 30 et 70. Les cases rouges dans les figures représentent les segmentations complètement mauvaises. Elles ont été exclues, car il est difficile de séparer correctement deux classes qui ont une interface relativement peu contrastée, surtout en présence d'un niveau de bruit élevé.

Enfin, nous avons mesuré les valeurs MCC sur une gamme de niveaux de bruit à chaque contraste. Fig. 7 illustre un exemple des relations entre la MCC et les niveaux de bruit avec les différents contrastes, dans le modèle-1.

Une série de résultats de segmentation indique que l'approche de segmentation proposée peut mieux fonctionner aux contrastes de 128 et148 dans le modèle à trois classes, et au contraste de 255 dans le modèle à deux classes.

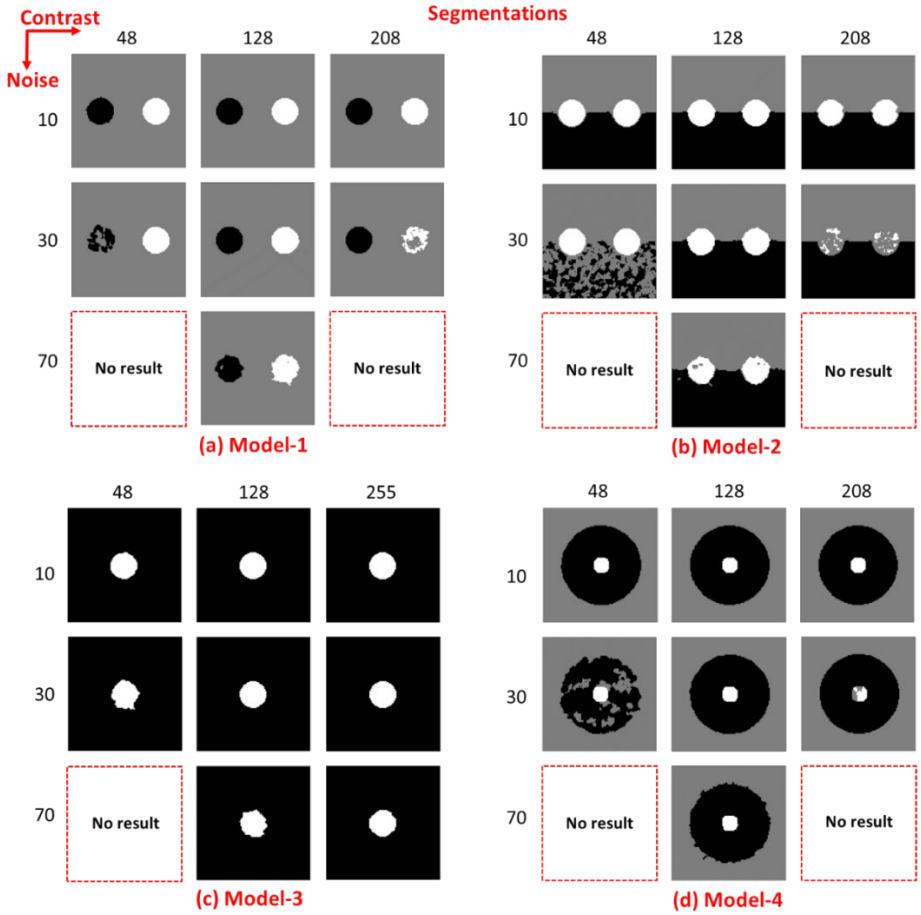

Fig. 6 Illustration des impacts des contrastes d'image et des niveaux de bruit sur les segmentations. (a) modèle-1, (b) modèle-2, (c) modèle-3, (d) modèle-4. 9 exemples de segmentations pour chaque modèle ont été obtenus à partir du VOI de volumes synthétiques avec des contrastes de 48, 128 et 208 (ou 255), ainsi que des niveaux de bruit de 10, 30 et 70. Toutes les tranches 2D ont été sélectionnées à partir des volumes 3D.

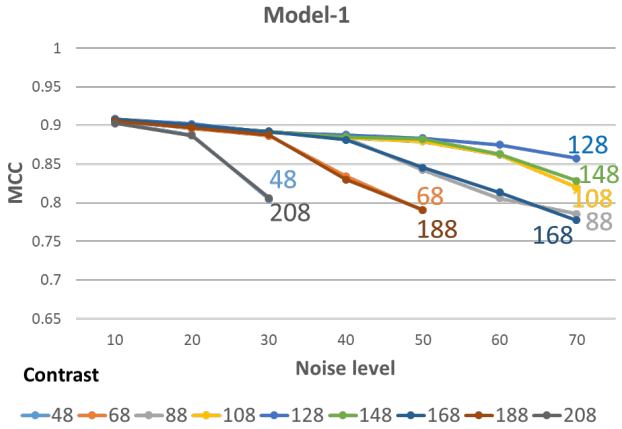

Fig. 7 Illustration des relations entre la MCC et les niveaux de bruit, dans le modèle-1. Les contrastes vont de 48 à 208, et les niveaux de bruit de 10 à 70.

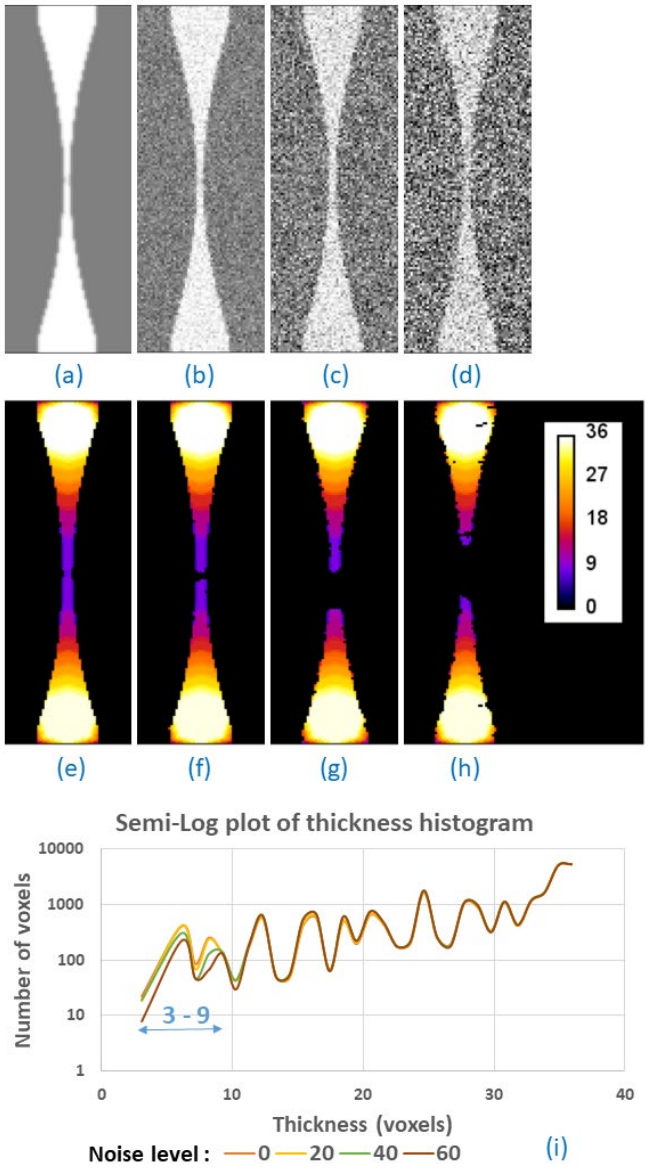

Fig. 8 Illustration de la capacité de segmentation sur une structure mince. (a) Fantôme sans bruit, qui est un VOI sélectionné dans le modèle-1. (b-d) images bruyantes, avec des niveaux de bruit de 20, 40 et 60, respectivement. (e-h) des cartes 3D d'épaisseur locale de structures en sablier, correspondant aux segmentations de (a-d) respectivement. Toutes les images de (a-h) sont des tranches 2D sélectionnées dans les volumes 3D. (i) Graphique semi-logarithmique, montrant le nombre de voxels à chaque épaisseur en (e-h).

De plus, nous avons étudié la capacité de segmentation sur une structure mince sous les différents niveaux de bruit gaussien. Les volumes générés sont représentés comme suit : Fig. 8 (a) sans bruit, Fig. 8 (b) avec des niveaux de bruit de 20, Fig. 8 (c) avec des niveaux de bruit de 40 et Fig. 8 (d) avec des niveaux de bruit de 60. Toutes les figures sont des tranches en 2D sélectionnées à partir du VOI du modèle-1. Ensuite, les structures en sablier de la Fig. 8 (a-d) ont été segmentées en utilisant la méthode proposée. Afin de quantifier la segmentation des

structures fines, nous avons d'abord sélectionné la structure en sablier à partir de la vérité de terrain, et mesuré sa carte d'épaisseur locale en 3D. Ensuite, nous avons masqué la carte d'épaisseur avec les segmentations de la structure en sablier, correspondant aux images originales avec différents niveaux de bruit, comme le montre la Fig. 8 (e-h). Enfin, nous avons mesuré le nombre de voxels à chaque épaisseur, comme le montre la Fig. 8 (i).

Les résultats montrent que la structure mince (épaisseur de 3 à 9 voxels) peut être bien segmentée à des niveaux de bruit inférieurs à 20, et la structure épaisse (épaisseur de 10 voxels ou plus) peut être bien segmentée même au niveau de bruit de 60 en utilisant la méthode proposée.

Chapitre 7: Analyse quantitative des données sur les souris à l'aide de SR-µCT

Introduction

Le cancer du sein est un cancer fréquent chez les femmes dans le monde entier, et la principale mortalité est causée par les métastases osseuses. Les métastases osseuses du cancer du sein peuvent non seulement provoquer des destructions osseuses, mais aussi faciliter la formation d'une vascularisation indésirable (Akhtari et al., 2008; Tang et al., 2014; Holen et al., 2016; Bray et al., 2018).

Une stratégie de traitement importante pour le cancer du sein avancé est le médicament anti-angiogénique. Il existe de nombreuses preuves que l'angiogenèse est une étape limitant le taux de croissance des tumeurs osseuses métastatiques, ce qui en fait une cible pertinente pour une intervention thérapeutique (Ebos and Kerbel, 2011). Cependant, dans un modèle murin de métastase osseuse du cancer du sein, les molécules anti-angiogéniques ciblant le VEGF (Bevacizumab) ou son récepteur (Vatalanib), n'ont pas réussi à réduire le développement des lésions osseuses lorsqu'elles étaient administrées seules, alors que leur combinaison l'a fait. Ainsi, l'hypothèse est que la combinaison des deux médicaments permettra une meilleure suppression des métastases (Bachelier et al., 2014).

Ce travail a été consacré à l'étude de la cinétique de la réponse des os et de la vascularisation à l'invasion et aux traitements des tumeurs. Pour mieux comprendre la pathologie, nous avons utilisé l'imagerie 3D pour l'analyse quantitative des os et des vaisseaux.

Préparation des échantillons et imagerie

Dans cette étude, des souris femelles ont reçu des injections de cellules tumorales du cancer du sein, et différents traitements préventifs. Nous considérerons quatre types de traitements reçus : un placebo, du Sorafenib (vatalanib, inhibant les récepteurs du VEGF), de l'Avastin (bevacizumab, inhibant le VEGF-A) et un traitement médicamenteux combiné comprenant à la fois du Sorafenib et de l'Avastin. Pour mieux décrire l'implication de l'angiogenèse dans le processus de métastases osseuses, nous avons considéré deux moments (au début et à la fin du développement des métastases osseuses), correspondant respectivement à 8 et 22 jours après l'inoculation des cellules tumorales. La procédure est illustrée à la Fig. 9. Les 70 échantillons ont été divisés en 8 groupes en fonction des différents temps et traitements reçus.

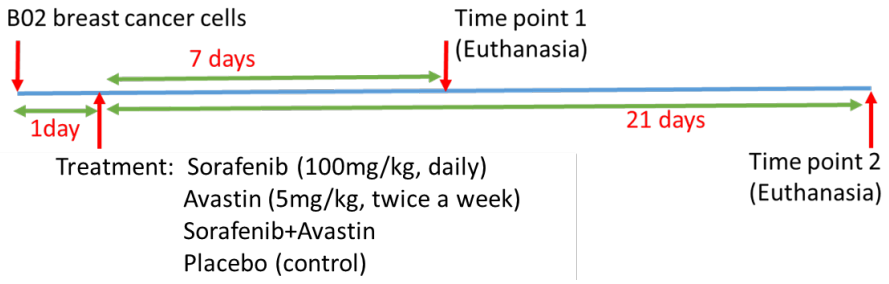

Fig. 9 Illustration de la préparation des échantillons. Il y a 3 traitements et 1 groupe placebo au début et à la fin de la période, correspondant respectivement à 8 et 22 jours après l'inoculation des cellules tumorales.

Les modèle de souris ont été préparés au LYOS, et la perfusion intravasculaire de sulfate de baryum réalisée au laboratoire Sainbiose. Des échantillons de tibia ont ensuite été prélevés pour être imagés par SR-µCT. Le schéma de l'installation d'imagerie est présenté à la Fig. 10.

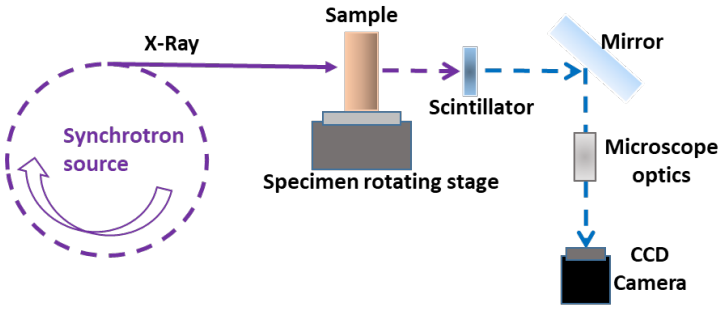

Fig. 10 Schéma de l'installation d'imagerie SR-µCT. Des X-ray de 26 keV ont illuminé un échantillon monté sur une platine de rotation 3D. Un détecteur à base de CCD a été utilisé pour enregistrer les images par le biais d'un système optique et d'un microscope.

Prétraitement sur le volume osseux

Les différents volumes osseux reconstruits étaient dans des orientations différentes, ce qui peut affecter les comparaisons de mesures suivantes dans l'analyse quantitative. Ainsi, nous avons tout d'abord effectué un prétraitement des images afin de réorienter les volumes osseux. De plus, pour éviter l'influence de l'épiphyse sur la sélection de la métaphyse, nous avons créé des masques pour enlever les épiphyses des volumes osseux. La Fig. 11 illustre une image originale (a) et le résultat final de prétraitement (b), après suppression de l'épiphyse, réorientation, recadrage et boîte englobante. Tous les traitements ont été effectués en 3D sur ITK- SNAP logiciel.

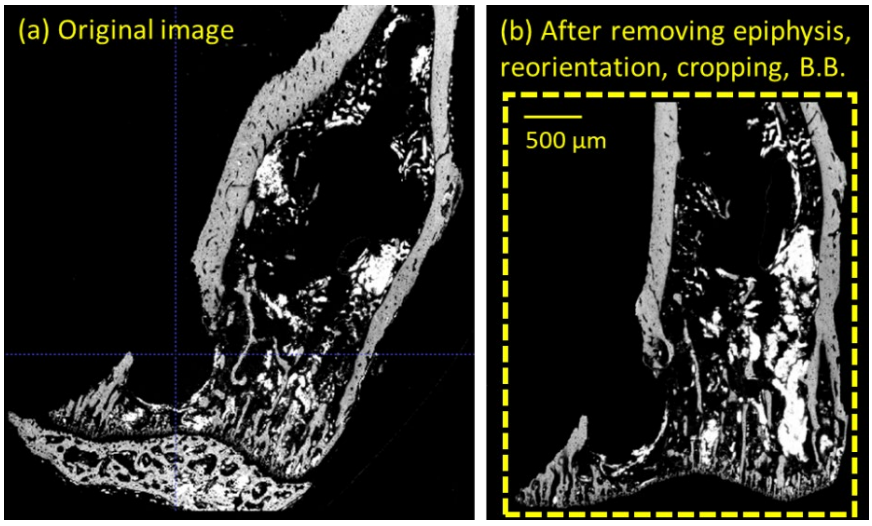

Fig. 11 Illustration du prétraitement sur le volume osseux. (a) Image originale. (b) Volume osseux final, après élimination de l'épiphyse, réorientation, recadrage et boîte englobante. Toutes les images sont des tranches en 2D des volumes en 3D. Les lignes de points bleus sont des réticules.

Segmentation

Ensuite, les images 3D prétraitées des os de souris ont été segmentées en vaisseaux, en os et en compartiments de fond à l'aide de l'algorithme de bassin versant contrôlé par marqueurs et de l'asymétrie de phase du signal monogénique, décrit précédemment. Pour comparer qualitativement l'échantillon sain avec l'échantillon métastatique, les rendus 3D des segmentations en volume sont présentés à la Fig. 12 (a-d). L'échantillon métastatique de la Fig. 12 (b) montre des lésions osseuses importantes évidentes, comparé à l'échantillon sain de la Fig. 12 (a). En outre, l'échantillon métastatique contient davantage de vaisseaux plus épais que l'échantillon sain, par comparaison la Fig. 12 (d) avec (c). Cela indique une vascularisation accrue et anormale due aux métastases osseuses, comme attendu.

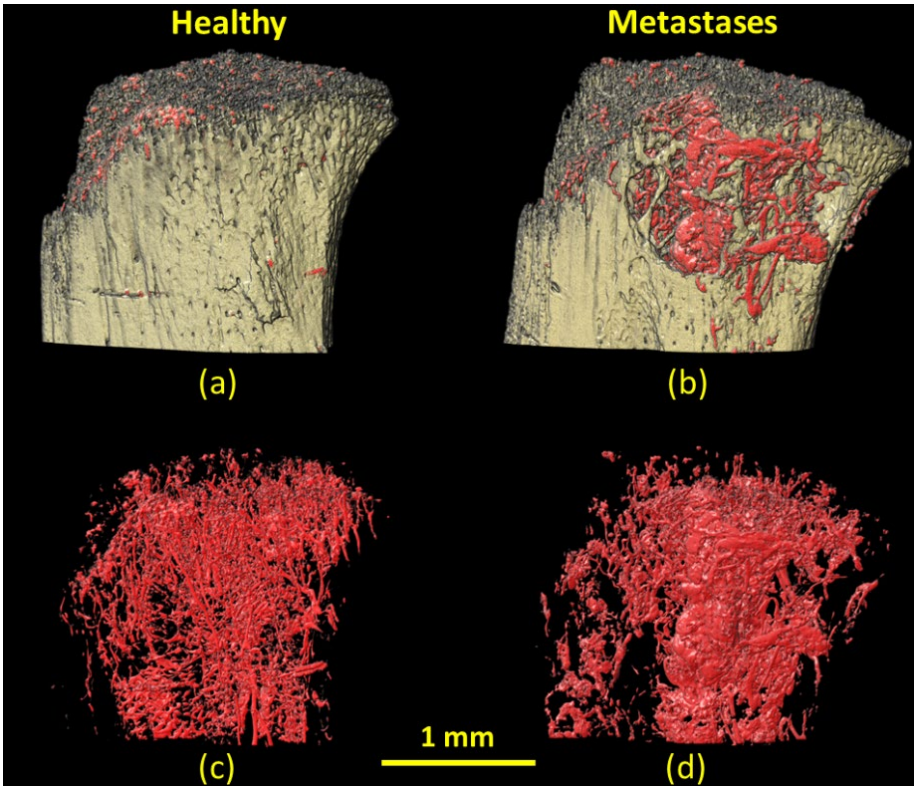

Fig. 12 Illustration des comparaisons entre échantillons sains et métastases. (a) Rendu 3D de l'os et du vaisseau dans un os sain. (b) Rendu 3D de l'os et du vaisseau dans un os métastatique. (c) Rendu 3D des vaisseaux dans un os sain. (d) Rendu 3D des vaisseaux dans un os métastatique.

Résultats

La qualité de la segmentation a été évaluée à l'aide du coefficient Dice et du MCC en la comparant aux segmentations manuelles. Il y a des améliorations substantielles dans le bassin versant contrôlé par marqueur proposé et l'asymétrie de phase du signal monogénique, par rapport à la méthode basée sur le seuil d'hystérésis ainsi qu'au bassin versant contrôlé par marqueur basé sur le gradient, en termes de Dice (à chaque compartiment individuel) et de MCC (à la segmentation globale), indiqué dans le Tableau 1.

Tableau 1. Évaluation de la qualité de la segmentation entre les différentes méthodes.

Evaluations / Methods	Dice (Vessel)	Dice (Bone)	Dice (Background)	MCC (Overall)
Hysteresis thresholding	0.84	0.81	0.85	0.77
Gradient + watershed	0.92	0.91	0.93	0.88
Phase asymmetry + watershed	0.97	0.92	0.97	0.94

Analyse quantitative

Pour caractériser les microstructures osseuses et les vaisseaux sanguins, plusieurs paramètres ont été calculés.

Les paramètres suivants ont été calculés : sur l'os entier (BV/TV, Ct.V/TV, Me.V/TV, Ct.Th), sur l'os trabéculaire de la métaphyse (Tb.V/Me.Ca.V, Tb.Th, FD, SMI, Conn.D, DA), la porosité corticale en diaphyse (Ct.Po.V/Ct.TV), sur les vaisseaux (VV/TV, V.Th, FD, DA). Une analyse statistique a ensuite été réalisée avec un test approprié pour étudier les effets des traitements médicamenteux sur les os et les vaisseaux.

- Bone volume (BV)
- Total volume (TV): volume à l'intérieur du contour extérieur de l'os cortical.
- Trabecular bone volume (Tb.V)
- Cortical bone volume (Ct.V)
- Metastases volume (Me.V)
- Medullary cavity volume (Me.Ca.V)
- Volume of pores in cortical bone (Ct.Po.V)
- Cortical envelope volume (Ct.TV): volume de l'os cortical dont la porosité est comblée.
- Vessel volume (VV)
- Mean trabecular thickness (Tb.Th)
- Mean cortical thickness (Ct.Th)
- Mean vessel thickness (V.Th)
- Fractal dimension (FD)
- Structure model index (SMI)
- Connectivity density (Conn.D)
- Degree of anisotropy (DA)

Résultats de l'analyse quantitative

Fig. 13 montre un exemple de diagramme en boîtes pour les fractions du volume osseux trabéculaire (Tb.V/Me.Ca.V) dans les différents groupes.

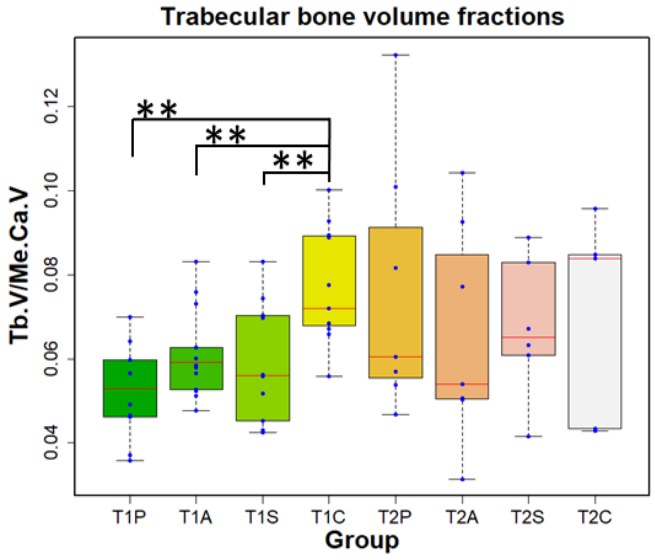

Fig. 13 Diagrammes en boîtes des fractions du volume osseux trabéculaire (Tb.V/Me.Ca.V) aux différents groupes, au premier point dans le temps (T1P, T1A, T1S et T1C) et au deuxième point dans le temps (T2P, T2A, T2S et T2C). La ligne rouge dans chaque case représente la valeur médiane de l'ensemble des données. L'astérisque ** indique une différence statistiquement significative, au niveau de la valeur p = 0,05. (P : Placebo, A : Avastin, S : Sorafenib, C : Combinaison A et S)

En considérant BV/TV, Ct.V/TV, Me.V/TV, Ct.Th, Tb.V/Me.Ca.V et Tb.Th, nous déduisons que des métastases se sont développées sur l'os trabéculaire, mais pas encore sur l'os cortical au premier point temporel. En outre, nous concluons que les médicaments anti-angiogenèse peuvent réduire la masse osseuse en érodant l'épaisseur de l'os, dans une interaction à long terme. Au deuxième point temporel, bien que des métastases se soient développées à la fois sur l'os trabéculaire et l'os cortical, la réduction des lésions osseuses et la diminution de l'épaisseur de l'os par les médicaments sont arrivées à un échantillon en même temps, ce qui n'a pas entraîné de différence significative entre les divers groupes pour la fraction du volume osseux.

En ce qui concerne la FD, la SMI, la Conn.D et la DA pour l'os trabéculaire en métaphyse, les mesures indiquent également l'existence de métastases au premier point temporel. En outre, les interactions à long terme avec les médicaments entraînent la perte d'os mince par érosion et affectent encore plus les structures morphologiques de l'os trabéculaire au deuxième point temporel. Il n'y a donc pas de différence significative entre les différents groupes pour ces paramètres.

En ce qui concerne la Ct.Po.V/Ct.TV, nous avons supposé que les porosités sur l'os cortical sont des canaux de microvascularisation. Dans un premier temps, d'après les mesures et les tests statistiques, il n'y a pas de différence significative entre les différents groupes pour la Ct.Po.V/Ct.TV, puisque les vascularisations anormales ne se sont pas encore développées. Au stade tardif des métastases osseuses, nous en déduisons que les porosités peuvent être réduites par la suppression sur le vaisseau par les médicaments anti-angiogénèse. De plus, nous devons considérer l'influence de l'érosion sur l'épaisseur de l'os par une interaction à long

terme avec les médicaments, car elle peut étendre la taille de la porosité et n'entraîner aucune différence significative entre les différents groupes.

Si l'on considère les paramètres VV/TV, V.Th, FD, DA pour les vaisseaux, il n'y a pas de différence significative entre les différents groupes au premier point temporel, car il est encore au stade précoce des métastases osseuses et les médicaments anti-angiogénèse n'ont pas encore supprimé les vascularisations anormales. Au deuxième point temporel, on trouve qu'il y a moins de vaisseaux, qu'ils sont plus fins, dans le groupe de traitement combiné par rapport aux autres groupes, comme prévu. En ce qui concerne la DA, il n'y a pas de différence significative entre les différents groupes au deuxième point temporel. Cela signifie que les médicaments anti-angiogenèse n'affectent pas l'orientation des vaisseaux.

Chapitre 8: Conclusion et perspective

Conclusion

L'objectif de cette thèse était de développer une nouvelle méthode d'analyse des os et des vaisseaux à partir d'images SR-μCT et de l'appliquer à des images de tibia de souris imagé dans le contexte des métastases osseuses.

La segmentation des vaisseaux peut être difficile en raison de la complexité du réseau vasculaire et du manque de diffusion de l'agent de contraste à certains endroits. Ici, nous avons proposé une méthode basée sur les bassins versants contrôlés par marqueur pour séparer les vaisseaux qui semblent toucher la surface osseuse, sans qu'il soit nécessaire de fusionner les régions après la segmentation. Nous avons mis au point une procédure pour générer les trois classes de marqueurs qui nous intéressent (os, vaisseaux et fond), à l'aide de seuillage par hystérésis et de filtres morphologiques, permettant d'obtenir une couverture de toutes les composantes connectées dans chaque classe et d'éviter les faux positifs. Nous avons ensuite proposé une méthode originale pour générer la surface de contrôle, en exploitant l'asymétrie de la phase du signal monogénique. Cette méthode permet d'améliorer la détection des bords aux interfaces os et vaisseaux, dans lesquelles le contraste était relativement faible par rapport aux interfaces os - fond et vaisseaux - fond, ce qui conduisait à une amplitude de gradient faible à ces bords.

Pour examiner la précision et la robustesse de la méthode, ainsi que sa généralisation à d'autres applications, nous avons créé des modèles synthétiques 3D pour simuler un ensemble de données réelles. Une série de volumes synthétiques multi-classes de différents contrastes et niveaux de bruit a été segmentée en utilisant la méthode proposée, et la qualité globale de la segmentation a été évaluée à l'aide du MCC en la comparant à la vérité terrain. Les résultats indiquent que le protocole proposé peut mieux fonctionner avec un contraste de 128 et 148 dans le modèle à trois classes, et avec un contraste de 255 dans le modèle à deux classes. En outre, nous avons étudié la capacité de segmentation de la structure mince avec la méthode proposée, sous différents niveaux de bruit gaussien. Les résultats montrent que les structures minces (épaisseur de 3 à 9 voxels) peuvent être bien segmentées à des niveaux de bruit inférieurs à 20, et que les structures épaisses (épaisseur de 10 voxels ou plus) peuvent être bien segmentées même au niveau de bruit de 60 en utilisant la méthode proposée. Par conséquent, ces évaluations montrent que la méthode proposée est bien adaptée à notre application et peut également être utilisées pour d'autres applications.

La méthode proposée a ensuite été appliquée à l'ensemble des images réelles d'os de souris acquises par SR-μCT et la qualité de la segmentation a été évaluée à l'aide du coefficient Dice et du MCC en la comparant à des segmentations manuelles. Les résultats montrent les améliorations substantielles obtenues en utilisant la méthode proposée, par rapport à la méthode basée sur le seuil d'hystérésis ainsi qu'au bassin versant contrôlé par marqueur basé sur le gradient.

Nous avons ensuite effectué une analyse quantitative des microstructures osseuses et vasculaires en calculant différents paramètres morphométriques sur l'os entier, l'os trabéculaire de la métaphyse, la porosité corticale dans la diaphyse les vaisseaux (VV/TV, V.Th, FD, DA). L'analyse statistique conduit aux observations suivantes.

En considérant BV/TV, Ct.V/TV, Me.V/TV, Ct.Th, Tb.V/Me.Ca.V et Tb.Th, nous déduisons que des métastases se sont développées sur l'os trabéculaire, mais pas encore sur l'os cortical au premier point temporel. En outre, nous concluons que les médicaments anti-angiogenèse peuvent réduire la masse osseuse en érodant l'épaisseur de l'os, dans une interaction à long terme. En ce qui concerne la FD, la SMI, la Conn.D et la DA pour l'os trabéculaire en métaphyse, les interactions à long terme avec les médicaments entraînent la perte d'os mince par érosion et affectent encore plus les structures morphologiques de l'os trabéculaire. En ce qui concerne la Ct.Po.V/Ct.TV, nous avons supposé que les porosités sur l'os cortical sont des canaux de microvascularisation. Dans un premier temps, les vascularisations anormales ne se sont pas encore développées. Au stade tardif des métastases osseuses, nous en déduisons que les porosités peuvent être réduites par la suppression sur le vaisseau par les médicaments anti-angiogénèse. VV/TV, V.Th, FD, au deuxième point dans le temps, indiquent des vaisseaux moins nombreux, plus fins et moins complexes dans le groupe de traitement combiné par rapport aux autres groupes. DA signifie que les médicaments anti-angiogenèse n'affectent pas l'orientation des vaisseaux.

Perspective

Nous avons donc dans ce travail développé une nouvelle méthode de segmentation et d'analyse de la vascularisation osseuse qui est maintenant opérationnelle et peut être utilisée dans des études biologiques ultérieures. Cependant, de nombreux autres développements peuvent être poursuivis en ce qui concerne les propriétés des structures des vaisseaux. En particulier, il serait intéressant d'investiguer des approches basées sur la squelettisation pour récupérer de nouveaux paramètres sur les réseaux de vaisseaux, tels que le nombre de jonctions, la longueur moyenne des branches et la tortuosité entre deux jonctions dans les structures arborescentes.

SYMBOL LIST

Volume fraction:

BV/TV, Tb.V/TV, Ct.V/TV, Me.V /TV, Tb.V/Me.Ca.V, Ct.Po.V/Ct.TV, VV/TV. Where,

- Bone volume (BV)
- Total volume (TV): volume inside the outer contour of the cortical bone.
- Trabecular bone volume (Tb.V)
- Cortical bone volume (Ct.V)
- Metastases volume (Me.V)
- Medullary cavity volume (Me.Ca.V)
- Volume of pores in cortical bone (Ct.Po.V)
- Cortical envelope volume (Ct.TV): volume of cortical bone with porosity filled in.
- Vessel volume (VV)

Thickness:

- Mean trabecular thickness (Tb.Th)
- Mean cortical thickness (Ct.Th)
- Mean vessel thickness (V.Th)

Morphological parameters: structural information

- Fractal dimension (FD): the complexity of a structure.
- Structure model index (SMI): value 0 is for the plate-like, 3 is for the rod-like structure.
- Connectivity density (Conn.D): the number of connected structures per unit volume.
- Degree of anisotropy (DA): the low value of DA indicates disorganized structures.

I. BACKGROUND

Chapter 1

1. Introduction

Contents

1.1 Background

Breast cancer is cancer that forms in the cells of the breast tissue. It is one of the most common diagnosed cancers in women worldwide (Bray et al., 2018). In the advanced phase, breast cancer can spread outside the breast through blood vessels and facilitate the formation of undesirable vascularization. Once tumor cells metastasize to bone, it can cause osteolytic lesions (Tang et al., 2014; Holen et al., 2016). Then, the breast cancer bone metastases may endanger the patient, and even lead to mortality (Akhtari et al., 2008; Tulotta et al., 2019). The median survival rate is about 24 to 65 months (Lote, Walløe and Bjersand, 1986; Nutter et al., 2014; Catarina et al., 2017). Unfortunately, the mechanism of breast cancer bone metastases is still partially understood, and substantial investigations and researches are required.

Angiogenesis is the formation of new blood vessels and can be a rate-limiting step in the growth of metastatic bone tumors. Therefore, anti-angiogenic drug has been used as a potential treatment strategy for breast cancer bone metastases (Ebos and Kerbel, 2011; Welti et al., 2013). However, the kinetics of bone vascularization response to tumor invasion and anti-angiogenic drugs are still not fully characterized at the bone-organ level. In this respect, it is necessary to develop efficient methods to image and analyze three-dimensional (3D) bone and vessels.

For 3D imaging of bone and vessels, 3D X-ray microcomputed tomography (μCT) is a powerful tool designed for achieving high spatial resolution and provides visual depictions of anatomy in preclinical studies (Swain and Xue, 2009; Cengiz, Oliveira and Reis, 2018). 3D X-ray μCT has been used to image trabecular bone micro-architecture (Kuhn et al., 1990) as well as cortical bone and its Haversian network (Cooper et al., 2003; Bousson et al., 2004). In addition, 3D X-ray μCT has been used to visualize the vascular architecture with a contrast agent (Moore et al., 2003; Zhang et al., 2005). However, these studies required to decalcify the bone. Thus, μCT was only used to image and analyze either bone microstructure or vascular architecture separately, and the relationships between vessels and bone remain poorly understood (Lafage-Proust et al., 2015).

Synchrotron radiation microcomputed tomography (SR-μCT) has significant advantage of yielding high spatial resolution images with a high signal-to-noise ratio, compared to standard μCT, due to the high photon flux of the synchrotron source (Salomé et al., 1999). SR-μCT has been applied to the quantitative analysis of human trabecular and cortical bone up to the micrometer scale (Peyrin et al., 1998a; Larrue et al., 2011; Langer and Peyrin, 2016; Gauthier et al., 2018). In addition, SR-μCT coupled with the use of a contrast agent permitted to visualize simultaneously the 3D bone microstructures and vascular networks in mouse (Schneider et al., 2009) or rat (Langer et al., 2010; Prisby et al., 2011).

Following the imaging, segmentation is an important step in quantitative analysis and has been widely used in biomedical researches (Goceri, Shah and Gurcan, 2017; Fohst, 2018). In particular, to be able to analyze the characteristics of blood vessels, the segmentation of vasculature is fundamental and prerequisite. However, this step may be challenging due to the complexity of the vascular network and the lack of diffusion of the contrast agent at some location.

Manual segmentation is a basic and robust approach to segment vessels in the preclinical study (Núñez et al., 2017). Although the manual segmentation can work well even with the noisy and little contrast image, it is time consuming and not able to apply to large data sets. Global thresholding is a widely used technique to segment vessels based on their contrasted intensities. For instance, the bone and vessel structures of mice, simultaneously imaged using SR-μCT with a contrast agent, have been segmented automatically using global thresholding (Schneider et al., 2009). Although the global thresholding is simple to perform, the segmentation quality can be affected by beam-hardening, artifacts, partial volume effects, and noise on the image. Region growing is a powerful segmentation technique considering the connectivity of regions making up a vessel tree (Erdt, Steger and Sakas, 2012). Previously, we proposed a 3D region growing based protocol to analyze bone and vessels of rats using SR-μCT associated to a contrast agent (Langer et al., 2010; Prisby et al., 2011).

To make more models of pathologies available, it would be desirable to image mice. However, this transition is not straightforward. As opposed to in rat bone, vessels may appear to be in contact with the bone surface in mice. This precludes the correct segmentations of bone and vessels using the previously proposed 3D region growing based protocol.

In this thesis, we aim to develop a new protocol to image and analyze bone and vessels of mouse tibia using SR-μCT with a contrast agent.

To segment vessels and bone, we proposed an algorithm based on marker-controlled watershed in conjunction with the monogenic signal phase asymmetry. The marker-controlled watershed was used to separate vessels appearing to be touching the bone surface, without the need for post-segmentation merging of regions. Monogenic signal phase asymmetry was used to improve the edge detections at the bone and vessel interfaces, in which the contrast was relatively weak, compared to the bone-background and the vessel-background interfaces, leading to weaker gradient magnitude at these edges.

Segmentation quality was evaluated using the Dice coefficient and the MCC by comparing to manual segmentation. Additionally, the accuracy and robustness of the proposed method were evaluated on a series of synthetic volumes generated to mimic the real vessel, bone and background structures. Different contrasts between various structures, different noise levels, and the segmentation of thin structure were considered. The simulation study indicates that the algorithm is performant in other multi-class segmentation problems.

Finally, we applied the proposed approach to the real datasets, in the context of breast cancer bone metastases. This work was devoted to studying the responses of bone and vessels to tumor invasion and treatments. Therefore, we evaluated the anti-angiogenic molecules targeting VEGF (Bevacizumab), its receptor (Vatalanib) and combination treatment of Bevacizumab and Vatalanib (Bachelier et al., 2014).

We used the proposed marker-controlled watershed and monogenic signal phase asymmetry to segment bone and vessels of mouse tibia, imaged using SR-μCT with a contrast agent. For the purpose of quantitative analysis, several parameters were extracted to characterize bone microstructure and vasculature. Moreover, statistical analysis was performed with appropriate tests.

1.2 Layout of the thesis

This thesis is split into two sections: background and contributions.

(1) Background part: this part present the related knowledge and the state of the art.

In Chapter 1, we briefly introduce the general background and point out the objective and the layout of this thesis.

In Chapter 2, we describe the basic knowledge about the structures of bone and the functions of vasculature. In addition, we review the existing techniques for imaging the bone and vessel.

In Chapter 3, we introduce the generic biomedical image segmentation methods and review the state of the art of techniques for segmenting the bone and vessel in µCT image.

In Chapter 4, we report the existing evaluation methods of segmentation quality.

(2) Contribution part: we present the contributions, conclude this thesis and suggest perspectives.

In Chapter 5, we propose marker-controlled watershed in conjunction with monogenic signal phase asymmetry to segment bone and vessels of mice tibia in SR-µCT image. Additionally, the evaluations of segmentation quality for the single compartment and the overall of multi-class are presented.

In Chapter 6, we describe the assessments of the proposed method. A series of synthetic volumes are generated for simulating the real dataset. We consider the different contrasts between the different structures, as well as different noise levels. A series of multi-class synthetic volumes are segmented using the proposed method, and the segmentation qualities are evaluated. In addition, we also report the study of thin structure segmentation.

In Chapter 7, we present the applications of the proposed method to the real dataset of mice bone and vessel, acquired by SR-µCT. The sample preparation and image acquisition are described. The image processing and the evaluation of segmentation quality are also reported in this chapter. Finally, the quantitative parameters are extracted and statistical analysis is finished.

In Chapter 8, we conclude this thesis and suggest the perspectives to the future works.

Chapter 2

Bone and vasculature

Contents

2.1 Introduction

In this thesis, we aim to develop a new protocol to analyze bone and vessels of mouse tibia using SR-μCT with a contrast agent. Therefore, the basic knowledge about the structures of bone and the functions of vasculature requires to be presented. In addition, we also review the existing techniques for imaging the bone and vessels.

2.2 Bone structure

Bone is composed of multiple tissue types like bone tissue (or osseous tissue), cartilage, dense connective tissue, epithelium, adipose tissue, and nervous tissue. Bone contributes to homeostasis of the body by producing blood cells, and storing minerals and triglycerides. The entire framework of bones works with ligaments and tendons to constitute the skeletal system, which protects the internal organs, provides stability and supports the framework of the body (Tortora and Derrickson, 2018). In addition, bone has two pairs of contradictory properties to maintain normal motor function, stiffness yet flexibility, and lightness yet strength, which are determined by the material composition and geometric structure of bone (Leali et al., 2009).

At the macroscopic level, the structure of long bone consists of diaphysis, epiphysis, metaphysis, articular cartilage, periosteum, medullary cavity and endosteum. It is illustrated in Fig. 2.1, showing the structure of an humerus (the arm bone) (Tortora and Derrickson, 2018). The diaphysis is the midsection of a bone. The epiphyses are the proximal and distal ends of the bone. The metaphyses are the regions between the diaphysis and the epiphyses. The articular cartilage covers the part of the epiphysis at the articulation (joint). The periosteum is a tough connective tissue sheath and covers the external surface of bone. The medullary cavity (or marrow cavity) is a hollow space within the diaphysis that stores bone marrow and produces blood cells. The endosteum is a thin membrane and overlays the inner surface of cortical bone, the trabecular bone and the cortical bone canals (Colnot, 2009).

Bone tissue is mineralized, dense and hard. It can be classified into the cortical (compact) and trabecular (cancellous or spongy) bone (Rho, Kuhn-Spearing and Zioupos, 1998). The cortical bone forms the outer shell of bone and makes up the bulk of the diaphysis. Cortical bone tissue protects inner components, supports weight of body and resists the stresses produced by movement (Tortora and Derrickson, 2018). Human cortical bone is dense with a porosity in the order of 6% (Fratzl and Weinkamer, 2007; Eliaz and Metoki, 2017). The trabecular bone is located at the inside of bone and includes basic structures: rod-rod, rod-plate, and plate-plate as shown in Fig. 2.2 (Bonnassie, Peyrin and Attali, 2003; Peyrin et al., 2007). The trabecular bone forms the core of the epiphyses and metaphysis bordering the medullary cavity of the diaphysis. Another difference between cortical bone and trabecular bone is that trabeculae supports and protects the red bone marrow (Tortora and Derrickson, 2018).

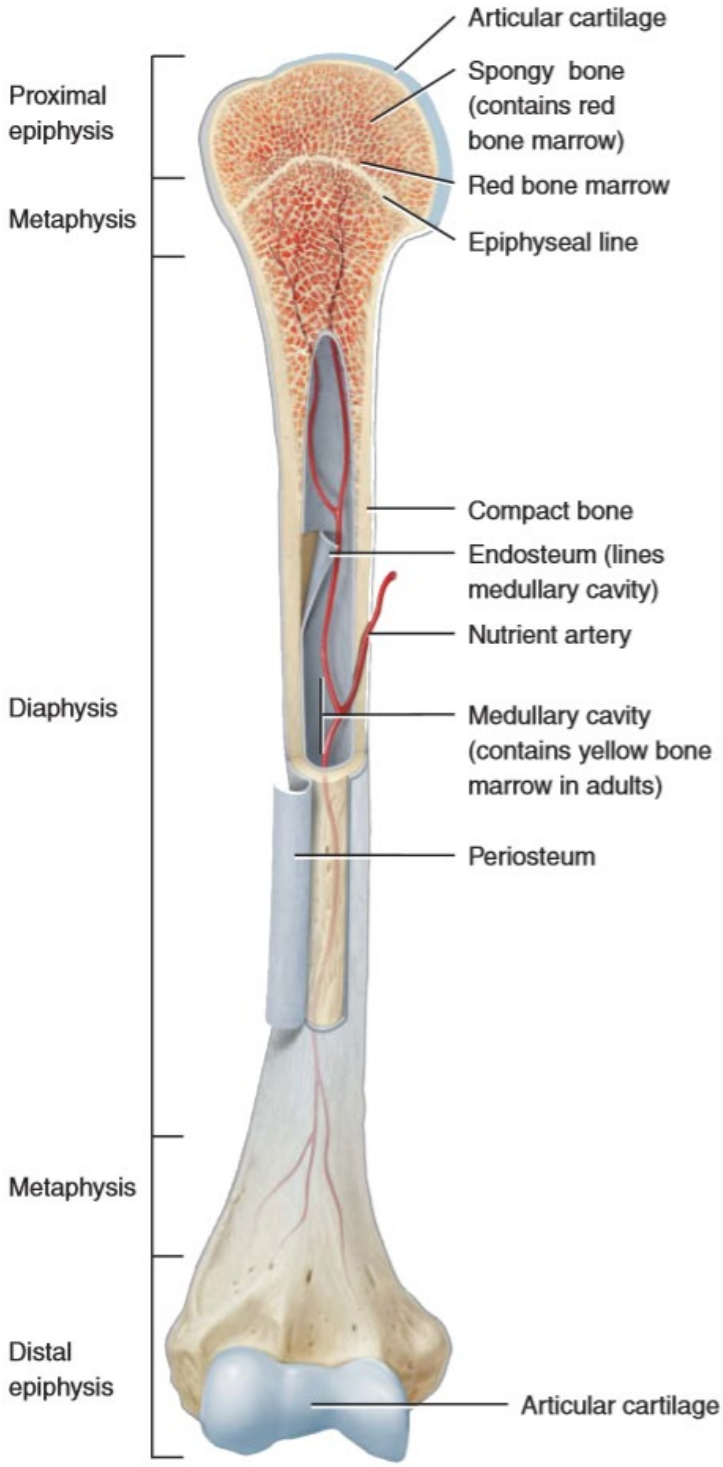

Fig. 2.1 Structures of a long bone (partially sectioned humerus). The epiphyses and metaphyses contain red bone marrow, and the medullary cavity of the diaphysis contains yellow bone marrow (in adults). The articular cartilage covers the joint surfaces of epiphyses. The external surface of the bone is covered with periosteum, while the endosteum overlays the inner surface of cortical bone (Tortora and Derrickson, 2018).

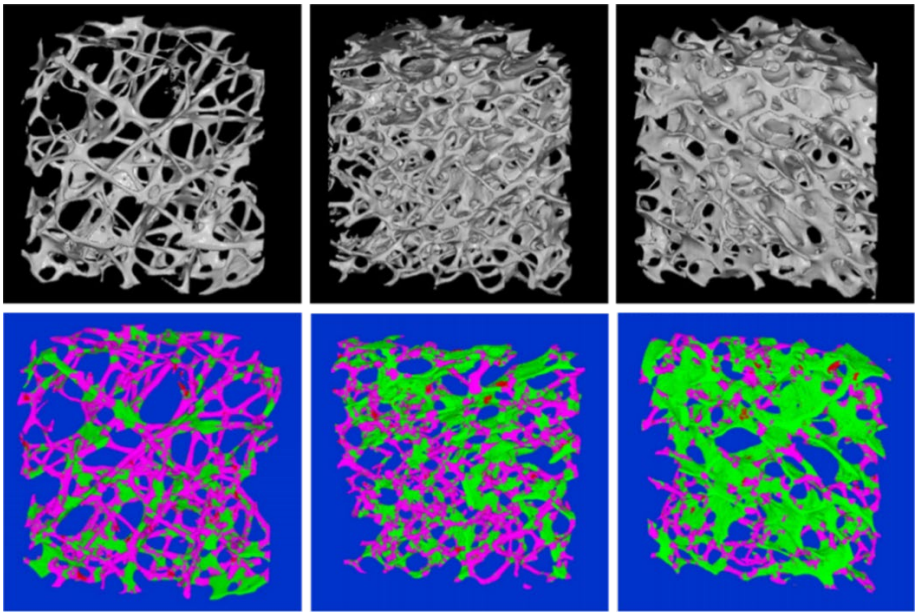

Fig. 2.2 Three trabecular architectures including rod-like (left), hybrid (middle), and plate-like (right). Rods and plates are depicted in pink and green, respectively (Peyrin et al., 2007)

2.3 Vasculature in bone

The blood vessel is essential for the health of every single tissue and organ, since it transports oxygen, nutrients, and inflammatory molecules to tissues, as well as removes carbon dioxide and waste products (Tse, 2018). There are abundant blood vessels in portions of bone, as shown in Fig. 2.3 (Tortora and Derrickson, 2018). Small periosteal arteries enter the diaphysis through many canals to supply the periosteum and the outer part of cortical bone. Large nutrient arteries pass through nutrient foramen, a hole in cortical bone, and enter the medullary cavity. The nutrient artery divides into branches and supplies the inner part of cortical bone, the trabecular bone, red bone marrow as far as the epiphyseal plates. The metaphyseal and epiphyseal arteries supply the red bone marrow and bone tissue of the metaphyses and epiphyses of a long bone, respectively. The periosteal, nutrient, epiphyseal and metaphyseal veins accompany their respective arteries and carry blood away from long bones (Tortora and Derrickson, 2018).

Therefore, when dysregulated, the formation of new blood vessels contributes to numerous malignant, ischemic, inflammatory, infectious and immune disorders (Carmeliet, 2003). The adverse changes to the blood circulatory system have been linked to a variety of diseases: diabetes (Shanbhogue et al., 2017), avascular necrosis (Lafforgue, 2006), cancer (Hoff and Machado, 2012; Lowerison et al., 2017), osteoporosis (Alagiakrishnan et al., 2003; Barzilay et al., 2016), and osteoarthritis (Findlay, 2007; Filipowska et al., 2017).

Angiogenesis is the formation of new blood vessels and can be a hallmark of cancer (Welti et al., 2013). For example, angiogenesis plays an important role in breast cancer development (Bachelier et al., 2014). There is a large body of evidence that angiogenesis is an anticancer therapeutic target. Therefore, many anti-angiogenic agents target VEGF or its receptors as potential anticancer drugs (Ebos and Kerbel, 2011).

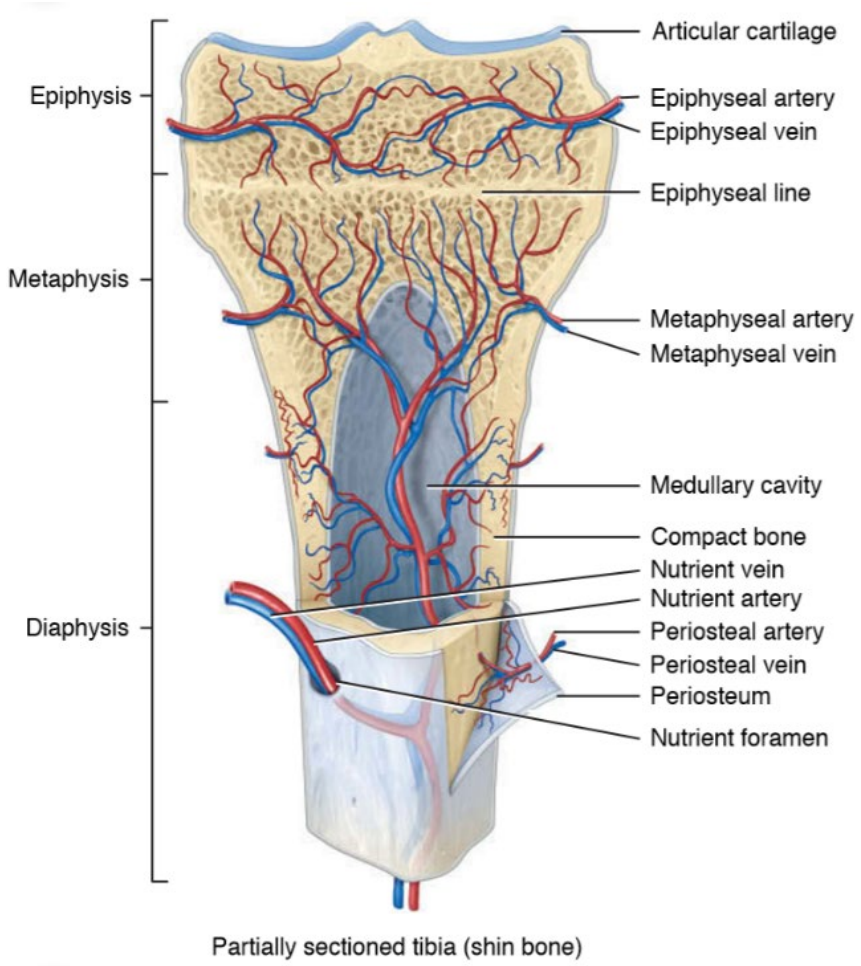

Fig. 2.3 Blood vessels in partially sectioned tibia (shin bone) including periosteal, nutrient, metaphyseal, epiphyseal arteries and veins (Tortora and Derrickson, 2018).

2.4 Imaging bone tissue

In this section, we briefly review the techniques reported in the literature for the imaging of bone tissue including histology, radiography, and X-ray computed tomography (CT) based techniques.

2.4.1 Histology

Histology is a well-established research tool to examine the undecalcified bone for obtaining qualitative and quantitative information. Histology of bone tissue requires the preparation of samples, such as sectioning and staining. Additionally, it is often coupled with a light microscopy. Descriptive histology and histomorphometry are two main types in histological analysis (Meunier, 1983). Descriptive histology is used to provide a general evaluation of bone tissue. Histomorphometry is a methodology for quantitatively analyzing bone features, such as length (perimeter or boundary), distance between points, area and the number of components (Partitt, 1987; An and Martin, 2003; Kulak and Dempster, 2010).

In particular, histology has been used to analyze the bone destructions in preclinical studies (Peyruchaud et al., 2001; Pecheur et al., 2002; Boucharaba et al., 2004; Zhao et al., 2007; Bachelier et al., 2014). For instance, the histology and histomorphometric analysis of bone tissue were performed to study the breast cancer bone metastases (Peyruchaud et al., 2001). In this study, seven-micrometer sections of undecalcified long bones were cut and stained with Goldner's trichrome. Mineralized bone was stained in green and bone marrow cells in red. The left panel of Fig. 2.4 shows the histology of a tibia from a mouse 29 days after inoculation with breast cancer tumor, and the right panel is histology of a normal tibia section. The left panel shows that both cortical and trabecular bone were destroyed and disappeared, compared to the normal tibia section (the right panel).

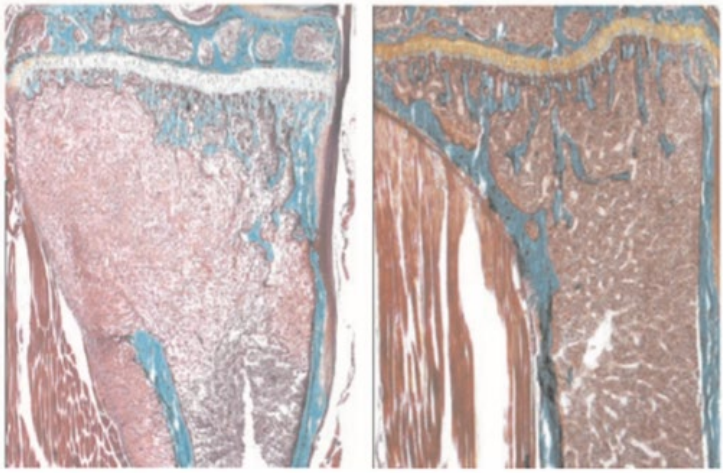

Fig. 2.4 Left panel is the histology of a tibia from a mouse 29 days after inoculation with breast cancer tumor cells. The right panel is histology of a normal tibia section. Tissue sections were stained with Goldner's trichrome. Mineralized bone is stained in green and bone marrow cells in red. The left panel shows that cortical bone was partially destroyed and that most of the trabecular bone disappeared (magnification x25) (Peyruchaud et al., 2001).

However, histology is normally assessed in 2D on sections. Although 3D parameters can be calculated from 2D measurements according to carefully considered assumptions, such as standard stereology theory, it is still impossible to reconstruct accurate 3D structure based on a single 2D image due to the anisotropy of bone tissue (Parfitt, 1983).

2.4.2 Radiography

Radiography is a noninvasive imaging technique for revealing the internal structure of the body in a 2D image. The radiography image can be produced by highlighting the differences of X-ray attenuation among various substances with differing densities (Shelledy and Peters, 2014). Especially, the denser substance, like bone tissue, is visible on a 2D radiograph image. Thus, radiography has been applied to the texture analysis of trabecular bone (Benhamou et al., 1994; Chinander et al., 1999; Apostol et al., 2006), and the detection of bone destructions in biomedical researches (Peyruchaud et al., 2001; Pecheur et al., 2002; Boucharaba et al., 2004; Zhao et al., 2007).

To validate the drug treatment on breast cancer bone metastasis, the tibia of mice has been imaged by radiography, as shown in Fig. 2.5 (Bachelier et al., 2014). In this study, the area and number of osteolytic lesions on the skeleton have been measured. Although radiography is a useful method to monitor the osteolytic lesions, it only allows the detection at a late stage when bone destruction is occurring, which is not working at the early disease diagnosis.

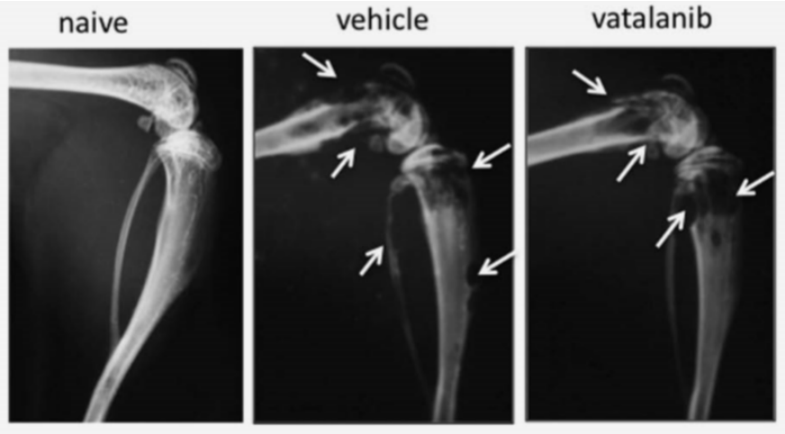

Fig. 2.5 Radiographic analysis of hind limbs from mice. The left is a radiograph of hind limb from a naive mouse that did not receive any tumor cells or treatment. The middle is a radiograph of hind limb from a vehicle mouse that was bearing tumors but did not receive any treatment. The right radiograph is a hind limb from a mouse that was bearing tumors and was treated by vatalanib. All images were obtained from different mice on day 32 after tumor cell inoculation. Arrows indicate osteolytic lesions (Bachelier et al., 2014).

2.4.3 X-ray computed tomography based techniques

X-ray computed tomography (CT) is a 3D imaging technique, which has been used to image slices from the human anatomy for clinical diagnostic since its first introduction in the early 1970s (Hounsfield, 1973). With further technological evolution, X-ray CT has permitted to image 3D volumes in reduced acquisition times. With the development of X-ray μCT and the improvement of spatial resolution, it has been transferred to preclinical and biological imaging. The 3D imaging of bone micro-architecture has been a driving force in the development of X-ray μCT (Feldkamp et al., 1989; Rüegsegger, Koller and Müller, 1996). In this field, X-ray μCT can provide non-destructive visualization and quantitative analysis of the 3D bone tissue, with spatial resolutions from millimeters down to nanometers (Peyrin et al., 2014; Langer and Peyrin, 2016).

2.4.3.1 Clinical computed tomography

To acquire an X-ray CT image, data acquisition and reconstruction are involved. Firstly, data acquisition is performed by recording several projections of a sample at different angular positions around a single axis of rotation. This process measures the attenuation of X-rays as they pass through the object. Secondly, tomographic reconstruction algorithm such as Filtered Back Projection (FBP) is used to obtain the final X-ray CT reconstructed image (Peyrin and Engelke, 2012).

Clinical CT is commonly used in humans typically producing 2D or 3D images with the spatial resolution of 1 mm, at organ level (Guldberg et al., 2003), or even a maximum spatial resolution of 0.3 mm. However, clinical CT can not offer a sufficient spatial resolution to resolve the micro-architecture of bone, at the micro level. Bone images obtained using clinical CT are degraded by partial volume effects, due to the limited spatial resolution (Peyrin *et al.*, 1998b). Since a gain in spatial resolution in clinical CT is achieved at the cost of an increase of radiation exposure, this limits the possibility for in vivo imaging (Peyrin et al., 2014).

2.4.3.2 Quantitative computed tomography

Quantitative computed tomography (QCT) is a technique to measure bone mineral density (BMD) with a calibration standard in vivo. QCT can be performed on the conventional body CT scanners (Adams, 2009). HR-pQCT (high-resolution peripheral quantitative computed tomography) is based on the same principles of QCT but can achieve a much higher resolution with the trade-off of a smaller field of view (Boutroy et al., 2005). HR-pQCT is restricted to peripheral sites (radius, tibia), as shown in Fig. 2.6 (Geusens et al., 2014). It is able to separate cortical and trabecular bone, as shown in Fig. 2.7 (Geusens et al., 2014). HR-pQCT can reach spatial resolution of 82 μm to quantify trabecular and cortical bone (Geusens et al., 2014). HR-pQCT is increasingly involved in clinic research and basic studies (Tsai et al., 2017; Figueiredo et al., 2018). Other in-vivo imaging methods for noninvasive assessment of 3D bone microarchitecture are listed as Fig. 2.8.

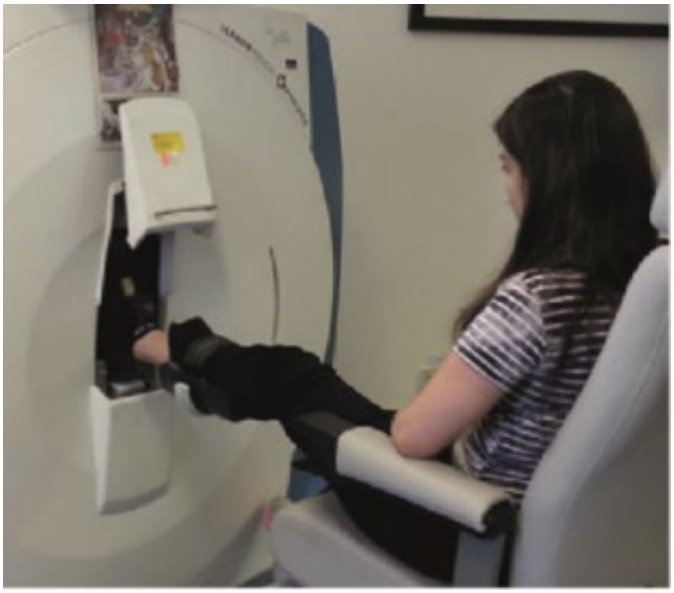

Fig. 2.6 Positioning of the patient on a HR-pQCT machine to scan the distal tibia (Geusens et al., 2014).

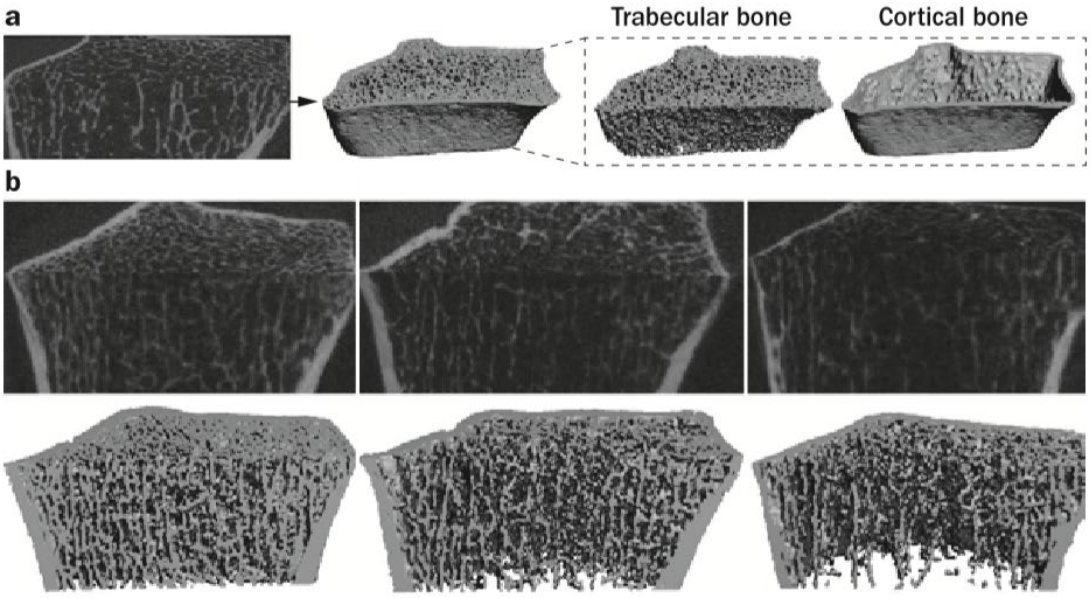

Fig. 2.7 Imaging bone using HR-pQCT. (a) Segmentations of cortical and trabecular bone. (b) Bone deteriorations with ageing: grayscale (top) and segmented bone 3D images (bottom) (Geusens et al., 2014).

Method	Nominal resolution (μm)	Effective radiation dose (μSv)	Acquisition time (min)	Parameters assessed
Conventional 2D radiography, hand	<50	10	<1	Bone size, cortical thickness, diseases
HR 2D radiography, hand	50	<5	<1	Trabecular structure, erosions
Adult DXA	1,000–2,500	5–20	<1	BMC, BMD
Musculoskeletal ultrasonography	200–500	0	>10	Synovitis, effusion, erosions, vascularization
MRI	150–200	0	10–30	BME, erosions, cartilage, effusion
3D QCT, spine 3D QCT, hip 3D QCT, wrist 3D HR-pQCT	250–300 250–300 250–300 82	1,500 2,900 <10 3–5	<1 <1 <1 3	BMD, cortical and trabecular structure, FEA

Abbreviations: BMC, bone mineral content; BMD, bone mineral density; BME, bone marrow oedema; DXA, dual-energy X-ray absorptiometry; FEA, finite element analysis; HR, high resolution; QCT, quantitative CT.

Fig. 2.8 Comparison of in vivo bone and joint imaging techniques (Geusens et al., 2014).

2.4.3.3 X-ray micro-computed tomography

X-ray micro-computed tomography (Micro-CT or μCT) was first developed in the late 1980s. μCT was designed for achieving high spatial resolution based on the physical principle of conventional CT. μCT typically produced images having the resolution in a range of 1 μm and 50μm, and allowed to investigate the microstructure of sample (Swain and Xue, 2009; Cengiz, Oliveira and Reis, 2018).

X-ray μCT system generally employs micro-focal spot (between 5μm–50μm FWHM) X-ray sources to obtain projections through multiple viewing directions (Flynn et al., 1994; Holdsworth and Thornton, 2002; Guldberg et al., 2003; Badea et al., 2008). In X-ray μCT

systems, there are two possible designs for rotating: either rotating the X-ray system (source and detector) and fixing the samples at stage or rotating specimen and fixing the X-ray system to scan, as shown in Fig. 2.9 (Holdsworth and Thornton, 2002; Badea et al., 2008; Ritman, 2011; Cengiz, Oliveira and Reis, 2018). The magnification in μCT system is generally obtained by the use of X-ray cone beam, as illustrated in Fig. 2.10 (Guldberg et al., 2004). The whole process of acquisition and reconstruction when using cone-beam X-rays to illuminate a rotating sample, is illustrated in Fig. 2.11, showing the acquisition of sets of 2D projections (radiographs) and their 3D reconstruction (Cengiz, Oliveira and Reis, 2018).

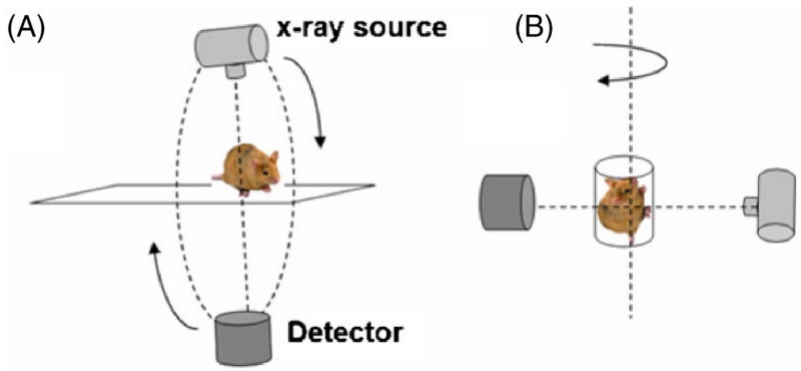

Fig. 2.9 Two designs for μCT rotation (A) rotating X-ray source and detector (B) rotating specimen. (Badea et al., 2008)

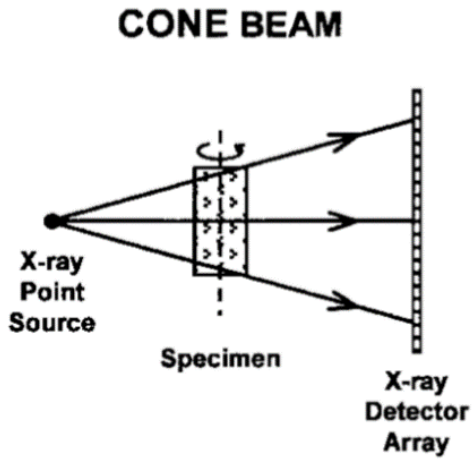

Fig. 2.10 Illustration of achieving the magnification in μCT using the X-ray cone beam (Guldberg et al., 2004).

X-ray μCT was first proposed to study the microstructures and density of trabecular bone architecture (Feldkamp et al., 1989; Kuhn et al., 1990; Rüegsegger, Koller and Müller, 1996). In this later study, a micro-focus X-ray tube associated to a CCD detector was used to nondestructively image a bone biopsy in a 32-year-old (healthy) woman, reaching a spatial resolution of 28 μm as shown as Fig. 2.12.

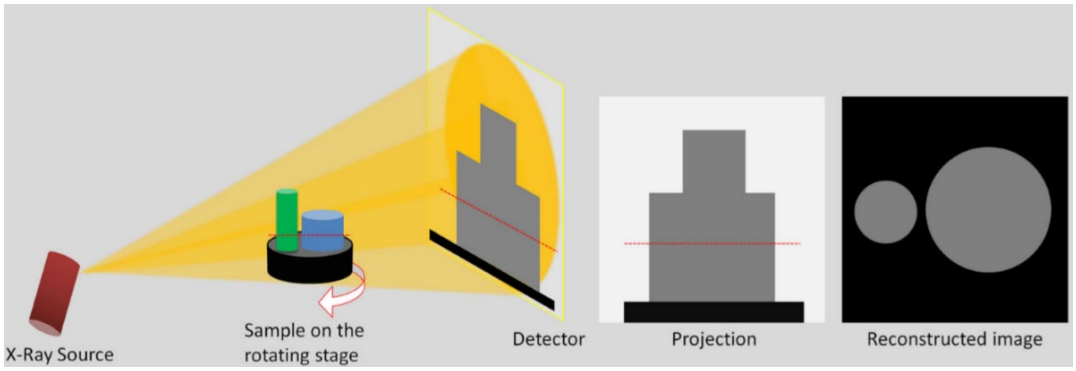

Fig. 2.11 Schematic illustration of µCT. Cone-beam X-rays illuminate the sample to acquire projection images at each rotation angle and then reconstruct 3D image. The red dashed line indicates the vertical position of the cross-sectional image (Cengiz, Oliveira and Reis, 2018).

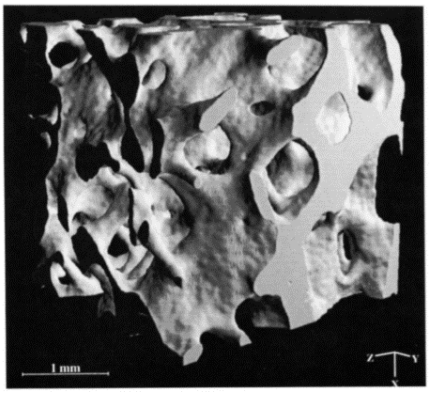

Fig. 2.12 3D reconstruction of biopsy trabecular bone from a 32-year-old healthy woman (Rüegsegger, Koller and Müller, 1996).

2.4.3.4 Synchrotron radiation micro-computed tomography

Synchrotron radiation micro-computed tomography (SR-µCT) first developed in the 1980s (Grodzins, 1983), possesses a number of significant advantages compared to standard X-ray µCT, in terms of image quality. SR-µCT uses synchrotron radiation beams with high photon fluxes instead of standard X-ray sources. Therefore, SR-µCT is able to acquire high spatial resolution images with a high signal-to-noise ratio (SNR). In addition, SR-µCT has obviously shorter data acquisition time to obtain the same spatial resolution and SNR image, compared to standard µCT (Peyrin and Engelke, 2012). A 3D SR-µCT parallel beam setup has been proposed to image and quantify the trabecular bone microstructure (Salomé et al., 1999). In this study, SR-µCT was used to image the human vertebra samples from women with 33, 55, and 72 years old, with a spatial resolution of 11µm, as shown in Fig. 2.13. In addition, SR-µCT was also used in animal models such as mice, as illustrated in Fig. 2.14 (Peyrin and Engelke, 2012).

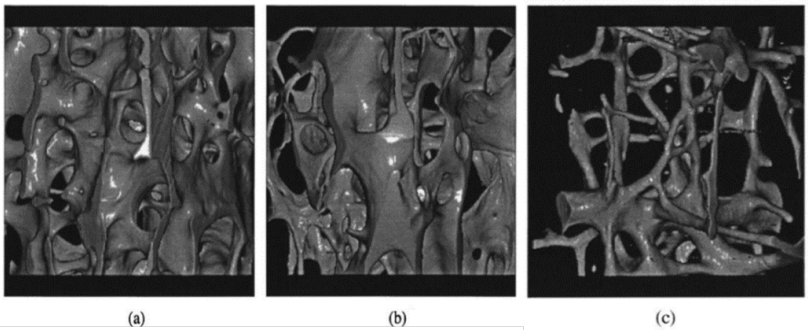

Fig. 2.13 3D reconstructions of human vertebrae using SR-μCT. (a) 33 year old female; (b) 55 year old female; (c) 72 year old female (Salomé et al., 1999).

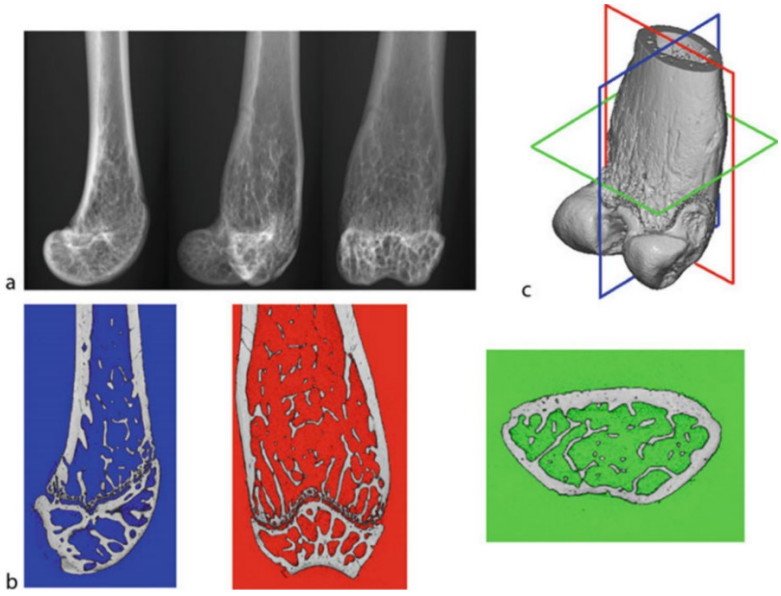

Fig. 2.14 Illustration of imaging a mice femur at 7μm resolution using SR μCT: (a) 2D projections between 0 degree and 90 degree, (b) transverse and sagittal slices, and (c) 3D rendering of bone surfaces (Peyrin and Engelke, 2012).

2.5 Imaging vasculature

In this section, we review the imaging techniques for vessels including histology, confocal microscopy, and X-ray CT based techniques.

2.5.1 Histology

Histological imaging is one of the most popular tool to visualize, characterize and quantify microvasculature using microscopy and staining, such as gelatin-india ink, barium sulfate, lead chromate-loaded silicon (Microfil, Flow Tech, Inc., Carver, MA, USA) (Lafage-Proust et al., 2015). For instance, histology has been used to analyze mouse hind limb long bone vascularization after infusion of contrast agent (barium sulfate). The histological imaging allows us to locate bone vasculatures whose diameter can be up to 10 μm, as illustrated in Fig.

2.15. (Roche et al., 2012). Histology can provide planar detailed information on microvasculature at high resolution, but lacks 3D architectural information for assessing structural aspects of pathologies. 2D assessment of the microvasculature may mislead interpretations, particularly in the restructured microvasculature during disease, where vessel morphometry can not be well predicted. Moreover, it is difficult to embed and section the vessels in specific directions using standard histologic sections, leading to misinterpretations of branching, bifurcations, and tortuosity of microvasculature (Xu et al., 2015).

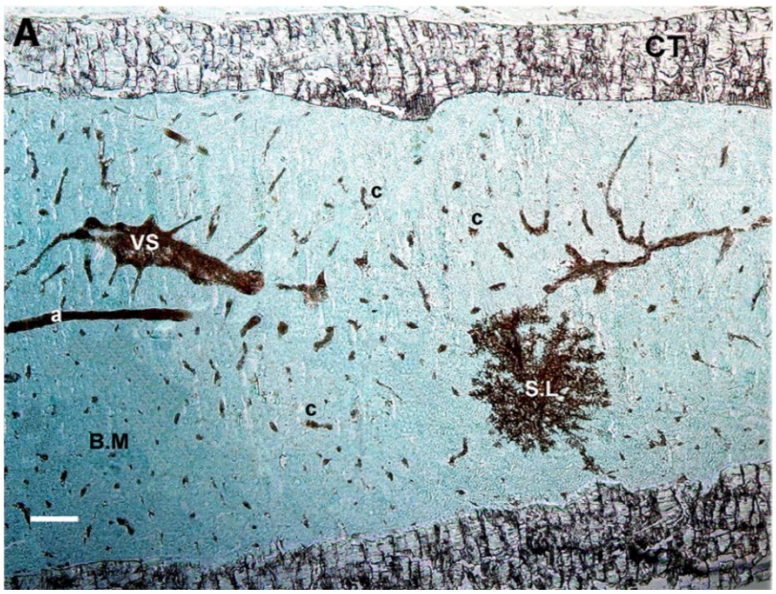

Fig. 2.15 Image of mid-diaphysis histology of mice infused with barium sulfate with magnifications of 100×. B.M: bone marrow, c: capillaries, CT: cortex, S.L: sinusoid lobules, a: arteriole, VS: venous sinus, scale bars=100 µm (Roche et al., 2012).

2.5.2 Confocal microscopy imaging

Laser confocal scanning microscopy (LCSM) is an optical microscopy technique, which can obtain a high resolution (0.2 µm to 0.5 µm) by means of using a detector aperture (pinhole) conjugated with the focal point of the lens to block out-of-focus light. It is also able to provide 3D reconstruction of an object by assembling a series of 2D images at varying depths within the specimen (Ross and Pawlina, 2006). This technique has been used to image vascularization with immunostaining, in human bone marrow biopsy specimen, as shown in Fig. 2.16. The vessel density, tortuous and branching were analyzed based on the confocal microscopy images (Lundberg et al., 2000). LCSM was also used extensively in the imaging of mice bone microvasculature with immunofluorescence staining and decalcification, as shown in Fig. 2.17. (Ubellacker et al., 2017; Allocca et al., 2019; Haider et al., 2020). LCSM is a powerful imaging tool in life sciences, but has a limited spectrum of molecules that can be visualized, according to probe availability. In addition, LCSM is limited by the field of view and depth of penetration, which can be low in hard tissues such as bone.

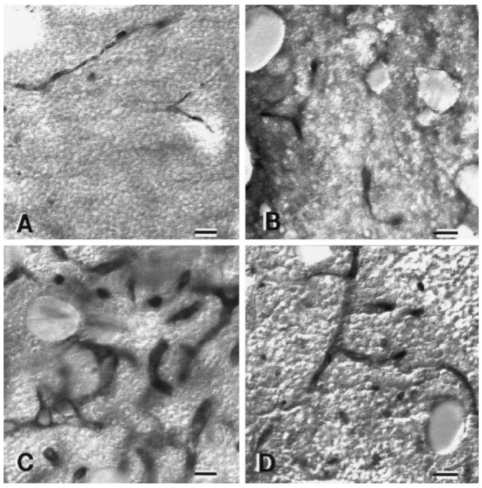

Fig. 2.16 Confocal micrographs of bone marrow biopsy specimens from normal bone marrow (A) or from patients with polycythemia vera (B), myelofibrosis (C) or chronic myelocytic leukemia (D). Specimens were sectioned to thicknesses of 25–200 μm, scale bars = 20 μm. immunostained microvessels is black (Lundberg et al., 2000).

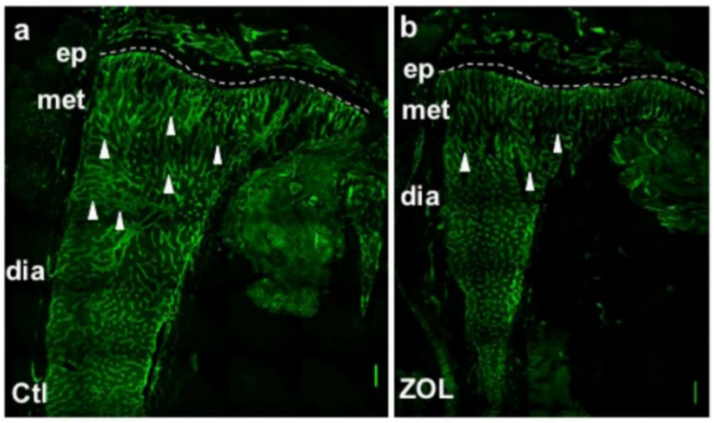

Fig. 2.17 Confocal microscopy imaging of mice bone marrow vasculature with immunofluorescence staining for studying the breast cancer bone metastases treatment. (a) Control (Ctl) treatment. (b) A single dose of zoledronic acid (ZOL) treatment. Scale bars = 250 μm. Arrows indicate branched vasculature. Dashed lines represent growth plate demarcation. Ep: epiphysis. Met: metaphysis. Dia: diaphysis. Specimens were sectioned to thicknesses of 30 μm (Ubellacker et al., 2017).

2.5.3 X-ray computed tomography based techniques

X-ray CT is a powerful technique to visualize materials with high electron densities such as bone. However, visualizing materials with low electron densities, such as vessel, is difficult due to the relatively low contrast difference compared to their surroundings. Therefore, the use of contrast agents is required (Tse, 2018). Clinically, iodine-based contrast agent is perfused into the vascular system for visualizing blood vessels (Lell et al., 2006). In addition, the visualizations of vessels using X-ray μCT, SR-μCT, and SR phase-contrast CT (SR-PCT) are presented in the following sections.

2.5.3.1 X-ray micro-computed tomography

Pre-clinically, barium based contrast agent (such as barium sulfate) and lead based contrast agent (such as lead chromate-loaded silicon) are injected into blood to enhance the x-ray attenuation (Roche et al., 2012). However, contrasted vessels present similar greyscale values as dense x-ray attenuating bone. Thus, it is indistinguishable and unable to separate contrasted vessels from bone.

To overcome this challenge, the bone can be decalcified in 10% EDTA solution before the visualization of contrasted 3D vessel structures using μCT (Moore et al., 2003; Zhang et al., 2005; Fei et al., 2010). However, μCT was only used to image and analyze either bone microstructure or vascular architecture separately, and these studies did not permit a complete analysis of the relationships between the bone and vasculature. In another relevant study, an undecalcified femur bone of rat, containing the contrasted vessel, was imaged by μCT, and a first 3D model was reconstructed, as shown in Fig. 2.18 (A). Then the bone was decalcified and the remaining vessel was imaged using μCT, and a second 3D model was reconstructed, as shown in Fig. 2.18 (B). Two models of 3D volumes were imaged at the same conditions, and were aligned using the ANT Software (Skyscan). Finally, two models of 3D volumes were overlapped, and provided a simultaneous visualization of bone and vessels, as shown in Fig. 2.18 (C) (Nyangoga et al., 2011). However, the limitation of this methodology is the susceptibility of image registrations between two 3D models, leading to misinterpretations regarding the anatomical relationship between vessel and bone.

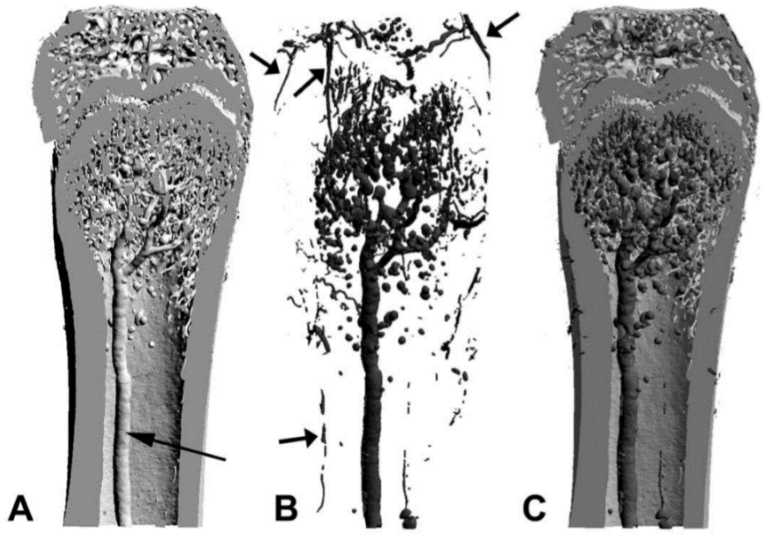

Fig. 2.18 Principle of over imposition of two 3D models. (A) 3D model obtained on the undecalcified bone. The arrow points on the central medullar artery. (B) 3D model of the vessel obtained after decalcification of the same femur. The arrows point on the periosteal arteries surrounding the bone shaft and epiphysis. (C) Over imposition of the two 3D models (Nyangoga et al., 2011).

2.5.3.2 Synchrotron radiation micro-computed tomography

Unlike the images obtained with conventional μCT, the reconstructed SR-μCT attenuation values in contrasted vessels and in bone can be clearly distinguished. Thus, SR-μCT coupled with the use of a contrast agent permitted to visualize simultaneously the 3D bone microstructures and vascular networks in mouse (Schneider et al., 2009) or rat (Fei et al., 2010; Langer et al., 2010; Prisby et al., 2011). SR-μCT can provide new insights to study the relationship between bone tissue and the vascular network. For instance, an automatic image analysis protocol, coupled to SR-μCT and contrast agent, has been proposed to simultaneously analyze, in 3D, the microvascularization and bone microstructure in a rat model (Langer et al., 2010). The volume rendering of bone and vessel compartments are shown as Fig. 2.19, cortical bone is in gray, trabecular bone in beige, vessel within trabecular bone in red and within cortical bone in orange.

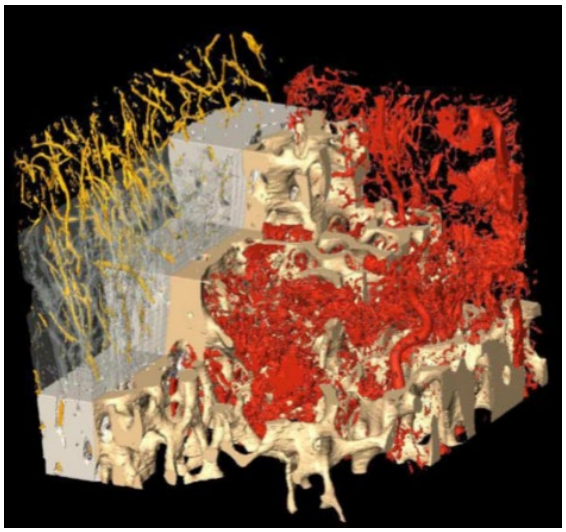

Fig. 2.19 Volume rendering of bone and vessel compartments in rat, obtained with SR-μCT and contrast agent. Cortical bone is in gray, trabecular bone in beige, vessel within trabecular bone in red and within cortical bone in orange (Langer et al., 2010).

2.5.3.3 Synchrotron radiation phase-contrast computed tomography

Synchrotron radiation phase-contrast computed tomography (SR-PCT) is a powerful approach to image the soft tissue without the addition of contrast agents. SR-PCT exploits the sample-induced phase shift to increase image contrast for soft tissues using synchrotron light sources. (Fratini et al., 2015). The simultaneous visualizations of the calcified bone microstructure and blood vessels were obtained using SR-PCT without contrast agent, in undecalficied murine bone (Núñez et al., 2017). In this study, after the image acquisition and processing, 3D visualizations of murine tibiofibular junction (Fig. 2.20 a, b), intra-cortical canal network (Fig. 2.20 c, d) and intra-cortical blood vessels (Fig. 2.20 e, f) are shown as Fig. 2.20. However, the field of view was limited due to the small pixel size used, and vessels were segmented by hand due to the relatively weak phase contrast in the vessels limiting the applications of the protocol to large data sets.

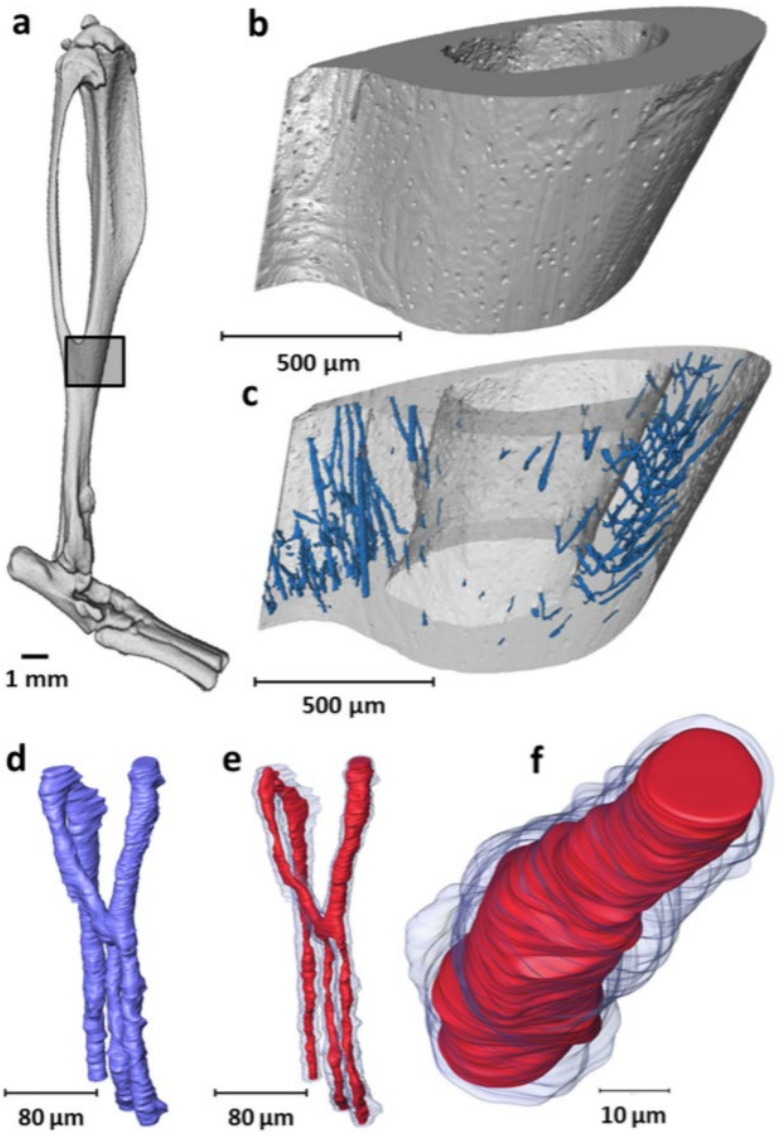

Fig. 2.20 3D visualization and extraction of intra-cortical blood vessel. (a) 3D rendering of murine tibia with identification of the tibiofibular junction. (b) 3D rendering of scanned tibiofibular junction region (1.3 µm voxel size) and (c) detection of intra-cortical canals (blue) as a negative imprint of the mineralized tissue (extracted from 1.3 µm voxel size dataset). (d) Magnified area of the 3D intra-cortical network (extracted from 0.325 µm voxel size dataset) and (e) detection of the soft tissue comprising blood vessels (red) within intra-cortical canals (blue) (extracted from 0.325 µm voxel size dataset). (f) Magnified segment of blood vessel (red) within intra-cortical canal (blue) (extracted from 0.325 µm voxel size dataset) (Núñez et al., 2017).

Chapter 3

Biomedical image segmentation techniques

Contents

3.1 Introduction

Image segmentation is a process that partitions an image into multiple regions with certain characteristics (Gonzalez and Woods, 2017). Image segmentation has been widely used in biomedical image (Goceri, Shah and Gurcan, 2017; Zhou et al., 2019; Li et al., 2020), remote sensing image (Nogueira et al., 2019; Peng et al., 2019), and natural image (Yang et al., 2008; Rao et al., 2009). The basic concepts and theory of digital image processing are common to the different applications, but they have their own particular challenges. For instance, in biomedical image, organs and other tissues can usually not be described with simple geometric shape models (Rubin, Greenspan and Brinkley, 2014).

In the next section, we will introduce the generic image segmentation techniques. In the section 3.3, we will review the state of the art of approaches for segmenting bone and vessels in X-ray µCT and SR-µCT images.

3.2 Image segmentation techniques

In this section, we will report manual and automatic image segmentation approaches. Specifically, the automatic methods can be classified based on three basic properties of images: discontinuity, similarity, and incorporated shape knowledge. In the first category, image segmentation is performed based on abrupt changes in intensity, such as edge detection. In the second category, image segmentation partitions an image into regions with similar characteristics according to a set of predefined criteria, such as threshold-based method and region-based method. In the third category, the segmentation approach has a strong focus on modeling the object's shape, such as deformable model.

Deep learning refers to learning patterns in data samples using neural networks containing multiple interconnected layers of artificial neurons. In particular, convolutional networks (CNNs) have become a methodology of choice for analyzing biomedical images (Litjens et al., 2017; Maier et al., 2019; Singh et al., 2020). However, few such approaches have been described for the segmentation of bone and vessels in preclinical µCT images. Therefore, in this work, deep learning methods are not considered part of the segmentation classification.

3.2.1 Manual segmentation

Manual segmentation refers to a technique to segment an image into several objects performed by a user by drawing with a mouse, a pen or a graphics tablet. This usually requires expert knowledge from for example radiologists, a specialized clinician and a trained user, to delineate the contour and specify each unit (pixel or voxel) of the object of interest, in a slice-by-slice manner or in 3D. Manual segmentation relies on the prior knowledge of the user to correctly segment the image. Therefore, manual segmentation is usually used as the 'gold standard' or ground truth for benchmarking the accuracy of automatic segmentation techniques (Poon, 2008; Preim and Botha, 2013; Starmans et al., 2020). However, for large datasets, manual segmentation is often tedious and time consuming (Parmar et al., 2014), making it an expensive technique, especially if expert users are solicited. For example, 3D structures of nasal cavity and the paranasal sinuses have been segmented by hand in CT

images. There were 50 CT datasets, and manual segmentation took on average 8–10 hours per dataset (Pirner et al., 2009). The other drawback of manual segmentation is that it is prone to intra and inter-observer variability, as shown in the Fig. 3.1 (Starmans et al., 2020). Inter-observer variation is the amount of variation between the results obtained by two or more observers examining the same material. Intra-observer variation is the amount of variation between the results obtained by one observer when observing the same material more than once.

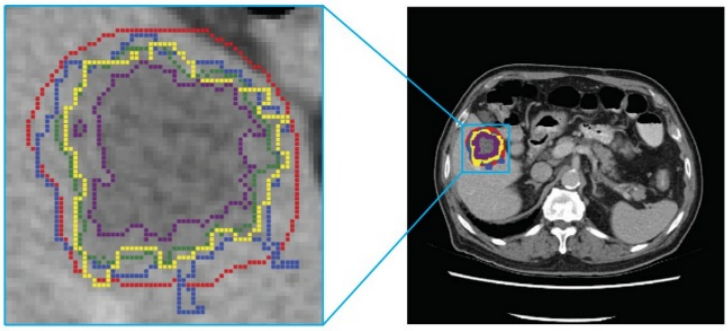

Fig. 3.1 Manual segmentations by multiple observers of a colorectal cancer liver metastasis on an axial slice of a CT image (Starmans et al., 2020)

3.2.2 Edge-based image segmentation methods

Edge detection is an approach used to find boundaries of objects, based on sudden discontinuity in intensity. The classical edge detection is often accomplished by yielding the gradient (the first order derivatives) of an image. It is usually computed using the operators such as Prewitt, Sobel, Roberts (Gonzalez and Woods, 2017). In addition, more advanced Canny edge detection has been proposed to preserve a complete boundaries of objects, even in a noisy image. Canny edge detection algorithm consists of the following steps: (1) Smooth the input image with a Gaussian filter. (2) Compute the gradient magnitude image. (3) Apply non-maxima suppression to the gradient magnitude image. (4) Use double thresholding and connectivity analysis to detect and link edges. Fig. 3.2 shows an example of edge detection in a 2D X-ray image using the Canny edge detector (Stolojescu-CriŞan and Holban, 2013).

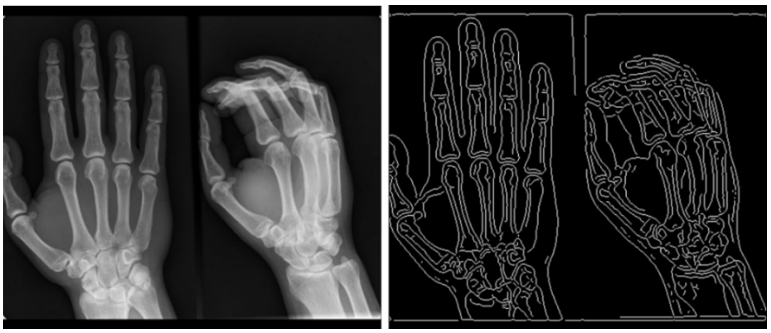

Fig. 3.2 Illustration of Canny edge detection in a 2D X-ray image. The left panel is the original image, and the right one is the edge detection result using Canny edge detector (Stolojescu-CriŞan and Holban, 2013)

Edge detection has been widely used in biomedical studies, since the boundaries of anatomical structures are often characterized by an intensity difference between various tissues (Erdt, Steger and Sakas, 2012). However, the edge detection alone may be not sufficient for the difficult and various segmentation tasks. Thus, it may need to incorporate with other techniques. For instance, edge detection was combined with deformable model to fit the edges of objects (McInerney and Terzopoulos, 1995).

3.2.3 Threshold-based image segmentation methods

Thresholding is a simple image segmentation method to partition a grayscale image into binary foreground and background images based on intensity. For example, any pixel or voxel in the original image is considered as a part of object when its intensity is greater than or equal to a threshold value, otherwise the pixel or voxel belongs to background. In order to determine an intensity value range containing the gray values of the structure to be segmented, one needs to determine a threshold value, either manually according to a priori knowledge, or automatically by image information. For instance, in CT imaging, the intensity of gray value correlates with material density of the tissue, and the threshold value can sometimes be set by operators when there is no ambiguities (for instance bone versus soft tissue). As for automatic methods, Otsu's method is one of the most popular methods to determine the thresholds. This method assumes that there are different intensities belonging to different objects in the original image. Otsu's method minimizes the intra-class intensity variance, or equivalently, maximizes the inter-class variance, and has been extended to multiple classes (Erdt, Steger and Sakas, 2012; Patil and Deore, 2013; Preim and Botha, 2013).

We can distinguish global and local thresholding methods. When the threshold value is constant for the entire image, the approach is called global thresholding. However, global thresholding may fail to segment binary foreground and background correctly due to the uneven illumination of original image of variations in background. When thresholding is performed with multiple thresholds values derived from the local properties of sub-images, the method is called local thresholding. Local thresholding approach can compensate for uneven illumination (Zuva et al., 2011; Patil and Deore, 2013).

Thresholding methods have the advantages to be simple and fast, however they have some limitations. The partial volume effect on the boundaries between the different objects may decrease the separation between the different peaks in the gray level histogram. This prevents the threshold-based segmentation to work correctly, especially, in the case of thin and small structures with large portion of boundaries. In addition, noise and artifacts in the original image corrupt the gray level histogram, and make it difficult to separate objects correctly (Withey and Koles, 2008; Erdt, Steger and Sakas, 2012; Patil and Deore, 2013; Preim and Botha, 2013).

3.2.4 Region-based image segmentation methods

Region-based image segmentation techniques divide the whole image into similar or homogenous sub-regions, where each of the pixels have similar characteristics such as intensity, color or texture (Zuva et al., 2011; Patil and Deore, 2013; Rubin, Greenspan and

Brinkley, 2014). In this section, we discuss three related approaches: region growing, region splitting and merging, and the watershed algorithm.

3.2.4.1 Region growing

Region growing segmentation methods start with seeds, which are initially placed in the original image, and the regions grow by aggregating adjacent pixels according to a predefined criterion (Erdt, Steger and Sakas, 2012). Selecting seed points can be performed manually or automatically. The operator can specify seed points on the target structures. Alternatively, when a priori information is not available, all connected components can be computed and eroded to one pixel as seeds automatically (Preim and Botha, 2013; Rubin, Greenspan and Brinkley, 2014; Masood et al., 2015). The other important step in region growing method is to set up a stopping rule or predicate. Therefore, the region growth could stop when no more connected pixels satisfy the predicate for inclusion in that region. The predefined criterion is often a threshold for the intensity values or a predicate based on texture or color (Withey and Koles, 2008; Erdt, Steger and Sakas, 2012; Patil and Deore, 2013).

Hysteresis thresholding is a particular case of region growing method with two threshold values, a low and a high threshold. When the intensity of the gray value is lower than the low threshold, the corresponding pixel or voxel is removed, and if it is higher than the high threshold, it will be retained. Then there is a loop for which a pixel or voxel between the low and high thresholds is retained only if it is connected to a pixel or voxel already retained. Hysteresis thresholding ensures segmentation of connected regions by keeping "certain" foreground elements, which are higher than the high threshold value, and checking neighbors. This method also suppresses the noisy background, which is lower than the lower threshold. Fig. 3.3 shows the thresholds generally selected from the histogram of the gray levels in the image (Wirjadi, 2007).

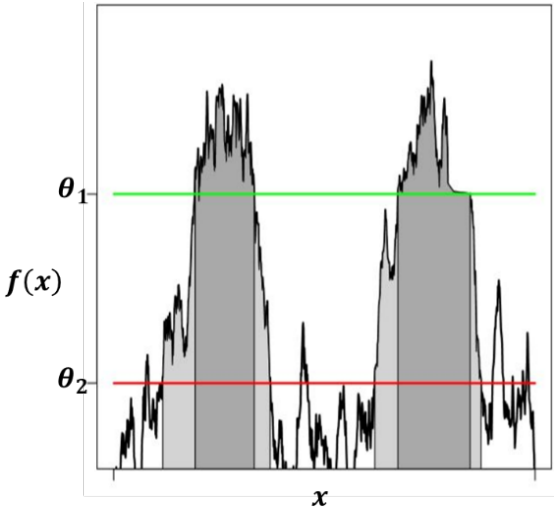

Fig. 3.3 Illustration of hysteresis thresholding: Foreground regions must contain voxels exceeding a "high threshold" but can be extended until reaching a lower threshold. This ensures connected regions and efficiently excludes background noise voxels. θ_1 and θ_2 are two thresholds, $\theta_1 \geq \theta_2$, $f(x)$ represents the intensity of gray value at the pixel or voxel x (Wirjadi, 2007).

Region growing methods are very well suited for the segmentation of homogeneous objects varying in shape, and guarantee to get connected regions. However, the disadvantage of region growing is its tendency to incorporate unwanted neighborhood with similar intensities. Especially, the noisy signals in the original image may limit the region growing work correctly (Erdt, Steger and Sakas, 2012; Zaitoun and Aqel, 2015).

3.2.4.2 Region splitting and merging

Rather than requiring seed points in region growing methods, an alternative is "region splitting and merging" methods, which attempt to segment an image into regions using a controlled homogeneity measure (Manousakas et al., 1998; Wirjadi, 2007; Withey and Koles, 2008). Firstly, the entire image is usually split into quadrants based on quad tree data theory. If a selected predicate for checking homogeneity of pixel intensities is false, the quadrant will be subdivided into sub-quadrants, until no further splitting is possible. However, the partitions may contain adjacent regions with identical properties, for instance similar intensity levels, leading to over-segmentation. Therefore, the second step is to aggregate these adjacent sub-regions according to a homogeneity criterion, and stop when no further merging is possible (Withey and Koles, 2008; Patil and Deore, 2013; Zaitoun and Aqel, 2015). The region splitting and merging method guarantees connected regions, and can be extended to 3D with a directionally uniform performance from the 2D method (Manousakas et al., 1998; Withey and Koles, 2008; Zaitoun and Aqel, 2015).

3.2.4.3 Watershed algorithm

The watershed algorithm is another region-based segmentation approach to find regions and their boundaries simultaneously (Serra, 1982; Preim and Botha, 2013). The classical watershed transform is often used to segment an image into multiple objects. This method visualizes an image as a topographic map with two spatial coordinates with the intensity as the elevation. In such a topographic interpretation, we consider the "catchment basin" as a set of points at which water would fall with certainty to a single minimum. In addition, we define "ridge lines" as a set of points at which water would be equally likely to fall to more than one such minimum (Gonzalez and Woods, 2017).

In the classical watershed algorithm, the "flooding" begins from the regional minimums on the "control surface", which is treated as a topographic map and can be the original image itself or the magnitude of gradient. Next, the watershed lines will be built to separate various catchment basins when the different sources of water are merging. Thus, the original image is separated into multiple regions.

Specifically, Fig. 3.4 (a) is a gray-scale image, and Fig. 3.4 (b) is its topographic map where the catchment basins and ridge lines are proportional to the intensity values in the original image. To prevent the rising "water" from spilling out through the boundaries of the image, the perimeter of entire image is set as an enclosed dams with the highest intensity value in the original image (Gonzalez and Woods, 2017).

To explain the working process of watershed algorithm, we suppose that there is a hole in each regional minimum (shown as dark areas in Fig. 3.4 (b)) and flooding happens from them at a uniform rate. Fig. 3.4 (c-e) show the different stages of flooding results, in which "water"

is shown as light gray corresponding to the relevant regional minimum. Next, "Water" continues to rise and begins to overflow into other basins, and the watershed lines will be constructed to prevent it from the merging. Fig. 3.4 (f-g) show the different stages of building watershed lines between different catchment basins. The whole process continues until the highest intensity value in the original image is reached. All of the watershed lines are obtained as the final segmentation boundaries between different objects in the image. Fig. 3.4 (h) shows the final segmentation lines (dark one-pixel-thick paths) superimposed on the original image.

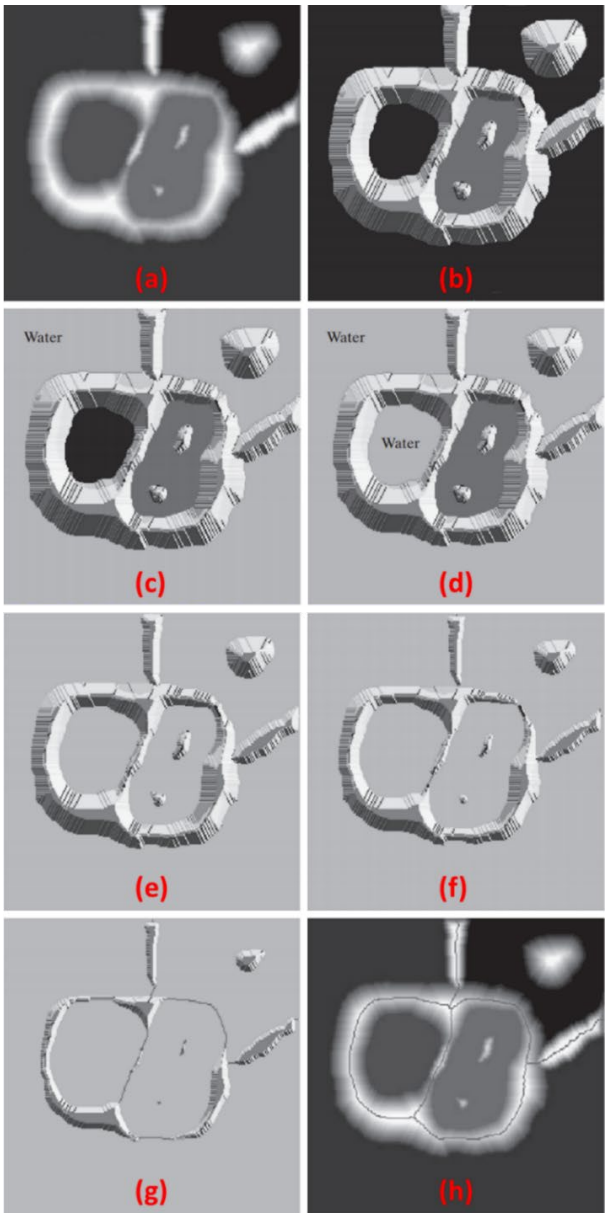

Fig. 3.4 Illustration of the classical watershed algorithm process. (a) Original image. (b) Topographic map of (a). (c-e) Different stages of flooding. (f-g) Different stages of building watershed lines. (h) Final watershed segmentation lines superimposed on the original image (Gonzalez and Woods, 2017).

However, in most cases, there are many undesired regional minimums due to noise or natural variations, which lead to over-segmentation (Bhabatosh, 2011). One way to avoid this problem is the marker-controlled watershed method, which initializes the watershed from the already identified markers (Beucher and Meyer, 1990). The method saves running time by reducing the number of iterations and prevents results from over-segmentation by simplifying the merging of the regions.

3.2.5 Model-based image segmentation methods

Model-based segmentation techniques are powerful approaches with employing priori knowledge of the location, size, and shape of object in the processing. The first step of model-based segmentation is often to determine the initial model manually or automatically. The second step is to adapt this initial model to the local features, usually with an iterative optimization (McInerney and Terzopoulos, 1996; Preim and Botha, 2013).

Deformable model is a common used model-based segmentation method combining with geometry, physical properties, and approximation theory. The goal of deformable models is to delineate object boundaries by deforming an initial model towards boundaries in the image under the influences of internal and external forces. Geometry is used to represent the shape of object permitting broad shape coverages. Physical properties can be used to impose constraints on how the shape may vary over space and time with the elasticity theory and Lagrangian dynamics setting. For instance, physical property is used to constrain the smoothness of the model and give internal forces to deform the initial model. Optimal approximation theory serves to fit the model to the measured data by providing external forces (McInerney and Terzopoulos, 1996; Phan, Xu and Price, 1998; Xu, Pham and Prince, 2000; Withey and Koles, 2008; Erdt, Steger and Sakas, 2012; Preim and Botha, 2013; Masood et al., 2015).

Deformable models have been developed for 2D and 3D image segmentation. In the 2D case, the model is a deformable curve or contour, and is called active contour or snake (Kass, Witkin and Terzopoulos, 1988). In the 3D case, the model is a 3D deformable surface, and is also known as balloon segmentation (Terzopoulos, Witkin and Kass, 1988). An example of deforming the initial balloon model to fit the edges of the left ventricle is shown as Fig. 3.5 (McInerney and Terzopoulos, 1995). Apart from deformable curves and surfaces, solid deformable models have also been proposed (Terzopoulos and Fleischer, 1988). To support the applications to medical images, where anatomic structures are solid or volumetric, the solid deformable models may be required rather than deformable surface models in 3D (McInerney and Terzopoulos, 1996; McInemey and Terzopoulos, 1999). Another important extension of deformable models is non-parametric model, which is also called geometric deformable model. This model is based on the theory of curve evolution and the level set method (Phan, Xu and Price, 1998; Xu, Pham and Prince, 2000; Masood et al., 2015).

Chan-Vese method is a new model for active contours to detect objects in a given image, based on techniques of curve evolution, Mumford–Shah functional for segmentation and level sets. Unlike the classical active contours methods, Chan-Vese is not based on an edge-function to stop the evolving curve on the desired boundary. Thus, Chan-Vese can detect and preserve the locations of boundaries, even if on a noisy image. In addition, the initial curve

does not necessarily surround the objects and can be anywhere in the image (Chan and Vese, 2001). However, Chan-Vese method is computationally heavy, and needs manual initialization.

To avoid manual intervention and the subjective errors, the modified version of Chan–Vese has been developed (Tassani, Korfiatis and Matsopoulos, 2014; Korfiatis, Tassani and Matsopoulos, 2017). Unlike the classical Chan–Vese method, the modified version proposed an automatic initialization, which is defined as the branch points calculated from the skeleton result.

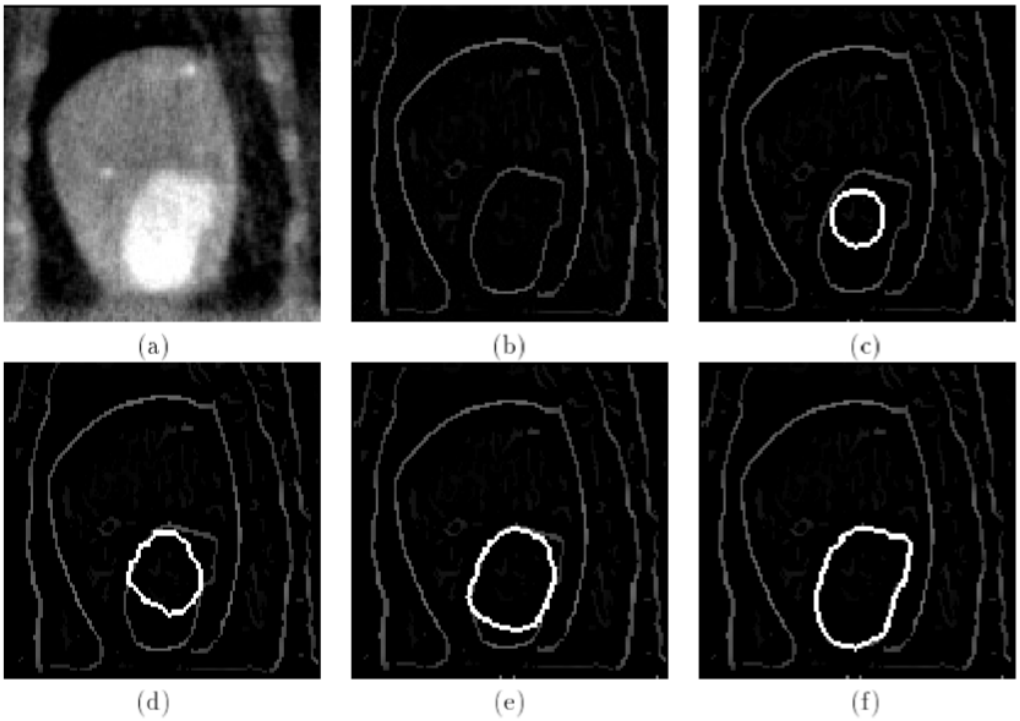

Fig. 3.5 Intensity and edge detected CT image slice of left ventricle. (a) Intensity image XZ plane slice 91. (b) Edge detected image. (c) Cross section of initial balloon model. (d)-(f) Cross section of balloon deforming to left ventricle (McInerney and Terzopoulos, 1995).

The main advantage of deformable models is that the method is less dependent on the image signal and can provide robustness to noise and spurious edges by incorporating priori knowledge about the shape of object. A disadvantage of deformable models is their strong dependence on a proper initialization and appropriate parameters. Therefore, reducing sensitivity to initialization has been a topic of research (Korfiatis, Tassani and Matsopoulos, 2017). Another drawback is the restriction of flexibility in deformable models. The internal forces constraints restrict the flexibility and prevent the deformable models from representing tube-like shapes, branching structures or objects with strong protrusions. Therefore, the deformable models are generally not applied for the segmentations of vascular or bronchial trees in medical images.

3.3 Segmentation of bone and vessels

In this section, we will review the state of the art of techniques for segmenting the bone and vessels in 3D X-ray μCT and SR-μCT image.

3.3.1 Bone segmentation

Bone tissue is dense and visible using 3D X-ray μCT with the adequate spatial resolution and high contrast. In this subsection, we review both threshold-based and model-based bone segmentation techniques.

3.3.1.1 Threshold-based method

Global thresholding method is the basic and most widely used bone segmentation technique in μCT. This method has been used to segment bone microstructures in rats (Coutel et al., 2018; Sharma et al., 2018), and in mice (Mehadji, Ahmed and Berteau, 2019; Oliviero et al., 2019).

Global thresholding is an efficient, fast and easy to implement segmentation technique for bone segmentation on μCT image, but the selection of a suitable threshold is critical to have a correct segmentation and produce an accurate estimation of the bone morphometric parameters (Zhang et al., 2008). Threshold value can be determined either by a manual selection or by an automatic algorithm (Christiansen, 2016). For instance, the manual selection of a threshold value can be performed, by analyzing the gray level histogram of the image (Waarsing, Day and Weinans, 2004). However, the manual intervention is often time-consuming and is prone to inter-observer variability, intra-observer variability, and subjective error result. The Otsu's method has been used to select threshold value automatically for segmenting trabecular bone on μCT images (Tassani, Korfiatis and Matsopoulos, 2014). In addition, Ding et al. presented another automatic method to determine the threshold value based on a calibration of volume fractions to the Archimedes-based volume fractions (Ding, Odgaard and Hvid, 1999). Moreover, the connectivity density as a measure was used to select a threshold value automatically by integrating both topological and geometric information (Zhang et al., 2008).

Despite the simple implementation and efficiency of global thresholding, it can be insufficient to segment bone correctly on some μCT images, in which the gray level values of bone varies in an individual sample or among the groups due to beam hardening and non-uniform mineralization. In addition, problems such as noise, artifacts and partial volume effect can also make global thresholding impractical (Dufresne, 1998; Waarsing, Day and Weinans, 2004; Scherf and Tilgner, 2009; Bouxsein et al., 2010; Korfiatis, Tassani and Matsopoulos, 2017; Irie et al., 2018; Peña Fernández et al., 2018).

Local or adaptive thresholding methods are also commonly used bone segmentation techniques on μCT images. As global thresholding may not be adequate for low quality images, more sophisticated local or adaptive thresholding segmentation techniques are necessary. This method can be less sensitive to the artifact, noise and beam hardening by examining small neighborhoods of voxels in local regions. There are various ways to determine the local thresholds (Bouxsein et al., 2010; Depyperre, 2013; Leszczyński et al.,

2016). Adaptive iterative thresholding is also an efficient and automatic method to segment bone from the background by calculating an optimal threshold value. In this method, for each iteration the mean grayscale values above and below a proposed threshold are calculated, and the mean of these two values is proposed as the threshold for the next iteration. Iteration continues until a stable solution is found (Ryan and Ketcham, 2002b, 2002a; Fajardo et al., 2007; Scherf and Tilgner, 2009).

The half maximum height (HMH) has been introduced as a local threshold value to determine the exact position of the boundary between bone and background on μCT image, since the tissue interface can be blurred due to the partial volume effects. In this method, HMH is calculated as the mean of the maximum and minimum gray level values on either side of the interface, along a row of pixels that span the interface transition (Spoor, Zonneveld and Macho, 1993). However, the application of this method is restricted in a small 2D region of interest. Therefore, researchers continued to make efforts to extend HMH method to the large 2D region and even 3D trabecular bone segmentations on μCT images (Fajardo, Ryan and Kappelman, 2002; Coleman and Colbert, 2007; Scherf and Tilgner, 2009).

Dufresne proposed another local segmentation method for bone segmentation in μCT images (Dufresne, 1998). This method calculates the histograms of local area at the neighborhoods of each voxel throughout the volume. Then, the algorithm calculates threshold in each local region. This method has been applied to segment the trabecular bone of rat vertebrae in μCT images. A single slice of the original image, the global thresholding segmentation, and the local thresholding segmentation are shown respectively as Fig. 3.6 (A), (B) and (C). In the global thresholding segmentation, the trabecular bone in the center of the vertebra is underestimated and the bone on the periphery is overestimated. In the local thresholding segmentation, the much better segmentation result is provided (Dufresne, 1998).

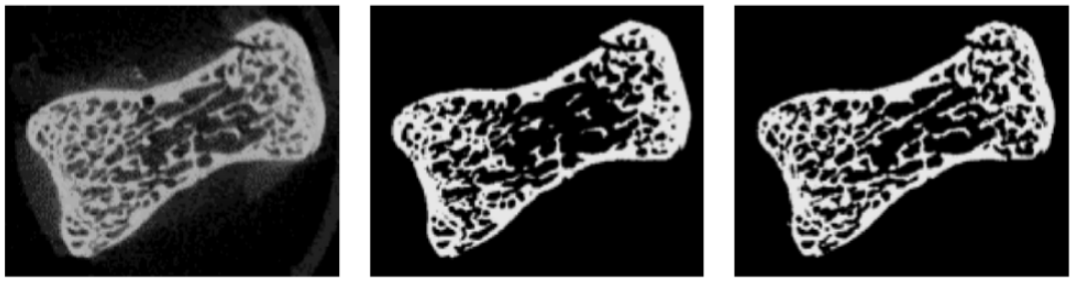

Fig. 3.6 Segmentation of trabecular bone of rat vertebrae from a μCT image. (A) The original image. (B) The global thresholding segmentation. (c) The local thresholding segmentation (Dufresne, 1998).

Kuhn et al., (Kuhn et al., 1990), Depyperre (Depyperre, 2013) and Leszczyński et al (Leszczyński et al., 2016) proposed a similar kind of local thresholding method with the mean of gray level values within a local region. This method gives each pixel (voxel) a local threshold value, which is calculated as a mean of minimal and maximal gray level values within a circle (sphere) with a selected radius. The circle (sphere) is the local region and the center is the considered pixel (voxel). This approach assumes that each local region contains bone as well as background. For the local regions containing only bone or only background, a

range of intensity values can be specified outside of which voxels are excluded from local thresholding. After each voxel has its own local threshold value, the gray level value of each voxel is compared to its calculated local threshold value. A voxel whose gray level value is higher than its local threshold value is classified as bone. Otherwise, it is classified as background. This local thresholding method is relatively fast and works well for the segmentation of bone in the μCT images (Kuhn et al., 1990; Depyperre, 2013; Leszczyński et al., 2016).

Waarsing et al. proposed a new kind of local threshold method to segment trabecular bone in μCT images (Waarsing, Day and Weinans, 2004). The first step of this technique is to detect 3D edges between bone and background using the Sobel operator. In order to keep as many edges as possible while rejecting edges due to noise, a high threshold value and a low threshold value are set to generate the final 3D edges. Edges with the magnitude larger than a high threshold value are retained, and the connected edges with the magnitude larger than a low threshold value as well. Secondly, the result of edge detection is used to obtain a local threshold value for each voxel. The gray level values of voxels in the set of edges are served as their local threshold values. If a voxel in the dataset is the neighborhood of an edge voxel, the local threshold value of this voxel is calculated by taking the Gaussian weighted average of the local threshold values of the voxels in the neighborhood. This procedure dilates iteratively and continues until each voxel has a local threshold value. The last step is to compare the gray level value of each voxel with its local threshold value. If the gray level value of the voxel is higher than its local threshold value, this voxel will be marked as bone, otherwise marked as background (Waarsing, Day and Weinans, 2004; Depyperre, 2013).

3.3.1.2 Model-based method

Although threshold-based method is the most common used bone segmentation technique in μCT, the partial volume effects may prevent the correct segmentation of the thin and small trabecular bone. To address this challenge, a modified Chan–Vese method was proposed (Tassani, Korfiatis and Matsopoulos, 2014; Korfiatis, Tassani and Matsopoulos, 2017). In the studies, human femoral head was imaged using μCT with isotropic voxel size of 19.5 μm. Next, the modified Chan–Vese method was used to segment trabecular bone on 2D slices. Fig. 3.7 shows the segmentation of trabecular bone using various approaches. The results proved its superior performance compared to the adaptive thresholding and Otsu's thresholding methods. In particular, the modified Chan–Vese method enhanced the identification of small structures. In addition, it was an automatic procedure not required any operator interaction, and robust even in a noisy image. However, the modified Chan–Vese method has not been implemented on 3D images.

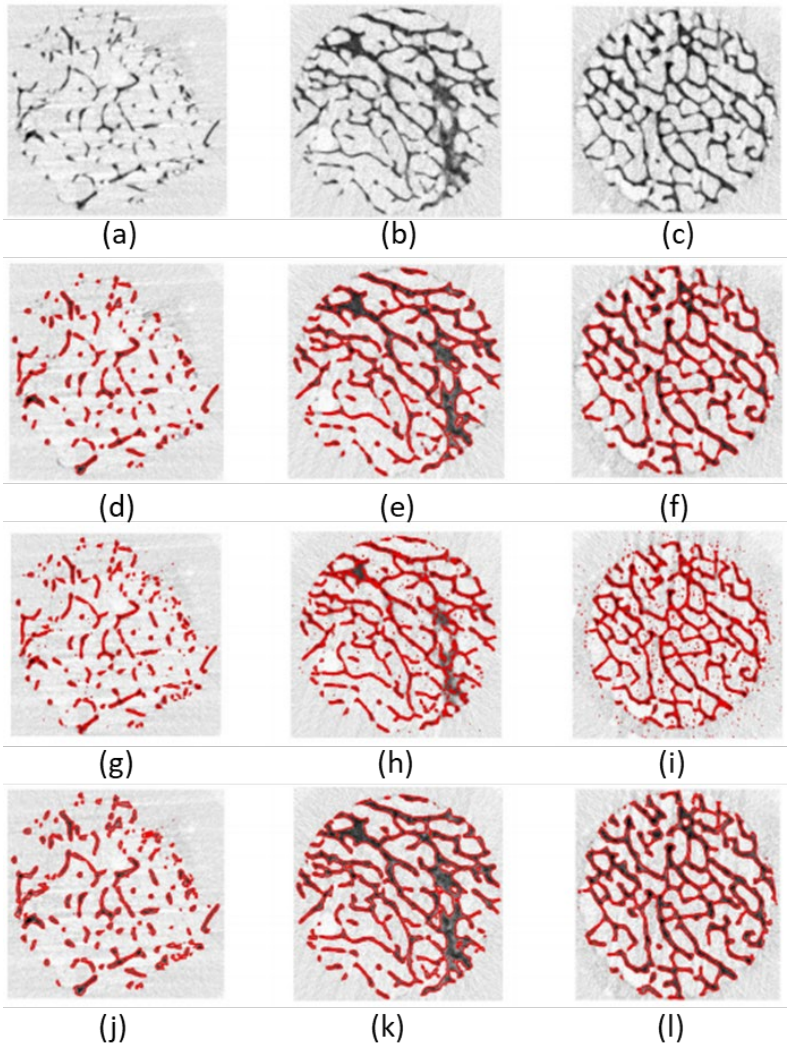

Fig. 3.7 Segmentation of trabecular bone using various techniques. (a)–(c) Original images. (d)–(f) Results of segmentation using the modified Chan–Vese method. (g)–(i) Results of segmentation using the adaptive thresholding. (j)–(l) Results of segmentation using the Otsu's method. (Korfiatis, Tassani and Matsopoulos, 2017).

3.3.2 Vasculature segmentation

To study vasculature related diseases, μCT based modalities are often used for imaging 3D vessels in preclinical research, where segmentation of vasculature is fundamental and prerequisite for the subsequent quantification and analysis. The segmentation techniques could be either manual or automatic (Zagorchev et al., 2010).

In manual segmentation, operators usually delineate regions of vasculature in 2D slices, and the segmented 3D volume is formed by stacking. In the study of simultaneous visualizations of the calcified mice bone and vessels using SR-PCT without contrast agent (Núñez et al., 2017), vessels were segmented by hand due to the relatively weak phase contrast in the vessels. Although the manual segmentation works well even with low quality images (the

noisy and little contrast) and artifacts, it is time consuming for the large data sets (Zagorchev et al., 2010).

Automated vascular segmentation in μCT images may require high contrast of blood vessels with the help of contrast agent. For instance, Microfil is a suitable contrast agent for imaging vessels located outside the bone, within muscles, as well as in soft organs. Barium sulfate agent (BaSO4) is a better tool for the visualization of bone marrow vessels (Lafage-Proust et al., 2015). However, the visualization of vasculature in bone using the μCT with contrast agent, requires to decalcify the bone, due to the similar gray level values between the opacified vessels and bone (Moore et al., 2003; Zhang et al., 2005; Schneider et al., 2009; Nyangoga et al., 2011), as shown in Fig. 3.8 (Nyangoga et al., 2011). Thus, μCT does not permit a complete analysis of relationship between the bone and vessels. SR-μCT coupled with a contrast agent allows to visualize simultaneously the 3D bone microstructures and vascular networks in preclinical studies (Schneider et al., 2009; Langer et al., 2010; Prisby et al., 2011). However, potential limitations include incomplete perfusion of the vasculature and artifacts from high pressure perfusing resulting in leakage of the contrast agent from the vessels (Bouxsein et al., 2010).

The common used automated vascular segmentation techniques, on the images obtained by μCT based modalities, include global thresholding, region growing.

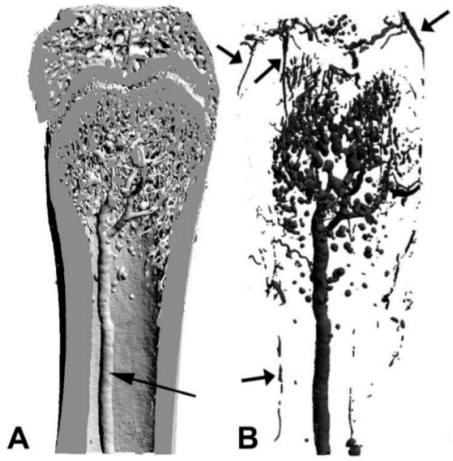

Fig. 3.8 Illustration of 3D models obtained on (A) undecalcified bone and (B) decalcified bone. The original images were acquired using μCT with contrast agent. These two 3D models were segmented by global thresholding. The arrows point on the artery vessels. (Nyangoga et al., 2011)

3.3.2.1 Global thresholding method

Global thresholding has been widely applied to the segmentation of vasculature in bone, on μCT image. To study the alterations of femur bone vasculature in diabetic rats, the contrast agent was injected into vessels, and the vascular network was visualized using μCT with decalcification. Following the 3D image acquisition and reconstruction, vessels were well segmented using a global thresholding technique (Zeitoun et al., 2019). In addition, Duvall et al (Duvall et al., 2004) demonstrated the quantitative analysis of mice bone vasculature with μCT and contrast agent. In this study, vasculature was segmented using global thresholding

after bone demineralization. To analyze vessel and bone simultaneously, Schneider et al (Schneider et al., 2009) adapted SR-μCT to image the hind limbs of mice with contrast agent of barium sulfate. The vasculature in bone was visualized without decalcifications, and global thresholding was used to segment vascular from the bone automatically, due to the significant difference in X-ray absorption between the contrast agent and bone (Schneider et al., 2009).

Although the global thresholding is the most common used vessel segmentation technique, the segmentation quality can be reduced by beam-hardening, artifacts, partial volume effects, and noise on the image.

3.3.2.2 Region growing method

Unlike global thresholding, region growing technique considers the connectivity of regions and can achieve a more robust vessels segmentation.

Within bone tissue, 3D region growing has been proposed to segment vessels from bone on SR-μCT image, in a rat model (Langer et al., 2010; Prisby et al., 2011) and in a mice model (Roche et al., 2012) associated to contrast agent. Specifically, in this automatic image analysis protocol, bone and vessels were first separated from the background by thresholding with the threshold on the linear attenuation coefficient, determined with Otsu's method. Then vessels were segmented using 3D region growing method to overcome partial volume effect, with a high threshold and a low threshold. Voxels having greater intensities than the high threshold value are considered as seeds of vessels, and regions grow from these seeds to include neighbors only if their intensity is between the high and low threshold values. Finally, the vessels were subtracted from the first segmentation including both bone and vessel structures to yield the bone compartment (Langer et al., 2010). 3D renderings of bone and vessels are shown in Fig. 3.9.

Region growing requires the spatially separated structures as the rat bone case. However, in mice tibia bone, vessels may appear to be touching the bone surface in SR-μCT image, at 3.5 μm resolution (Xu, Langer and Peyrin, 2020), precluding the correct segmentations of bone and vessels using the 3D region growing based protocol.

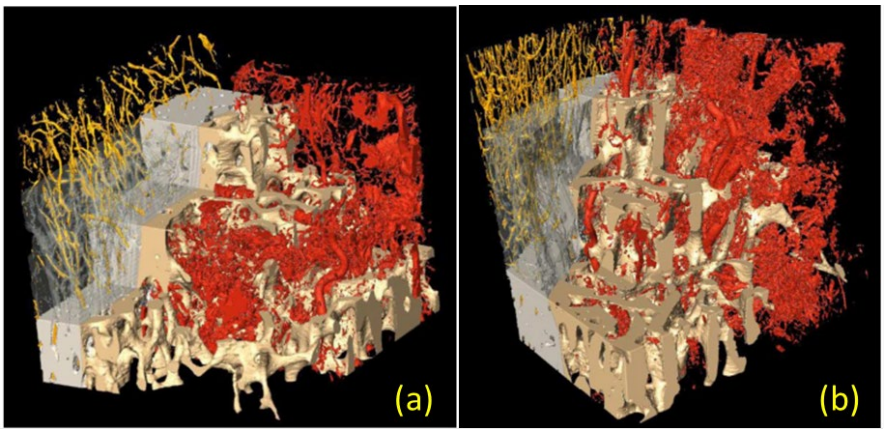

Fig. 3.9 Volume rendering showing bone and vessel compartments. (a) Control sample (b) parathyroid hormone (PTH) sample. Cortical bone is in gray, trabecular bone in beige, vessel within trabecular bone in red and within cortical bone in orange (Langer et al., 2010).

3.4 Conclusion

In this chapter, we introduced the generic image segmentation techniques, including manual segmentation, edge-based, threshold-based, region-based, and model-based image segmentation methods. Additionally, we reviewed the state of the art of approaches for segmenting bone and vessels in X-ray μCT and SR-μCT images, such as global thresholding, region growing, and deformable model methods.

In the next chapter, we will introduce the evaluation of segmentation quality.

Chapter 4

Evaluation of image segmentation quality

Contents

4.1 Introduction

An important step in the design and use of image segmentation algorithms is to assess the segmentation quality. This permits to evaluate different algorithms, and to know how much confidence to put in the segmentation for later steps in the analysis procedure. The evaluation of segmentation quality is often performed by comparing the segmentation result with a reference image, often manually segmented by experts, considered the "gold standard" or "ground truth". This can be done in two-class as well as in multi-class segmentation (Mohan and Subashini, 2019; Wang, Wang and Zhu, 2020).

In this chapter, we will introduce the commonly used evaluation measures of image segmentation quality, restricted to the case of overlap-based metrics. In section 4.2, we will first introduce the confusion matrix, which can be used to calculate evaluation measures. In section 4.3, we will present an overview of the various evaluation measures including the sensitivity, specificity, precision, accuracy, Jaccard index, Dice coefficient, and Matthews correlation coefficient (MCC) for the two-class segmentation. In section 4.4, we will introduce the extended accuracy, F_1 score, and MCC for the evaluation of multi-class segmentation. In section 4.5, we will discuss the effects of evaluation measures on imbalanced data. In section 4.6, we will conclude this chapter.

4.2 Confusion matrix

The confusion matrix is a specific contingency table layout allowing the assessment of a classification process, and in particular of segmentation performance (Powers, 2011), and has been widely exploited to calculate the evaluation measures for segmentation quality.

Given the segmentation of an original image and its reference image, the confusion matrix is defined as a square matrix: $C \in M(N \times N, \mathbb{N})$, $N \geq 2$ to summarize the N classes segmentation results. The ij-th entry C_{ij} is the number of image elements (pixels in 2D or voxels in 3D) of true class i assigned to class j: $C_{ij} = |\{\text{true class} = i, \text{prediction class} = j\}|$. For instance, C_{kk} indicates how many image elements are correctly segmented in the class k (Jurman and Furlanello, 2010; Wei et al., 2010; Delgado and Núñez-González, 2019).

		True Class: Positive	True Class: Negative
Predicted Class	Positive	True positive (TP)	False positive (FP)
Predicted Class	Negative	False negative (FN)	True negative (TN)

Fig. 4.1 Illustrative example of two-class confusion matrix (Tharwat, 2020).

Fig. 4.1 shows an example of two-class confusion matrix. The diagonal elements (in red) stand for the correct segmentation, and the off-diagonal elements represent the incorrect segmentation (Tharwat, 2020). If a positive image element is correctly segmented as positive, it is counted as a true positive (TP); if a positive image element is segmented as negative, it is

considered as a false negative (FN). In addition, if a negative image element is correctly segmented as negative, it is counted as a true negative (TN); if a negative image element is segmented as positive, it is considered as false positive (FP). Each element (TP, FN, TN, or FP) in the confusion matrix indicates the number of corresponding image elements (Chicco and Jurman, 2020).

Fig. 4.2 shows an example of three-class confusion matrix (classes: 1, 2, and 3). C_{11}, C_{22}, C_{33} are the numbers of correctly segmented image elements of class 1, class 2, and class 3, respectively. False negative or false positive of a class can be calculated by adding the errors in that column or row. For example, the false negatives of class 1 is the sum of C_{12} and C_{13}, where C_{12} is the number of image elements in class 1 that are incorrectly segmented as class 2 and C_{13} is the number of image elements in class 1 that are incorrectly segmented as class 3 (Tharwat, 2020).

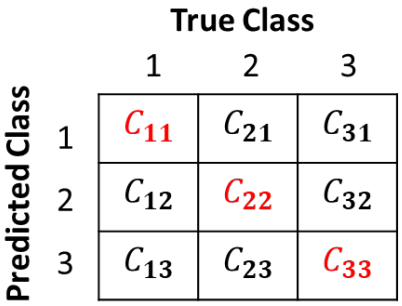

Fig. 4.2 Illustrative example of three-class confusion matrix (Tharwat, 2020).

4.3 Two-class evaluation measures

Two-class or binary segmentation is a basic problem in image analysis. A number of evaluation measures for the segmentation quality have been proposed, and can be calculated based on the confusion matrix (Sokolova, Japkowicz and Szpakowicz, 2006; Powers, 2011; Bekkar, Djemaa and Alitouche, 2013; Chicco and Jurman, 2020; Tharwat, 2020).

4.3.1 Sensitivity

Sensitivity, also known as recall or true positive rate (TPR), measures the proportion of true positives among the whole positive image elements, and is estimated as

$$TPR = \frac{TP}{TP + FN}. \tag{4.1}$$

4.3.2 Specificity

Specificity, also known as selectivity or true negative rate (TNR), represents the proportion of true negatives. In other words, this evaluation measures the ratio of the correctly segmented negative image elements to the total number of negative image elements as

$$TNR = \frac{TN}{TN + FP}. \tag{4.2}$$

4.3.3 Precision

Precision or positive predictive value (PPV) denotes the proportion of correctly segmented positive image elements to the total number of positive predicted image elements, as

$$PPV = \frac{TP}{TP + FP}. \tag{4.3}$$

4.3.4 Accuracy

Accuracy (ACC) represents the proportion of the all correctly segmented image elements, including both true positives and true negatives, among the total number of image elements as

$$ACC = \frac{TP + TN}{TP + TN + FP + FN}. \tag{4.4}$$

4.3.5 Jaccard index

The Jaccard index (J), or Jaccard similarity coefficient is defined as the intersection divided by the union between segmentation and reference image, as

$$J = \frac{|A \cap B|}{|A \cup B|} \tag{4.5}$$

where $|A|$ and $|B|$ are the cardinalities of the two sets A and B, representing respectively the segmentation and reference image. The Jaccard index can also be measured based on confusion matrix, as

$$J = \frac{TP}{TP + FP + FN} \tag{4.6}$$

where the correct segmentation of negative is ignored.

4.3.6 Dice coefficient

The Dice coefficient, also known as F_1 score or Dice similarity coefficient (DSC), is a statistical parameter to assess spatial overlapping between the segmentation and reference image (Zou et al., 2004). Its expression is given by (Aaron et al., 2020)

$$Dice = F_1 = \frac{2|A \cap B|}{|A| + |B|}. \tag{4.7}$$

Dice coefficient can also be measured based on confusion matrix, as

$$Dice = F_1 = \frac{2TP}{2TP + FP + FN} \tag{4.8}$$

where the correct segmentation of negative is also ignored.

4.3.7 Matthews correlation coefficient

The Matthews correlation coefficient (MCC) (Matthews, 1975) is widely used as a measure of quality of classifications to indicate how well observations (reference image) and predictions (segmentation) agree. $MCC = 1$ indicates a perfect classification, $MCC = 0$ indicates no better than random prediction, and $MCC = -1$ indicates a total misclassification (Matthews, 1975). In its original form, MCC applies to assessing the quality of two-class classifications, and can be measured from confusion matrix, as

$$MCC = \frac{TP \times TN - FP \times FN}{\sqrt{(TP + FP)(TP + FN)(TN + FP)(TN + FN)}}. \tag{4.9}$$

4.4 Multi-class evaluation measures

Multi-class image segmentation has also been widely studied in the field of image analysis. Here, for example, we want to analyze bone and vessel microstructures simultaneously, based on SR-μCT images. We thus have three classes: bone, vessels, and background, which need to be segmented and evaluated (Xu, Langer and Peyrin, 2020).

4.4.1 Overall evaluation of Accuracy

Accuracy is one of the most commonly used overall evaluation measures. Its definition can be simply extended from binary to multi-class segmentation, since it considers all classes of the correct segmentation among the total number of image elements (Delgado and Núñez-González, 2019; Chicco and Jurman, 2020; Tharwat, 2020).

4.4.2 Extended F_1 score

F_1 score, also known as Dice coefficient in statistics, can be extended to the multi-class evaluation by employing an averaging procedure on all classes (Chicco and Jurman, 2020), such as $F_{1-macro}$ and $F_{1-micro}$.

$F_{1-macro}$ is the macro-averaged version of the F_1 measure (Lewis et al., 2004; Tsoumakas, Katakis and Vlahavas, 2010; Lipton, Elkan and Naryanaswamy, 2014; Pillai, Fumera and Roli, 2017). It is defined as the unweighted mean of two-class F_1 scores across all classes, given by

$$F_{1-macro} = \frac{1}{N}\sum_{\lambda=1}^{N}\frac{2TP_\lambda}{2TP_\lambda + FP_\lambda + FN_\lambda} \tag{4.10}$$

where $N \geq 2$ represents N classes, and λ denotes a certain class. For a two-class case, $N = 2$ and $F_{1-macro}$ is given by

$$F_{1-macro} = \frac{1}{2}\left(\frac{2TP_1}{2TP_1 + FP_1 + FN_1} + \frac{2TP_2}{2TP_2 + FP_2 + FN_2}\right)$$

where the two-class F_1 scores for the class $\lambda = 1$ and $\lambda = 2$ are equal in binary segmentation ($\frac{2TP_1}{2TP_1+FP_1+FN_1} = \frac{2TP_2}{2TP_2+FP_2+FN_2}$). Therefore, $F_{1-macro}$ can also be written as

$$F_{1-macro} = \frac{2TP_1}{2TP_1 + FP_1 + FN_1} = \frac{2TP_2}{2TP_2 + FP_2 + FN_2},$$

which is consistent with the formula (4.8) for the two-class F_1 score. For a three-class case, $N = 3$ and $F_{1-macro}$ is given by

$$F_{1-macro} = \frac{1}{3}\left(\frac{2TP_1}{2TP_1 + FP_1 + FN_1} + \frac{2TP_2}{2TP_2 + FP_2 + FN_2} + \frac{2TP_3}{2TP_3 + FP_3 + FN_3}\right).$$

To calculate the binary F_1 score for each class, the three-class confusion matrix needs to be transformed into three two-class confusion matrix, as shown in Fig. 4.3. Firstly, three classes are separated into one class and the other combined two classes, such as Fig. 4.3 (a) $\lambda = 1$ (given by green) and $\lambda = 2, 3$ (given by blue), Fig. 4.3 (b) $\lambda = 2$ (given by green) and $\lambda = 1, 3$ (given by blue), and Fig. 4.3 (c) $\lambda = 3$ (given by green) and $\lambda = 1, 2$ (given by blue). Next, the two-class confusion matrix is generated by considering the combined two classes as a new class. Fig. 4.3 (d) is the transformed two-class confusion matrix based on (a). Fig. 4.3 (e) is the transformed two-class confusion matrix based on (b). Fig. 4.3 (f) is the transformed two-class confusion matrix based on (c).

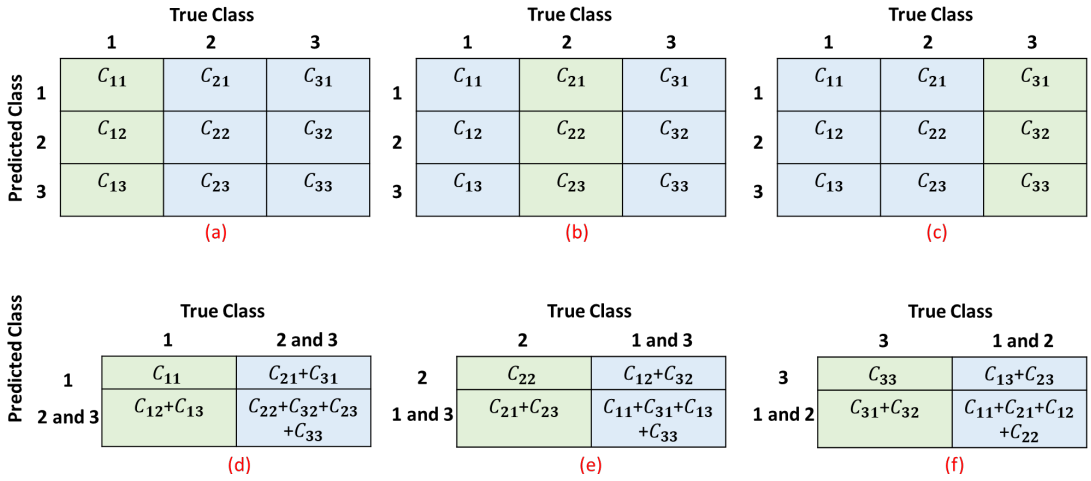

Fig. 4.3 Illustration of the transform from a three-class to three binary confusion matrix. (a) Three-class confusion matrix separated into class $\lambda = 1$ (given by green) and $\lambda = 2, 3$ (given by blue). (b) Three-class confusion matrix separated with class $\lambda = 2$ (given by green) and $\lambda = 1, 3$ (given by blue). (c) Three-class confusion matrix separated with class $\lambda = 3$ (given by green) and $\lambda = 1, 2$ (given by blue). (d) The transformed two-class confusion matrix based on (a). (e) The transformed two-class confusion matrix based on (b). (f) The transformed two-class confusion matrix based on (c).

Therefore, the two-class F_1 score for each class can be calculated by

$$\frac{2TP_1}{2TP_1 + FP_1 + FN_1} = \frac{2C_{11}}{2C_{11} + (C_{21} + C_{31}) + (C_{12} + C_{13})},$$

$$\frac{2TP_2}{2TP_2 + FP_2 + FN_2} = \frac{2C_{22}}{2C_{22} + (C_{12} + C_{32}) + (C_{21} + C_{23})},$$

$$\frac{2TP_3}{2TP_3 + FP_3 + FN_3} = \frac{2C_{33}}{2C_{33} + (C_{13} + C_{23}) + (C_{31} + C_{32})}.$$

$F_{1-micro}$ is the micro-averaged version of the F_1 measure. It can be computed from the sum of all classes at each element of confusion matrix (Lewis et al., 2004; Tsoumakas, Katakis and Vlahavas, 2010; Lipton, Elkan and Naryanaswamy, 2014; Pillai, Fumera and Roli, 2017) as,

$$F_{1-micro} = \frac{\sum_{\lambda=1}^{N} 2TP_\lambda}{\sum_{\lambda=1}^{N}(2TP_\lambda + FP_\lambda + FN_\lambda)}. \tag{4.11}$$

For a three-class confusion matrix, $N = 3$ and $F_{1-micro}$ is given by

$$F_{1-micro} = \frac{2(TP_1 + TP_2 + TP_3)}{2(TP_1 + TP_2 + TP_3) + (FP_1 + FP_2 + FP_3) + (FN_1 + FN_2 + FN_3)}$$

where the elements of confusion matrix can be computed based on Fig. 4.3 (d-f), as

$TP_1 = C_{11}$, $TP_2 = C_{22}$, $TP_3 = C_{33}$,

$FP_1 = C_{21} + C_{31}$, $FP_2 = C_{12} + C_{32}$, $FP_3 = C_{13} + C_{23}$,

$FN_1 = C_{12} + C_{13}$, $FN_2 = C_{21} + C_{23}$, $FN_3 = C_{31} + C_{32}$.

4.4.3 Extended Matthews correlation coefficient

The Matthews correlation coefficient (MCC) has also been applied to evaluate the quality of multi-class segmentation (Gorodkin, 2004) as,

$$MCC = \frac{\sum_{klm} C_{kk}C_{lm} - C_{kl}C_{mk}}{\sqrt{\sum_k(\sum_l C_{kl})\left(\sum_{\substack{l' \\ k'\neq k}} C_{k'l'}\right)}\sqrt{\sum_k(\sum_l C_{lk})\left(\sum_{\substack{l' \\ k'\neq k}} C_{l'k'}\right)}} \tag{4.12}$$

where ij-th entry C_{ij} is the number of image elements of observation class i assigned to class j, in the confusion matrix, as introduced before. Additionally, to be more easily understand the definition of MCC, the formula can also be expressed with intermediate variables, given by

$$MCC = \frac{\mathrm{cs} - \vec{t}\cdot\vec{p}}{\sqrt{s^2 - \vec{p}\cdot\vec{p}}\sqrt{s^2 - \vec{t}\cdot\vec{t}}} \tag{4.13}$$

where $c = \sum_k C_{kk}$ denotes the total number of the correctly segmented image elements, $s = \sum_i\sum_j C_{ij}$ represents the total number of image elements, $\vec{t} = (t_1, t_2, \dots, t_k)$ and $t_k = \sum_i C_{ik}$ stands for the number of image elements at class k truly occurred, $\vec{p} = (p_1, p_2, \dots, p_k)$ and $p_k = \sum_i C_{ki}$ represents the number of image elements predicted at class k.

4.5 Evaluation on imbalanced data sets

An imbalanced data set is where the classes contain very different number of members (here pixels or voxels). Imbalanced data sets are common in image segmentation. However, some evaluation measures can be sensitive to the imbalanced data sets. It means that classes with

few elements may have too little impact on evaluation measures (Bekkar, Djemaa and Alitouche, 2013; Tharwat, 2020).

Predicted Class \ True Class	1	2
1	C_{11}=90	C_{21}=5
2	C_{12}=4	C_{22}=1

Fig. 4.4 Generated two-class confusion matrix with an imbalanced data set.

To study the influence of imbalanced data set on two-class evaluation measures, we created a confusion matrix with an imbalanced data set, as shown in Fig. 4.4. In this example, the segmentation performed well in class 1, but not in class 2. However, the resulting F_1 score ($F_1 = 0.95$, according to the equation (4.8)) and accuracy score ($ACC = 0.91$, according to the equation (4.4)) were extremely high, indicating that they were sensitive to the imbalanced data set. Obviously, they placed more weight on larger classes than smaller classes, leading to an overoptimistic estimation of the evaluations. Finally, we calculated Matthews correlation coefficient (MCC) as: $MCC = 0.14$, according to the equation (4.9). On the contrary, it indicated that the segmentation was performing similarly to random guessing. Therefore, MCC avoided the dangerous misleading illusions (Chicco, 2017; Chicco and Jurman, 2020).

To analyze the effects of imbalanced data set on multi-class evaluation measures, we generated three-class confusion matrix with an imbalanced data set, as Fig. 4.5. In this example, the segmentation performed well in class 1, but not in class 2 and 3. However, the resulting $F_{1-micro}$ score ($F_{1-micro} = 0.90$, according to the equation (4.11)) and accuracy score ($ACC = 0.90$, according to the equation (4.4)) were extremely high, indicating that they were misleading and not suggested as an evaluation measure of the multi-class segmentation quality. In addition, the other extended F_1 score was calculated as: $F_{1-macro} = 0.38$, according to the equation (4.10). The sensitivity to the imbalanced data set was reduced by the averaging procedure. Moreover, the extended MCC was calculated as: $MCC = 0.27$, according to the equation (4.13), indicating that the segmentation was performing poorly. It was consistent with the fact, and suitable for the imbalanced data sets.

Predicted Class \ True Class	1	2	3
1	C_{11}=385	C_{21}=10	C_{31}=4
2	C_{12}=8	C_{22}=2	C_{32}=5
3	C_{13}=7	C_{23}=8	C_{33}=1

Fig. 4.5 Generated three-class confusion matrix with an imbalanced data set.

4.6 Conclusion

In this thesis, we aim to segment and evaluate three classes of bone, vessels, and background in the SR-µCT images. Thus, we need a suitable evaluation measure to assess segmentation quality in multiple classes. The overall evaluation of accuracy, the extended F_1 score, and Matthews correlation coefficient (MCC) can be exploited to evaluate segmentation quality in multi-class case, based on confusion matrix.

Although the accuracy measure is commonly employed in statistics, it can be misleading in the imbalanced data sets, since the size of class is ignored in the computation. $F_{1-macro}$ and $F_{1-micro}$ are the extended F_1 score to assess multi-class segmentation quality. However, even if $F_{1-macro}$ reduces the sensitivity to the imbalanced data set by the unweighted mean across all classes, it still can be dangerous and overoptimistic to the segmentation quality. On the other hand, the averaging procedure of $F_{1-micro}$ cannot remove the effects caused by the imbalanced data set.

Instead, MCC is a more reliable evaluation measure in the imbalanced data set, since it considers all elements of confusion matrix and takes into account the proportion of size in each class. The score of MCC is high only if the segmentation is robust in all classes. For these reasons, we select the multi-class MCC as an overall evaluation measure of segmentation quality in this thesis.

II. CONTRIBUTION

Chapter 5

Image segmentation approaches and quality evaluation

Contents

5.1 Introduction

To quantitatively analyze bone microvasculature, a robust image segmentation is a prerequisite. Several approaches have been developed to segment bone and vessels in the preclinical studies. For example, the bone and vessels in the hind limbs of mice, simultaneously imaged using SR-μCT with contrast agent, have been segmented automatically using global thresholding (Schneider et al., 2009). Although global thresholding is the most common used segmentation technique, the segmentation quality can be affected by beam-hardening, artifacts, partial volume effects, and noise in the image. Region growing is another technique used to segment bone and vessels. Unlike global thresholding, this method considers the connectivity of regions making up a vessel tree. In the analysis of bone vasculature, 3D region growing has been used to segment bone and vessel compartments of rats in 3D SR-μCT imaging with a contrast agent (Langer et al., 2010; Prisby et al., 2011).

The aim of this work is to transfer the previous protocol (Langer et al., 2010) to mice in order to make more models of pathologies available. However, this transition is not straightforward. Firstly, as opposed to in rat bone, vessels may appear to be in contact with the bone surface in mice, precluding the correct segmentations of bone and vessels using the previously proposed hysteresis thresholding based protocol, at 3.5 μm resolution. Further, the contrasted interfaces between bone and vessels may be relatively weak compared to the bone-background and the vessel-background interfaces, leading to weaker gradient magnitude at these edges, as shown in Fig. 5.1. Finally, the proposed method should be adapted to the large data sets.

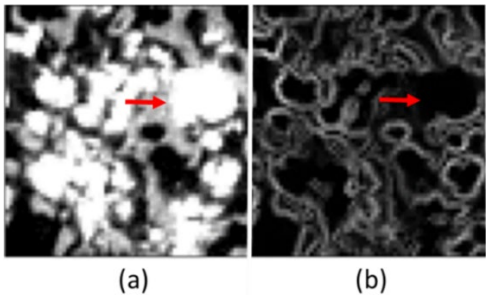

Fig. 5.1 Illustration of the bone (gray) and vessels (white) of mice tibia in SR-μCT image. (a) Original image. (b) Gradient image. The red arrow shows the interface between bone and vessel. All images are 2D slices from the 3D volume.

To address these challenges, we propose to use the marker-controlled watershed algorithm (Beucher and Meyer, 1990) in conjunction with the monogenic signal phase asymmetry to segment and quantify the bone microstructure and vascular network from SR-μCT images of mice. The marker-controlled watershed is used to separate vessels appearing to be touching the bone surface, without the need for post-segmentation merging of regions. An important step of the algorithm is to generate the marker image to initialize the watershed algorithm. Here, we use three classes of markers: bone, vessels and background, which are generated using hysteresis thresholding and morphological filters, with the aim to achieve coverage of all connected components in each class and no false positives. The other essential step is to

generate a control surface image, in which the "flooding" of the watershed algorithm happens from the markers to find boundaries between different compartments. Here, we propose the use of the monogenic signal phase asymmetry to improve the edge detections at the bone and vessel interfaces, in which the contrast is relatively weak. The monogenic signal phase has the property of invariance to signal intensity. The phase asymmetry can therefore quantify whether the image is locally edge-like or line-like independently of the intensity of the structure (Bridge, 2017; Felsberg and Sommer, 2001).

In order to evaluate the segmentation quality, we manually segmented two representative volumes (64×64×64 voxels) as reference images. These two small volumes respectively represent a simple and complex structure in the dataset. The segmentation quality at each single compartment (bone, vessel, or background) was validated using Dice coefficient, and the overall segmentation quality was evaluated using the Matthews correlation coefficient, by comparing to the manual segmentation.

5.2 The classical watershed approach

In this study, the aim of segmentation is to classify SR-μCT image voxels into three classes: bone, vessels and background. To understand the proposed marker-controlled watershed approach, we will first discuss the classical watershed in this section.

5.2.1 Fundamentals

The introduction of the classical watershed approach has been introduced in Section 3.2.4.3. The aim of the classical watershed approach is to separate an image into different regions by detecting the catchment basins and watershed lines.

An important part of performing watershed approach is to determine a control surface, which is treated as a topographic map. Although the original image itself can be used as a control surface, its gradient image is generally more often used. Especially, in the case of segmenting uniform objects, the gradient image can avoid detecting unwanted regional minimums in the catchment basins.

The other essential part is to build watershed lines to separate the different catchment basins into segments. Fig. 5.2 (a) and Fig. 5.2 (b) show the catchment basins at two flooding steps of $n-1$ and n, respectively. There are two connected components in Fig. 5.2 (a), and only one component in Fig. 5.2 (b) that encompasses the earlier two components as shown in dashed lines. Therefore, the water from two basins begins to merge, and a watershed line has to be constructed to prevent this from happening.

To construct a watershed line between two catchment basins, the morphological dilation is often used. The catchment basins in Fig. 5.2 (a) is dilated by the structuring element in Fig. 5.2 (c), subject to two conditions: (1) The dilation has to be constrained to the catchment basins at the flooding step n, thus the center of the structuring element needs to be located in it. (2) The dilation cannot be performed on points that would cause the merging of basins and becoming a single connected component.

Fig. 5.2 (d) shows the construction of watershed line with two dilation processes. In the first dilation, all of the points satisfy the condition (1) and none of the points would cause

merging in condition (2), thus the basins are expanded uniformly as shown in light gray. In the second dilation, not all of points can satisfy the condition (1) and there are several points would cause merging in condition (2), thus only few points can be dilated, as shown in black. Finally, the watershed line can be obtained by performing the difference between the structure in Fig. 5.2 (b) and the expanded structure after the two dilation processes. Therefore, a one-pixel-thick crossed-hatched connected path is shown in Fig. 5.2 (d). Furthermore, to prevent water from merging as the increasing level of flooding, the construction of the watershed line is completed by setting all the points in the path with the maximum intensity value of the image (Gonzalez and Woods, 2017).

Although the fundamentals introduced above is based on a simple example, the basic ideas are the same even for more complex cases and can be extended to 3D images.

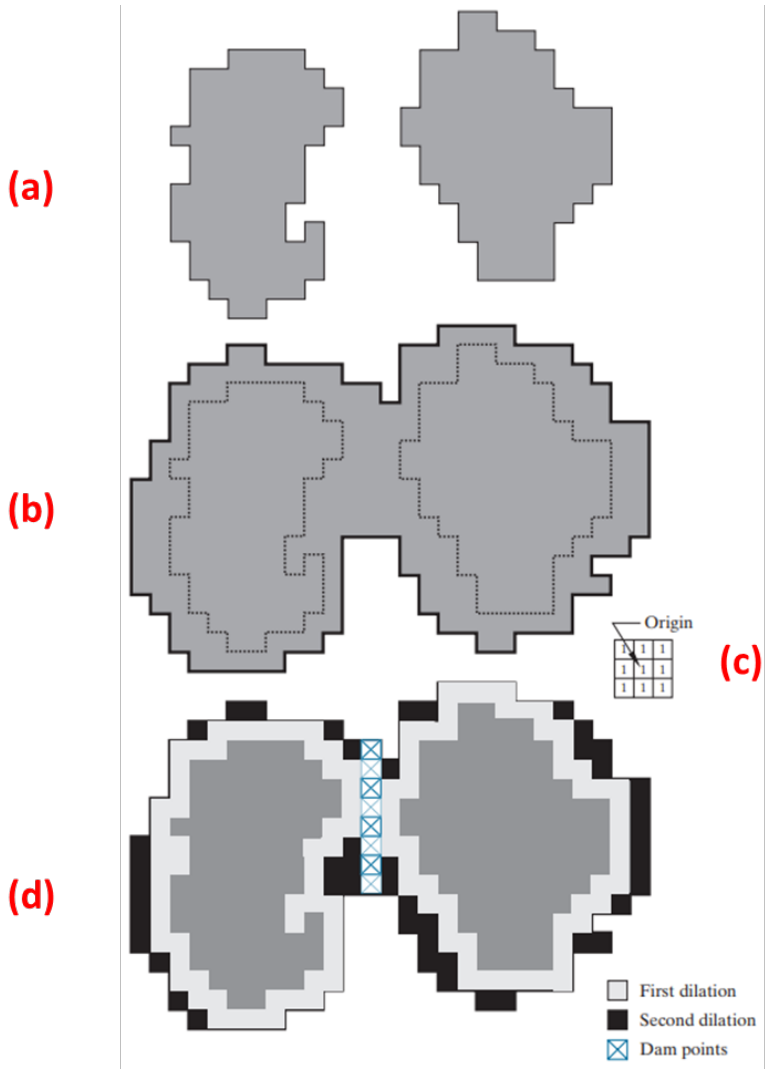

Fig. 5.2 Illustration of the construction of watershed line. (a) Two partially flooded catchment basins at stage $n-1$ of flooding. (b) Flooding at stage n, showing that water has merged between basins. (c) Structuring element used for dilation. (d) Result of the construction of watershed line (Gonzalez and Woods, 2017).

5.2.2 Algorithms

Let $g(x,y)$ be the original 2D image, and $(x,\mathrm{y}) \in \mathbb{R}$ is the spatial coordinate. Let $M_1, M_2, \dots, M_R$ represent the sets of coordinates of the regional minima in image $g(x,y)$. Let $C(M_i)$ stand for the set of coordinates of points in the catchment basin associated with regional minimum M_i. Let $T[n]$ be a set denoting the coordinates $(s,t) \in \mathbb{R}$ for which $g(s,t) < n$. It means that the value at these coordinates in $T[n]$ geometrically lie below the plane $g(x,y) = n$, as expressed as

$$T[n] = \{(s,t) \in \mathbb{R} | g(s,t) < n\}. \tag{5.1}$$

The flooding happens in integer increments, from $n = min + 1$ to $n = max + 1$. The min and max here are the minimum and maximum intensity values of the image. At any step n of the flooding process, let $C_n(M_i)$ be the set of coordinates of points in the catchment basin associated with minimum M_i, given by

$$C_n(M_i) = C(M_i) \bigcap T[n]. \tag{5.2}$$

Here, the logical AND operator is used to isolate the portion of $T[n]$ associated with regional minimum M_i at stage n. Next, we let $C[n]$ stand for the union of the flooded catchment basins at stage n, as expressed as (Gonzalez and Woods, 2017)

$$C[n] = \bigcup_{i=1}^{R} C_n(M_i). \tag{5.3}$$

The second part of the classical watershed segmentation algorithm is to find watershed lines. The algorithm is initialized with: $C[min + 1] = T[min + 1]$, and recursively computes $C[n]$ from $C[n-1]$. Let $Q[n]$ represent the set of connected components in $T[n]$. Then, for each connected component $q \in Q[n]$, only if $q \cap C[n-1]$ contains two or more connected components of $C[n-1]$, the watershed lines will be constructed to prevent the merging from different basins. As discussed before, a one-pixel-thick watershed line can be built when needed by dilating $q \cap C[n-1]$ with a structuring element.

To illustrate the concepts of watershed algorithm in a simple way, a one-dimensional example is created as shown in Fig. 5.3. $C_{n-1}(M_1)$ stands for the coordinates of points in the catchment basin associated with the regional minimum M_1, at the flooding stage $n-1$, as given by Equations (5.1) and (5.2). Next, the union of the flooded catchment basins at stage n can be expressed by Equation (5.3), as $C[n] = C_n(M_1) \cup C_n(M_3)$, and at the stage m: $C[m] = C_m(M_1) \cup C_m(M_2) \cup C_m(M_3)$.

Furthermore, the process of building watershed line can also be illustrated in Fig. 5.3. Water floods towards stage m from $m-1$, and two catchment basins associated with regional minimum M_1 and M_2 encounter. Considering a connected component l associated with regional minimum M_1 at stage m, the $l \cap C[m-1]$ contains two connected components of $C[m-1]$. Then the watershed line will be constructed to prevent overflow between these two catchment basins, as the red dash line in Fig. 5.3.

In the case of no need to construct watershed line, water floods towards stage n from $n-1$. Considering a connected component p associated with the regional minimum M_1 at stage n, $p \cap C[n-1]$ contains only one connected component of $C[n-1]$. It indicates that no water merging happens between two catchment basins.

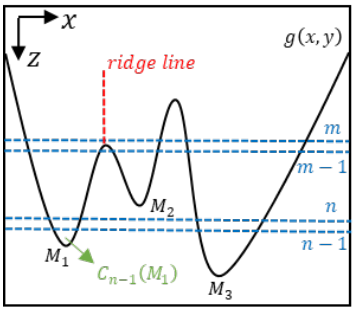

Fig. 5.3 Illustration of concepts and process of building watershed line in watershed algorithm using a simple one-dimensional example.

5.3 Marker-controlled watershed approach

In the classical watershed approach, the flooding begins from the regional minima on the gradient of original image taken as the control surface image. In general, this approach can provide more stable multi-class segmentations than the threshold-based and region growing method. However, in most cases, there are many unwanted regional minima due to noise or natural variations, leading to over-segmentation and requiring a posteriori merging of the segments, as shown in Fig. 5.4. A practical solution to this problem is to limit the number of segmented regions by incorporating a preprocessing stage designed to bring additional knowledge into the segmentation procedure (Beucher and Meyer, 1990; Bhabatosh, 2011).

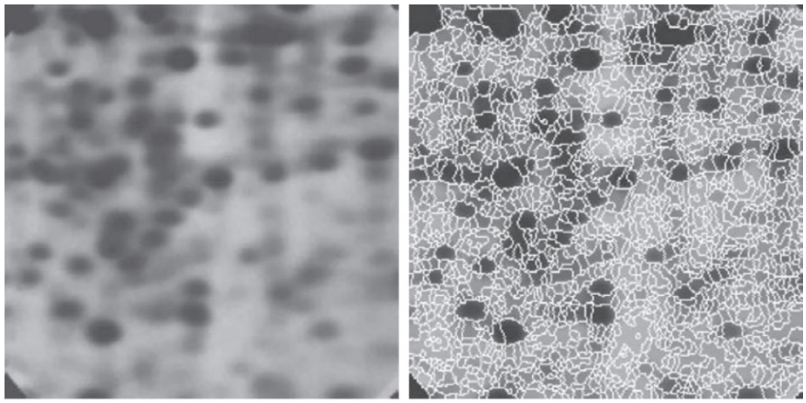

Fig. 5.4 Illustration of over-segmentation caused by the classical watershed algorithm. (a) Electrophoresis image. (b) Watershed segmentation result. Over-segmentation is evident (Gonzalez and Woods, 2017).

The marker-controlled watershed approach permits to initialize the flooding from already identified markers on the control surface, and can remove the effects caused by undesired

regional minima. A common choice for the markers are the points or regions either selected manually by the user or determined automatically by a preprocessing algorithm. In addition, this approach saves computing time by reducing the number of iterations, and simplifies the posteriori merging of segments. (Beucher and Meyer, 1990; Gonzalez and Woods, 2017). Fig. 5.5 shows an example of marker-controlled watershed segmentation on an image of nucleus of Arabidopsis thaliana. In this example, water floods from the specific markers on the gradient image to find boundaries between different compartments.

Fig. 5.5 Example of marker-controlled watershed segmentation on an image of a nucleus of Arabidopsis thaliana (image courtesy of Kaori Sakai and Javier Arpon, INRA-Versailles).

Thus, the marker-controlled watershed algorithm requires to define the processes of building the markers and the control surface. In this study, we will follow this approach and describe below how we generated the markers of different classes by using hysteresis thresholding and morphological filters, and constructed the control surface using the monogenic signal phase asymmetry.

5.3.1 Markers generation

An important step of the marker-controlled watershed algorithm is to generate the marker image. To achieve coverage of all connected components in each class and minimize the false positives, the markers can be created using some feature detection methods or by hand (Wang and Vallotton, 2010). Here, we propose to use hysteresis thresholding and morphological thinning to generate the marker image automatically.

In this study, the marker generation procedure is introduced by using an example of mouse bone in SR-µCT image, as shown in Fig. 5.6. Markers are generated for three segments in the image: bone, vessels and background. The background and vessel markers are given by blue and red arrows, respectively. The initial segmentations are obtained using the hysteresis thresholding with two thresholds. The selections of the low and high threshold of hysteresis thresholding depend on the gray level distributions in the SR-µCT image. Then, the initial segmentations are followed by one iteration of morphological thinning to reduce the false-positive rate. The procedure to obtain bone marker is given by the green arrows. The whole foreground structure, containing both bone and vessel, is first segmented using hysteresis thresholding. Then, the dilated vessel markers are subtracted to obtain the initial bone markers. Lastly, the isolated small particles are removed using morphological opening, and minimizing false positives is achieved by using morphological thinning. The final marker image is generated by adding the background markers, vessel markers, and bone markers, in blue, red and green, respectively.

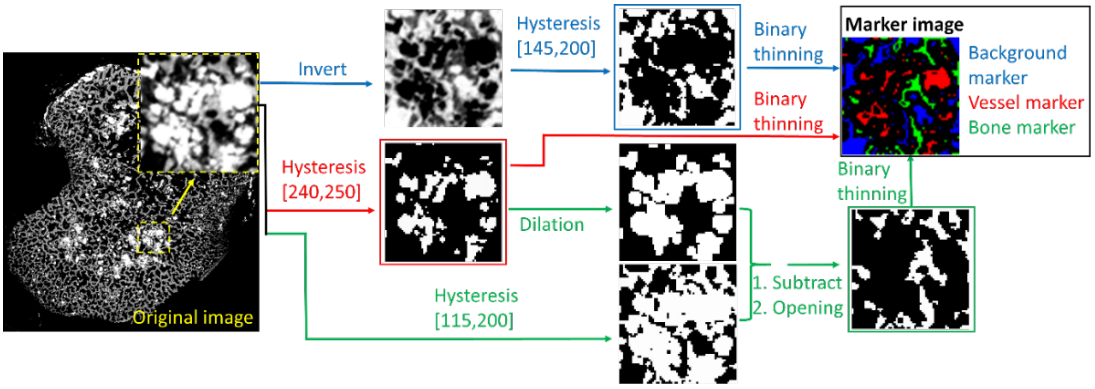

Fig. 5.6 Generation procedures of the markers image for the marker-controlled watershed: the background, vessel and bone markers are given by blue, red and green arrows, respectively.

5.3.2 Control surface generation

The other essential step of marker-controlled watershed algorithm is the generation of a control surface from the original image. Classically, the magnitude of the gradient or the distance map can be used as the control surface, which is related to the intensity changes in the original image (Bhabatosh, 2011). However, in our case, the relatively weak contrast at the interfaces between bone and vessels results in weaker gradient magnitude at these edges, as shown in Fig. 5.1.

Therefore, a measure that is insensitive to the signal magnitude is needed. One such measure is the phase of the analytical signal. This can be approximated by calculating the monogenic signal. Ideally, the measure should distinguish between lines and edges. A measure that has this feature is the local phase asymmetry. Therefore we propose the use of the local phase asymmetry of monogenic signal as the control surface for the watershed algorithm (Felsberg and Sommer, 2001; Bridge, 2017).

Below, we present the monogenic signal, which can be seen as an extension of the concept of analytic signal. We will first recall the definition and properties of 1D analytic signal and local phase.

5.3.2.1 Analytic signal

The 1D analytic signal is defined as a complex-valued signal associated to a real-valued signal, and can be extended to the multi-dimensional case by using the monogenic signal (Granlund and Knutsson, 2013; Bridge, 2017).

The 1D analytic signal only uses the components at positive Fourier frequencies to represent the original signal by simply discarding the negative Fourier frequencies components. This process does not lose any information for a real valued signal due to the Hermitian symmetry of its Fourier transform, as $F(-\omega) = \overline{F(\omega)}$, where $F(\omega)$ is the Fourier transform of signal $f(t)$ in time domain, and $\bar{k}$ denotes the complex conjugation operation on k. It indicates that the negative frequencies are the complex conjugate of the positive frequency components.

The removing of negative frequency components from the original spectrum can be obtained by adding a constructed odd symmetric spectrum $F_h(\omega)$ to the original signal spectrum. Therefore, the spectrum of the analytic signal $F_a(\omega)$ is given by

$$F_a(\omega) = F(\omega) + F_h(\omega), \tag{5.4}$$

$$F_h(\omega) = \begin{cases} F(\omega), & \omega > 0 \\ -F(\omega), & \omega < 0 \\ 0, & \omega = 0, \end{cases} \tag{5.5}$$

$$F_a(\omega) = \begin{cases} 2F(\omega), & \omega > 0 \\ 0, & \omega < 0 \\ F(0), & \omega = 0. \end{cases} \tag{5.6}$$

As introduced before, the original spectrum $F(\omega)$ is symmetric in the frequency domain, thus it represents a purely real time-domain signal. Furthermore, $F_h(\omega)$ is odd symmetric, thus it represents a purely imaginary time-domain signal. Therefore, in the time domain, the analytic signal is given by

$$f_a(t) = f(t) + f_h(t). \tag{5.7}$$

The imaginary part of the analytic signal can also be expressed as the Hilbert Transform of the real signal. Fig. 5.7 shows the formation of the analytic signal, using Hilbert transform of the original signal as the odd symmetric spectrum $F_h(\omega)$. Notice that we double the $F_a(\omega)$ at $\omega = 0$ for keeping the same power of the resulting signal.

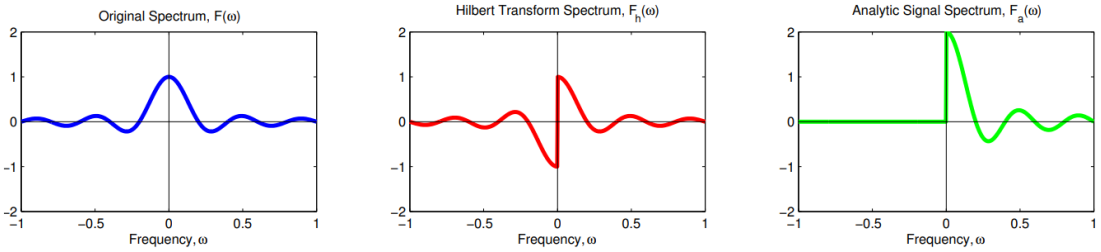

Fig. 5.7 Formation of the analytic signal in the frequency domain. The left figure is the spectrum of the original that displays conjugate symmetry. The center figure is the Hilbert transform of the original signal that is odd symmetric. The right figure shows the analytic signal by adding the two of the spectrum (Bridge, 2017).

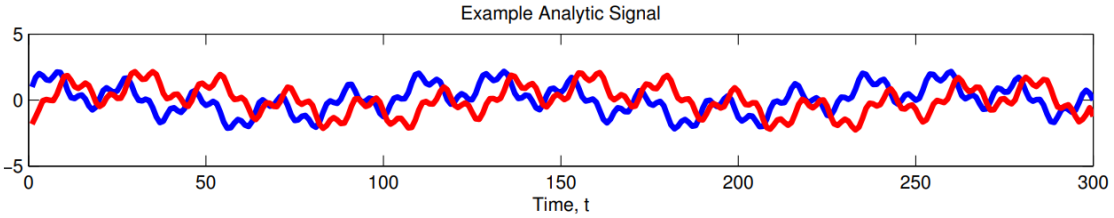

Fig. 5.8 An analytic signal in time domain. The analytic signal has a real part (blue) that is the same as the original signal, and an imaginary part (red) formed from the Hilbert transform of the original signal (Bridge, 2017).

Fig. 5.8 shows an analytic signal in time domain. The real part is the same as the original signal, given by blue. The imaginary part is formed from the Hilbert transform of the original signal, given by red.

5.3.2.2 Local phase

The local phase of the signal is defined from the analytic complex valued signal. It contains structural information of the signal, and has an interesting property of invariance to signal energy. It means that the local phase varies in the same manner regardless if there are small or large signal variations (Granlund and Knutsson, 2013). By using the analytic signal, the local phase can be expressed by (Bridge, 2017):

$$f_a(t) = A(t)e^{i\emptyset(t)}, \tag{5.8}$$

$$A(t) = \sqrt{f(t)^2 + f_h(t)^2}, \tag{5.9}$$

$$\emptyset(t) = arctan\left(\frac{f_h(t)}{f(t)}\right) \tag{5.10}$$

where $A(t)$ denotes the local amplitude, and $\emptyset(t)$ represents the local phase of analytic signal.

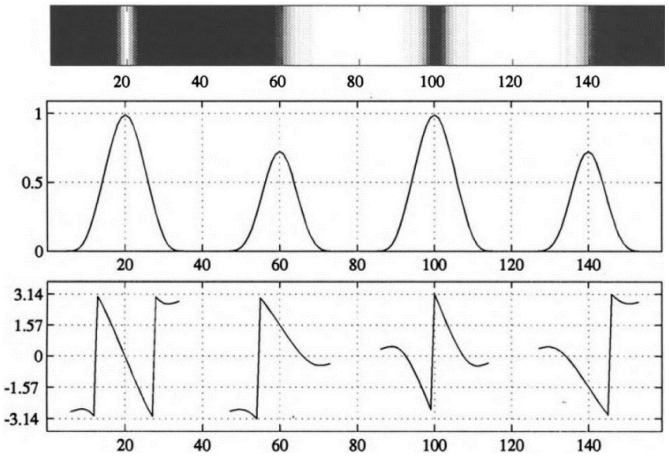

Fig. 5.9 Illustrations of line and edge detections using the quadrature filter. Top: the input image. Second: The corresponding output magnitude has one peak for each line or edge, and the peak value depends only on the signal energy and the filter pass band. Bottom: the corresponding local phase indicates the lines and edges. Bright line has local phase $\emptyset = 0$, dark line has $\emptyset = \pi$, dark to bright edge has $\emptyset = \pi/2$, and bright to dark edge has $\emptyset = -\pi/2$ (Granlund and Knutsson, 2013).

An alternative way to approach the concept of local phase is to relate it to the detections of lines and edges. Generating a quadrature filter is the formal way to define a line/edge filter pair as a complex filter. Firstly, the edge filter can be generated from a line filter using the Hilbert transform. Next, the line filter (even function) is used as the real part of the quadrature filter, and the edge filter (odd function) is used as the imaginary part. The quadrature filter is then generated by combining the even function with the odd function (Granlund and Knutsson, 2013).

Fig. 5.9 shows the illustrations of line and edge detections using the quadrature filter. The top figure is an input image. The middle figure shows the corresponding output magnitude, which has one peak for each line or edge. The peak value depends only on the signal energy and the filter pass band. The bottom figure shows the corresponding local phase, which indicates the lines and edges. The local phase is a measure of the signal shape, and can be used to separate edge-like or line-like structures in an image. The bright line has the local phase $\emptyset = 0$, dark line has $\emptyset = \pi$, dark to bright edge has $\emptyset = \pi/2$, and bright to dark edge has $\emptyset = -\pi/2$. In addition, the local phase is invariant to the signal energy (Granlund and Knutsson, 2013).

5.3.2.3 Monogenic signal

In general, the extension of the 1D analytic signal to 2D and 3D images is not straightforward, and is often performed by generating a quadrature pair of oriented band-pass filter, such as an oriented multi- dimensional Log-Gabor filter (Mulet-Parada and Noble, 2000; Rajpoot, Grau and Noble, 2009). However, this multi-dimensional extension gives rise to complexity of computation, and has to deal with the selections of appropriate orientations.

In this study, we used the concept of 3D monogenic signal as the isotropic and multi-dimensional extension of the 1D analytic signal which does not need to consider the orientation selectivity issue (Felsberg and Sommer, 2001). 3D monogenic signal can be defined by the combination of the original image and its three Riesz transform components (Chenouard and Unser, 2012):

$$f_m(\boldsymbol{x}) = \big(f(\boldsymbol{x}), R_1 f(\boldsymbol{x}), R_2 f(\boldsymbol{x}), R_3 f(\boldsymbol{x})\big), \tag{5.11}$$

$$\boldsymbol{R}f(\boldsymbol{x}) = \big(R_1 f(\boldsymbol{x}), R_2 f(\boldsymbol{x}), R_3 f(\boldsymbol{x})\big) \tag{5.12}$$

where $f(\boldsymbol{x})$ denotes the original 3D image, and $\boldsymbol{x} = (x_1, x_2, x_3) \in \mathbb{R}^3$ is the spatial coordinate. $\boldsymbol{R}$ stands for the Riesz transform, and its operator component $R_\alpha: \mathbb{R}^3 \longmapsto \mathbb{R}$ is characterized by its frequency response:

$$F[R_\alpha f](\boldsymbol{\omega}) = -j\frac{\omega_\alpha}{\|\boldsymbol{\omega}\|}\hat{f}(\boldsymbol{\omega}), \alpha = 1, \dots, 3 \tag{5.13}$$

where, F represents the Fourier transform operator, $\boldsymbol{\omega} = (\omega_1, \omega_2, \omega_3) \in \mathbb{R}^3$ is the angular frequency variable conjugate to $\boldsymbol{x}$. α gives the 3D direction of the Riesz transformed components, corresponding to the directions of the basis vectors. In addition, structure features must be selected with an appropriate scale using a band-pass filter, for example a Log-Gabor filter, since structure in an image is generally scale dependent (Bridge, 2017). Thus, the 3D monogenic signal $f_{mg}(\boldsymbol{x})$ is constructed as:

$$f_{mg}(\boldsymbol{x}) = (f(\boldsymbol{x}) * g(\boldsymbol{x}), R_1 f(\boldsymbol{x}) * g(\boldsymbol{x}), R_2 f(\boldsymbol{x}) * g(\boldsymbol{x}), R_3 f(\boldsymbol{x}) * g(\boldsymbol{x})) \tag{5.14}$$

where $g(\boldsymbol{x})$ stands for log-Gabor filter in spatial domain, and $*$ represents the 3D convolution operation. The 3D monogenic signal can also be constructed as the combination of its even and odd components (Rajpoot, Grau and Noble, 2009):

$$f_{mg}(\boldsymbol{x}) = f_{mge}(\boldsymbol{x}) + i \cdot f_{mgo}(\boldsymbol{x}) \tag{5.15}$$

where the even component is:

$$f_{mge}(\boldsymbol{x}) = f(\boldsymbol{x}) * g(\boldsymbol{x}) \tag{5.16}$$

and the odd component is:

$$f_{mgo}(\boldsymbol{x}) = \left(\sum_{\alpha=1}^{3} |R_\alpha f(\boldsymbol{x}) * g(\boldsymbol{x})|^2 \right)^{1/2}. \tag{5.17}$$

The monogenic signal of 2D images (Bridge, 2017), as well as 3D images (Rajpoot, Grau and Noble, 2009) have been applied to the various studies.

5.3.2.4 Phase asymmetry measurement

To detect the edges in original image, the phase asymmetry measurement can be used to quantify the local structures. As discussed in Section 5.3.2.2, a line-like structure has a local phase of 0 or π, and for an edge-like structure, the local phase is π/2 or 3π/2. Then, the phase asymmetry can be given by (Kovesi, 1997; Bridge, 2017):

$$ASym(\boldsymbol{x}) = \frac{\lfloor |sin(\emptyset(\boldsymbol{x}))| - |cos(\emptyset(\boldsymbol{x}))| - T \rfloor}{\mathrm{A}(\boldsymbol{x}) + \epsilon}, \tag{5.18}$$

$$A(\boldsymbol{x}) = \sqrt{sin^2(\emptyset(\boldsymbol{x})) + cos^2(\emptyset(\boldsymbol{x}))} \tag{5.19}$$

where $\lfloor . \rfloor$ denotes an operator replacing negative values with zero. $A(\boldsymbol{x})$ stands for the local amplitude, and $\emptyset(\boldsymbol{x})$ represents the local phase. T is a threshold to suppress noise ($0 < T < 1$), and ϵ is a small positive number to avoid division by zero. In addition, $sin(\emptyset(\boldsymbol{x}))$ can be seen as an odd component, and $cos(\emptyset(\boldsymbol{x}))$ is even component. Normalizing by the local amplitude makes the phase asymmetry independent of the amplitude. Therefore, the value of phase asymmetry measurement lies in $0 \leq ASym(\boldsymbol{x}) < 1$. For example, if the local structure is edge-like, then the local phase $\emptyset(\boldsymbol{x})$ is π/2 or 3π/2, $ASym(\boldsymbol{x}) = \frac{1-T}{1+\epsilon} < 1$. If the local structure is line-like, then the local phase $\emptyset(\boldsymbol{x})$ is 0 or π, so $ASym(\boldsymbol{x}) = 0$, as indicated in Equation (5.18).

The definition of phase asymmetry measurement in Equation (5.18) can be written in terms of the 3D monogenic signal with a number of scales, combining the even and odd components as Equations (5.16) and (5.17). Therefore, the multiscale phase asymmetry is measured by (Rajpoot, Grau and Noble, 2009; Bridge, 2017):

$$ASym(\boldsymbol{x}) = \sum_i \frac{\lfloor |f_{mgo,\lambda_i}(\boldsymbol{x})| - |f_{mge,\lambda_i}(\boldsymbol{x})| - T \rfloor}{\sqrt{(f_{mgo,\lambda_i}(\boldsymbol{x}))^2 + (f_{mge,\lambda_i}(\boldsymbol{x}))^2} + \epsilon} \tag{5.20}$$

where $\{\lambda_i\}$ are a set of center-wavelengths (λ_i=$2\pi/\omega_i$) of the log-Gabor filters to define the scales. Here, the selections of scales depend on the image structures.

Finally, the edge detections in 3D image can be obtained using the phase asymmetry measurement of the 3D monogenic signal, which is independent with the intensity of structure (Bridge, 2017; Felsberg and Sommer, 2001).

In this study, we used the phase asymmetry measurement as the control surface of marker-controlled watershed to improve the edge detections at the bone and vessel interfaces, in which the contrast is relatively weak. In our case, phase asymmetry with lower scales detects too much edge detail so that useful structures cannot be recognized. Conversely, the method with higher scales misses too much detail.

5.4 Evaluation of segmentation quality

After the image segmentation, it is very important to evaluate whether the segmentation quality is high enough for the quantitative analysis. In this study, we manually segmented two representative volumes as reference images. These two small volumes were selected from a 3D image to stand for a simple and a complex structure respectively. Then the segmentation quality was validated using Dice coefficient and Matthews correlation coefficient by comparing to the reference images.

5.4.1 Manual segmentation for reference image

To create reference images by manual segmentation, we used VGStudio Max (Volume Graphics GmbH, Heidelberg, Germany), which is a software system designed to support interactive 3D image analysis and visualization in the application areas of industry and life sciences research.

In this software, we used the 3D Magic Wand tool to create the selection of object in the whole 3D image. This tool is based on the region growing algorithm, and can select all voxels that are connected to a seed point within a tolerance of voxel value. The larger tolerance value will include the more areas into the selection.

Specifically, we first activated the 3D Magic Wand mode, and applied an initial tolerance value. Then, we moved the mouse cursor over one of the objects, such as a vessel compartment in the 3D image, and clicked to have the selection we wanted. Here, the position of mouse cursor is the seed point of region growing. Furthermore, we can optimize the selection by choosing another tolerance values.

After choosing one connected component of object, we can keep creating other connected components in the same way, and add them to the previous Magic Wand selections. For example, there are several connected components of vessel structure in a 3D image, and we need to use 3D Magic Wand tool to include all of the vessel compartments.

At the end, we need to check the result slice by slice, and correct the misclassified selections using 2D Segmentation mode. Here, we can simply draw a required selection, and perform adding or subtracting on the previous selections.

In our study, we first created the selections of vessel compartments as the procedure introduced above. Next, we removed them from the original image, and created the selections of bone compartments based on the remaining original image in the same way. Then, the structures, which were not belonging to the both selections of vessels and bone, were

identified as background selections. Finally, we created a reference image with three classes of vessels, bone, and background.

However, the manual segmentation can be time consuming for the large datasets. Therefore, in this study, we first selected two small volumes (64×64×64 voxels) from a 3D original image. They respectively represent a simple and a complex structure in the dataset. Then, we manually segmented these two volumes of interests (VOI) as reference images.

Fig. 5.10 shows the manual segmentation results for the simple structure. Fig. 5.10 (a) represents the whole original image. Fig. 5.10 (b) stands for the representative small original image. Fig. 5.10 (c) shows the manual segmentation of vessel compartments. Fig. 5.10 (d) denotes the manual segmentation of bone compartments. Fig. 5.10 (e) is the composite of manual segmentations including both vessel (white) and bone (gray) compartments. All images in Fig. 5.10 are 2D slices selected from the 3D volumes.

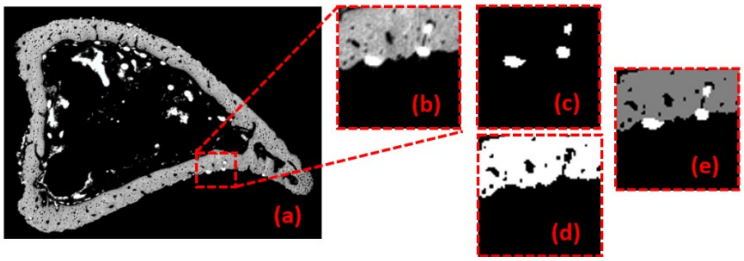

Fig. 5.10 Illustration of manual segmentation for simple structure. (a) The whole original image. (b) The representative small original image. (c) The manual segmentation of vessel compartments. (d) The manual segmentation of bone compartments. (e) The composite of manual segmentations including both vessel (white) and bone (gray) compartments. All images are 2D slices selected from the 3D volumes.

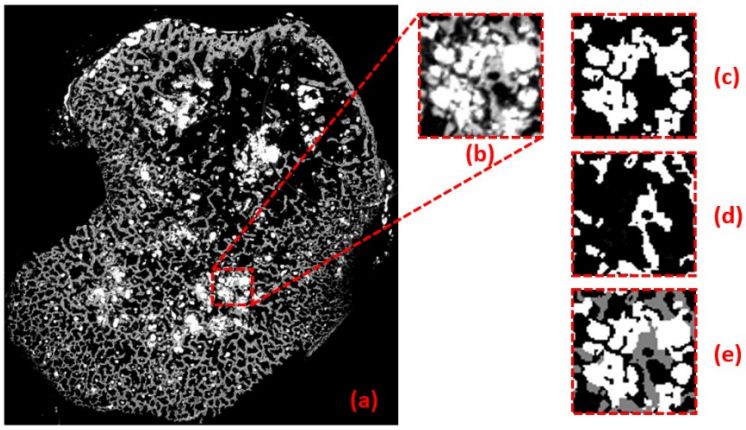

Fig. 5.11 Illustration of manual segmentation for complex structure. (a) The whole original image. (b) The representative small original image. (c) The manual segmentation of vessel compartments. (d) The manual segmentation of bone compartments. (e) The composite of manual segmentations including both vessel (white) and bone (gray) compartments. All images are 2D slices selected from the 3D volumes.

Fig. 5.11 shows the manual segmentation results for the complex structure. Fig. 5.11 (a) stands for the whole original image. Fig. 5.11 (b) is the representative small original image. Fig. 5.11 (c) shows the manual segmentation of vessel compartments. Fig. 5.11 (d) shows the manual segmentation of bone compartments. Fig. 5.11 (e) denotes the composite of manual segmentations including both vessel (white) and bone (gray) compartments. All images in Fig. 5.11 are 2D slices selected from the 3D volumes.

5.4.2 Dice coefficient and Matthews correlation coefficient

Apart from the generations of reference images, we need to select the evaluation matrix to assess the segmentation quality. In Chapter 4, we discussed the effects on the evaluation caused by the imbalanced data sets, in which the classes contain widely varying number of voxels than other classes. MCC is reliable to assess an overall evaluation measure of segmentation quality.

In our study, to assess the segmentation quality at each single compartment (bone, vessel, or background), we used Dice coefficient by comparing to the reference images. Here, we recall the Dice coefficient as Equation (4.7) and Equation (4.8). To validate the overall segmentation quality in multi-class, we used the extended Matthews correlation coefficient, as Equation (4.12) and Equation (4.13).

Chapter 6

Assessment of segmentation approach on synthetic data

Contents

6.1 Introduction

The proposed segmentation approach combining the monogenic signal phase asymmetry with marker-controlled watershed has been described in the Chapter 5. To assess the accuracy and robustness of the segmentation method, as well as its generalization to other applications, the tests on synthetic datasets are often required (Lee et al., 2007). Thus, the examination of the proposed segmentation approach on various 3D synthetic volumes is carried out in this chapter.

Firstly, we generated 3D synthetic volumes to mimic the real datasets. Here, we considered the validation of thin structure segmentation, the different contrasts between different classes, as well as various noise levels. Then, the created multi-class synthetic volumes were segmented using the proposed method, and the overall segmentation quality was evaluated using the Matthews correlation coefficient (MCC) by comparing to the ground truth. The final analysis indicates that the proposed segmentation approach is performant in general multi-class segmentation problems.

6.2 Generation of 3D synthetic datasets

To perform the numerical simulation study, we created 3D synthetic models. Here, we first used OpenSCAD, which is an open source software for creating 3D CAD models. In OpenSCAD, 3D models are created by defining them in a proprietary scripting language, based on the functional programming paradigm. This makes certain types of 3D models simple to define. OpenSCAD allows to preview and render the created 3D models, and allows to export the model in DXF, STL and OFF file formats (Nilsiam and Pearce, 2017; M Kintel and C Wolf, 2020).

To investigate the influence on the segmentation of thin structures in the presence of different disturbances, a 3D model with an hourglass shape was created using OpenSCAD. Fig. 6.1 shows its generation process. Firstly, a 3D cylinder model was easily generated using the scripting language in OpenSCAD, as shown in Fig. 6.1 (a). The parameters of radius and height were defined to be 8 and 20, respectively $(\mathrm{Radius} = 8, \mathrm{Height} = 20)$. Next, the second cylinder (in red) with the same radius and height $(\mathrm{Radius} = 8, \mathrm{Height} = 20)$ was generated, as shown in Fig. 6.1 (b). The red cylinder was placed in a distance of 20 away from the yellow cylinder ($\mathrm{D} = 20$, distance between centers of two cylinders). The yellow cylinder was rotated 45 degree around the X-axis. Spatially, the line formed by the center points of two cylinders is in the direction of X-axis, and parallel to the XY-plane. Finally, the simple 3D hourglass shape was created by subtracting a rotated cylinder (in red) from the other cylinder (in yellow), as shown in Fig. 6.1 (c-e). It should be noticed that the distance between the centers of the two cylinders determines the shape of 3D hourglass model, such as Fig. 6.1 (c) where $\mathrm{D} = 15$ apart, Fig. 6.1 (d) where $\mathrm{D} = 10$ apart, and Fig. 6.1 (e) where $\mathrm{D} = 8.5$ apart. The finally created 3D model of hourglass shape is shown as Fig. 6.1 (f).

After rendering the created 3D model using OpenSCAD, we exported it in a STL file format. Since the STL file only describes the surface geometry of a 3D model, we need to convert it into a stack of voxel images (binary voxelization volume) (Sun et al., 2016). Here, we used 3D Slicer, which is an open source software for image visualization and analysis.

Specifically, we first loaded the STL file as a segmentation mode in 3D Slicer, and exported the visible segments as a binary label map in RAW file formats.

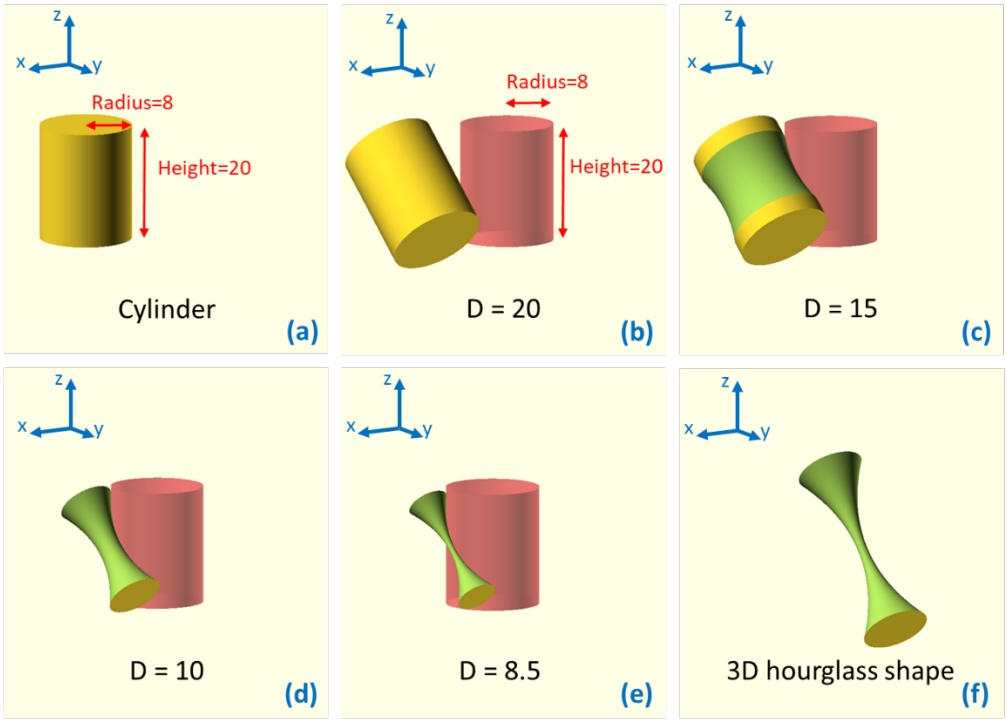

Fig. 6.1 The generation of 3D model with hourglass shape using OpenSCAD. (a) The created 3D cylinder model (Radius = 8, Height = 20). (b) Two cylinders (Radius = 8, Height = 20) are angled at 45 degree (angle between the axis of two cylinders), and with D = 20 apart (D: distance between centers of two cylinders). (c-e) The created 3D hourglass models obtained by subtracting a rotated cylinder (in red) from the other cylinder (in yellow). D determines the shape of 3D hourglass model, such as (c) where D = 15 apart, (d) where D = 10 apart, and (e) where D = 8.5 apart. (f) The finally created 3D model with hourglass shape.

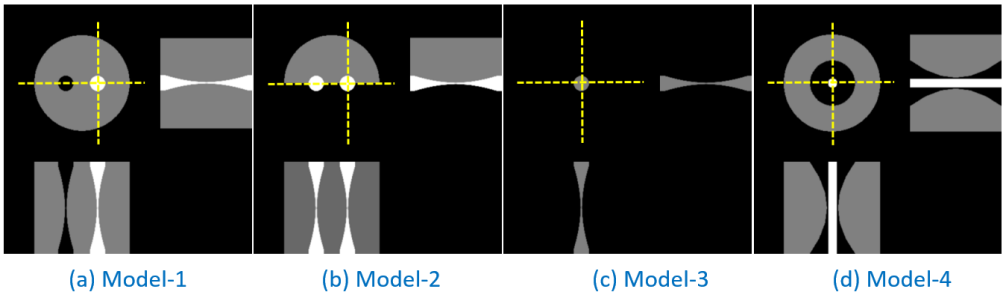

Fig. 6.2 Three orthogonal slices in the 3D synthetic models (256×256×150 voxels): (a) Model-1 stands for vessel structure (gray level 255) and bone porosity (gray level 0) with various thickness, which are surrounded by the bone (gray level 128). (b) Model-2 simulates that vessels are in contact with bone surface and background at the same time. (c) Model-3 represents an isolated structure in the real-world dataset. (d) Model-4 describes the situation that a vessel is passing through a varying bone porosity.

Finally, the voxelized volume was created by summing the binary volumes containing the various shapes, each scaled by the desired gray level value. We used the open source image processing software Fiji/ImageJ to perform the 3D image manipulations. In this study, four kinds of 3D synthetic models were created, as shown in Fig. 6.2. Each volume is an 8-bit 3D image with 256×256×150 voxels.

The aims of designing 3D synthetic models are to mimic the kinds of structures that can be found for vessel, bone and background in the experimental data. In particular, we will study the influence of the contrast and noise on the segmentation quality, and specifically on the thin structures that can be segmented.

Model-1 was designed to simulate 3D vessel structure (gray level 255) and bone porosity (gray level 0) with various thickness, surrounded by bone (gray level 128), corresponding to a completely filled and an empty Haversian canal, as shown in Fig. 6.2 (a). The first step of creating this model was to generate three binary images, which respectively contained a white cylinder, a white hourglass structure and a black hourglass structure. The relative sizes and locations of cylinder and hourglass structures were set as Fig. 6.2 (a). The second step was to remove an hourglass structure from the cylinder for generating a bone porosity. The binary image, which contained a black hourglass structure, was used as a mask to remove an hourglass structure from the cylinder. Then, the gray level of foreground was divided by 2, set as 128 for bone. The third step was to add a white hourglass structure to the bone, as a vessel. The last generated binary image, which contained a white hourglass structure, was first duplicated. Therefore, the original image can be inverted as a mask to remove the other hourglass structure from the bone result of the last step, and then the duplicated one can be added to it for generating a white hourglass structure of vessel.

Model-2 mimics vessels (gray level 255) in contact with the bone surface (gray level 128) without being completely enveloped, as shown in Fig. 6.2 (b). The first step of creating this model was to generate two binary images. One contained two white hourglass structures and the other one contained a white half cylinder. Their relative sizes and locations were set as Fig. 6.2 (b). The second step was to remove hourglass structures from the half cylinder, as a bone. The binary image, which contained two white hourglass structures, was first duplicated. Then the original image was inverted as a mask to remove hourglass structures from the half cylinder. Then the gray level of foreground was divided by 2, set as 128 of bone. The third step was to add white hourglass structures to the bone, as vessel structures. The duplicated image was added to the bone result of the last step for generating white hourglass structures of vessel.

Model-3 was designed to simulate an isolated bone or vessel in the experimental dataset, as shown in Fig. 6.2 (c). Here, we generated a binary image, which contained a white hourglass structure. Then the gray level of foreground was divided by 2, set as 128.

Model-4 described a situation that a vessel (gray level 255) was passing through a narrowing bone porosity (gray level 0), as shown in Fig. 6.2 (d), to emulate the common case where a vessel is close to, but not in contact with, the bone surface in a Haversian canal. The thin cylinder in the center corresponds to a vessel, and the structure surrounding this cylinder corresponds to bone (gray level 128). The first step of creating this model was to generate three binary images, which contained a white cylinder (thick), the other white cylinder (thin)

and a white hourglass structure respectively. The relative sizes and locations of cylinders and hourglass structure were set as Fig. 6.2 (d). The second step was to remove the hourglass structure from the thick cylinder, for generating bone porosity. Here, the binary image, which contained a white cylinder (thick), subtracted the binary image containing a white hourglass structure. Then as a preparation for the next step, the gray level of foreground was divided by 2, set as 128 of bone. The last step was adding the binary image containing a white cylinder (thin) to the bone result of the last step, as vessel structures.

In the real experiment, there may be various contrast ratios between vessels and bone, physically came from the different types of contrast agent, X-ray energy, and range for 8 bit resampling. This may affect the segmentation quality with the proposed protocol. To investigate the impact of different contrast ratios between vessels and bone on the segmentation, in Model-1, Model-2 and Model-4, the gray levels of cylinders, which simulated bone structures in the real data, were set to increase starting from the intensity of 48 to 208 (defined contrasts 48 to 208 referring to the background). In Model-3, the gray level of the hourglass structure was increasing from the intensity of 48 to 255 (defined contrast 48 to 255 referring to the background). This would permit to ideally find an optimal contrast ratio and optimize the experiment.

For the purpose of mimicking the partial volume effect, which is a reduction of gray level in small object and interface between two classes, the generated volumes as above were resized by scale 4 times and 0.25 times successively. The synthetic phantoms without partial volume effects were used as reference images (ground truth).

In addition, to explore the impact of noise on the segmentation, different levels of Gaussian noise were added on the 3D synthetic phantoms. The noise level was defined by the standard deviation of Gaussian noise, increasing from 10 to 70.

The settings of image contrasts and noise levels were performed automatically using Fiji/ImageJ macro scripts in the JavaScript programming language.

6.3 Image segmentation

In this section, we examine the proposed segmentation method in the Chapter 5 (phase asymmetry based marker-controlled watershed) on two examples of 3D synthetic volumes.

The segmentations of Model-1 with various contrasts and Gaussian noise levels, are reported as shown in Fig. 6.3. All 2D slices were selected from the 3D volumes. Fig. 6.3 (a) and (b) show respectively noise-free and noisy (standard deviation of 10) slices in Model-1 phantom with contrast of 128. Fig. 6.3 (c) shows the markers overlaid on the control surface image, generated from Fig. 6.3 (b). Fig. 6.3 (d) is the final segmentation of Fig. 6.3 (b) using the proposed method. Fig. 6.3 (e) and (f) show respectively a noise-free and noisy (standard deviation of 30) slices in Model-1 phantom with contrast of 208. As previously, Fig. 6.3 (g) and (h) respectively present the markers overlaid on the control surface image and the final segmentation result, which were generated from the original image of Fig. 6.3 (f) using the proposed method.

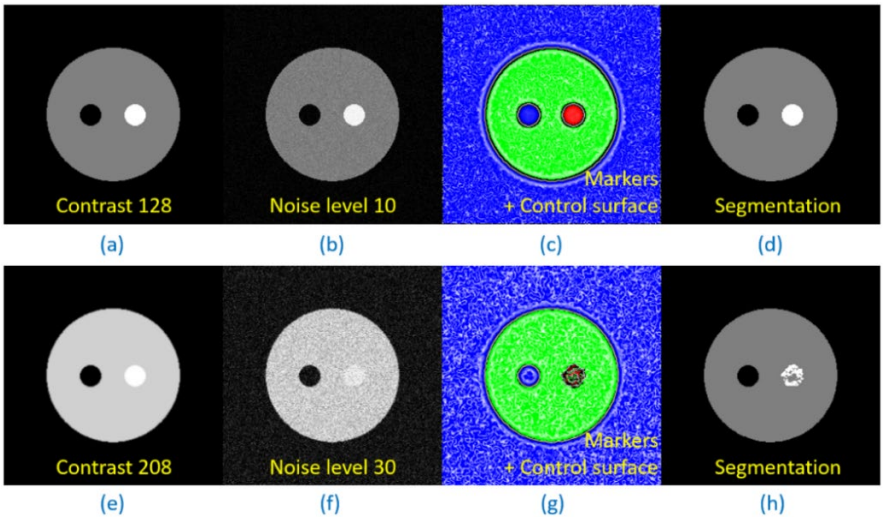

Fig. 6.3 Illustration of segmentations on two examples of synthetic volumes (Model-1). (a) The noise-free phantom with contrast 128 (the gray level of bone structure, referring to the background). (b) Original image, after adding the level of 10 Gaussian noise to (a). (c) Markers overlapping on the control surface image, generated from (b). Color blue, green and red represent markers of background, bone and vessel, respectively. (d) Multi-class segmentations, generated from (b) using the proposed method. (e) The noise-free phantom with contrast 208 (the gray level of bone structure, referring to the background). (f) Original image, after adding the level of 30 Gaussian noise to (e). (g) Markers overlapping on the control surface image, generated from (f). (h) Multi-class segmentations, generated from (f) using the proposed method. All images are 2D slices from the 3D volumes.

6.4 The influence of contrast and noise on segmentation

To explore the impacts of image contrasts and noise levels on segmentations, we generated 189 synthetic volumes for three-class models (Model-1, Model-2 and Model-4). Among them, 63 synthetic volumes were generated for each model, with 9 contrasts (48, 68, 88, 108, 128, 148, 168, 188 and 208). To these volumes, we added 7 levels of noise (standard deviation of Gaussian noise: 10, 20, 30, 40, 50, 60 and 70). In addition, we generated 70 synthetic volumes for a two-class model (Model-3), with 10 contrasts (48, 68, 88, 108, 128, 148, 168, 188, 208 and 255). Also here, 7 levels of noise were added, using the same noise levels as before.

Multi-class compartments of each synthetic volume were segmented using the proposed method in the Chapter 5. We show 9 examples of segmentations for each model, obtained from the volume of interest (VOI) of synthetic volume, under the various contrasts and levels of noise, as shown in Fig. 6.4. All 2D slices were selected from the 3D volumes. Fig. 6.4 (a), (b), (c) and (d) represent Model-1, Model-2, Model-3 and Model-4, respectively. In each model, segmentations were obtained from the synthetic volumes with contrasts of 48, 128 and 208 (or 255) as well as noise levels of 10, 30 and 70. Where the algorithm failed to achieve a good segmentation, the result was represented by a red box.

To evaluate the overall segmentation quality, the MCC value was calculated as introduced before. Fig. 6.5 illustrates the relationships between MCC and noise levels with the various contrasts. Fig. 6.5 (a), (b), (c) and (d) represent Model-1, Model-2, Model-3 and Model-4, respectively. Contrasts range from 48 to 208 (or 255), and noise levels range from 10 to 70.

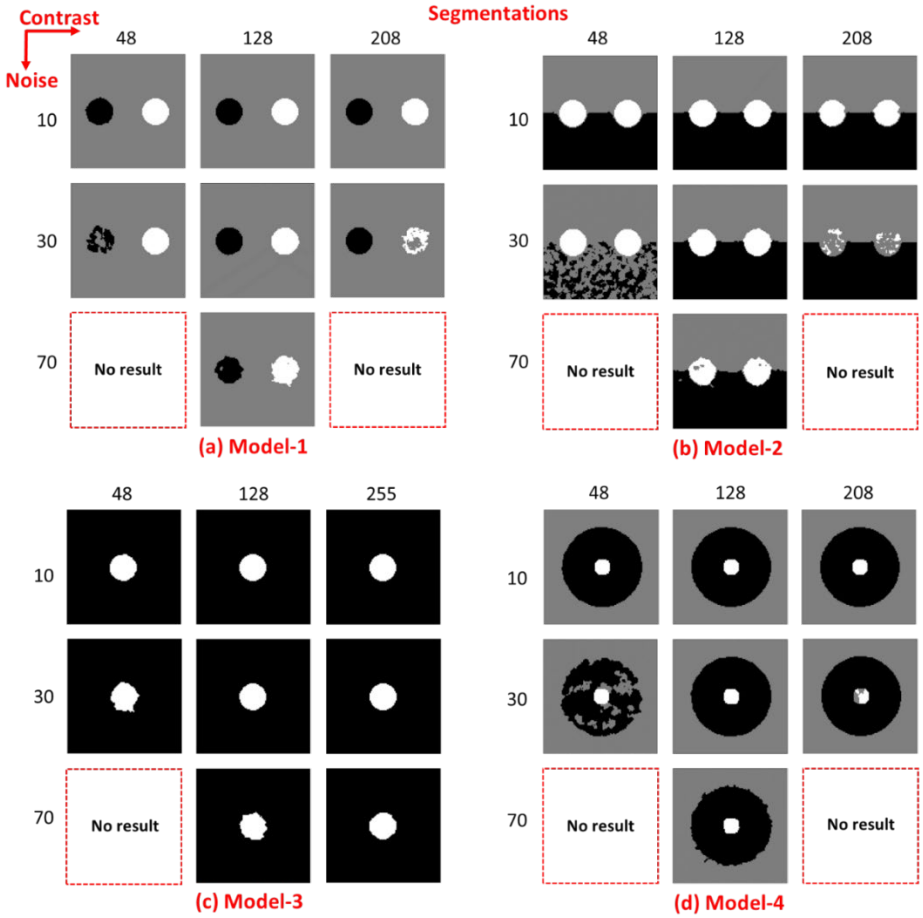

Fig. 6.4 Illustration of the impacts of image contrasts and noise levels on segmentations. (a) model-1, (b) model-2, (c) model-3, (d) model-4. 9 examples of segmentations for each model were obtained from the VOI of synthetic volumes with contrasts of 48, 128 and 208 (or 255), as well as noise levels of 10, 30 and 70. All 2D slices were selected from the 3D volumes.

MCC values were plotted over a range of noise levels at each contrast, excluding extremely low values obtained where the algorithm failed to yield a result (red boxes in Fig. 6.4). For example, as Fig. 6.5 (a), over the noise level of 30, for the contrast 48 and 208, the segmentation capabilities may hit their limits using the proposed method.

In summary, for three-class models of Fig. 6.5 (a), (b) and (d), at a fixed noise level, MCC values at the middle contrasts of 128 and 148 are higher than at the other contrasts. It indicates that the proposed protocol can work better at the contrasts of 128 and 148 in a three-class image. For the two-class model of Fig. 6.5 (c), MCC reaches the highest value at the highest contrast of 255, as expected.

Finally, as the examinations on a series of synthetic volumes with the various contrasts and noise levels, the obtained high MCC values support a broad applicability of the proposed method.

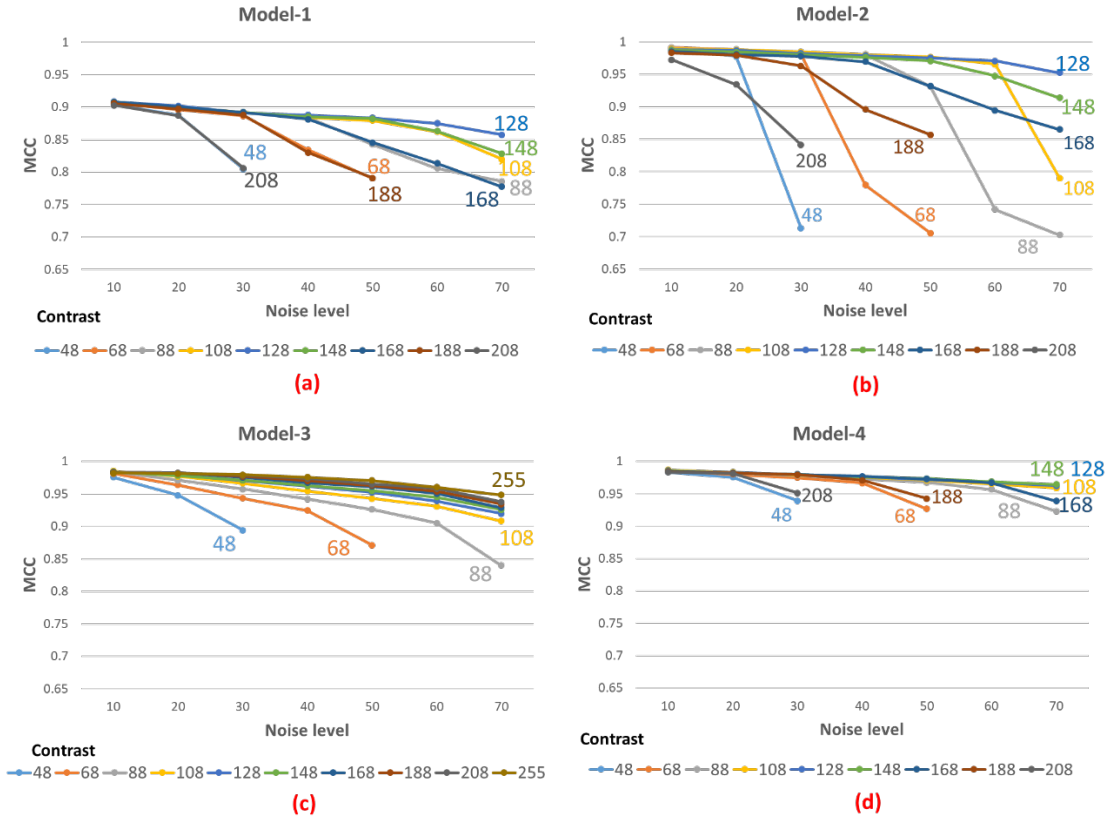

Fig. 6.5 Illustration of relationships between MCC and noise levels. (a) model-1, (b) model-2, (c) model-3, (d) model-4. Contrasts range from 48 to 208 (or 255), and noise levels range from 10 to 70.

6.5 The validation of thin structure segmentation

Fig. 6.6 illustrates the capability of segmentation on thin structure, under various levels of Gaussian noise. Here, we first selected a VOI from the noise-free phantom of Model-1 as Fig. 6.6 (a). Then we added various noise levels of 20, 40 and 60 on Fig. 6.6 (a) to generate Fig. 6.6 (b), Fig. 6.6 (c) and Fig. 6.6 (d) respectively. All figures are 2D slices selected from the 3D volumes.

Next, the hourglass structures of Fig. 6.6 (a-d) were segmented using the proposed method. For the purpose of quantifying the thin structure segmentation, we measured the 3D local thickness map, which provides at each point of the volume the diameter of the largest sphere that fits inside the compartment of the point under consideration (T. Hildebrand and Rüegsegger, 1997). Firstly, we selected the hourglass structure from the VOI of ground truth as the foreground to generate a new binary volume, and measured its 3D local thickness map. Secondly, the 3D local thickness map was masked with the binary images of the hourglass structure segmentations corresponding to Fig. 6.6 (a-d), and results are shown as Fig. 6.6 (e-h). As expected, the segmentation quality of thin structure is continuously degraded with the increasing noise, as the disconnection of structure visible.

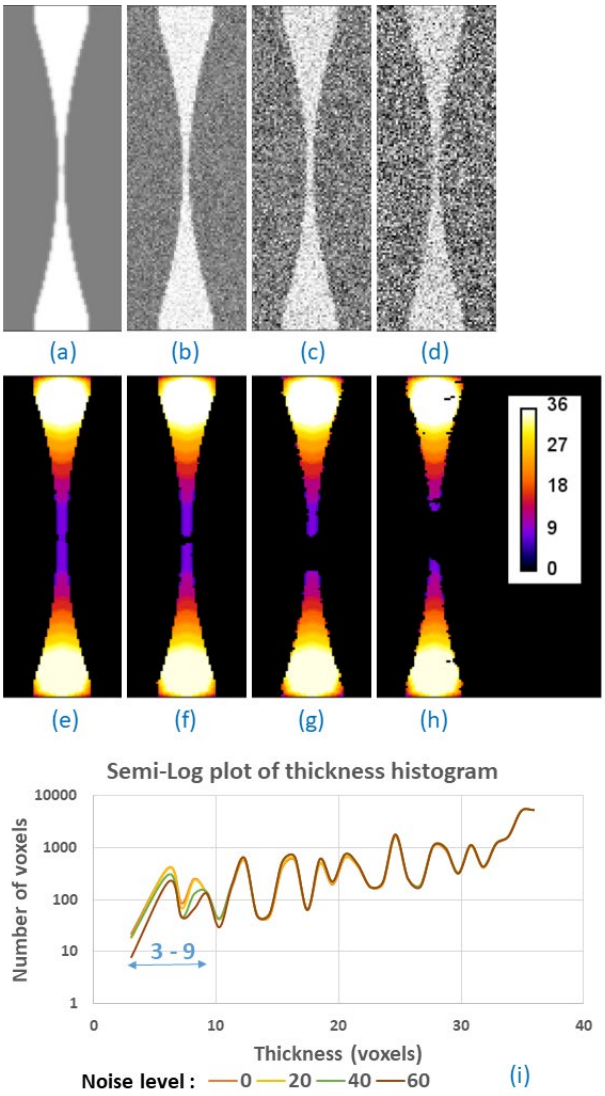

Fig. 6.6 Illustration of the segmentation capability on thin structure. (a) Noise-free phantom, which is a VOI selected from Model-1. (b-d) noisy images, with noise levels of 20, 40 and 60, respectively. (e-h) 3D local thickness maps of hourglass structures, corresponding to (a-d) respectively. All images of (a-h) are 2D slices selected from the 3D volumes. (i) Semi-Log plot, showing the number of voxels at each thickness in (e-h).

Lastly, the number of voxels at each thickness in Fig. 6.6 (e-h), was plotted in Fig. 6.6 (i). In a thickness range of 3 to 9 voxels (thin structure), the numbers of voxels corresponding to the noise levels of 0 and 20 are higher than the values at the noise levels of 40 and 60. It indicates that there are more thin structures correctly segmented in the former case. Therefore, we can say that the thin structure can be well segmented at the noise levels of less than 20, using the proposed method. For the segmentations of thick structure (thickness of 10 voxels or more), noise levels have little effects on the number of voxels at each thickness. The thick structures can be well segmented even at the noise level of 60 using the proposed method.

6.6 Conclusion

In this chapter, we examined the accuracy and robustness of the proposed segmentation method, as well as its generalization to other applications.

Firstly, we created 3D synthetic models to simulate the real datasets, and considered the impacts of contrasts and noise levels on segmentations. The multi-class compartments were segmented using the proposed method, and the overall segmentation quality was evaluated using the MCC by comparing to the ground truth. A series of segmentation results indicate that the proposed segmentation approach can work better at the contrasts of 128 and148 in the three-class model, and at the contrast of 255 in the two-class model.

In addition, we studied the segmentation capability of thin structure under a various levels of Gaussian noise. The results show that the thin structure (thickness of 3 to 9 voxels) can be well segmented at noise levels of less than 20, and the thick structure (thickness of 10 voxels or more) can be well segmented even at the noise level of 60 using the proposed method.

In conclusion, the proposed segmentation method appears to be robust with respect to noise and contrast and is a good candidate for our application to the segmentation of complex bone and vessel networks.

Chapter 7

Analysis of bone and vessels of mouse tibia in SR-μCT images

Contents

7.1 Introduction

In this chapter, we describe the application of the proposed method in Chapter 5 to the analysis of bone and vessels in mice tibia for studying breast cancer bone metastases.

Breast cancer is the most frequently diagnosed cancer in women worldwide (Bray et al., 2018). In terms of mortality, there are approximately 508,000 deaths annually around world (Tulotta et al., 2019). The major morbidity and mortality are caused by bone metastases, generally leading to osteolytic lesions. Around 70% of breast cancer patients develop to the advanced phase where tumors metastasize to bone (Akhtari et al., 2008). Once metastases locate in bone, the existing treatments are not able to cure the disease, and the median survival rate is about 24 to 65 months (Lote, Walløe and Bjersand, 1986; Nutter et al., 2014; Catarina et al., 2017). Breast cancer bone metastases cannot only bring about bone destructions but also facilitate the formation of undesirable vascularization (Tang et al., 2014; Holen et al., 2016).

An important treatment strategy for advanced breast cancer is anti-angiogenic drugs. There is a large body of evidence that angiogenesis is a rate-limiting step in the growth of metastatic bone tumors, making it a relevant target for therapeutic intervention (Ebos and Kerbel, 2011). However, in a mouse model of breast cancer bone metastasis, the anti-angiogenic molecules targeting VEGF (Bevacizumab) or its receptor (Vatalanib), failed to reduce bone lesions development when administered alone, whereas their combination did. Thus, the hypothesis is that the combination of the two drugs will yield a better metastasis suppression (Bachelier et al., 2014).

The aim of this work is to study the kinetics of bone vascularization response to tumor invasion and treatment. To have a better understanding of the pathology, the 3D imaging and quantitative analysis of bone and vessels are necessary.

µCT is a tool of choice to image bone micro-architectures (Kuhn et al., 1990; Cooper et al., 2003; Bousson et al., 2004) and vasculature with a contrast agent (Moore et al., 2003; Zhang et al., 2005). However, imaging vessels requires to decalcify the bone, and µCT does not permit a simultaneous visualization of bone and vessels. SR-µCT possesses significant advantage of yielding high spatial resolution images with a high signal-to-noise ratio, compared to standard µCT, due to the high photon flux of the synchrotron source (Salomé et al., 1999). SR-µCT coupled with a contrast agent permits to visualize simultaneously the bone and vessels in mouse (Schneider et al., 2009) and rat (Langer et al., 2010; Prisby et al., 2011).

The segmentation step requires identifying different phases of the samples: vessels, bone and background. This step has been performed automatically using global thresholding (Schneider et al., 2009) and 3D region growing (Langer et al., 2010; Prisby et al., 2011).

In this thesis, female mice were injected with breast cancer tumor cells, and the preventive treatments were performed with anti-angiogenic drugs. 3D SR-µCT was used to image the bone and vessels in tibia of mice with a contrast agent. For the segmentation, the proposed marker-controlled watershed in conjunction with monogenic signal phase asymmetry was applied to separate vessels appearing to be touching the bone surface. The segmentation quality was evaluated using the Dice coefficient and MCC by comparing to manual segmentations. Segmentation quality of the proposed method was quantitatively compared to

the hysteresis thresholding based method and gradient based marker-controlled watershed. For the purpose of quantitative analysis of vessel and bone in various groups, several parameters were extracted to characterize bone microstructures and vasculatures. Then, statistical analysis was performed to study the influence of the drug treatments on bone and vessels using appropriate tests.

7.2 Experimental setup

To analyze the impact of anti-angiogenesis drugs on bone and vascularization, female mice were injected with breast cancer tumor cells, and various preventive treatments were performed. Then, 3D SR-μCT was used to image the bone vasculatures with intravascular infusion of barium sulfate. Finally, the reconstructed 3D images were pre-processed for the segmentation step.

7.2.1 Sample preparation

8 week-old female Balb/c nude mice were injected with luciferase-expressing human B02 breast cancer tumor cells (Fradet et al., 2011). One day later, the preventive treatments with anti-angiogenic drugs were injected. The mice were divided into four treatment groups: placebo, Sorafenib (vatalanib, inhibiting VEGF-receptors, 100 mg/kg, per bone daily), Avastin (bevacizumab, inhibiting VEGF-A, 5 mg/kg intraperitoneally, twice a week) and combination drugs treatment including both Sorafenib and Avastin. To better describe angiogenesis involvement in bone metastatic processes, we propose here to analyze the impact of drugs treatment on bone vascularization at the early and late stages in the development of bone metastases, corresponding to 8 and 22 days after the inoculation of tumor cells, respectively. The procedure is illustrated as Fig. 7.1. In addition, all of the mice were injected with contrast agent (barium sulfate) for the vascular imaging. Finally, untreated and treated mice will receive Tetracycline (25mg/kg) 5 and 2 days before sacrifice. Here, I acknowledge Marie-Hèlène Lafage-Proust and Bernard Roche from the SAINBIOSE Lab (INSERM U1059, Université de Lyon), Lamia Bouazza and Philippe Clezardin from the Lyos, Lyon (INSERM UMR 1033, Université de Lyon) for the animal protocol and sample preparation.

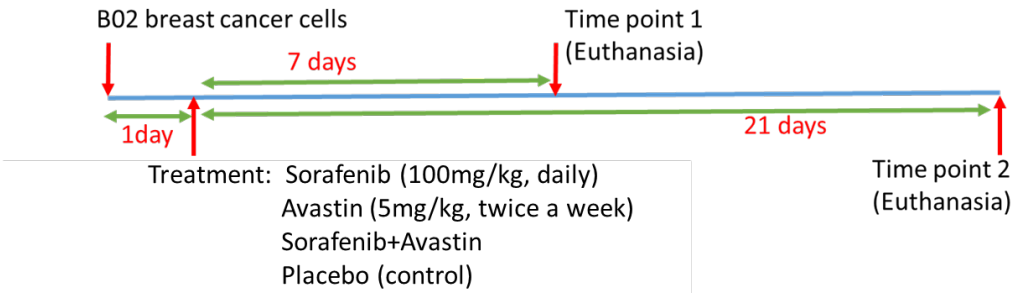

Fig. 7.1 Illustration of the procedure of sample preparation. There are 3 drug treatments and 1 placebo groups at the early and late time points, corresponding to 8 and 22 days after the inoculation of tumor cells respectively.

Specifically, all 70 samples were divided into 8 groups according to the various time points and treatments, as shown in Table 7.1. In the first time point (8 days after injection of tumor cells), T1P, T1A, T1S and T1C represent the groups of placebo, Avastin, Sorafenib, and combination treatment (Avastin + Sorafenib), respectively. In the second time point (22 days after injection of tumor cells), T2P, T2A, T2S and T2C represent the corresponding treatment groups of placebo, Avastin, Sorafenib, and combination treatment (Avastin + Sorafenib), respectively.

Table 7.1 Sample groups divided based on the different time points and treatments

Treatments / Time points	Placebo	Avastin	Sorafenib	Combination (Avastin+ Sorafenib)
Time point 1 (8 days after)	T1P (10 samples)	T1A (14 samples)	T1S (10 samples)	T1C (11 samples)
Time point 2 (22 days after)	T2P (7samples)	T2A (7 samples)	T2S (6 samples)	T2C (5 samples)

7.2.2 Image acquisition

To image the bone microstructure and vasculature simultaneously in 3D, we used contrast-agent SR-μCT. Imaging experiments were performed at the European Synchrotron Radiation Facility (ESRF), Grenoble, France, on the ID19 beamline. The schematic of the SR-μCT imaging setup is shown as Fig. 7.2. A 2048×2048 pixel CCD-based detector with effective pixel size of 3.5 μm was used to record images at evenly spaced angles of view over a 360° rotation. The exposure time and X-ray energy were set to 0.15 s and 26 keV, respectively. The acquisition of 2000 radiographs of one sample lasted approximately 8 minutes. After the image acquisition, 3D images of 2048×2048×1200 voxels were reconstructed using a filtered back projection algorithm yielding a cylindrical field of view (FOV) of 7 mm diameter. Here, the reconstruction was carried out using the ESRF in-house developed software PyHST. The processing involved corrections to take into account beam inhomogeneity, response of the detector and decrease of current during acquisition. Here, I thank Cécile Olivier (CREATIS) for data acquisition and the following technical supports.

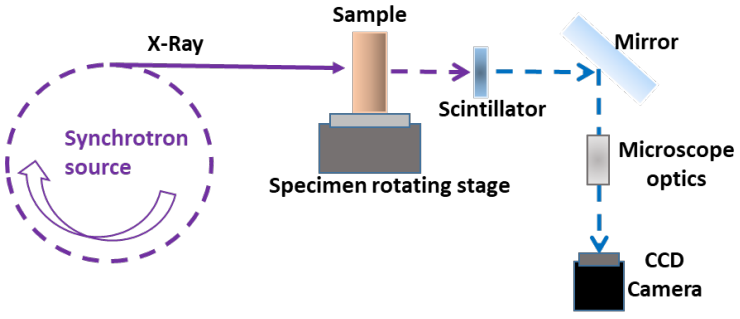

Fig. 7.2 Schematic of the SR-μCT imaging setup. 26 keV X-rays illuminated a sample mounted on a 3D rotation stage. A CCD-based detector was used for recording images through optics and microscope system.

7.2.3 Image pre-processing

As introduced before, various samples of mice bone were prepared and imaged using SR-μCT. However, the reconstructed bone structures are in different orientations, as shown in Fig. 7.3. The figure shows 2D slices (the frontal plane) from 3 different bone volumes. The different orientations among samples may affect the following comparisons of measurements in quantitative analysis. Therefore, we re-orientated the volumes so that the samples have the same orientation in the images. In addition, to avoid the influence of epiphysis on the selection of metaphysis, we created masks to remove epiphyses from the bone volumes. Fig. 7.4 illustrates the different steps of the pre-processing detailed below. Fig. 7.4 (a) is an original image. Fig. 7.4 (b) represents a mask image generated for removing the epiphysis of bone. Fig. 7.4 (c) shows a bone without epiphysis. Fig. 7.4 (d) is the final bone volume, after reorientation, cropping and bounding box from Fig. 7.4 (c). All images are 2D slices from the 3D volumes, and the blue dot lines are crosshairs.

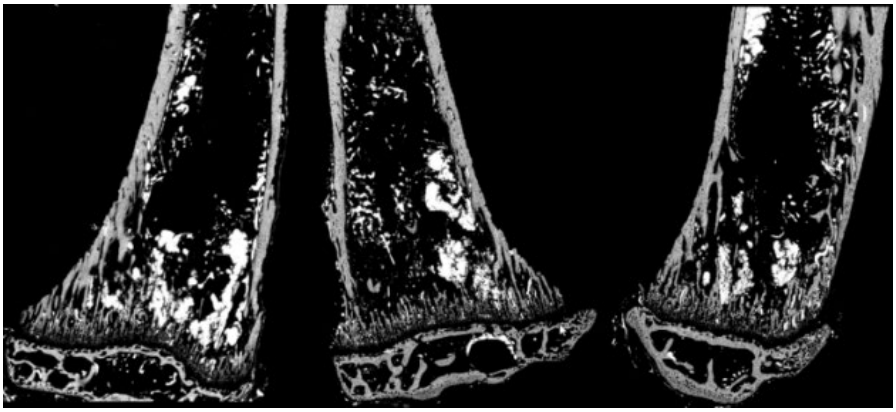

Fig. 7.3 Illustration of the reconstructed bone images with different orientations. All images are 2D slices (the frontal plane) from 3 different bone samples.

Specifically, the mask for removing epiphysis (Fig. 7.4 (b)) was generated as shown in Fig. 7.5. Firstly, the initial bone segmentation (Fig. 7.5 (b)) was obtained by thresholding the original image (Fig. 7.5 (a)). In Fig. 7.5 (b), cortical bone is not connected, as shown by yellow arrow. To generate a mask image containing the whole region inside the outer contour of cortical bone, we plan to use “BinaryFillholeImageFilter” in ITK. In the case the contour of the bone was not connected, this had to be filled in manually using the 3D painting brush tool in ITK-SNAP software. In addition, we also used binary closing operation to fill small holes and gaps on the bone, as shown in Fig. 7.5 (c). Then, we used the “BinaryFillholeImageFilter” in ITK to fill the region inside the closed cortical bone, and generated an initial mask image, as shown Fig. 7.5 (d). Finally, to remove the epiphysis and generate the final mask image (Fig. 7.4 (b)), we kept the largest connected component from the initial mask image (Fig. 7.5 (d)).

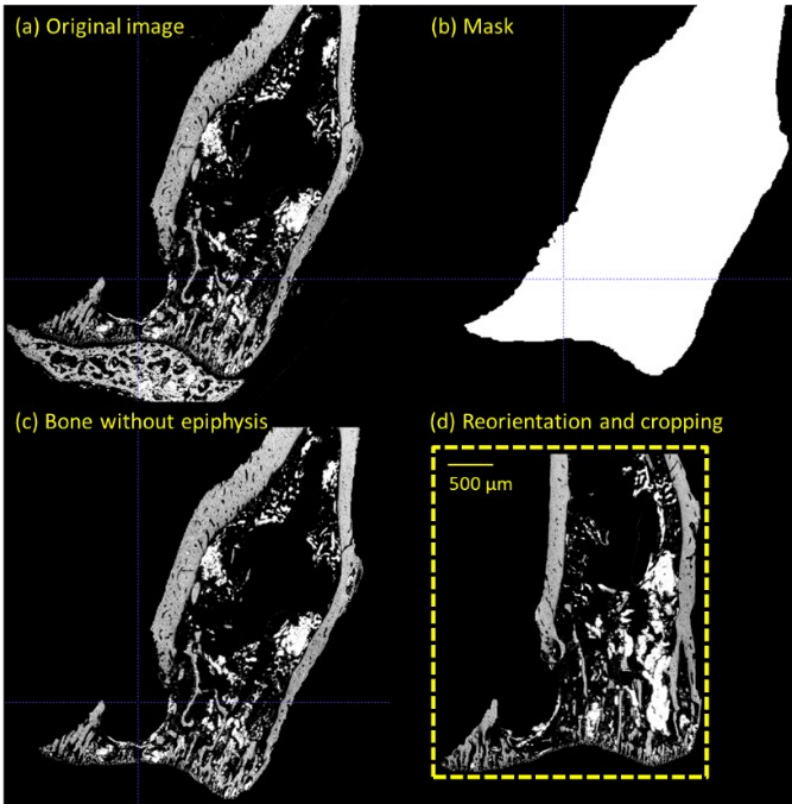

Fig. 7.4 Illustration of the pre-processing procedure on bone volumes. (a) Original image. (b) Mask image generated for removing the epiphysis of bone. (c) Bone sample without epiphysis. (d) Final sample image, after reorientation, cropping and bounding box. All images are 2D slices from the 3D volumes. The blue dot lines are crosshairs.

After removing the epiphysis below the growth plate (Fig. 7.4 (c)), we used ITK-SNAP software to perform reorientation on bone samples. In particular, we first opened two arbitrary bone samples in ITK-SNAP and used Registration tool. One sample was used as an initial base image, and the other one was rotated in Euler angles by manually spinning a wheel showing in the software window. Here, the purpose of rotation was to keep the bone long axis being parallel to the vertical axis, regardless of the orientation of the initial base image. Thus, we generated an upright bone sample as the final base image. Next, we opened the final base image and another bone sample in the ITK-SNAP. The manually spinning was repeated to align two bone samples. Additionally, the position of bone sample may need to be translated by simply dragging.

Additionally, to let samples have a similar bone length, we cropped a new volume for each sample, and bounding box was used on each volume for saving storage memory and speeding up computation, as shown in Fig. 7.4 (d).

We repeated the pre-processing procedure on all samples, as Annex 1. Several volumes are listed as examples to show the results, as given in Fig. 7.6. Here, we display 2D slices from the 3D volumes. The blue dot lines are crosshairs.

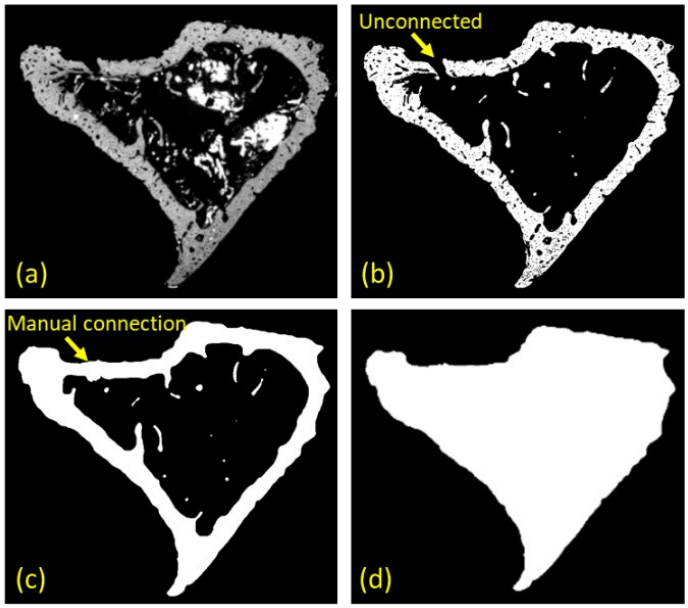

Fig. 7.5 The generation of mask for removing the epiphysis. (a) Original image. (b) Initial bone segmentation using thresholding method. Cortical bone is unconnected as shown by yellow arrow. (c) Manually connected bone. Moreover, we used binary closing operation to fill small holes and gaps on the bone. (d) Initial mask image, after filling the region inside a closed cortical bone, using "BinaryFillholeImageFilter" in ITK. Then, to remove the epiphysis, the final mask image (Fig. 7.4 (b)) was generated by keeping the largest connected component from (d). All images are 2D slices (axial plane) from the 3D volumes.

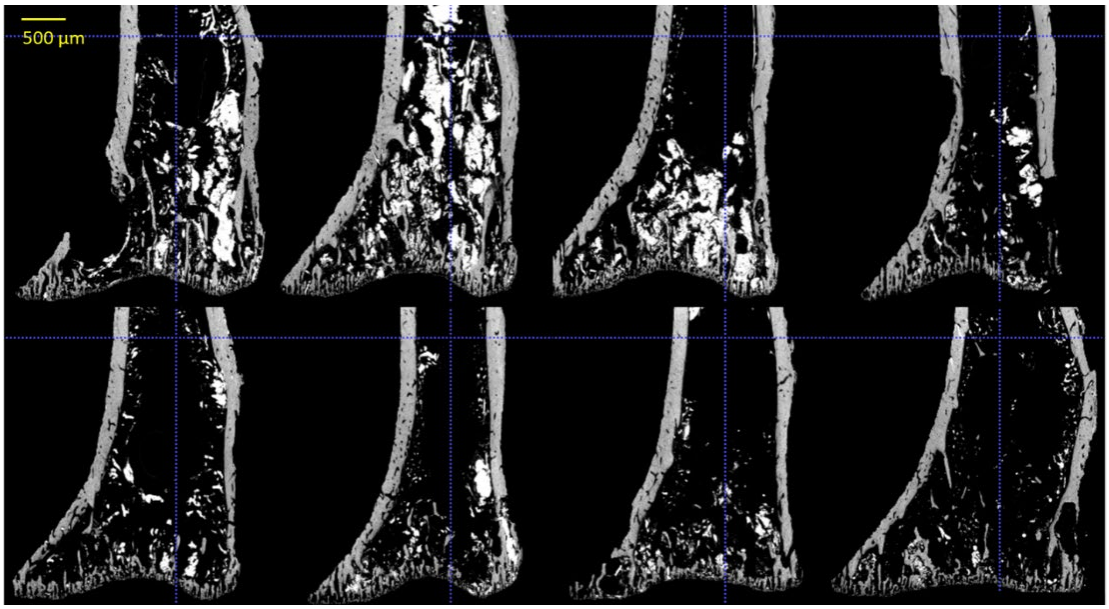

Fig. 7.6. Examples of bone samples, as the results of pre-processing. All images are 2D slices from the 3D volumes. The blue dot lines are crosshairs.

7.3 Image segmentation and evaluation

After the pre-processing steps providing more normalized volume, we applied the proposed segmentation approach as described in chapter 5, to segment bone and vessels in mouse tibia.

For the generation of control surface, we used the multiscale 3D monogenic signal phase asymmetry. The selections of scales depended on the image structures, as shown in Fig. 7.7. In our case, phase asymmetry with lower scales detected too much edge detail so that useful structures could not be recognized. Conversely, the method with higher scales missed too much detail. Therefore, we selected the multiscale $\lambda = 6, 7, 8$ manually by visual feedback on the results, for all samples. The algorithm for the calculation multiscale 3D monogenic signal phase asymmetry was written in Matlab code.

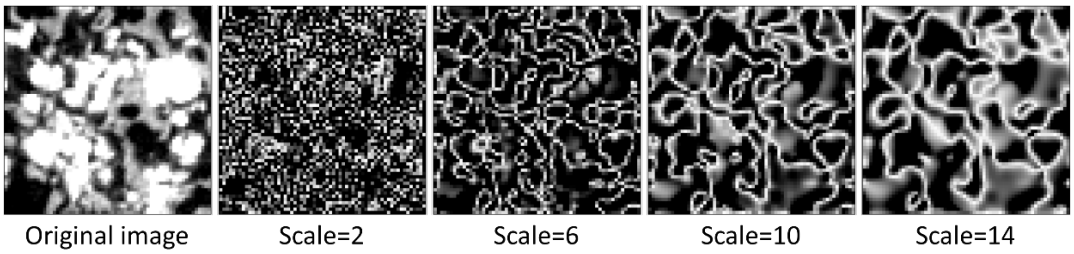

Fig. 7.7. Illustration of 3D monogenic signal phase asymmetry with various scales. All images are 2D slices from the 3D volumes.

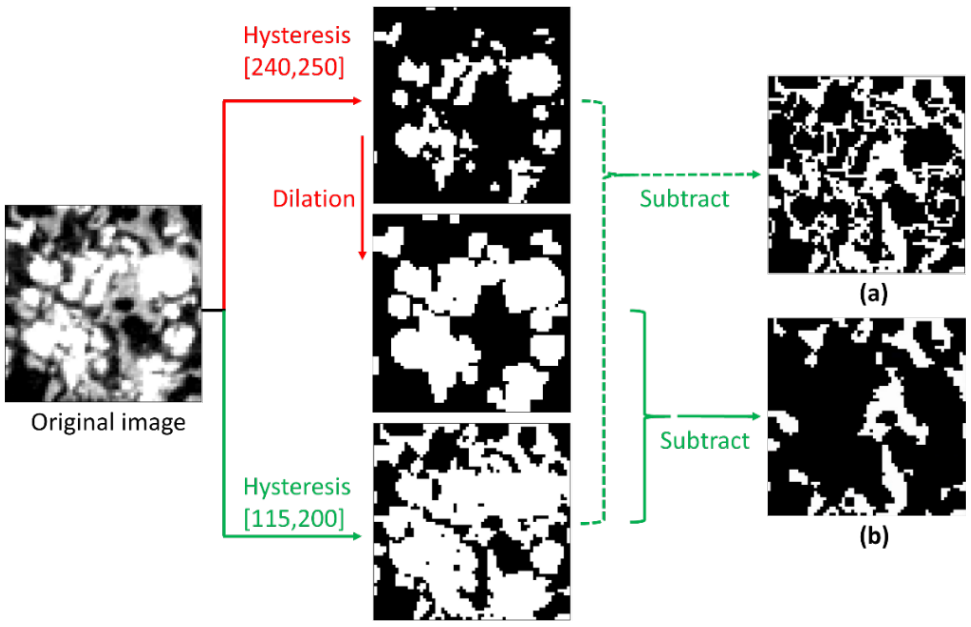

Fig. 7.8. Illustration of bone marker generation. (a) Bone markers generated by subtracting vessel structure. (b) Bone markers generated by subtracting dilated vessel structure. All images are 2D slices from the 3D volumes.

Considering the automatic generation of markers, we used hysteresis thresholding to create the initial segments. Hysteresis thresholds were decided manually according to the testing

results. We applied the same parameters on all samples, since all images had a similar gray level distribution for bone and vessels. Additionally, bone marker was generated by subtracting dilated vessel structure, as shown in Fig. 7.8 (b). Here, the aim of dilation is to remove the "halo" caused by subtraction as Fig. 7.8 (a), thus a 3×3 ball structuring element is enough. The isolated small particles were removed using morphological opening. The shape of structuring element was ball and the size was 3×3.

We implemented the complete algorithm by a shell script, including the generation of control surface, the generation of markers using various ITK functions, marker-controlled watershed, and quantitative measurements. The jobs were submitted to ESRF clusters with nodes=1, and the total running time for each 3D image (whole bone sample) was around 4 hours.

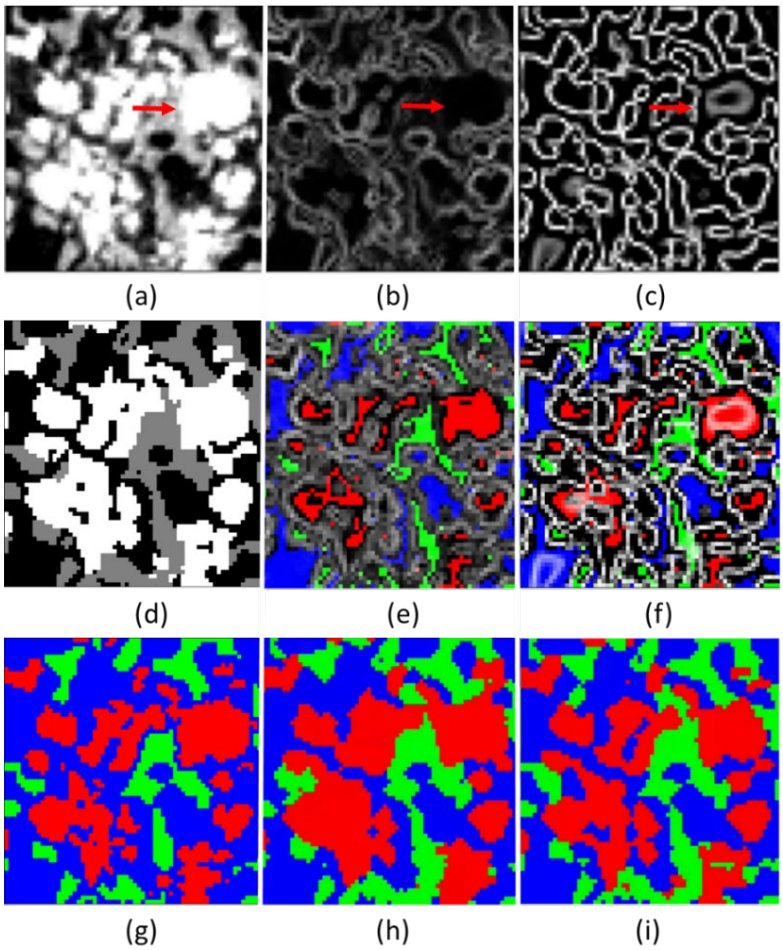

Fig. 7.9 Illustration of control surfaces, markers and segmentations. (a) Original image. (b) Control surface using the image gradient. (c) Control surface using the multiscale phase asymmetry measurement. (d) Manual segmentation. (e) Vessels marker (red), bone marker (green) and background marker (blue) superposed on gradient based control surface. (f) Markers superposed on phase asymmetry based control surface. (g) Hysteresis thresholding segmentation. (h) Marker-controlled watershed segmentation based on (e). (i) Marker-controlled watershed segmentation based on (f). All images are 2D slices from the 3D volumes.

Qualitative results of control surfaces, markers and segmentations are shown in Fig. 7.9. A zoom on a 2D slice from the 3D original volume is shown as Fig. 7.9 (a). The red arrow shows the relatively low contrast interface between bone and vessel. The control surface is generated using the 3D edge detection methods. For instance, Fig. 7.9 (b) shows the image gradient of original image as control surface. The low contrast boundary (indicated by the red arrow) between bone and vessel cannot be well detected in the gradient. Fig. 7.9 (c) shows the 3D phase asymmetry (multiscale $\lambda = 6, 7, 8$) of original image as control surface. As the Fig. 7.9 (c), even though there are some spurious edges detected in homogeneous areas with the phase asymmetry method, they are always covered by a marker in solid areas. Hence they do not influence the marker-controlled watershed segmentation. Comparing the control surfaces using the phase asymmetry Fig. 7.9 (c) to using the image gradient Fig. 7.9 (b), there are substantial improvements at low contrast interface edge detections, as red arrow shows. Fig. 7.9 (d) shows the manual segmentation of original image. Fig. 7.9 (e) shows the markers overlaid on the gradient based control surface. Vessel, bone and background markers are shown in red, green and blue, respectively. Fig. 7.9 (f) shows these markers superposed on the phase asymmetry based control surface. Fig. 7.9 (g) shows the segmentation using hysteresis thresholding. Fig. 7.9 (h) shows the marker-controlled watershed segmentation based on Fig. 7.9 (e), in which flooding happens from vessel, bone and background markers to find boundaries between different compartments. Fig. 7.9 (i) shows the marker-controlled watershed segmentation based on Fig. 7.9 (f). Qualitatively, the result of segmentation using the phase asymmetry based marker-controlled watershed is much improved compared to hysteresis thresholding or gradient based watershed segmentations.

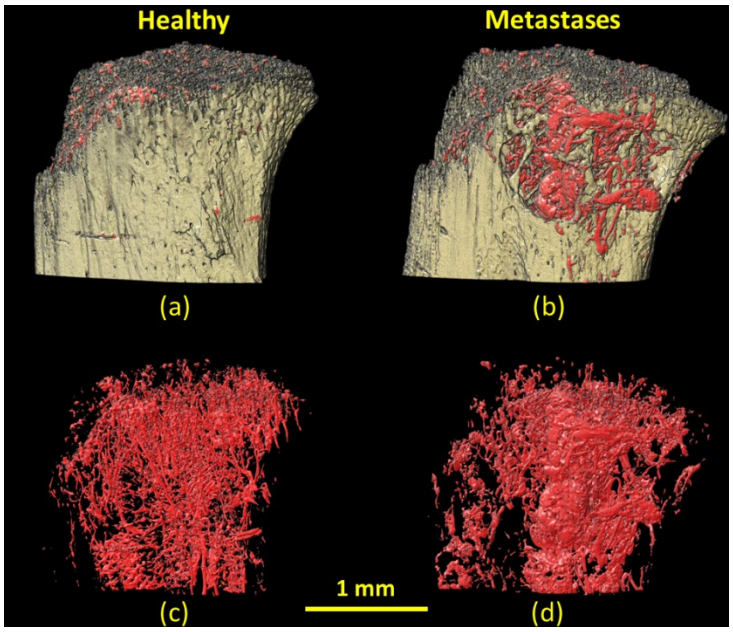

Fig. 7.10 Illustration of comparisons between healthy and metastases samples. (a) 3D rendering of bone and vessel in healthy bone. (b) 3D rendering of bone and vessel in metastases bone. (c) 3D rendering of vessels in healthy bone. (d) 3D rendering of vessels in metastases bone.

To compare the healthy sample with metastatic sample qualitatively, 3D volume renderings of segmentations using the proposed method are shown as Fig. 7.10 (a-d). The metastatic sample in Fig. 7.10 (b) shows evident large bone lesions, compared to healthy sample in Fig. 7.10 (a). In addition, there are more and thicker vessels in the metastatic sample than in the healthy sample as a comparison of Fig. 7.10 (d) and (c). This indicates an increased and abnormal vascularization due to the bone metastases, as expected.

The segmentation quality was evaluated quantitatively using the Dice coefficient and the MCC by comparing to manual segmentation. A representative volume was manually segmented using VGStudio Max (Volume Graphics GmbH, Heidelberg, Germany). Dice coefficients corresponding to vessel, bone and background compartments were calculated separately. An overall segmentation quality was evaluated using multi-class MCC. As the comparison in Table 7.2, there are substantial improvements at each single compartment segmentation and overall segmentation in the proposed method of phase asymmetry based marker-controlled watershed, compared to the hysteresis thresholding based method as well as to gradient based marker-controlled watershed, in terms of the Dice coefficient and MCC.

Table 7.2 Evaluation of segmentation quality

Evaluations / Methods	Dice (Vessel)	Dice (Bone)	Dice (Background)	MCC (Overall)
Hysteresis thresholding	0.84	0.81	0.85	0.77
Gradient + watershed	0.92	0.91	0.93	0.88
Phase asymmetry + watershed	0.97	0.92	0.97	0.94

7.4 Quantitative analysis of bone and vasculature

To quantitatively analyze bone microstructures and vasculatures in mouse model, several parameters were extracted. Furthermore, statistical analysis with an appropriate parametric or non-parametric test was performed to investigate the impacts of the drug treatments on bone and vessels.

7.4.1 Quantitative parameters

7.4.1.1 Volume fraction

Volume fraction is an important parameter to characterize the proportion of volume of the different structures. In this study, we extracted several volume fractions, including BV/TV, Tb.V/TV, Ct.V/TV, Me.V /TV, Tb.V/Me.Ca.V, Ct.Po.V/Ct.TV, VV/TV, denoted as follows:

- Bone volume (BV)
- Total volume (TV): volume inside the outer contour of the cortical bone.
- Trabecular bone volume (Tb.V)
- Cortical bone volume (Ct.V)
- Metastases volume (Me.V)
- Medullary cavity volume (Me.Ca.V)
- Volume of pores in cortical bone (Ct.Po.V)
- Cortical envelope volume (Ct.TV): volume of cortical bone with porosity filled in.
- Vessel volume (VV)

BV and VV were measured by counting voxels on the automatically segmented bone and vessels, respectively.

To measure TV for each bone sample, we generated a volume containing all voxels inside the outer contour of the cortical bone. Here, we used Avizo 9.7 (Thermo Scientific), which is a commercial software for 3D image visualization, analysis and modeling. We assumed changes from slice-to-slice are small, and interpolated the marked regions between slices. Firstly, we manually marked the region inside the outer contour of the cortical bone using the 2D brush (painting) tool, at the first slice of a 3D volume. Then, we went to the next 50th slice, and marked the region inside the bone again, as before. This procedure was repeated until the whole volume was throughout. Next, the marked regions were interpolated linearly between slices. Three orthogonal slices of a 3D original image and its total volume are shown as Fig. 7.11, in which the left is original image and the right is the generated total volume. Finally, the value of TV was measured by counting voxels on total volume.

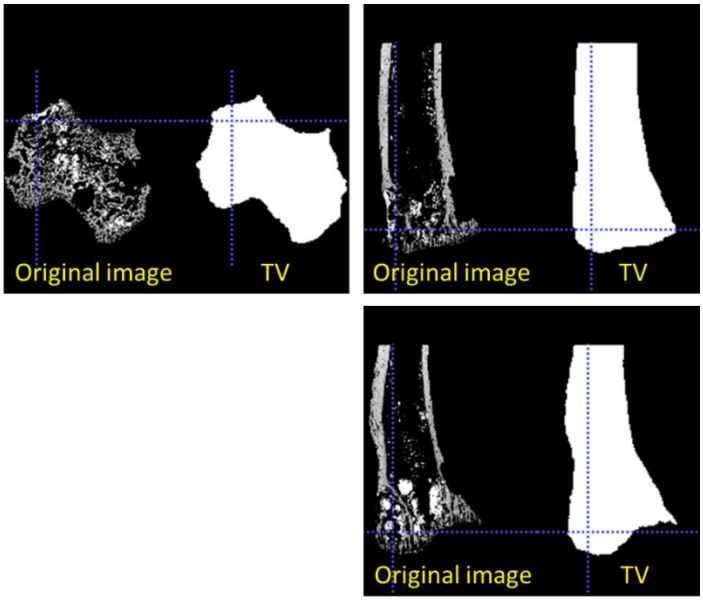

Fig. 7.11 Three orthogonal slices of a 3D original image (left) and the generated total volume (right).

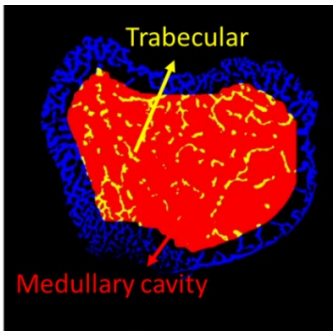

Fig. 7.12 Illustration of separating results of medullary cavity, trabecular bone, and cortical bone. The medullary cavity is marked as red region, trabecular bones are marked as yellow, and cortical bone is marked as blue.

Medullary cavity is the central cavity of bone. In this study, we separate the medullary cavity from bone by eroding the total volume until approaching the inner contour of the cortical bone. Then, the trabecular bones were separated from cortical bone by masking the medullary cavity with the automatically segmented bone compartment. The value of Me.Ca.V, Tb.V and Ct.V were measured by counting voxels. Fig. 7.12 shows the separating results of medullary cavity, trabecular bone, and cortical bone.

Even though bone metastases are not directly visible on the SR-μCT image, when they occur in the cortical bone, it is possible to estimate the contour of metastases. To this aim, we manually segmented metastases using the ITK-SNAP software. In particular, we used the 3D brush tool to delineate metastases on cortical bone. Fig. 7.13 shows three orthogonal slices of a 3D original image (left), the bone segmentation (right), and metastases given in red. The value of Me.V was measured by counting voxels. It was not possible to identify metastases on trabecular bone.

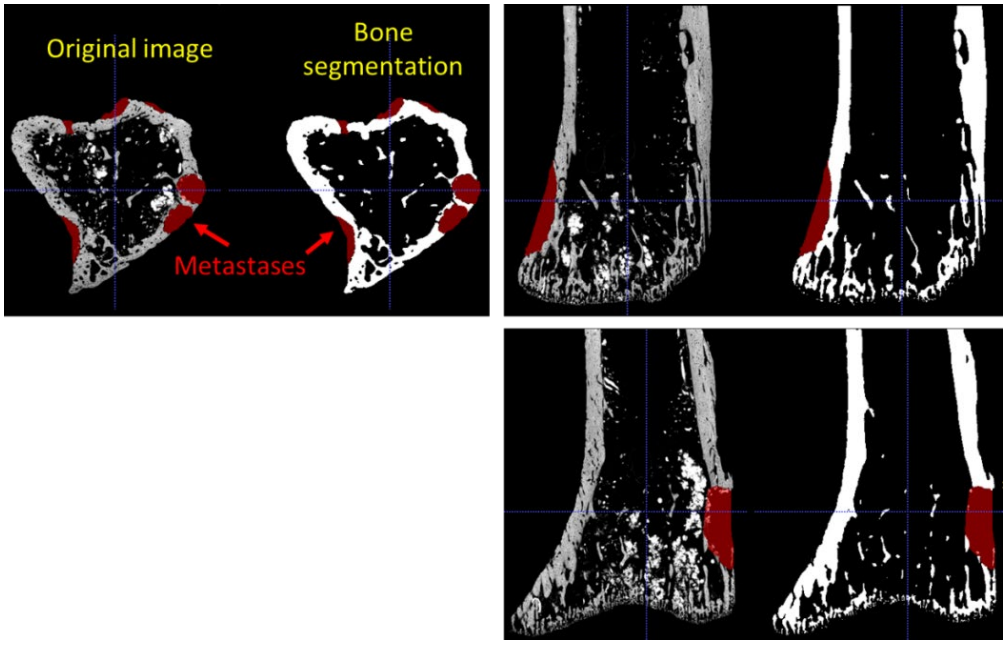

Fig. 7.13 Three orthogonal slices of a 3D original image (left) and the bone segmentation (right). Metastases were segmented by hand, given in red.

To segment the cortical bone porosity, we first filled the holes on the cortical bone using the binary closing method. Next, we did the subtraction between the cortical bone with porosity filled in and cortical bone itself. A 3D rendering of cortical bone porosity is shown in Fig. 7.14, given by color purple. The value of Ct.TV and Ct.Po.V were measured by counting voxels.

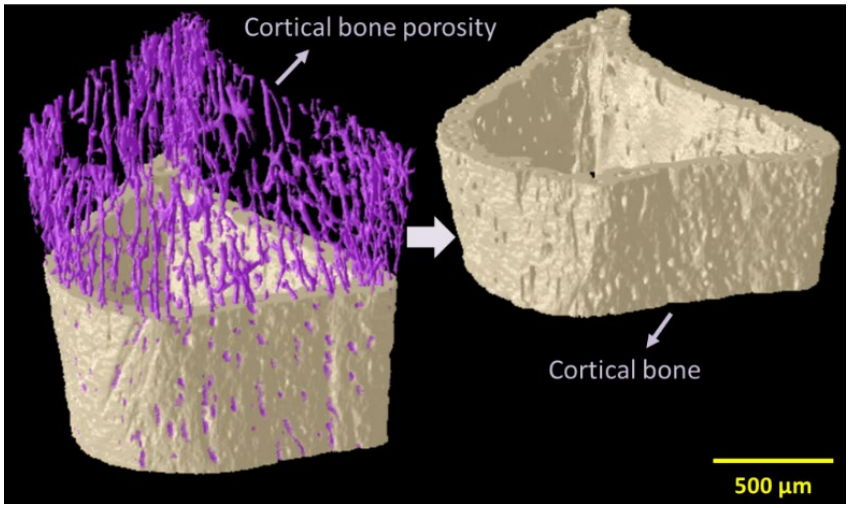

Fig. 7.14 3D rendering of cortical bone porosity (given by purple)

7.4.1.2 Local thickness

The thickness of the segmented compartment can be described by measuring the local thickness, which was calculated using the method that provides at each point of the volume the diameter of the largest sphere that fits inside the compartment of the point (T. Hildebrand and Rüegsegger, 1997; Langer et al., 2010). Thus, we can extract the mean thickness of different compartments, yielding mean trabecular thickness (Tb.Th), mean cortical thickness (Ct.Th), and mean vessel thickness (V.Th).

7.4.1.3 Fractal dimension

Fractal dimension (FD) is a means of quantifying structures with complex form, indicating that structure tends to fill space at different scales. The box-counting is a commonly used method to compute fractal dimension, due to the easiness of implementation (Alberich-Bayarri et al., 2010).

To quantify the complexity of 3D object, the box-counting algorithm can be extended to 3D space domain. The surface of 3D structure is overlaid by different 3D cube meshes with varying cube sizes. The number of cubes containing the surface is calculated for each cube size. The 3D fractal dimension can be calculated by $log(N) = -FD \cdot log(\lambda) + log(\alpha)$ where N is the number of cubes, λ is the corresponding size of box, FD is the box counting fractal dimension parameter, and α is a proportionality constant (Alberich-Bayarri et al., 2010). 3D box counting has been widely used in the analysis of trabecular bone (Alberich-Bayarri et al., 2010; Arnold et al., 2020) and 3D vasculature (Helmberger et al., 2014; Ward, Ding and Bai, 2014).

In this thesis, the 3D box counting algorithm implemented for the quantification of 3D fractal complexity was validated by its application to the Menger sponge, which has a known fractal dimension of $log20/log3 = 2.7268$.

7.4.1.4 Structure model index

Structure model index (SMI) is a morphometric parameter to quantify the characteristic form of a 3D object in terms of the amount of plates and rod composing the structure. For an ideal plate structure, the SMI value is 0, and for an ideal rod structure it is 3, independent of the physical dimensions. For a structure with a mixed structure of plates and rods, the SMI value lies between 0 and 3, depending on the volume ratio of rods and plates. The SMI is originally defined as a function of volume, surface area and first derivative of the specific surface area: $SMI = 6 \cdot \frac{S' \cdot V}{S^2}$, in which S is the structure surface, S' is approximal derivative of the surface area, and V is the structure volume. Here the derivative is defined and computed using a surface meshing (T. O. R. Hildebrand and Rüegsegger, 1997).

To define SMI without referring to a discretization with surface meshing, S' can be defined via the Steiner formula with mean curvature. Therefore, SMI is given by $SMI = 12\frac{V \cdot M}{S^2}$, where M represents integral of mean curvature (Ohser, Redenbach and Schladitz, 2009). In this thesis, we used this equation to evaluate trabecular bone.

7.4.1.5 Connectivity density

Connectivity density (Conn.D) is calculated by dividing the connectivity by the volume. Where the connectivity is the number of connected structures, and can be calculated using Euler characteristic (Odgaard and Gundersen, 1993; Toriwaki and Yonekura, 2002).

7.4.1.6 Degree of anisotropy

Degree of anisotropy (DA) is calculated based on the mean intercept length (MIL), the low value of DA indicates disorganized structures (Whitehouse, 1974; Harrigan and Mann, 1984; Cole et al., 2014).

7.4.2 Statistical analysis

Statistical testing was performed on each measured parameter among various groups. To test the normality of the data in each group, the Lilliefors test was used. If the data comes from a normally distributed population, we will use ANOVA (Analysis of variance) to test whether there is a significant difference between the groups. In addition, since only a very few number of groups are non-normal, and on inspection they are not bimodal, we judge that ANOVA can be used anyway. In case a significant difference between the groups is found, a post-hoc Tukey's HSD test will be applied to identify which group is significantly different from the other, following the ANOVA test. We considered the difference statistically significant at p = 0.05 and the difference acceptably significant at p = 0.1.

Parameters were extracted from the whole bone sample (BV/TV, Ct.V/TV, Me.V/TV, Ct.Th), trabecular bone in metaphysis (Tb.V/Me.Ca.V, Tb.Th, FD, SMI, Conn.D, DA), cortical porosity in diaphysis (Ct.Po.V/Ct.TV) and vessels (VV/TV, V.Th, FD, DA). Box plots were given at each parameter.

7.5 Results

7.5.1 Bone and metastases

7.5.1.1 Bone volume fractions

Box plots of bone volume fractions (BV/TV) at the various groups are shown as Fig. 7.15. Due to the low number of samples, all data points were plotted along with the box plots. The results of statistical tests are shown in Table 7.3.

In the first time point, the data points in the group of T1A ($p = 0.0418$) cannot be considered normally distributed at $p = 0.05$ level, and T1C ($p = 0.0568$) is not follow normal distribution at $p = 0.1$ level, according to the Lilliefors test. However, we still used ANOVA test ($p = 0.691$) to show no significant difference among the various groups.

In the second time point, the BV/TV data points in the group of T2P ($p = 0.0684$) and T2S ($p = 0.0946$) are not follow normal distribution at $p = 0.1$ level, according to the Lilliefors test. However, the ANOVA test ($p = 0.421$) was still used to show no significant difference among the various groups.

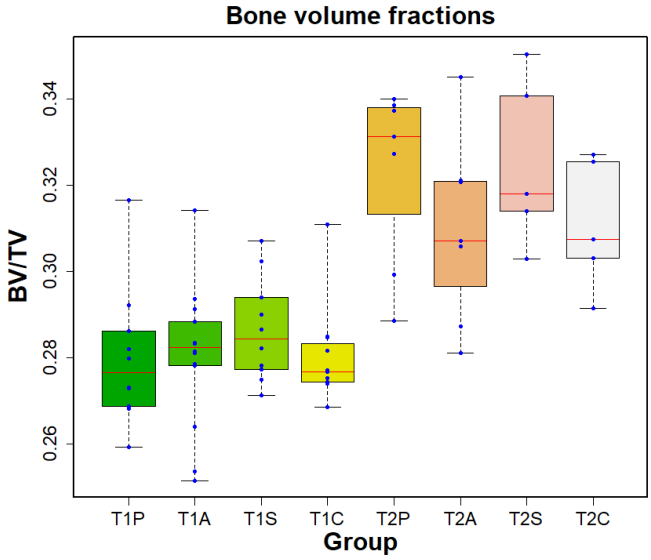

Fig. 7.15 Box plots of bone volume fractions (BV/TV) at the different groups, at the first time point (T1P, T1A, T1S and T1C) and the second time point (T2P, T2A, T2S and T2C). Red line in each box represents the median value for the data set. All data points (blue) were plotted along with the box plots. (P: Placebo, A: Avastin, S: Sorafenib, C: Combination A and S)

Table 7.3 Statistical tests on BV/TV at different groups. (Asterisk * indicates acceptably significant difference, at $p = 0.1$ level. ** denotes statistically significant difference, at $p = 0.05$ level.)

Groups / p-value	T1 : 8 days after injection of tumor				T2 : 22 days after injection of tumor			
	T1P	T1A	T1S	T1C	T2P	T2A	T2S	T2C
Lilliefors test	0.6371	0.0418**	0.734	0.0568*	0.0684*	0.8645	0.0946*	0.512
ANOVA test	0.691				0.421			

7.5.1.2 Cortical bone volume fractions

Fig. 7.16 shows the box plots of cortical bone volume fractions (Ct.V/TV) at the various groups. The results of statistical tests are shown in Table 7.4.

In the first time point, the normal distributions of Ct.V/TV data in each group were verified using Lilliefors test at p = 0.05 level. Then, the ANOVA test (p = 0.253) shows no significant difference among the various groups.

In the second time point, although Ct.V/TV data points in the group of T2P (p = 0.076) is not follow normal distribution at p = 0.1 level according to Lilliefors test, the ANOVA test (p = 0.412) was still used to show no significant difference among the various groups.

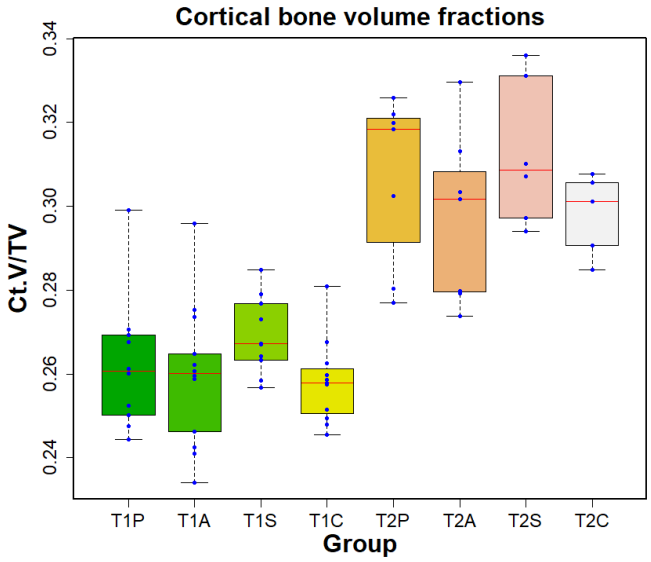

Fig. 7.16 Box plots of cortical bone volume fractions (Ct.V/TV) at the various groups, in the first time point (T1P, T1A, T1S and T1C) and the second time point (T2P, T2A, T2S and T2C). Red line in each box represents the median value for the data set. All data points (blue) were plotted along with the box plots. (P: Placebo, A: Avastin, S: Sorafenib, C: Combination A and S)

Table 7.4 Statistical tests of Ct.V/TV at different groups. (Asterisk * indicates acceptably significant difference, at p = 0.1 level)

Groups / p-value	T1 : 8 days after injection of tumor				T2 : 22 days after injection of tumor			
	T1P	T1A	T1S	T1C	T2P	T2A	T2S	T2C
Lilliefors test	0.3098	0.1714	0.4916	0.602	0.076*	0.3175	0.4703	0.5341
ANOVA test	0.253				0.412			

7.5.1.3 Metastases volume fractions

Box plots of metastases volume fractions (Me.V/TV) at each group are shown as Fig. 7.17. Here, we only present the measurements in the second time point (T2P, T2A, T2S and T2C), since mice usually develop bone metastases 18 days after tumor cell inoculation (Bachelier et al., 2014), and we cannot find any metastases on the cortical bone at the first time point.

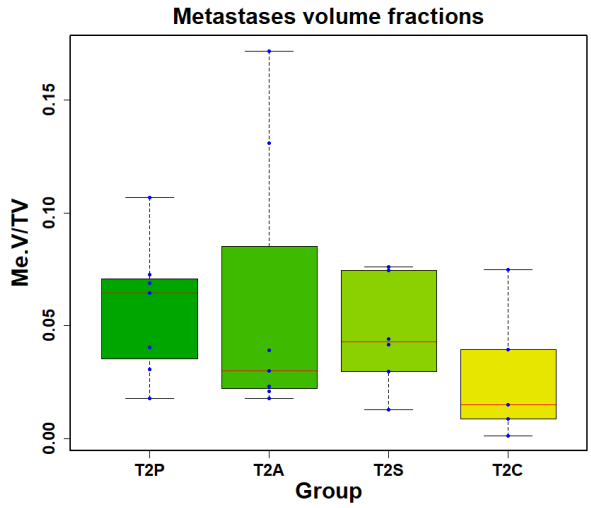

Fig. 7.17 Box plots of metastases volume fractions (Me.V/TV) at the different groups, in the second time point (T2P, T2A, T2S and T2C). Red line in each box represents the median value for the data set. All data points (blue) were plotted along with the box plots. (P: Placebo, A: Avastin, S: Sorafenib, C: Combination A and S)

Table 7.5 Statistical tests of Me.V/TV at various groups. (** denotes statistically significant difference, at p = 0.05 level.)

Groups / Tests: p-value	Time point 2 (22 days after injection of tumor cells)			
	T2P	T2A	T2S	T2C
Lilliefors test	0.8096	0.0073 **	0.5906	0.2935
ANOVA test	0.523			

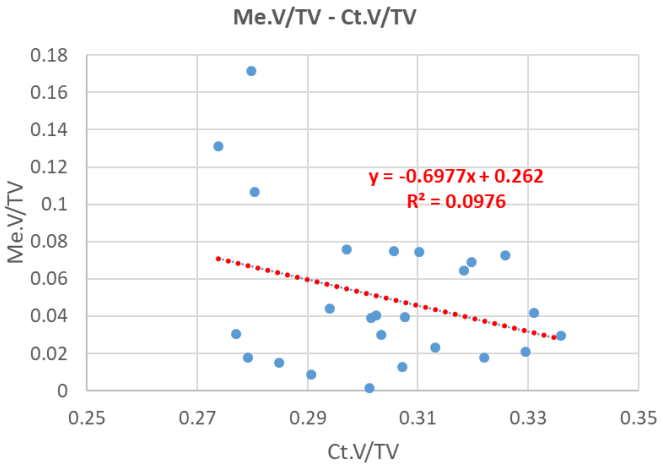

Fig. 7.18 Relation between Me.V/TV and Ct.V/TV. Blue points in the plot represent the data points at the second time points, and the red dot line is the result of linear regressions.

The results of statistical tests are shown in Table 7.5. Although the data sets in the group of T2A (p = 0.0073) cannot be considered normally distributed at p = 0.05 level according to the

Lilliefors test, ANOVA test (p = 0.523) was still used to show no significant difference among the various groups.

Furthermore, to illustrate the relationship between Me.V/TV and Ct.V/TV, we performed linear regressions on data points at the second time point, as shown in Fig. 7.18. We discover that there is no significant linear correlation between Me.V/TV and Ct.V/TV with $R^2 = 0.0976$ and p-value = 0.1284.

To investigate the effects of drugs on the thickness of bone, we measured the local thickness of cortical bone, and calculated the mean as the value of data points.

7.5.1.4 Thickness of cortical bone

Fig. 7.19 shows the box plots of the mean thickness of cortical bone (Ct.Th) at the different groups. The results of statistical tests are shown in Table 7.6. The normal distributions of Ct.Th in each group were verified using the Lilliefors test (p > 0.05). Thus, the ANOVA approach was used to test whether there is significant difference among the various groups. The results show that there is no significant difference for p = 0.611 at the first time point, and p = 0.315 at the second time point.

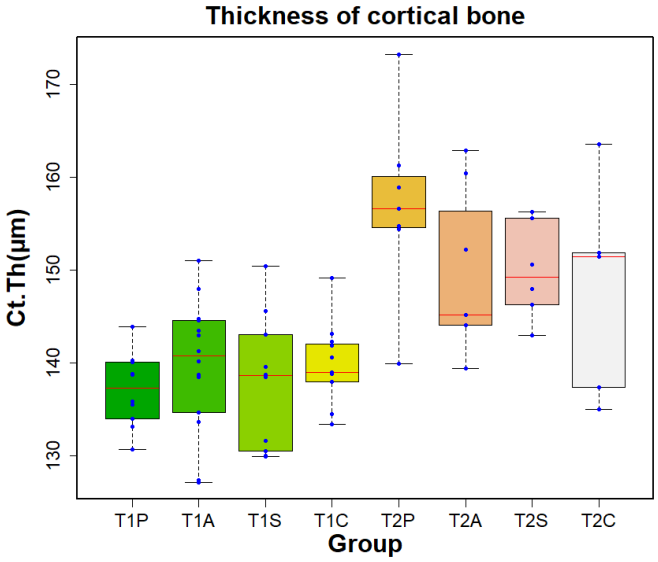

Fig. 7.19 Box plots of the mean thickness of cortical bone (Ct.Th) at the various groups, in the first time point (T1P, T1A, T1S and T1C) and the second time point (T2P, T2A, T2S and T2C). Red line in each box represents the median value for the data set. All data points (blue) were plotted along with the box plots. (P: Placebo, A: Avastin, S: Sorafenib, C: Combination A and S)

Table 7.6 Statistical tests of Ct.Th at various groups.

Groups / p-value	T1 : 8 days after injection of tumor				T2 : 22 days after injection of tumor			
	T1P	T1A	T1S	T1C	T2P	T2A	T2S	T2C
Lilliefors test	0.6816	0.6185	0.2853	0.7062	0.1879	0.139	0.6856	0.5901
ANOVA test	0.611				0.315			

7.5.2 Trabecular bone in metaphysis

7.5.2.1 Trabecular bone volume fractions

To investigate the effects of drugs on trabecular bone, we selected a volume of interest (VOI) at the metaphysis of bone, since trabecular bone mainly locates in this part. In addition, we extracted the parameter of Tb.V/Me.Ca.V rather than Tb.V/TV for excluding the influence of cortical bone.

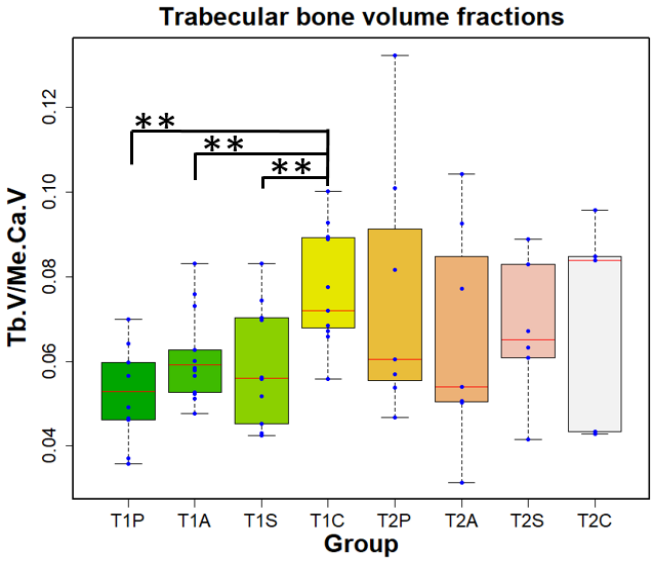

Fig. 7.20 Box plots of the trabecular bone volume fractions (Tb.V/Me.Ca.V) at the different groups, in the first time point (T1P, T1A, T1S and T1C) and the second time point (T2P, T2A, T2S and T2C). Red line in each box represents the median value for the data set. Asterisk ** denotes statistically significant difference, at the p = 0.05 level. All data points (blue) were plotted along with the box plots. (P: Placebo, A: Avastin, S: Sorafenib, C: Combination A and S)

Fig. 7.20 shows the box plots of the trabecular bone volume fractions (Tb.V/Me.Ca.V) at the different groups. The results of statistical tests are shown in Table 7.7.

In the first time point, even though Tb.V/Me.Ca.V data points in the group of T1A (p = 0.066) is not follow normal distribution at p = 0.1 level according to Lilliefors test, we still used the ANOVA test (p = 0.0003) to show that there is significant difference among the various groups. Then, we used a post-hoc Tukey's HSD test to identify which group is significantly different from the other. According the results, Tb.V/Me.Ca.V in T1C is significantly different from T1P (p = 0.0002), T1A (p = 0.011) and T1S (p = 0.0088), respectively.

In the second time point, the normal distributions of Tb.V/Me.Ca.V data in each group were verified using Lilliefors test (p > 0.05). Then, the ANOVA test (p = 0.883) shows no significant difference among the various groups.

To investigate the effects of drugs on the thickness of trabecular bone, we measured the local thickness of trabecular bone, and calculated the mean as the value of data points.

Table 7.7 Statistical tests of Tb.V/Me.Ca.V at various groups. (Asterisk * indicates acceptably significant difference, at p = 0.1 level. ** denotes statistically significant difference, at p = 0.05 level.)

Groups / p-value	T1 : 8 days after injection of tumor				T2 : 22 days after injection of tumor			
	T1P	T1A	T1S	T1C	T2P	T2A	T2S	T2C
Lilliefors test	0.8473	0.066*	0.4484	0.2831	0.1428	0.2326	0.7683	0.1256
ANOVA test	0.0003**				0.883			
Tukey's HSD test	T1C-T1A : 0.0110** T1P-T1A : 0.3476 T1S-T1A : 0.9841 T1P-T1C : 0.0002** T1S-T1C : 0.0088** T1S-T1P : 0.6158				-			

7.5.2.2 *Thickness of trabecular bone*

Fig. 7.21 shows the box plots of the thickness of trabecular bone (Tb.Th) at the different groups. The results of statistical tests are shown in Table 7.8.

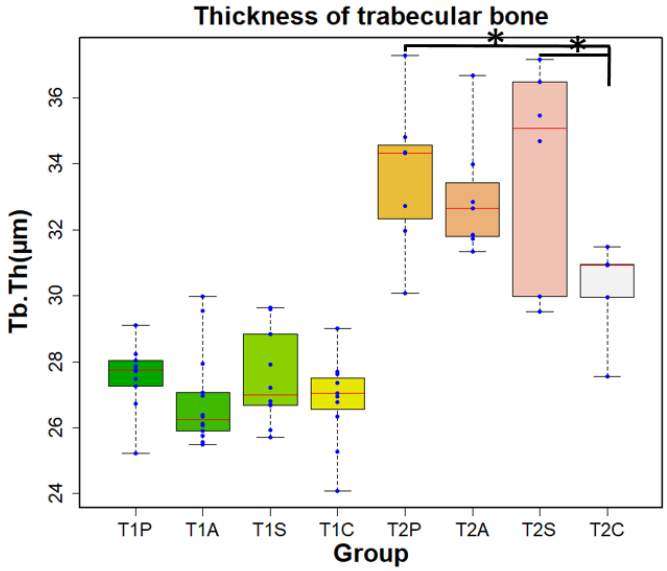

Fig. 7.21 Box plots of the thickness of trabecular bone (Tb.Th) at the different groups, in the first time point (T1P, T1A, T1S and T1C) and the second time point (T2P, T2A, T2S and T2C). Red line in each box represents the median value for the data set. Asterisk * indicates acceptably significant difference, at p = 0.1 level. All data points (blue) were plotted along with the box plots. (P: Placebo, A: Avastin, S: Sorafenib, C: Combination A and S)

In the first time point, although the data points in the group of T1A (p = 0.013) cannot be considered normally distributed at p = 0.05 level according to the Lilliefors test, we still used ANOVA test (p = 0.391) to show no significant difference among the various groups.

In the second time point, normal distributions of Tb.Th in each group were verified using the Lilliefors test (p > 0.05). Thus, the ANOVA approach was used to test whether there is significant difference among the different groups. Although there is no significant difference

in Tb.Th (p = 0.0657), we still consider that there is acceptably significant difference, at p = 0.1 level. Then, we used a post-hoc Tukey's HSD test to identify which group is significantly different from the other. According to the results, there is acceptably significant difference between T2P and T2C (p = 0.0881), T2S and T2C (p = 0.0746).

Table 7.8 Statistical tests of Tb.Th at various groups. (Asterisk * indicates acceptably significant difference, at p = 0.1 level. ** denotes statistically significant difference, at p = 0.05 level.)

Groups / p-value	T1 : 8 days after injection of tumor				T2 : 22 days after injection of tumor			
	T1P	T1A	T1S	T1C	T2P	T2A	T2S	T2C
Lilliefors test	0.3877	0.013**	0.4143	0.2442	0.659	0.2043	0.2219	0.1957
ANOVA test	0.391				0.0657*			
Tukey's HSD test	-				T2C-T2A : 0.2017 T2P-T2A : 0.9588 T2S-T2A : 0.9108 T2P-T2C : 0.0881* T2S-T2C : 0.0746* T2S-T2P : 0.9978			

7.5.2.3 *Fractal dimension*

Fig. 7.22 shows the box plots of fractal dimension (FD) for trabecular bone in metaphysis. The results of statistical tests are shown in Table 7.9. The normal distributions of FD in each group were verified using the Lilliefors test (p > 0.05). Thus, the ANOVA approach was used to test whether there is significant difference among the different groups.

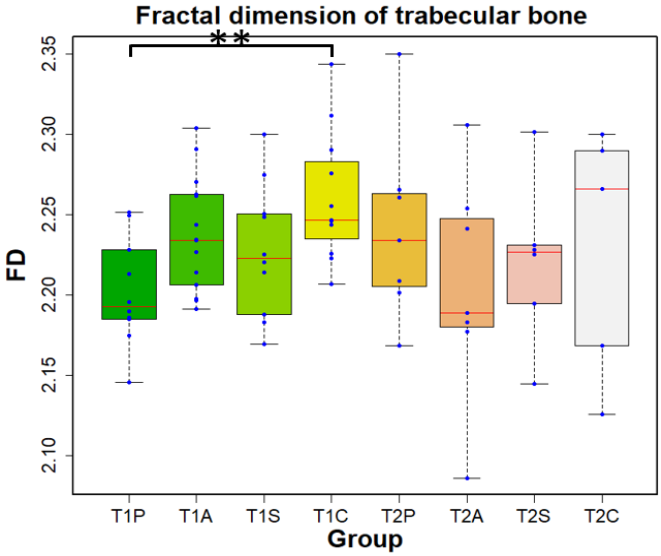

Fig. 7.22 Box plots of fractal dimension (FD) for trabecular bone in metaphysis, in the first time point (T1P, T1A, T1S and T1C) and the second time point (T2P, T2A, T2S and T2C). Red line in each box represents the median value for the data set. Asterisk ** denotes statistically significant difference, at p = 0.05 level. All data points (blue) were plotted along with the box plots. (P: Placebo, A: Avastin, S: Sorafenib, C: Combination A and S)

In the first time point, the ANOVA test (p = 0.0094) shows that there is significant difference for FD. Thus, we used a post-hoc Tukey's HSD test to identify which group is significantly different from the other. According the result, FD in T1C is significantly different from T1P (p = 0.0052). In the second time point, the ANOVA test (p = 0.766) shows no significant difference for FD.

Table 7.9 Statistical tests of FD for trabecular bone in metaphysis. (Asterisk ** denotes statistically significant difference, at p = 0.05 level.)

Groups / Test: p-value	T1 : 8 days after injection of tumor				T2 : 22 days after injection of tumor			
	T1P	T1A	T1S	T1C	T2P	T2A	T2S	T2C
Lilliefors test	0.5458	0.9004	0.9182	0.3416	0.5613	0.5219	0.2621	0.2287
ANOVA test	0.0094**				0.766			
Tukey's HSD test	T1C-T1A : 0.4571 T1P-T1A : 0.1139 T1S-T1A : 0.9025 T1P-T1C : 0.0052** T1S-T1C : 0.1991 T1S-T1P : 0.4474				-			

7.5.2.4 Structure model index

Fig. 7.23 shows the box plots of structure model index (SMI) for trabecular bone in metaphysis. The results of statistical tests are shown in Table 7.10.

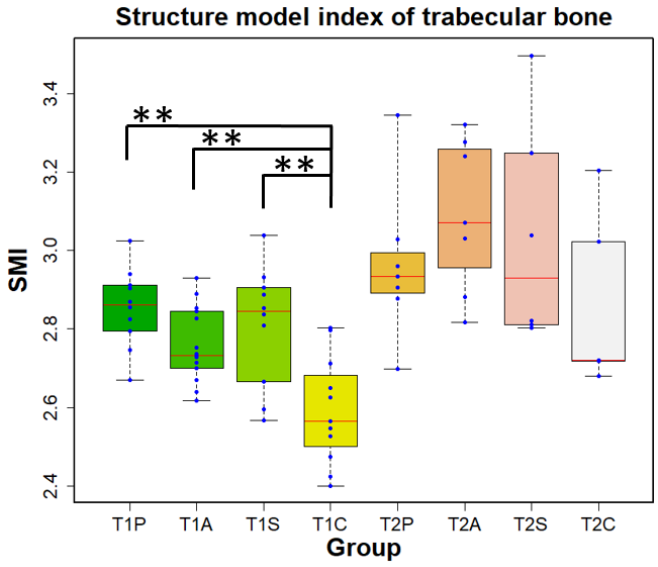

Fig. 7.23 Box plots of structure model index (SMI) for trabecular bone in metaphysis, in the first time point (T1P, T1A, T1S and T1C) and the second time point (T2P, T2A, T2S and T2C). Red line in each box represents the median value for the data set. Asterisk ** denotes statistically significant difference, at p = 0.05 level. All data points (blue) were plotted along with the box plots. (P: Placebo, A: Avastin, S: Sorafenib, C: Combination A and S)

In the first time point, the normal distributions of SMI in each group were verified using the Lilliefors test ($p > 0.05$). Thus, the ANOVA approach was used to test whether there is significant difference among the different groups. It ($p = 0.0001$) shows that there is significant difference for SMI. Thus, we used a post-hoc Tukey's HSD test to identify which group is significantly different from the other. According the results, SMI in T1C is significantly different from T1P ($p = 0.0001$), T1A ($p = 0.0082$) and T1S ($p = 0.0012$), respectively. In the second time point, even though SMI data points in the group of T2C ($p = 0.0619$) is not follow normal distribution at $p = 0.1$ level according to Lilliefors test, the ANOVA test ($p = 0.401$) was still used to show that there is no significant difference among the various groups.

Table 7.10 Statistical tests of SMI for trabecular bone in metaphysis. (Asterisk * indicates acceptably significant difference, at p = 0.1 level. ** denotes statistically significant difference, at p = 0.05 level.)

Groups / Test: p-value	T1 : 8 days after injection of tumor				T2 : 22 days after injection of tumor			
	T1P	T1A	T1S	T1C	T2P	T2A	T2S	T2C
Lilliefors test	0.9904	0.3164	0.319	0.9008	0.3306	0.5121	0.1673	0.0619*
ANOVA test	0.0001**				0.401			
Tukey's HSD test	T1C-T1A : 0.0082** T1P-T1A : 0.2609 T1S-T1A : 0.765 T1P-T1C : 0.0001** T1S-T1C : 0.0012** T1S-T1P : 0.8444				-			

7.5.2.5 *Connectivity density*

Fig. 7.24 shows the box plots of connectivity density (Conn.D) for trabecular bone in metaphysis. The results of statistical tests are shown in Table 7.11. The normal distributions of Conn.D in each group were verified using the Lilliefors test ($p > 0.05$). Thus, the ANOVA approach was used to test whether there is significant difference among the various groups.

In the first time point, the ANOVA test ($p = 0.0001$) shows that there is significant difference for Conn.D. Thus, we used a post-hoc Tukey's HSD test to identify which group is significantly different from the other. According the results, Conn.D in T1C is significantly different from T1P ($p = 0.0001$), T1A ($p = 0.0033$) and T1S ($p = 0.0012$), respectively.

In the second time point, ANOVA test ($p = 0.765$) shows no significant difference for Conn.D of trabecular bone in metaphysis.

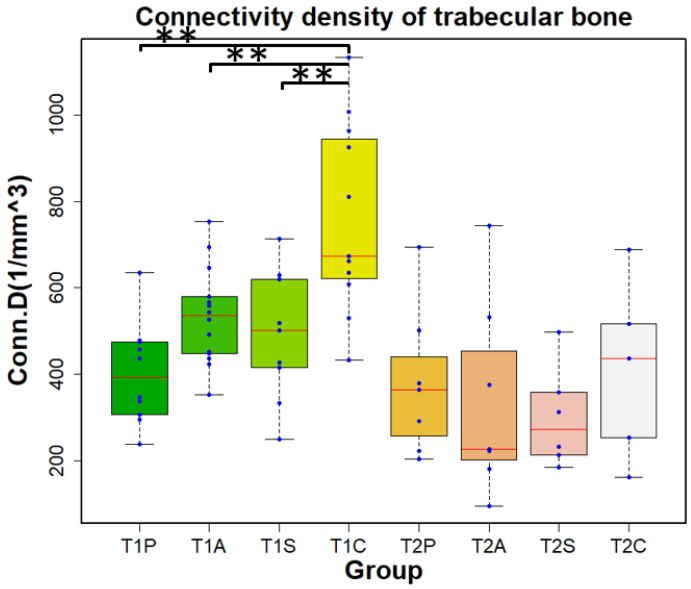

Fig. 7.24 Box plots of connectivity density (Conn.D) for trabecular bone in metaphysis, in the first time point (T1P, T1A, T1S and T1C) and the second time point (T2P, T2A, T2S and T2C). Red line in each box represents the median value for the data set. Asterisk ** denotes statistically significant difference, at p = 0.05 level. All data points (blue) were plotted along with the box plots. (P: Placebo, A: Avastin, S: Sorafenib, C: Combination A and S)

Table 7.11 Statistical tests of Conn.D for trabecular bone in metaphysis. (Asterisk ** denotes statistically significant difference, at p = 0.05 level.)

Groups / Test: p-value	T1 : 8 days after injection of tumor				T2 : 22 days after injection of tumor			
	T1P	T1A	T1S	T1C	T2P	T2A	T2S	T2C
Lilliefors test	0.5254	0.7827	0.9034	0.2451	0.431	0.1535	0.4891	0.8899
ANOVA test	0.0001**				0.765			
Tukey's HSD test	T1C-T1A : 0.0033** T1P-T1A : 0.1684 T1S-T1A : 0.9046 T1P-T1C : 0.0001** T1S-T1C : 0.0012** T1S-T1P : 0.5551				-			

7.5.2.6 Degree of anisotropy

Fig. 7.25 shows the box plots of degree of anisotropy (DA) at the different groups. The results of statistical tests are shown in Table 7.12. The normal distributions of DA in each group were verified using the Lilliefors test ($p > 0.05$). Thus, the ANOVA approach was used to test whether there is significant difference among the different groups.

At the first time point, although ANOVA test ($p = 0.102$) shows no significant difference among various groups, we can still see that DA value is lower in the placebo group than other treatment groups. At the second time point, ANOVA test ($p = 0.514$) shows no significant difference among various groups, for DA of trabecular bone in metaphysis.

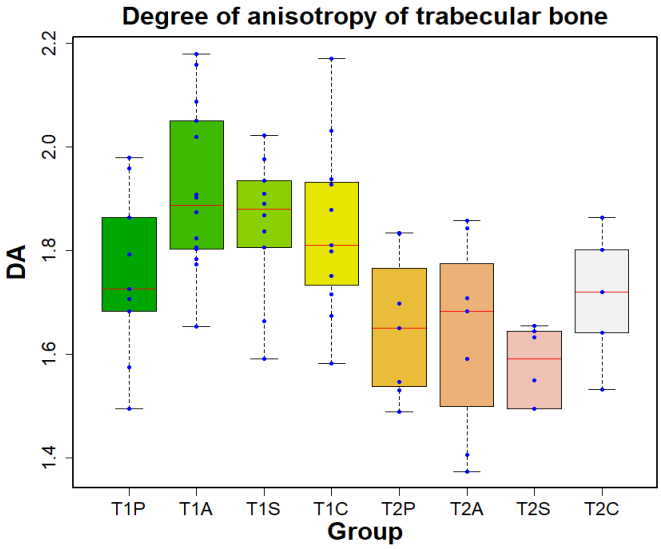

Fig. 7.25 Box plots of degree of anisotropy (DA) for trabecular bone in metaphysis, in the first time point (T1P, T1A, T1S and T1C) and the second time point (T2P, T2A, T2S and T2C). Red line in each box represents the median value for the data set. All data points (blue) were plotted along with the box plots. (P: Placebo, A: Avastin, S: Sorafenib, C: Combination A and S)

Table 7.12 Statistical tests of DA for trabecular bone in metaphysis.

Groups / Test: p-value	T1 : 8 days after injection of tumor				T2 : 22 days after injection of tumor			
	T1P	T1A	T1S	T1C	T2P	T2A	T2S	T2C
Lilliefors test	0.6361	0.4001	0.5739	0.9123	0.504	0.7747	0.1958	0.961
ANOVA test	0.102				0.514			

7.5.3 Cortical porosity in diaphysis

Fig. 7.26 shows the box plots of cortical porosity volume fractions (Ct.Po.V/Ct.TV) in diaphysis at the different groups. The results of statistical tests are shown in Table 7.13. The normal distributions of Ct.Po.V/Ct.TV in each group were verified using the Lilliefors test ($p > 0.05$). Thus, the ANOVA approach was used to test whether there is significant difference among the different groups.

At the first time point, ANOVA test ($p = 0.804$) shows no significant difference among various groups.

At the second time point, Although ANOVA test ($p = 0.132$) shows no significant difference among various groups, the p-value is small and still indicates Ct.Po.V/Ct.TV is lower in the combination group comparing to the placebo group.

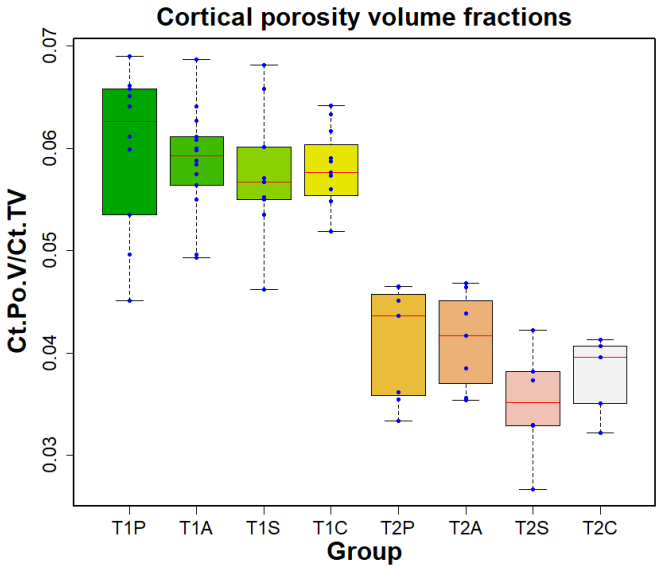

Fig. 7.26 Box plots of cortical porosity volume fractions (Ct.Po.V/Ct.TV) in diaphysis, in the first time point (T1P, T1A, T1S and T1C) and the second time point (T2P, T2A, T2S and T2C). Red line in each box represents the median value for the data set. All data points (blue) were plotted along with the box plots. (P: Placebo, A: Avastin, S: Sorafenib, C: Combination A and S)

Table 7.13 Statistical tests of Ct.Po.V/Ct.TV in diaphysis.

Groups / Test: p-value	T1 : 8 days after injection of tumor				T2 : 22 days after injection of tumor			
	T1P	T1A	T1S	T1C	T2P	T2A	T2S	T2C
Lilliefors test	0.3078	0.8391	0.1756	0.8293	0.2038	0.827	0.7977	0.2333
ANOVA test	0.804				0.132			

7.5.4 Vessels

7.5.4.1 Vessel volume fractions

Fig. 7.27 shows the box plots of vessel volume fractions (VV/TV) at the different groups. The results of statistical tests are shown in Table 7.14. The normal distributions of VV/TV in each group were verified using the Lilliefors test ($p > 0.05$). Thus, the ANOVA approach was used to test whether there is significant difference among the different groups.

At the first time point, ANOVA test ($p = 0.728$) shows no significant difference among various groups.

At the second time point, although ANOVA test ($p = 0.228$) shows no significant difference among various groups, possibly due to the limited sample size, it still indicates that there are less VV/TV in the combination group comparing to the placebo group, due to the anti-angiogenesis drugs, as expected.

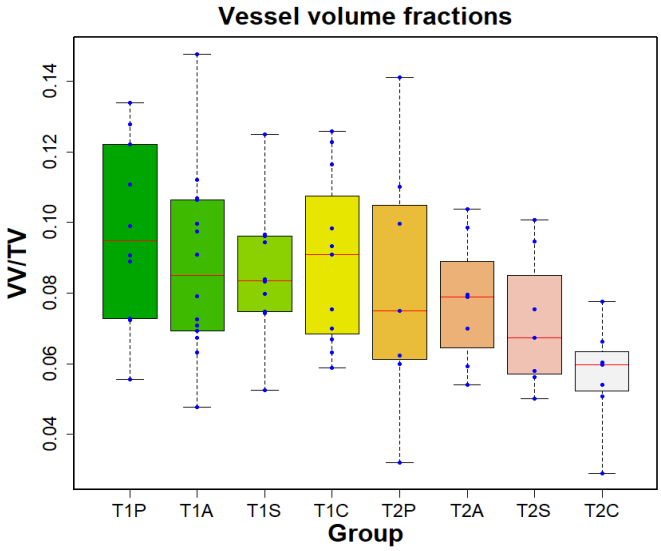

Fig. 7.27 Box plots of vessel volume fractions (VV/TV), in the first time point (T1P, T1A, T1S and T1C) and the second time point (T2P, T2A, T2S and T2C). Red line in each box represents the median value for the data set. All data points (blue) were plotted along with the box plots. (P: Placebo, A: Avastin, S: Sorafenib, C: Combination A and S)

Table 7.14 Statistical tests of VV/TV

Groups / Test: p-value	T1 : 8 days after injection of tumor				T2 : 22 days after injection of tumor			
	T1P	T1A	T1S	T1C	T2P	T2A	T2S	T2C
Lilliefors test	0.9128	0.4962	0.3909	0.5169	0.8611	0.733	0.6312	0.5507
ANOVA test	0.728				0.228			

7.5.4.2 Thickness of vessel

Fig. 7.28 shows the box plots of the thickness of vessel (V.Th) at the different groups. The results of statistical tests are shown in Table 7.15.

In the first time point, although the data points in the group of T1C ($p = 0.0375$) cannot be considered normally distributed at $p = 0.05$ level according to the Lilliefors test, we still used ANOVA test ($p = 0.569$) to show no significant difference among the various groups.

In the second time point, normal distributions of V.Th in each group were verified using the Lilliefors test ($p > 0.05$). Thus, the ANOVA approach was used to test whether there is significant difference among the different groups. Although there is no significant difference in V.Th ($p = 0.0549$), we still consider that there is acceptably significant difference, at $p = 0.1$ level. Then, we used a post-hoc Tukey's HSD test to identify which group is significantly different from the other. According the results, there is acceptably significant difference between T2C and T2S ($p = 0.0652$).

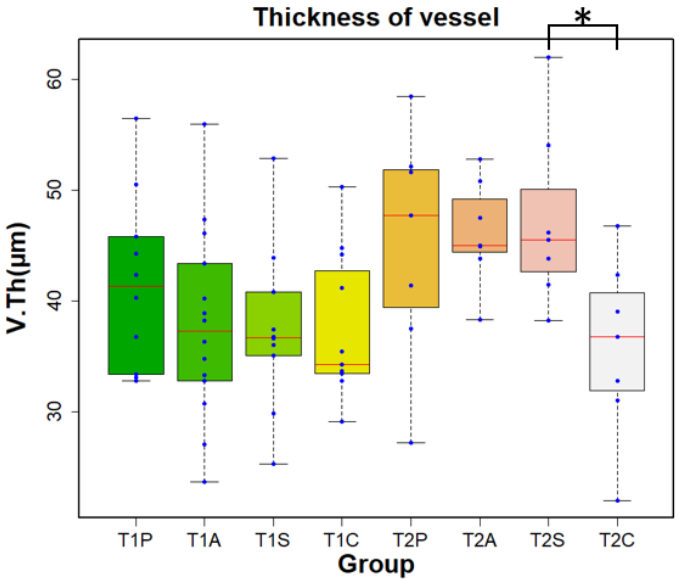

Fig. 7.28 Box plots of the thickness of vessel (V.Th), in the first time point (T1P, T1A, T1S and T1C) and the second time point (T2P, T2A, T2S and T2C). Red line in each box represents the median value for the data set. Asterisk * indicates acceptably significant difference, at p = 0.1 level. All data points (blue) were plotted along with the box plots. (P: Placebo, A: Avastin, S: Sorafenib, C: Combination A and S)

Table 7.15 Statistical tests of V.Th (Asterisk * indicates acceptably significant difference, at p = 0.1 level. ** denotes statistically significant difference, at p = 0.05 level.)

Groups / p-value	T1 : 8 days after injection of tumor				T2 : 22 days after injection of tumor			
	T1P	T1A	T1S	T1C	T2P	T2A	T2S	T2C
Lilliefors test	0.7652	0.9648	0.2927	0.0375**	0.7975	0.7809	0.1227	0.9653
ANOVA test	0.569				0.0549*			
Tukey's HSD test	-				T2C-T2A : 0.1098 T2P-T2A : 0.9952 T2S-T2A : 0.9937 T2P-T2C : 0.1705 T2S-T2C : 0.0652* T2S-T2P : 0.9591			

7.5.4.3 Fractal dimension

Fig. 7.29 shows the box plots of fractal dimension (FD) of vessel at the different groups. The results of statistical tests are shown in Table 7.16. The normal distributions of FD in each group were verified using the Lilliefors test ($p > 0.05$). Thus, the ANOVA approach was used to test whether there is significant difference among the different groups.

There are no significant difference among various groups for FD of vessels, at the first time point (ANOVA test, $p = 0.654$), and at the second time point (ANOVA test, $p = 0.386$).

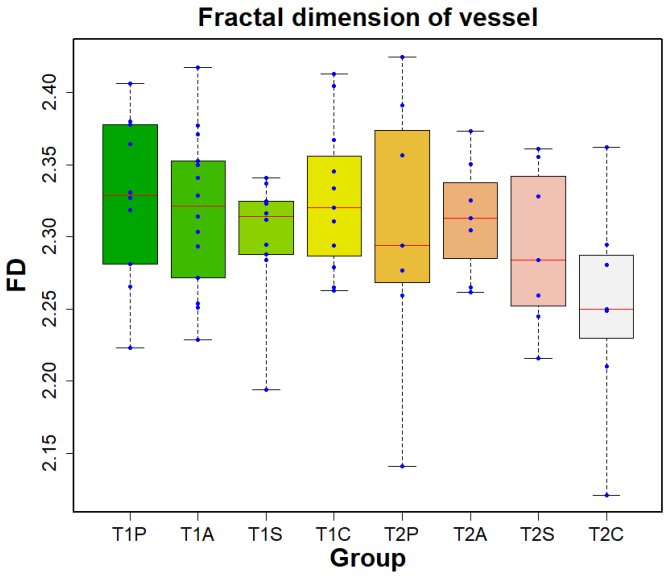

Fig. 7.29 Box plots of the fractal dimension (FD) of vessel, in the first time point (T1P, T1A, T1S and T1C) and the second time point (T2P, T2A, T2S and T2C). Red line in each box represents the median value for the data set. All data points (blue) were plotted along with the box plots. (P: Placebo, A: Avastin, S: Sorafenib, C: Combination A and S)

Table 7.16 Statistical tests of FD of vessel

Groups / Test: p-value	T1 : 8 days after injection of tumor				T2 : 22 days after injection of tumor			
	T1P	T1A	T1S	T1C	T2P	T2A	T2S	T2C
Lilliefors test	0.8331	0.9805	0.1087	0.9549	0.7969	0.817	0.8264	0.5846
ANOVA test	0.654				0.386			

7.5.4.4 Degree of anisotropy

Fig. 7.30 shows the box plots of degree of anisotropy (DA) of vessel at the different groups. The results of statistical tests are shown in Table 7.17.

In the first time point, the DA data points in the group of T1A ($p = 0.0417$) cannot be considered normally distributed at $p = 0.05$ level, and T1C ($p = 0.0721$) is not follow normal distribution at $p = 0.1$ level, according to the Lilliefors test. However, we still used ANOVA test ($p = 0.319$) to show no significant difference among the various groups.

In the second time point, although the data points in the group of T2S ($p = 0.0637$) is not follow normal distribution at $p = 0.1$ level according to the Lilliefors test, the ANOVA test ($p = 0.948$) was still used to show no significant difference among the various groups.

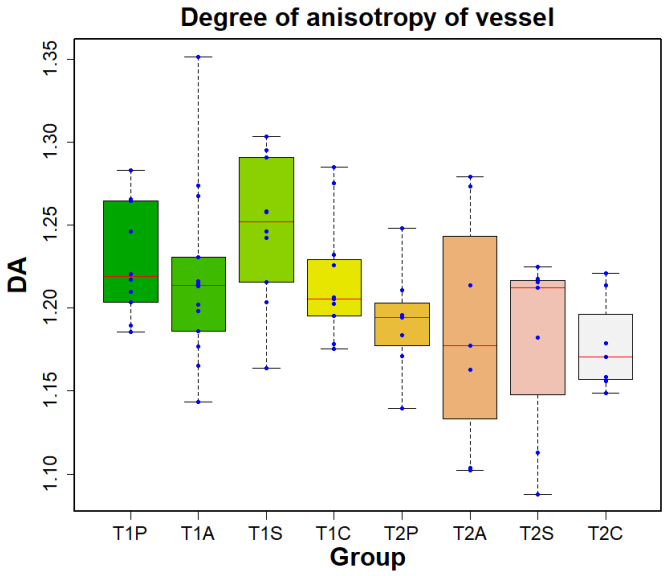

Fig. 7.30 Box plots of the degree of anisotropy (DA) of vessel, in the first time point (T1P, T1A, T1S and T1C) and the second time point (T2P, T2A, T2S and T2C). Red line in each box represents the median value for the data set. All data points (blue) were plotted along with the box plots. (P: Placebo, A: Avastin, S: Sorafenib, C: Combination A and S)

Table 7.17 Statistical tests of DA of vessel. (Asterisk * indicates acceptably significant difference, at p = 0.1 level. ** denotes statistically significant difference, at p = 0.05 level.)

Groups / p-value	T1 : 8 days after injection of tumor				T2 : 22 days after injection of tumor			
	T1P	T1A	T1S	T1C	T2P	T2A	T2S	T2C
Lilliefors test	0.3769	0.0417**	0.7362	0.0721*	0.7929	0.7988	0.0637*	0.5106
ANOVA test	0.319				0.948			

7.6 Discussion

To quantitatively analyze bone and vessels in the preclinical studies, a robust image segmentation approach is a prerequisite. Global thresholding is one of the most common used method, and has been used to segment the bone and vessels in the hind limbs of mice, simultaneously imaged using SR-μCT with a contrast agent (Schneider et al., 2009). However, the segmentation quality can be affected by beam-hardening, artifacts, partial volume effects, and noise on the image. Unlike global thresholding, the method of region growing considers the connectivity of regions making up a vessel tree. In the analysis of bone and vasculature in rat tibia, 3D region growing has been used to segment bone and vessels, imaged by SR-μCT with a contrast agent (Langer et al., 2010; Prisby et al., 2011).

In this thesis, 3D SR-μCT was used to image the bone and vessels in tibia of mice with a contrast agent. However, as opposed to in rat bone, vessels appeared to be in contact with the bone surface in mice. This precluded the correct segmentations of bone and vessels using 3D region growing method. Therefore, we proposed marker-controlled watershed to separate vessels and bone without the need for post-segmentation merging of regions. To initialize the watershed algorithm, markers of bone, vessels and background were generated to achieve

coverage of all connected components in each class and no false positives. In addition, for the generation of control surface, we proposed the use of the monogenic signal phase asymmetry to improve the edge detections at the bone and vessel interfaces, in which contrast was relatively weak compared to the bone-background and the vessel-background interfaces.

The proposed segmentation method, specifically developed and described in the previous chapters could be successfully applied to all the images in the different groups. To process experimental we had however to develop a pre-processing step to re-orientate the various samples in order to get interpretable results. Then a quantitative analysis based on the extraction of a number of parameters and their statistical analysis was realized. Below we analyze the results of the study.

In the boxplots of bone volume fraction (BV/TV Fig. 7.15), cortical bone volume fraction (Ct.V/TV Fig. 7.16) and mean thickness of cortical bone (Ct.Th Fig. 7.19), we discovered that the bone volume, the cortical bone volume were increased from the first time point to the second time point. This is possibly due to the growth of mice bone from the 8th to 22nd days after injection of tumor cells. To have a robust analysis, it is not appropriate to perform the statistical tests at both time points, but at each time point separately. Thus, although we presented the boxplots of various groups in a figure including both time points, we performed the statistical tests at each time point separately for all parameters.

Comparing the boxplots of Ct.V/TV (Fig. 7.16) with BV/TV (Fig. 7.15), we found that the distributions of data points are similar. This is owing to the fact that the cortical bone takes a large proportion of bone. According to the statistical tests for BV/TV (Table 7.3) and Ct.V/TV (Table 7.4), there are no significant differences among the various groups at the second time point. This is inconsistent with the scientific report that the combination treatment reduces bone lesions and results in a significantly higher BV/TV values than single drug treatments and placebo groups (Bachelier et al., 2014).

To further investigate this situation, we studied the effects of drugs on metastases. Here, we manually segmented metastases on cortical bone, and measured metastases volume fraction (Me.V/TV) values of different groups at the second time point. According to the boxplots (Fig. 7.17) and statistical tests (Table 7.5), even though there is no significant difference among various groups for Me.V/TV, possibly due to the limited sample size, the box plots still indicate that there are less metastases in the combination treatment group comparing to in the placebo group.

To quantitatively study the relationship between Me.V/TV and Ct.V/TV, we performed a linear regression on data points at the second time point (Fig. 7.18). The result shows no significant linear correlation between Me.V/TV and Ct.V/TV. Thus, this is inconsistent with our expectation that Me.V/TV is negatively correlated with Ct.V/TV.

In summary, no negatively linear correlation between Me.V/TV and Ct.V/TV indicates that bone metastasis is not the only reason to cause bone loss. Here, we hypothesize that anti-angiogenesis drugs can reduce bone mass by decreasing the thickness of bone, in a long-term interaction.

Therefore, to investigate the effect of drugs on the thickness of cortical bone, we measured the local thickness and calculated the mean as the value of data points (Fig. 7.19). Even though there is no significant difference among various groups for Ct.Th at the second time

point, the box plots still indicate that there are thinner cortical bone in the combination treatment group comparing to in the placebo group. This is possibly caused by the reduction influence of drugs, in a long-term interaction.

Moreover, we studied the effects of anti-angiogenic drugs on trabecular bone. Here, we selected a volume of interest (VOI) at the metaphysis of bone, since trabecular bones mainly locate in this part.

According to the measures on mean thickness of trabecular bone (Tb.Th Fig. 7.21, and Table 7.8), there is no significant difference among various groups at the first time point, but there is an acceptably significant difference at the second time point. In particular, Tb.Th in combination treatment group is lower than in placebo group with an acceptably significant difference, at the second time point. Thus, it indicates that the reduction of thickness by drugs requires a long-term interaction.

As the boxplots (Fig. 7.20) and statistical tests (Table 7.7), the trabecular bone volume fraction (Tb.V/Me.Ca.V) value in the combination treatment group is significantly higher comparing to in other groups, at the first time point. Thus, it indicates that combination treatment reduced bone lesion at the early stage of metastases development, without the effects of the thickness reduction by drugs. Although it has been reported that bone metastases are often developed in 18 days after tumor cell inoculation (Bachelier et al., 2014), it was judged only by radiography that cannot visualize trabeculae inside a bone. Therefore, we infer that metastases have been developed on trabecular bone but not yet on cortical bone, at the early stage of metastases development (8 days after injection of tumor cell). This can be interesting for the prediction of breast cancer bone metastases.

At the second time point, the statistical tests (Table 7.7) show no significant difference among the various groups for Tb.V/Me.Ca.V. Even though, the Tb.V/Me.Ca.V values in the combination treatment group are supposed to be significantly higher than in the placebo group by reducing bone lesions, the drugs reduced bone mass in a long-term interaction resulting in no significant difference among various groups.

For trabecular bone in metaphysis, we also measured fractal dimension (FD), structure model index (SMI), connectivity density (Conn.D) and degree of anisotropy (DA).

According to the boxplots (Fig. 7.22) and statistical tests (Table 7.9) on FD, the values in combination treatment group are significantly higher comparing to in placebo group at the first time point. This indicates that the combination treatment reduced the bone lesions and kept the complete trabecular bone structures (high FD value). At the second time point, although there are supposed to be more complex and complete trabecular bones in the combination treatment group, the drugs reduced bone thickness in a long-term interaction, especially decreased the relatively thin bone until it missing. This results in damaging to structural integrity of trabecular bone, decrease of FD value in combination group, and no significant difference among groups.

As the box plots and statistical tests of SMI (Fig. 7.23 and Table 7.10) for trabecular bone in metaphysis, the SMI value in combination treatment group is significantly lower than in other groups, at the first time point. This indicates that there are more plate-like trabecular bone structures in the combination treatment group, due to the reduced bone lesions by drug treatment. At the second time point, there is no significant difference among the various

groups. Although, there are supposed to be more plate-like trabecular bones in the combination treatment group, the drugs reduced bone thickness in a long-term interaction, and even reduced the thin plate-like structures to disappear. This leads to breaking the plate-like trabecular bone to become more rod-like structures, increasing SMI values in combination treatment group, and no significant difference among groups.

Fig. 7.24 and Table 7.11 respectively show the box plots and statistical tests of Conn.D for trabecular bone in metaphysis. At the first time point, the Conn.D value in combination treatment group is significantly higher than in other groups. This indicates that the combination treatment reduced the bone lesions and preserved more connected trabecular bones. At the second time point, ANOVA test shows no significant difference for Conn.D among the various groups. Although, there are supposed to be more connected trabecular bones in the combination treatment group, the drugs reduced bone thickness and even made the thin bone missing. This results in the decrease of Conn.D value in combination treatment group and leads to no significant difference among various groups.

According to the box plots (Fig. 7.25) and statistical tests (Table 7.12) of DA for trabecular bone in metaphysis, there is no significant difference among the various groups at each time point separately. However, we can still see that DA value is relatively lower in the placebo group than in other treatment groups, at the first time point (ANOVA test, $p = 0.102$). This coincide with the statement that the osteolytic and the structurally disorganized bone has a lower anisotropic comparing to the healthy bone (Cole et al., 2014). At the second time point, long-term interactions with drugs lead to loss of thin bone by the reduction of thickness. This results in the structurally disorganized trabecular bone, a decrease of DA values in the drug treatment groups, and no significant difference among all groups at the second time point (ANOVA test, $p = 0.514$).

About cortical porosity volume fraction (Ct.Po.V/Ct.TV) in diaphysis, we assumed that the porosities on cortical bone are microvasculature canals. As the box plots and statistical tests of Ct.Po.V/Ct.TV (Fig. 7.26 and Table 7.13), there is no significant difference among the various groups at the first time point (ANOVA test, $p = 0.804$), since the abnormal vasculatures on cortical bone have not developed yet. At the second time point, although there is no significant difference among the various groups, we still can see that the values of Ct.Po.V/Ct.TV in combination treatment group is lower comparing to in placebo group (ANOVA test, $p = 0.132$). It means that the porosities as microvasculature canals were reduced with the suppressing on vessel by the anti-angiogenesis drugs. Moreover, we have to consider the influence of reduction on bone thickness by long-term interaction with drugs, since it can extend the size of porosity. For instance, $p = 0.132$ can be smaller and even be significant, if no reduction of bone thickness by drugs.

Apart from parameters on bone, we also extracted several parameters from vessel segmentations, such as vessel volume fraction (VV/TV), mean thickness of vessel (V.Th), FD, DA.

Fig. 7.27 shows the box plots of VV/TV, and Table 7.14 presents the results of statistical tests. At the first time point, there is no significant difference among various groups, since it is still at the early stage of bone metastases and anti-angiogenesis drugs have not suppressed the abnormal vasculatures yet. At the second time point, although ANOVA test ($p = 0.228$)

shows no significant difference among various groups, possibly due to the limited sample size, it still indicates that there are less VV/TV in the combination treatment group comparing to in the placebo group, due to the anti-angiogenesis drugs, as expected.

According to the box plots (Fig. 7.28) and statistical tests (Table 7.15) of V.Th, there is no significant difference among various groups at the first time point, since it is still at the early stage of development. At the second time point, the V.Th value in the combination treatment group is lower than in other groups with an acceptably significant difference ($p = 0.0652$). This is consistent with the hypothesis that the combination treatment decreases the thickness of vessel comparing to in the placebo group.

As the boxplots (Fig. 7.29) and statistical tests (Table 7.16) of FD for vessel, there is no significant difference among various groups at the first time point. At the second time point, although there is no significant difference among various groups, it still indicates that vessels are less complex in the combination treatment group comparing to in the placebo group, due to the anti-angiogenesis drugs.

Fig. 7.30 shows the box plots of DA for vessels, and Table 7.17 presents the results of statistical tests. According to statistical tests, there is no significant difference among various groups at the first or second time point. It means that the anti-angiogenesis drugs do not affect the orientations of vessels.

7.7 Conclusion

In this study, the kinetics of bone and vascularization response to the anti-angiogenesis drugs were investigated. Firstly, 3D SR-μCT was used to image bone and vessels of mice with contrast agent. Then, the acquired 3D images were segmented into vessels, bone and background compartments using the marker-controlled watershed algorithm in conjunction with the monogenic signal phase asymmetry. To quantitatively analyze vessels and bone among various groups, several parameters were extracted. Finally, statistical analysis was performed with appropriate tests.

Considering BV/TV, Ct.V/TV, Me.V/TV, Ct.Th, Tb.V/Me.Ca.V and Tb.Th, we infer that metastases have developed on trabecular bone, but not yet on cortical bone at the first time point. In addition, it may indicate that anti-angiogenesis drugs can reduce bone mass by reducing the thickness of bone, in a long-term interactions. At the second time point, although metastases have developed on both trabecular and cortical bone, reducing bone lesions and decreasing bone thickness by drugs happened to a sample at the same time, leading to no significant difference among various groups for bone volume fraction.

Regarding the FD, SMI, Conn.D, and DA for trabecular bone in metaphysis, the measures may indicate the existence of metastases at the first time point. Moreover, long-term interactions with drugs may lead to the loss of thin bone by reduction of thickness, and further affect the morphological structures of trabecular bone at the second time point. This results in no significant difference among various groups for these parameters.

About Ct.Po.V/Ct.TV, we assumed that the porosities on cortical bone are microvasculature canals. At the first time point, according to the measures and statistical tests, there is no significant difference among various groups for Ct.Po.V/Ct.TV, since the abnormal vasculatures have not developed yet. At the late stage of bone metastases, we infer that the

porosities can be reduced with the suppressing on vessel by the anti-angiogenesis drugs. Moreover, we need to consider the influence of reduction on bone thickness by long-term interaction with drugs, since it can extend the size of porosity and result in no significant difference among various groups.

Considering parameters of VV/TV, V.Th, FD, DA for vessels, there is no significant difference among various groups at the first time point, since it is still at the early stage of bone metastases and anti-angiogenesis drugs have not suppressed the abnormal vasculatures yet. At the second time point, it indicates that there are less, thinner and simpler vessels in the combination treatment group comparing to in other groups, as expected. Regarding DA, there is no significant difference among various groups at the second time point. This means that anti-angiogenesis drugs do not affect the orientations of vessels.

Chapter 8

8. Conclusion and perspective

Breast cancer bone metastasis is common and dangerous in women. It can not only facilitate the undesirable vascularization but also damage bone. However, the kinetics of bone vascularization response to tumor invasion and treatment are still partially understood. The aim of this thesis was to develop a new method to analyze bone and vessels in SR-µCT images, and that this was applied to a study of metastasis in mouse tibiae. To segment vessels and bone in mouse tibia imaged using SR-µCT with a contrast agent, we proposed an algorithm based on marker-controlled watershed in conjunction with the monogenic signal phase asymmetry. The segmentation quality was evaluated using the Dice coefficient and the Matthews correlation coefficient (MCC) by comparing to manual segmentation. Additionally, the accuracy and robustness of the proposed method were evaluated on a series of synthetic volumes generated to mimic the real vessel, bone and background structures. The simulation study indicates that the algorithm is performant in other multi-class segmentation problems. For the purpose of quantitatively analyzing vessels and bone in the real data sets, several parameters were extracted to characterize bone microstructures and vasculatures. Then, statistical analysis was performed with appropriate tests to gains a better understanding of bone and vessels in bone metastatic processes.

The image segmentation in our study is difficult, not only due to the complexity of the vascular network, but also due to the lack of diffusion of the contrast agent at some location. In addition, we addressed the problem of the structures not being spatially separate, which makes previous region growing based protocol non-applicable. Specifically, the marker based watershed was selected explicitly to find the intersections between the two structures, not to avoid merging of regions, since the structures can be relatively reliably separated by hysteresis thresholding to generate seeds. On the other hand, although the control surface for the watershed is often generated by the magnitude of the gradient, the contrasts between bone and vessels are relatively weak leading to weak edge detections at these boundaries. Therefore, we chose to use the phase asymmetry of monogenic signal, which is invariant to signal amplitude, to generate control surface.

To examine the accuracy and robustness of the method, as well as its generalization to other applications, we created 3D synthetic models to simulate real dataset. Firstly, we considered different contrasts and noise levels to investigate their impacts on the segmentations. A series of multi-class synthetic volumes were segmented using the proposed method, and the overall segmentation quality was evaluated using the MCC by comparing to the ground truth. The results indicate that the protocol works best around 50% contrast, or slightly more, of the intermediate class relative to the maximum amplitude (255 in 8 bit), in the three-class model. In addition, it seems that noise prevents thin structure segmentation. To investigate this problem, we studied the capability of thin structure segmentation with the proposed method,

under a various levels of Gaussian noise. The results show that thin structures (thickness of 3 to 9 voxels) can be well segmented at noise levels (standard deviation of Gaussian noise) of less than 20, and thick structures (thickness of 10 voxels or more) can be well segmented even at the noise level of 60 using the proposed method. Therefore, as the evaluations of segmentations under various contrasts and noise levels as well as on thin structures, the proposed method can support the broad applications.

We applied the proposed method to the real dataset of mouse bone acquired using SR-μCT with a contrast agent. The segmentation quality was evaluated using the Dice and the MCC by comparing to manual segmentation. The results show substantial improvements at each single compartment segmentation (Dice) and overall segmentation (MCC) using the proposed method, compared to the hysteresis thresholding based method as well as to the gradient based marker-controlled watershed.

In addition, to quantitatively analyze bone microstructures and vasculatures in a mouse model, several parameters were extracted from the whole bone sample (BV/TV, Ct.V/TV, Me.V/TV, Ct.Th), trabecular bone in metaphysis (Tb.V/Me.Ca.V, Tb.Th, FD, SMI, Conn.D, DA), cortical porosity in diaphysis (Ct.Po.V/Ct.TV) and vessels (VV/TV, V.Th, FD, DA).

Considering BV/TV, Ct.V/TV, Me.V/TV, Ct.Th, Tb.V/Me.Ca.V and Tb.Th, we hypothesize that metastases have developed on trabecular bone, but not yet on cortical bone at the first time point. In addition, we conclude that anti-angiogenesis drugs can decrease bone mass by reducing the thickness of bone, in a long-term interactions. At the second time point, although metastases have developed on both trabecular and cortical bone, reducing bone lesions and decreasing bone thickness by drugs happened to a sample at the same time, leading to no significant difference among various groups for bone volume fraction.

Regarding the FD, SMI, Conn.D, and DA for trabecular bone in metaphysis, the measures also indicate the existence of metastases at the first time point. Moreover, long-term interactions with drugs lead to the loss of thin bone by reducing the thickness, and further affect the morphological structures of trabecular bone at the second time point. This results in no significant difference among various groups for these parameters.

About Ct.Po.V/Ct.TV, we assumed that the porosities on cortical bone are microvasculature canals. At the first time point, according to the measures and statistical tests, there is no significant difference among various groups for Ct.Po.V/Ct.TV, since the abnormal vasculatures have not developed yet. At the second time point, the cortical porosity is reduced in combination treatment group. This might be due to the anti-angiogenic drugs reducing the cortical vascularization. Moreover, we need to consider the influence of reduction on bone thickness by long-term interaction with drugs, since it can extend the size of porosity and result in no significant difference among various groups.

Considering parameters of VV/TV, V.Th, FD, DA for vessels, there is no significant difference among various groups at the first time point. This might be due to that it is still at the early stage of bone metastases and anti-angiogenesis drugs have not suppressed the abnormal vasculatures yet. At the second time point, it indicates that there are less, thinner and less complex vessels in the combination treatment group comparing to in other groups, as expected. Regarding DA, there is no significant difference among various groups at the

second time point. This means that anti-angiogenesis drugs do not affect the orientations of vessels.

In this work, we achieved the observation and quantification of the vessels and bone in mouse tibia using SR-μCT with a contrast agent. All our quantitative results are expected to help understand the kinetics of bone and vascularization response to the anti-angiogenesis drugs for breast cancer bone metastases.

Concerning our contributions in the characterization of vessels, the parameters were quite mature and can be used in further biological studies. However, many further developments can be pursued regarding to the properties of vessel structures. Particularly, approaches based on skeletonization can be used to retrieve the morphological parameters of vessel networks, such as the number of junctions, average branch length and the tortuosity between two junctions in tree structures. In addition, the most promising seems to be presenting the results as descriptive statistics, and searching for further metastasis study. Moreover, since accurate morphological analysis is the aim, special attention will be given to connectivity-preserving methods, for example minimum cost paths and geodesic voting. Finally, the proposed protocol in this thesis can be applied to other data sets and anatomical locations. CNN based methods can also be explored to apply to segmenting vessels and bone in our data sets.

Annex 1

In this annex, we attached all 70 results of pre-processing (the frontal planes, the 2D slices of 3D volume). For the sample preparation, female mice were injected with breast cancer tumor cells and the preventive treatments with anti-angiogenic drugs. The mice were divided into four treatment groups: placebo, Avastin, Sorafenib, and combination drugs treatment including both Sorafenib and Avastin. In addition, we considered two time points: at 8 and 22 days after the injection of tumor cells. Thus, there were 8 groups in total. In addition, all samples were injected with contrast agent (barium sulfate) for the vascular imaging. Therefore, the bright structures in the figures below indicate vessels, the gray structures indicate bone tissue, and the black is background.

Placebo, Time point 1 (8 days after):

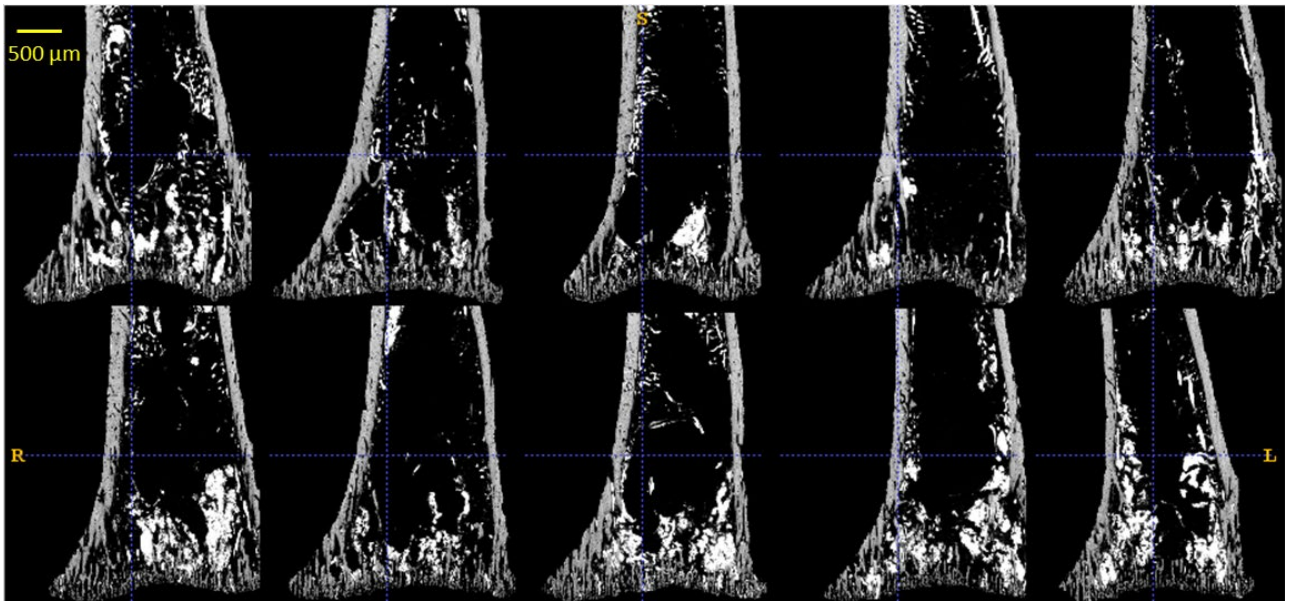

Avastin, Time point 1 (8 days after)

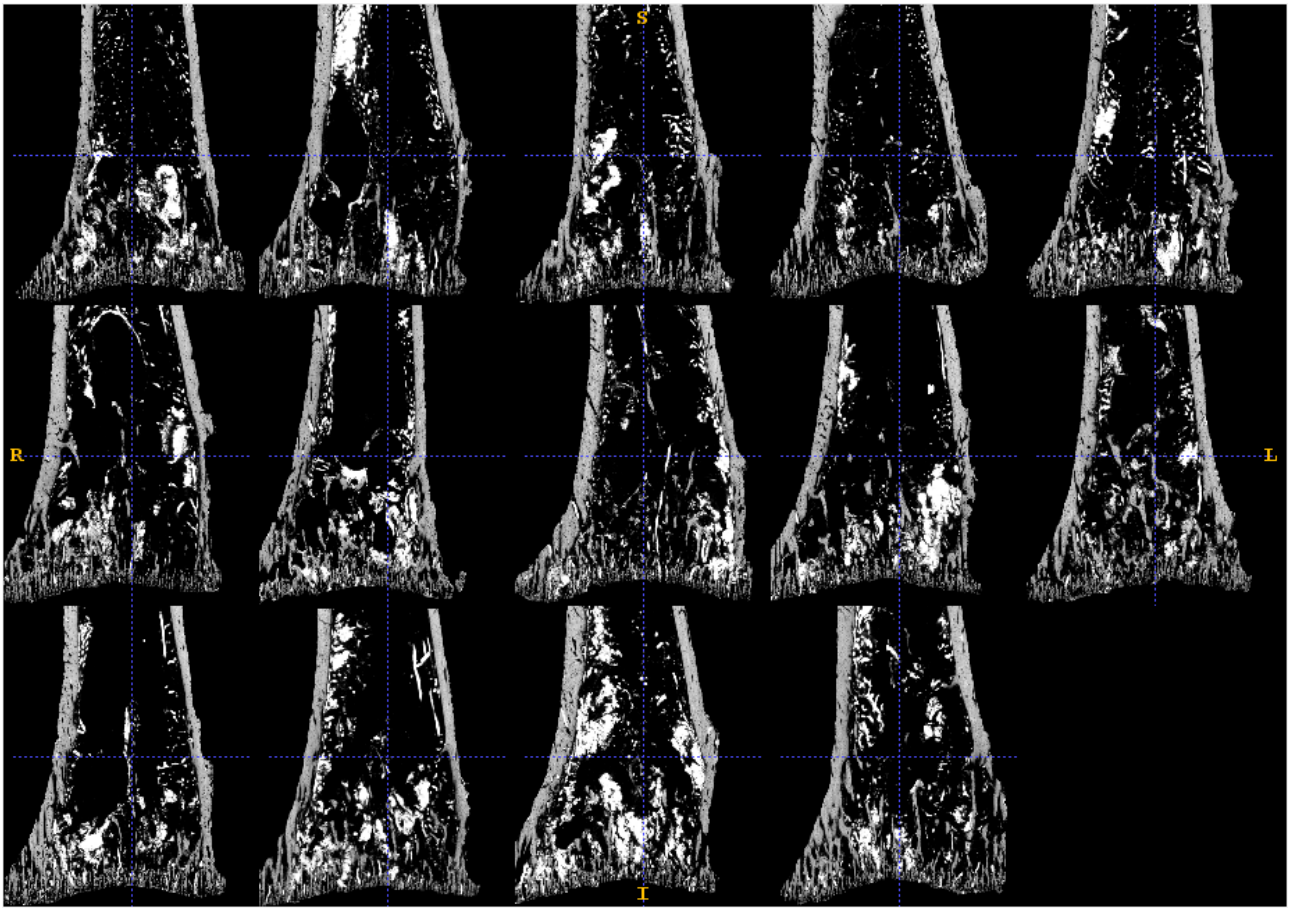

Sorafenib, Time point 1 (8 days after)

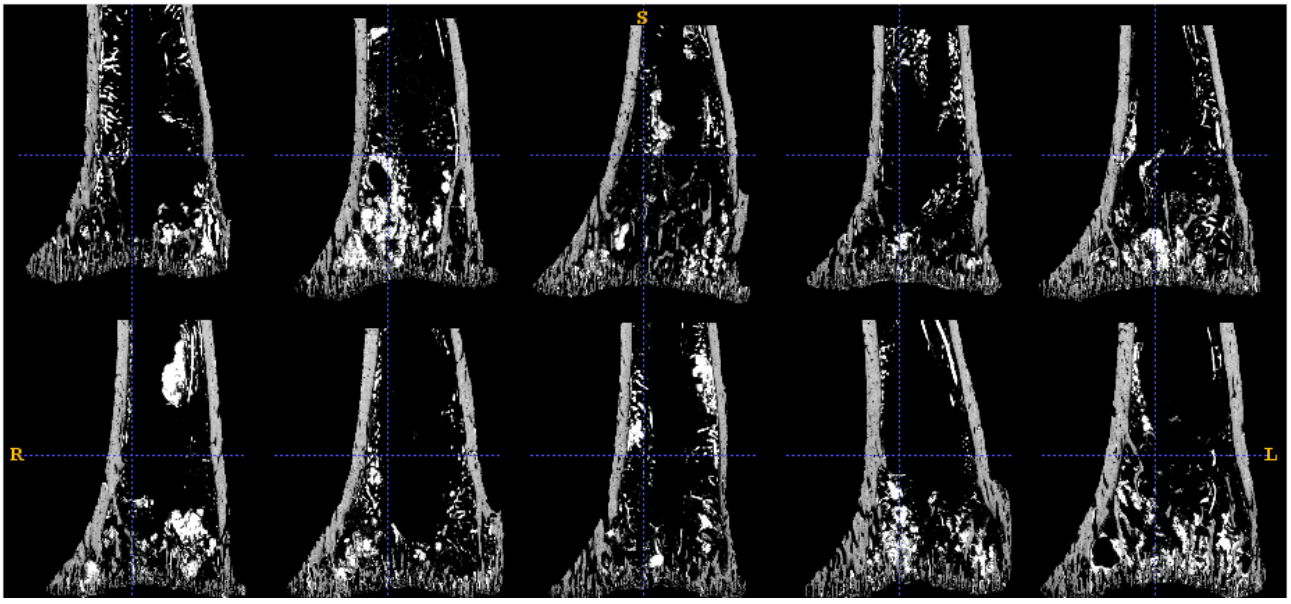

Combination drugs treatment (Sorafenib + Avastin), Time point 1 (8 days after)

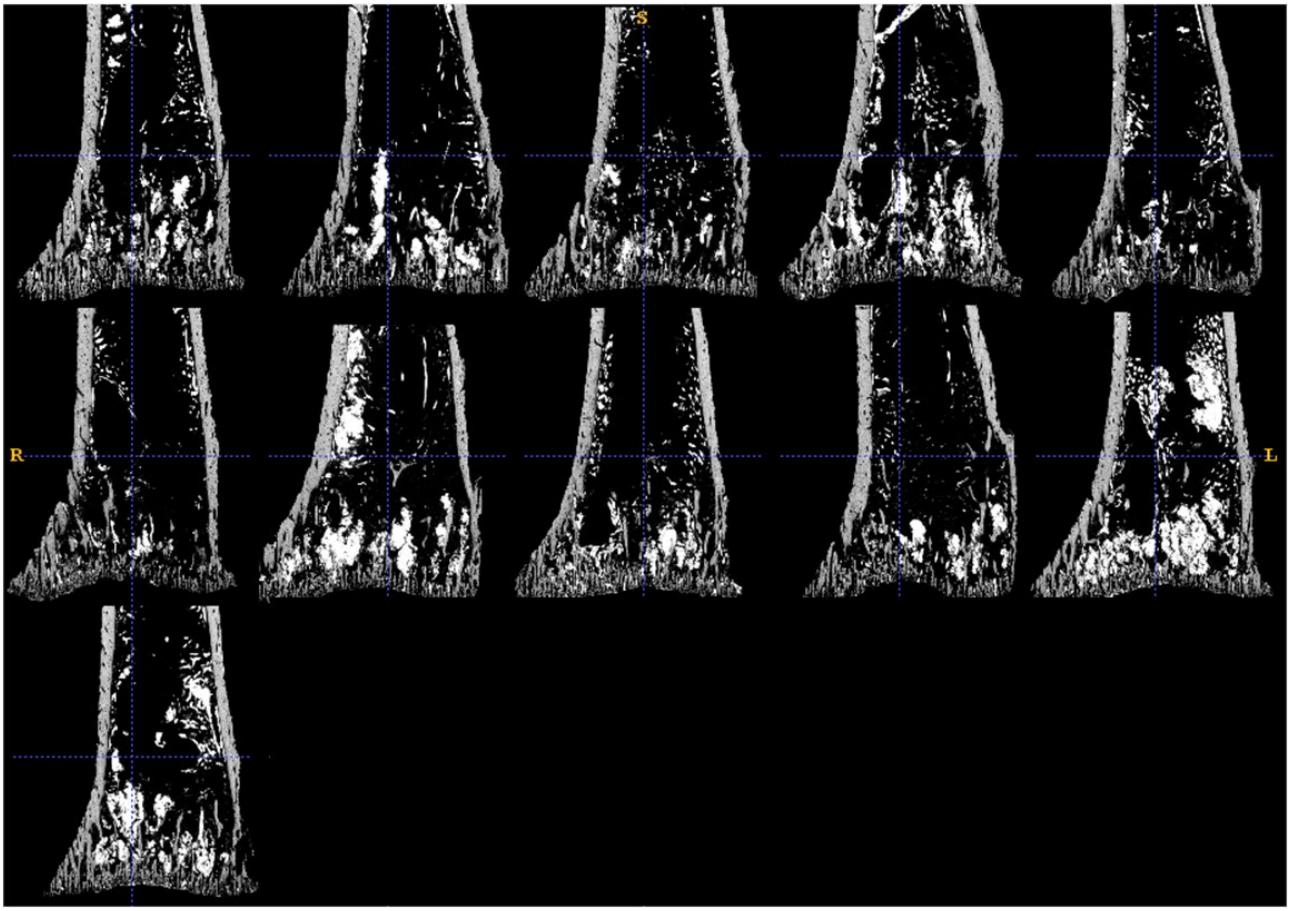

Placebo, Time point 2 (22 days after)

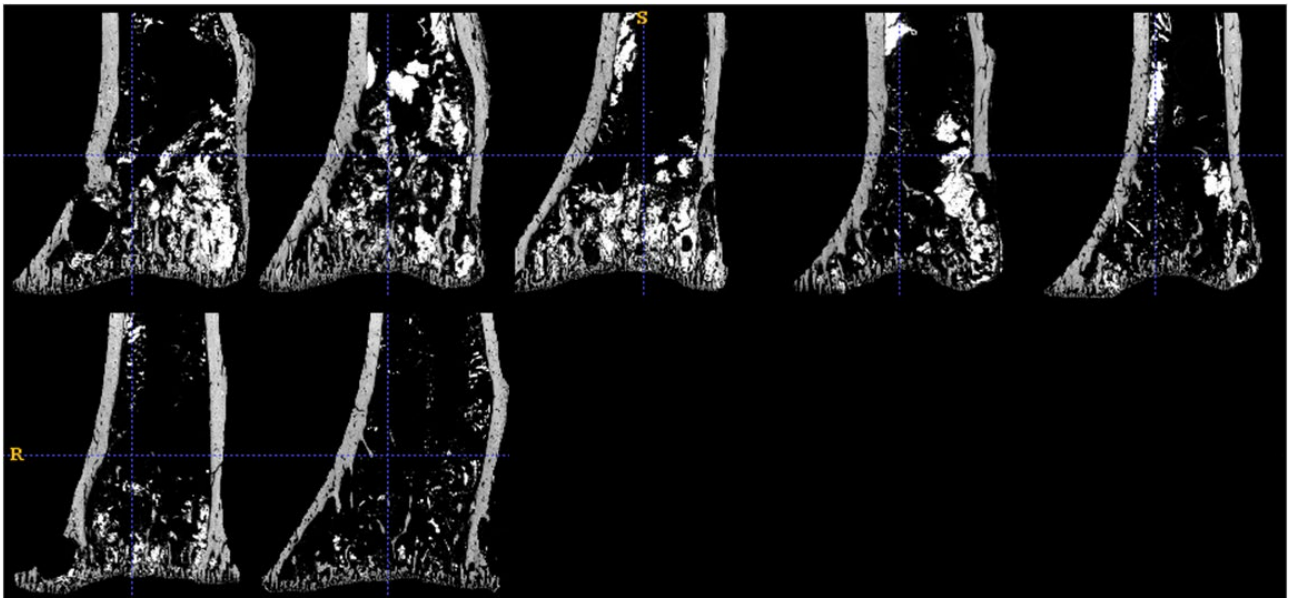

Avastin, Time point 2 (22 days after)

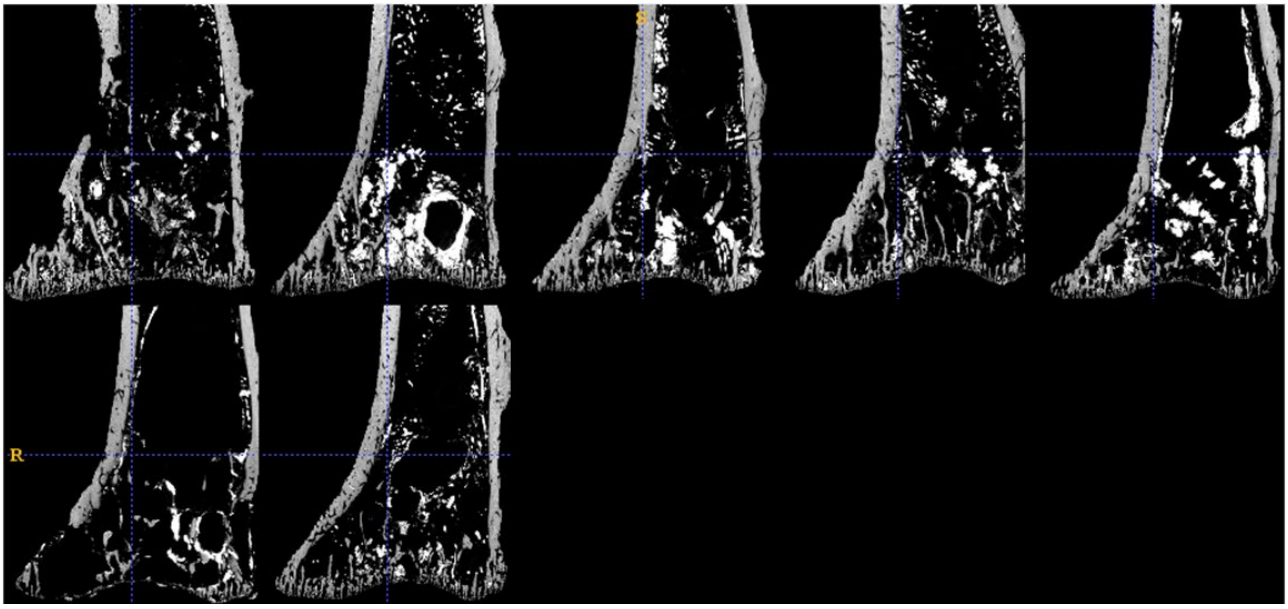

Sorafenib, Time point 2 (22 days after)

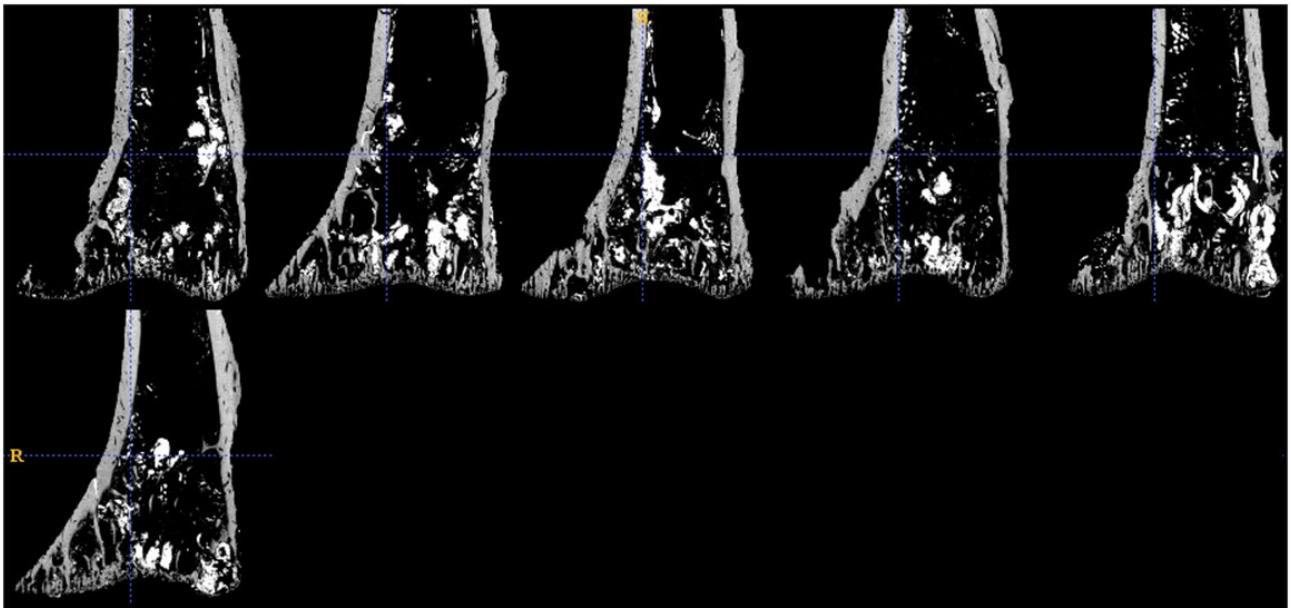

Combination drugs treatment (Sorafenib + Avastin), Time point 2 (22 days after)

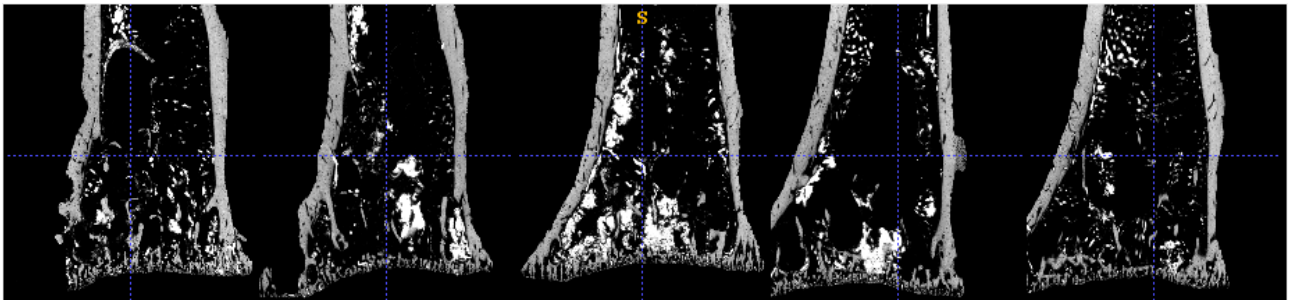

PUBLICATIONS

Journal article

[1] Xu, Hao, Max Langer, and Françoise Peyrin. " Quantitative Analysis of 3D SR-μCT Bone vasculature in Breast Cancer Bone Metastasis Using the Monogenic Signal Phase Asymmetry and Watershed", PMB. (Accepted)

Conference paper

[2] Xu, H., Langer, M. and Peyrin, F., 2020, April. Segmentation of Bone Vessels in 3D Micro-CT Images Using the Monogenic Signal Phase and Watershed. In 2020 IEEE 17th International Symposium on Biomedical Imaging (ISBI) (pp. 741-744). IEEE.

Conferences abstract

[3] Xu, Hao, Max Langer, and Françoise Peyrin. Segmentation of bone microvasculature in breast cancer bone metastases, The IEEE International Symposium on Biomedical Imaging (ISBI), Venice, 2019.

[4] Xu, Hao, Max Langer, and Françoise Peyrin. Engineering small vessels and micro-vascularisation for 3D models and regenerative medicine, GDR-SFA symposium, Paris, 2019.

[5] Xu, Hao, Max Langer, and Françoise Peyrin. Segmentation d' images biomédicales: quels outils pour l'analyse des données massives, hétérogènes et multimodales. GDR ISIS symposium, Paris, 2018.

BIBLIOGRAPHY

Aaron, C. *et al.* (2020) 'Evaluating White Matter Lesion Segmentations with Refined Sørensen-Dice Analysis', *Scientific Reports (Nature Publisher Group)*, 10(1).

Adams, J. E. (2009) 'Quantitative computed tomography', *European journal of radiology*, 71(3), pp. 415–424.

Akhtari, M. *et al.* (2008) 'Biology of breast cancer bone metastasis', *Cancer biology & therapy*, 7(1), pp. 3–9.

Alagiakrishnan, K. *et al.* (2003) 'Role of vascular factors in osteoporosis', *The Journals of Gerontology Series A: Biological Sciences and Medical Sciences*, 58(4), pp. M362–M366.

Alberich-Bayarri, A. *et al.* (2010) 'Assessment of 2D and 3D fractal dimension measurements of trabecular bone from high-spatial resolution magnetic resonance images at 3 T', *Medical Physics*, 37(9), pp. 4930–4937.

Allocca, G. *et al.* (2019) 'The bone metastasis niche in breast cancer: potential overlap with the haematopoietic stem cell niche in vivo', *Journal of Bone Oncology*, 17, p. 100244.

An, Y. H. and Martin, K. L. (2003) *Handbook of histology methods for bone and cartilage*. Springer.

Apostol, L. *et al.* (2006) 'Relevance of 2D radiographic texture analysis for the assessment of 3D bone micro-architecture', *Medical physics*, 33(9), pp. 3546–3556.

Arnold, E. L. *et al.* (2020) 'The use of μCT and fractal dimension for fracture prediction in osteoporotic individuals', *Journal of the Mechanical Behavior of Biomedical Materials*, 103, p. 103585.

Bachelier, R. *et al.* (2014) 'Combination of anti-angiogenic therapies reduces osteolysis and tumor burden in experimental breast cancer bone metastasis', *International journal of cancer*, 135(6), pp. 1319–1329.

Badea, C. T. *et al.* (2008) 'In vivo small-animal imaging using micro-CT and digital subtraction angiography', *Physics in Medicine & Biology*, 53(19), p. R319.

Barzilay, J. I. *et al.* (2016) 'Systemic markers of microvascular disease and bone mineral density in older adults', *Osteoporosis International*, 27(11), pp. 3217–3225.

Bekkar, M., Djemaa, H. K. and Alitouche, T. A. (2013) 'Evaluation measures for models assessment over imbalanced data sets', *J Inf Eng Appl*, 3(10).

Benhamou, C. L. *et al.* (1994) 'Fractal organization of trabecular bone images on calcaneus radiographs', *Journal of bone and mineral research*, 9(12), pp. 1909–1918.

Beucher, S. and Meyer, F. (1990) *Morphological segmentation*. Academic Press.

Bhabatosh, C. (2011) *Digital image processing and analysis*. PHI Learning Pvt. Ltd.

Bonnassie, A., Peyrin, F. and Attali, D. (2003) 'A new method for analyzing local shape in three-dimensional images based on medial axis transformation', *IEEE Transactions on Systems, Man, and Cybernetics, Part B (Cybernetics)*, 33(4), pp. 700–705.

Boucharaba, A. *et al.* (2004) 'Platelet-derived lysophosphatidic acid supports the progression of osteolytic bone metastases in breast cancer', *The Journal of clinical investigation*, 114(12), pp. 1714–1725.

Bousson, V. *et al.* (2004) 'Cortical bone in the human femoral neck: three-dimensional appearance and porosity using synchrotron radiation', *Journal of Bone and Mineral Research*, 19(5), pp. 794–801.

Boutroy, S. *et al.* (2005) 'In vivo assessment of trabecular bone microarchitecture by high-resolution peripheral quantitative computed tomography', *The Journal of Clinical Endocrinology & Metabolism*, 90(12), pp. 6508–6515.

Bouxsein, M. L. *et al.* (2010) 'Guidelines for assessment of bone microstructure in rodents using micro–computed tomography', *Journal of bone and mineral research*, 25(7), pp. 1468–1486.

Bray, F. *et al.* (2018) 'Global cancer statistics 2018: GLOBOCAN estimates of incidence and mortality worldwide for 36 cancers in 185 countries', *CA: a cancer journal for clinicians*, 68(6), pp. 394–424.

Bridge, C. P. (2017) 'Introduction to the monogenic signal', *arXiv preprint arXiv:1703.09199*.

Carmeliet, P. (2003) 'Angiogenesis in health and disease', *Nature medicine*, 9(6), pp. 653–660.

Catarina, P. *et al.* (2017) 'Bone metastasis risk factors in breast cancer', *ecancermedicalscience*, 11.

Cengiz, I. F., Oliveira, J. M. and Reis, R. L. (2018) 'Micro-CT–a digital 3D microstructural voyage into scaffolds: a systematic review of the reported methods and results', *Biomaterials research*, 22(1), p. 26.

Chan, T. F. and Vese, L. A. (2001) 'Active contours without edges', *IEEE Transactions on image processing*, 10(2), pp. 266–277.

Chenouard, N. and Unser, M. (2012) '3D steerable wavelets in practice', *IEEE Transactions on Image Processing*, 21(11), pp. 4522–4533.

Chicco, D. (2017) 'Ten quick tips for machine learning in computational biology', *BioData mining*, 10(1), pp. 1–17.

Chicco, D. and Jurman, G. (2020) 'The advantages of the Matthews correlation coefficient (MCC) over F1 score and accuracy in binary classification evaluation', *BMC genomics*, 21(1), p. 6.

Chinander, M. R. *et al.* (1999) 'Computerized radiographic texture measures for characterizing bone strength: a simulated clinical setup using femoral neck specimens', *Medical physics*, 26(11), pp. 2295–2300.

Christiansen, B. A. (2016) 'Effect of micro-computed tomography voxel size and segmentation method on trabecular bone microstructure measures in mice', *Bone reports*, 5, pp. 136–140.

Cole, H. A. *et al.* (2014) 'Micro-computed tomography derived anisotropy detects tumor provoked deviations in bone in an orthotopic osteosarcoma murine model', *PloS one*, 9(6), p. e97381.

Coleman, M. N. and Colbert, M. W. (2007) 'CT thresholding protocols for taking measurements on three-dimensional models', *American Journal of Physical Anthropology*, 133(1), pp. 723–725.

Colnot, C. (2009) 'Skeletal cell fate decisions within periosteum and bone marrow during bone regeneration', *Journal of Bone and Mineral Research*, 24(2), pp. 274–282.

Cooper, D. M. *et al.* (2003) 'Quantitative 3D analysis of the canal network in cortical bone by micro-computed tomography', *The Anatomical Record Part B: The New Anatomist: An Official Publication of the American Association of Anatomists*, 274(1), pp. 169–179.

Coutel, X. *et al.* (2018) 'A novel microCT method for bone and marrow adipose tissue alignment identifies key differences between mandible and tibia in rats', *Calcified tissue international*, 103(2), pp. 189–197.

Delgado, R. and Núñez-González, J. D. (2019) 'Enhancing Confusion Entropy (CEN) for binary and multiclass classification', *PloS one*, 14(1), p. e0210264.

Depyperre, M. (2013) 'MicroCT imaging of bone architecture and vasculature', *Faculty of Engineering Science, Katholieke Universiteit Leuven, Leuven, Belgium*.

Ding, M., Odgaard, A. and Hvid, I. (1999) 'Accuracy of cancellous bone volume fraction measured by micro-CT scanning', *Journal of biomechanics*, 32(3), pp. 323–326.

Dufresne, T. (1998) 'Segmentation techniques for analysis of bone by three-dimensional computed tomographic imaging', *Technology and Health Care*, 6(5–6), pp. 351–359.

Duvall, C. L. *et al.* (2004) 'Quantitative microcomputed tomography analysis of collateral vessel development after ischemic injury', *American Journal of Physiology-Heart and Circulatory Physiology*, 287(1), pp. H302–H310.

Ebos, J. M. and Kerbel, R. S. (2011) 'Antiangiogenic therapy: impact on invasion, disease progression, and metastasis', *Nature reviews Clinical oncology*, 8(4), pp. 210–221.

Eliaz, N. and Metoki, N. (2017) 'Calcium phosphate bioceramics: a review of their history, structure, properties, coating technologies and biomedical applications', *Materials*, 10(4), p. 334.

Erdt, M., Steger, S. and Sakas, G. (2012) 'Regmentation: A new view of image segmentation and registration', *Journal of Radiation Oncology Informatics*, 4(1), pp. 1–23.

Fajardo, R. J. *et al.* (2007) 'Nonhuman anthropoid primate femoral neck trabecular architecture and its relationship to locomotor mode', *The Anatomical Record: Advances in Integrative Anatomy and Evolutionary Biology: Advances in Integrative Anatomy and Evolutionary Biology*, 290(4), pp. 422–436.

Fajardo, R. J., Ryan, T. M. and Kappelman, J. (2002) 'Assessing the accuracy of high-resolution X-ray computed tomography of primate trabecular bone by comparisons with histological sections', *American Journal of Physical Anthropology: The Official Publication of the American Association of Physical Anthropologists*, 118(1), pp. 1–10.

Fei, J. *et al.* (2010) 'Imaging and quantitative assessment of long bone vascularization in the adult rat using microcomputed tomography', *The Anatomical Record: Advances in Integrative Anatomy and Evolutionary Biology*, 293(2), pp. 215–224.

Feldkamp, L. A. *et al.* (1989) 'The direct examination of three-dimensional bone architecture in vitro by computed tomography', *Journal of bone and mineral research*, 4(1), pp. 3–11.

Felsberg, M. and Sommer, G. (2001) 'The monogenic signal', *IEEE transactions on signal processing*, 49(12), pp. 3136–3144.

Figueiredo, C. P. *et al.* (2018) 'Methods for segmentation of rheumatoid arthritis bone erosions in high-resolution peripheral quantitative computed tomography (HR-pQCT)', in *Seminars in arthritis and rheumatism*. Elsevier, pp. 611–618.

Filipowska, J. *et al.* (2017) 'The role of vasculature in bone development, regeneration and proper systemic functioning', *Angiogenesis*, 20(3), pp. 291–302.

Findlay, D. M. (2007) *Vascular pathology and osteoarthritis*. Oxford University Press.

Flynn, M. J. *et al.* (1994) 'Microfocus x-ray sources for 3D microtomography', *Nuclear Instruments and Methods in Physics Research Section A: Accelerators, Spectrometers, Detectors and Associated Equipment*, 353(1–3), pp. 312–315.

Fohst, S. (2018) '3D Image Analysis of Capillary Vessels in Mouse Organs'. Available at: https://kluedo.ub.uni-kl.de/frontdoor/deliver/index/docId/5456/file/thesis_sonja_foehst.pdf.

Fradet, A. *et al.* (2011) 'Dual function of ERRα in breast cancer and bone metastasis formation: implication of VEGF and osteoprotegerin', *Cancer research*, 71(17), pp. 5728–5738.

Fratini, M. *et al.* (2015) 'Simultaneous submicrometric 3D imaging of the micro-vascular network and the neuronal system in a mouse spinal cord', *Scientific reports*, 5, p. 8514.

Fratzl, P. and Weinkamer, R. (2007) 'Nature's hierarchical materials', *Progress in materials Science*, 52(8), pp. 1263–1334.

Gauthier, R. *et al.* (2018) '3D micro structural analysis of human cortical bone in paired femoral diaphysis, femoral neck and radial diaphysis', *Journal of structural biology*, 204(2), pp. 182–190.

Geusens, P. *et al.* (2014) 'High-resolution in vivo imaging of bone and joints: a window to microarchitecture', *Nature Reviews Rheumatology*, 10(5), pp. 304–313.

Goceri, E., Shah, Z. K. and Gurcan, M. N. (2017) 'Vessel segmentation from abdominal magnetic resonance images: adaptive and reconstructive approach', *International journal for numerical methods in biomedical engineering*, 33(4), p. e2811.

Gonzalez, R. C. and Woods, R. E. (2017) *Digital image processing, 4th edn. ISBN: 9780133356724*. Pearson.

Gorodkin, J. (2004) 'Comparing two K-category assignments by a K-category correlation coefficient', *Computational Biology and Chemistry*, 28(5), pp. 367–374. doi: 10.1016/j.compbiolchem.2004.09.006.

Granlund, G. H. and Knutsson, H. (2013) *Signal processing for computer vision*. Springer Science & Business Media.

Grodzins, L. (1983) 'Optimum energies for x-ray transmission tomography of small samples: Applications of synchrotron radiation to computerized tomography I', *Nuclear Instruments and Methods in Physics Research*, 206(3), pp. 541–545.

Guldberg, R. E. *et al.* (2003) 'Analyzing bone, blood vessels, and biomaterials with microcomputed tomography', *IEEE engineering in medicine and biology magazine*, 22(5), pp. 77–83.

Guldberg, R. E. *et al.* (2004) 'Microcomputed tomography imaging of skeletal development and growth', *Birth Defects Research Part C: Embryo Today: Reviews*, 72(3), pp. 250–259.

Haider, M.-T. *et al.* (2020) 'Breast cancer bone metastases are attenuated in a Tgif1-deficient bone microenvironment', *Breast Cancer Research*, 22, pp. 1–16.

Harrigan, T. P. and Mann, R. W. (1984) 'Characterization of microstructural anisotropy in orthotropic materials using a second rank tensor', *Journal of Materials Science*, 19(3), pp. 761–767.

Helmberger, M. *et al.* (2014) 'Quantification of tortuosity and fractal dimension of the lung vessels in pulmonary hypertension patients', *PloS one*, 9(1), p. e87515.

Hildebrand, T. O. R. and Rüegsegger, P. (1997) 'Quantification of bone microarchitecture with the structure model index', *Computer Methods in Biomechanics and Bio Medical Engineering*, 1(1), pp. 15–23.

Hildebrand, T. and Rüegsegger, P. (1997) 'A new method for the model-independent assessment of thickness in three-dimensional images', *Journal of microscopy*, 185(1), pp. 67–75.

Hoff, P. M. and Machado, K. K. (2012) 'Role of angiogenesis in the pathogenesis of cancer', *Cancer treatment reviews*, 38(7), pp. 825–833.

Holdsworth, D. W. and Thornton, M. M. (2002) 'Micro-CT in small animal and specimen imaging', *Trends in Biotechnology*, 20(8), pp. S34–S39.

Holen, I. *et al.* (2016) 'IL-1 drives breast cancer growth and bone metastasis in vivo', *Oncotarget*, 7(46), p. 75571.

Hounsfield, G. N. (1973) 'Computerized transverse axial scanning (tomography): Part 1. Description of system', *The British journal of radiology*, 46(552), pp. 1016–1022.

Hsu, J.-T. *et al.* (2013) 'The assessment of trabecular bone parameters and cortical bone strength: a comparison of micro-CT and dental cone-beam CT', *Journal of biomechanics*, 46(15), pp. 2611–2618.

Irie, M. S. *et al.* (2018) 'Use of micro-computed tomography for bone evaluation in dentistry', *Brazilian dental journal*, 29(3), pp. 227–238.

Jurman, G. and Furlanello, C. (2010) 'A unifying view for performance measures in multi-class prediction', *arXiv preprint arXiv:1008.2908*.

Kass, M., Witkin, A. and Terzopoulos, D. (1988) 'Snakes: Active contour models', *International journal of computer vision*, 1(4), pp. 321–331.

Korfiatis, V. C., Tassani, S. and Matsopoulos, G. K. (2017) 'An independent active contours segmentation framework for bone micro-CT images', *Computers in Biology and Medicine*, 87, pp. 358–370.

Kovesi, P. (1997) 'Symmetry and asymmetry from local phase', in *Tenth Australian joint conference on artificial intelligence*. Citeseer, pp. 2–4.

Kuhn, J. L. *et al.* (1990) 'Evaluation of a microcomputed tomography system to study trabecular bone structure', *Journal of Orthopaedic Research*, 8(6), pp. 833–842.

Kulak, C. A. M. and Dempster, D. W. (2010) 'Bone histomorphometry: a concise review for endocrinologists and clinicians', *Arquivos Brasileiros de Endocrinologia & Metabologia*, 54(2), pp. 87–98.

Lafage-Proust, M.-H. *et al.* (2015) 'Assessment of bone vascularization and its role in bone remodeling', *BoneKEy reports*, 4.

Lafforgue, P. (2006) 'Pathophysiology and natural history of avascular necrosis of bone', *Joint Bone Spine*, 73(5), pp. 500–507.

Langer, M. *et al.* (2010) 'Simultaneous 3D imaging of bone and vessel microstructure in a rat model', *IEEE Transactions on Nuclear Science*, 58(1), pp. 139–145.

Langer, M. and Peyrin, F. (2016) '3D X-ray ultra-microscopy of bone tissue', *Osteoporosis International*, 27(2), pp. 441–455.

Larrue, A. *et al.* (2011) 'Synchrotron radiation micro-CT at the micrometer scale for the analysis of the three-dimensional morphology of microcracks in human trabecular bone', *PLoS one*, 6(7).

Leali, P. T. *et al.* (2009) 'Bone fragility: current reviews and clinical features', *Clinical cases in mineral and bone metabolism*, 6(2), p. 109.

Lee, J. *et al.* (2007) 'Automatic segmentation of 3D micro-CT coronary vascular images', *Medical image analysis*, 11(6), pp. 630–647.

Lell, M. M. *et al.* (2006) 'New techniques in CT angiography', *Radiographics*, 26(suppl_1), pp. S45–S62.

Leszczyński, B. *et al.* (2016) 'Global and local thresholding methods applied to X-ray microtomographic analysis of metallic foams', *Journal of Nondestructive Evaluation*, 35(2), p. 35.

Lewis, D. D. *et al.* (2004) 'Rcv1: A new benchmark collection for text categorization research', *Journal of machine learning research*, 5(Apr), pp. 361–397.

Li, H. *et al.* (2020) 'Color space transformation and multi-class weighted loss for adhesive white blood cell segmentation', *IEEE Access*, 8, pp. 24808–24818.

Lipton, Z. C., Elkan, C. and Naryanaswamy, B. (2014) 'Optimal thresholding of classifiers to maximize F1 measure', in *Joint European Conference on Machine Learning and Knowledge Discovery in Databases*. Springer, pp. 225–239.

Litjens, G. *et al.* (2017) 'A survey on deep learning in medical image analysis', *Medical image analysis*, 42, pp. 60–88.

Lote, K., Walløe, A. and Bjersand, A. (1986) 'Bone metastasis prognosis, diagnosis and treatment', *Acta Radiologica: Oncology*, 25(4–6), pp. 227–232.

Lowerison, M. R. *et al.* (2017) 'Compound speckle model detects anti-angiogenic tumor response in preclinical nonlinear contrast-enhanced ultrasonography', *Medical physics*, 44(1), pp. 99–111.

Lundberg, L. G. *et al.* (2000) 'Bone marrow in polycythemia vera, chronic myelocytic leukemia, and myelofibrosis has an increased vascularity', *The American journal of pathology*, 157(1), pp. 15–19.

M Kintel and C Wolf (2020) *OpenSCAD, The Programmers Solid 3D CAD Modeller*. Available at: https://www.openscad.org/documentation.html.

Maier, A. *et al.* (2019) 'A gentle introduction to deep learning in medical image processing', *Zeitschrift für Medizinische Physik*, 29(2), pp. 86–101.

Manousakas, I. N. *et al.* (1998) 'Split-and-merge segmentation of magnetic resonance medical images: performance evaluation and extension to three dimensions', *Computers and Biomedical Research*, 31(6), pp. 393–412.

Masood, S. *et al.* (2015) 'A survey on medical image segmentation', *Current Medical Imaging*, 11(1), pp. 3–14.

Matthews, B. W. (1975) 'Comparison of the predicted and observed secondary structure of T4 phage lysozyme', *Biochimica et Biophysica Acta (BBA)-Protein Structure*, 405(2), pp. 442–451.

McInemey, T. and Terzopoulos, D. (1999) 'Topology adaptive deformable surfaces for medical image volume segmentation', *IEEE transactions on medical imaging*, 18(10), pp. 840–850.

McInerney, T. and Terzopoulos, D. (1995) 'A dynamic finite element surface model for segmentation and tracking in multidimensional medical images with application to cardiac 4D image analysis', *Computerized Medical Imaging and Graphics*, 19(1), pp. 69–83.

McInerney, T. and Terzopoulos, D. (1996) 'Deformable models in medical image analysis: a survey', *Medical image analysis*, 1(2), pp. 91–108.

Mehadji, B., Ahmed, Y. and Berteau, J.-P. (2019) 'A novel approach for computing 3D mice distal femur properties using high-resolution micro-computed tomography scanning', *Micron*, 121, pp. 1–7.

Meunier, P. J. (1983) 'A yearly survey of developments in the field of bone and mineral metabolism', *WA Peck, Amsterdam, The Netherlands*.

Mohan, G. and Subashini, M. M. (2019) 'Medical Imaging With Intelligent Systems: A Review', in *Deep learning and parallel computing environment for bioengineering systems*. Elsevier, pp. 53–73.

Moore, D. C. *et al.* (2003) 'Physiologic weight-bearing increases new vessel formation during distraction osteogenesis: A micro-tomographic imaging study', *Journal of orthopaedic research*, 21(3), pp. 489–496.

Mulet-Parada, M. and Noble, J. A. (2000) '2D+ T acoustic boundary detection in echocardiography', *Medical image analysis*, 4(1), pp. 21–30.

Newton, M. D., Junginger, L. and Maerz, T. (2020) 'Automated MicroCT-based bone and articular cartilage analysis using iterative shape averaging and atlas-based registration', *Bone*, p. 115417.

Nilsiam, Y. and Pearce, J. M. (2017) 'Free and open source 3-D model customizer for websites to democratize design with OpenSCAD', *Designs*, 1(1), p. 5.

Nogueira, K. *et al.* (2019) 'Dynamic multicontext segmentation of remote sensing images based on convolutional networks', *IEEE Transactions on Geoscience and Remote Sensing*, 57(10), pp. 7503–7520.

Núñez, J. A. *et al.* (2017) 'Simultaneous visualisation of calcified bone microstructure and intracortical vasculature using synchrotron X-ray phase contrast-enhanced tomography', *Scientific reports*, 7(1), pp. 1–9.

Nutter, F. *et al.* (2014) 'Different molecular profiles are associated with breast cancer cell homing compared with colonisation of bone: evidence using a novel bone-seeking cell line', *Endocrine-related cancer*, 21(2), pp. 327–341.

Nyangoga, H. *et al.* (2011) 'Three-dimensional characterization of the vascular bed in bone metastasis of the rat by microcomputed tomography (MicroCT)', *PLoS One*, 6(3).

Odgaard, A. and Gundersen, H. J. G. (1993) 'Quantification of connectivity in cancellous bone, with special emphasis on 3-D reconstructions', *Bone*, 14(2), pp. 173–182.

Ohser, J., Redenbach, C. and Schladitz, K. (2009) 'Mesh free estimation of the structure model index', *Image Analysis & Stereology*, 28(3), pp. 179–185.

Oliviero, S. *et al.* (2019) 'Effect of repeated in vivo microCT imaging on the properties of the mouse tibia', *PloS one*, 14(11), p. e0225127.

Parfitt, A. M. (1983) 'Stereologic basis of bone histomorphometry: Theory of quantitative microscopy and reconstruction of the third dimension', *Bone histomorphometry: techniques and interpretation*, pp. 53–88.

Parmar, C. *et al.* (2014) 'Robust radiomics feature quantification using semiautomatic volumetric segmentation', *PloS one*, 9(7), p. e102107.

Partitt, A. M. (1987) 'Bone histomorphometry: standardization of nomenclature symbols and units', *J. Bone Miner. Res.*, 2, pp. 595–610.

Patil, D. D. and Deore, S. G. (2013) 'Medical image segmentation: a review', *International Journal of Computer Science and Mobile Computing*, 2(1), pp. 22–27.

Pecheur, I. *et al.* (2002) 'Integrin αvβ3 expression confers on tumor cells a greater propensity to metastasize to bone', *The FASEB Journal*, 16(10), pp. 1266–1268.

Peña Fernández, M. *et al.* (2018) 'Optimization of digital volume correlation computation in SR-microCT images of trabecular bone and bone-biomaterial systems', *Journal of microscopy*, 272(3), pp. 213–228.

Peng, C. *et al.* (2019) 'Densely based multi-scale and multi-modal fully convolutional networks for high-resolution remote-sensing image semantic segmentation', *IEEE Journal of Selected Topics in Applied Earth Observations and Remote Sensing*, 12(8), pp. 2612–2626.

Peyrin, F. *et al.* (1998a) 'Micro-CT examinations of trabecular bone samples at different resolutions: 14, 7 and 2 micron level', *Technology and Health Care*, 6(5–6), pp. 391–401.

Peyrin, F. *et al.* (1998b) 'Micro-CT examinations of trabecular bone samples at different resolutions: 14, 7 and 2 micron level', *Technology and Health Care*, 6(5–6), pp. 391–401.

Peyrin, F. *et al.* (2007) 'Local geometrical analysis of 3d porous networks based on the medial axis: application to bone microarchitecture microtomography images', *Image Analysis & Stereology*, 26(3), pp. 179–185.

Peyrin, F. *et al.* (2014) 'Micro-and nano-CT for the study of bone ultrastructure', *Current osteoporosis reports*, 12(4), pp. 465–474.

Peyrin, F. and Engelke, K. (2012) 'CT imaging: Basics and new trends', *hopd*, p. 883.

Peyruchaud, O. *et al.* (2001) 'Early detection of bone metastases in a murine model using fluorescent human breast cancer cells: application to the use of the bisphosphonate zoledronic acid in the treatment of osteolytic lesions', *Journal of Bone and Mineral Research*, 16(11), pp. 2027–2034.

Phan, D. L., Xu, C. and Price, J. (1998) 'A survey of current methods in medical image segmentation', *Annual review of biomedical engineering*.

Pillai, I., Fumera, G. and Roli, F. (2017) 'Designing multi-label classifiers that maximize F measures: State of the art', *Pattern Recognition*, 61, pp. 394–404.

Pirner, S. *et al.* (2009) 'CT-based manual segmentation and evaluation of paranasal sinuses', *European archives of oto-rhino-laryngology*, 266(4), pp. 507–518.

Poon, M. (2008) *3D livewire and live-vessel: minimal path methods for interactive medical image segmentation*. PhD Thesis. University of British Columbia.

Powers, D. M. (2011) 'Evaluation: from precision, recall and F-measure to ROC, informedness, markedness and correlation', *arXiv preprint arXiv:2010.16061*.

Preim, B. and Botha, C. P. (2013) *Visual computing for medicine: theory, algorithms, and applications*. Newnes.

Prisby, R. *et al.* (2011) 'Intermittent PTH (1–84) is osteoanabolic but not osteoangiogenic and relocates bone marrow blood vessels closer to bone-forming sites', *Journal of Bone and Mineral Research*, 26(11), pp. 2583–2596.

Rajpoot, K., Grau, V. and Noble, J. A. (2009) 'Local-phase based 3D boundary detection using monogenic signal and its application to real-time 3-D echocardiography images', in *2009 IEEE International Symposium on Biomedical Imaging: From Nano to Macro*. IEEE, pp. 783–786.

Rao, S. R. *et al.* (2009) 'Natural image segmentation with adaptive texture and boundary encoding', in *Asian conference on computer vision*. Springer, pp. 135–146.

Rho, J.-Y., Kuhn-Spearing, L. and Zioupos, P. (1998) 'Mechanical properties and the hierarchical structure of bone', *Medical engineering & physics*, 20(2), pp. 92–102.

Ritman, E. L. (2011) 'Current status of developments and applications of micro-CT', *Annual review of biomedical engineering*, 13, pp. 531–552.

Roche, B. *et al.* (2012) 'Structure and quantification of microvascularisation within mouse long bones: what and how should we measure?', *Bone*, 50(1), pp. 390–399.

Ross, M. H. and Pawlina, W. (2006) *Histology*. Lippincott Williams & Wilkins.

Rubin, D. L., Greenspan, H. and Brinkley, J. F. (2014) 'Biomedical imaging informatics', in *Biomedical Informatics*. Springer, pp. 285–327.

Rüegsegger, P., Koller, B. and Müller, R. (1996) 'A microtomographic system for the nondestructive evaluation of bone architecture', *Calcified tissue international*, 58(1), pp. 24–29.

Ryan, T. M. and Ketcham, R. A. (2002a) 'Femoral head trabecular bone structure in two omomyid primates', *Journal of Human Evolution*, 43(2), pp. 241–263.

Ryan, T. M. and Ketcham, R. A. (2002b) 'The three-dimensional structure of trabecular bone in the femoral head of strepsirrhine primates', *Journal of human evolution*, 43(1), pp. 1–26.

Salomé, M. *et al.* (1999) 'A synchrotron radiation microtomography system for the analysis of trabecular bone samples', *Medical Physics*, 26(10), pp. 2194–2204.

Scherf, H. and Tilgner, R. (2009) 'A new high-resolution computed tomography (CT) segmentation method for trabecular bone architectural analysis', *American Journal of Physical Anthropology: The Official Publication of the American Association of Physical Anthropologists*, 140(1), pp. 39–51.

Schneider, P. *et al.* (2009) 'Simultaneous 3D visualization and quantification of murine bone and bone vasculature using micro-computed tomography and vascular replica', *Microscopy research and technique*, 72(9), pp. 690–701.

Serra, J. (1982) 'Image analysis and mathematical morphol-ogy'.

Shanbhogue, V. V. *et al.* (2017) 'Bone disease in diabetes: another manifestation of microvascular disease?', *The lancet Diabetes & endocrinology*, 5(10), pp. 827–838.

Sharma, D. *et al.* (2018) 'The effects of estrogen deficiency on cortical bone microporosity and mineralization', *Bone*, 110, pp. 1–10.

Shelledy, D. C. and Peters, J. I. (2014) *Respiratory care: patient assessment and care plan development*. Jones & Bartlett Publishers.

Singh, S. P. *et al.* (2020) '3D deep learning on medical images: a review', *Sensors*, 20(18), p. 5097.

Sokolova, M., Japkowicz, N. and Szpakowicz, S. (2006) 'Beyond accuracy, F-score and ROC: a family of discriminant measures for performance evaluation', in *Australasian joint conference on artificial intelligence*. Springer, pp. 1015–1021.

Spoor, C. F., Zonneveld, F. W. and Macho, G. A. (1993) 'Linear measurements of cortical bone and dental enamel by computed tomography: applications and problems', *American journal of physical anthropology*, 91(4), pp. 469–484.

Starmans, M. P. *et al.* (2020) 'Radiomics: data mining using quantitative medical image features', in *Handbook of Medical Image Computing and Computer Assisted Intervention*. Elsevier, pp. 429–456.

Stolojescu-CriȘan, C. and Holban, Ș. (2013) 'A comparison of X-ray image segmentation techniques', *Advances in Electrical and Computer Engineering Engineering*, 13(3).

Sun, K. *et al.* (2016) 'Voxelization Algorithm Based on STL Model', in *International Conference on Human Centered Computing*. Springer, pp. 913–918.

Swain, M. V. and Xue, J. (2009) 'State of the art of Micro-CT applications in dental research', *International journal of oral science*, 1(4), pp. 177–188.

Tang, L. *et al.* (2014) 'Computational modeling of 3D tumor growth and angiogenesis for chemotherapy evaluation', *PloS one*, 9(1), p. e83962.

Tassani, S., Korfiatis, V. and Matsopoulos, G. K. (2014) 'Influence of segmentation on micro-CT images of trabecular bone', *Journal of microscopy*, 256(2), pp. 75–81.

Terzopoulos, D. and Fleischer, K. (1988) 'Deformable models', *The visual computer*, 4(6), pp. 306–331.

Terzopoulos, D., Witkin, A. and Kass, M. (1988) 'Constraints on deformable models: Recovering 3D shape and nonrigid motion', *Artificial intelligence*, 36(1), pp. 91–123.

Tharwat, A. (2020) 'Classification assessment methods', *Applied Computing and Informatics*.

Toriwaki, J. and Yonekura, T. (2002) 'Euler number and connectivity indexes of a three dimensional digital picture', *FORMA-TOKYO-*, 17(3), pp. 183–209.

Tortora, G. J. and Derrickson, B. H. (2018) *Principles of anatomy and physiology*. John Wiley & Sons.

Tsai, J. N. *et al.* (2017) 'Effects of denosumab and teriparatide transitions on bone microarchitecture and estimated strength: the DATA-Switch HR-pQCT Study', *Journal of Bone and Mineral Research*, 32(10), pp. 2001–2009.

Tse, J. J. (2018) 'Analysis of Subchondral Bone and Microvessels Using a Novel Vascular Perfusion Contrast Agent and Optimized Dual-Energy Computed Tomography'.

Tsoumakas, G., Katakis, I. and Vlahavas, I. (2010) 'Random k-labelsets for multilabel classification', *IEEE Transactions on Knowledge and Data Engineering*, 23(7), pp. 1079–1089.

Tulotta, C. *et al.* (2019) 'Endogenous production of IL1B by breast cancer cells drives metastasis and colonization of the bone microenvironment', *Clinical Cancer Research*, 25(9), pp. 2769–2782.

Ubellacker, J. M. *et al.* (2017) 'Zoledronic acid alters hematopoiesis and generates breast tumor-suppressive bone marrow cells', *Breast Cancer Research*, 19(1), pp. 1–15.

Waarsing, J. H., Day, J. S. and Weinans, H. (2004) 'An improved segmentation method for in vivo μCT imaging', *Journal of Bone and Mineral Research*, 19(10), pp. 1640–1650.

Wang, D. and Vallotton, P. (2010) 'Improved marker-controlled watershed segmentation with local boundary priors', in *2010 25th International Conference of Image and Vision Computing New Zealand*. IEEE, pp. 1–6.

Wang, Z., Wang, E. and Zhu, Y. (2020) 'Image segmentation evaluation: a survey of methods', *Artificial Intelligence Review*, pp. 1–38.

Ward, W. O., Ding, Y. and Bai, L. (2014) 'Analysis of three-dimensional vasculature using multifractal theory', in *2014 IEEE Symposium on Computational Intelligence in Healthcare and e-health (CICARE)*. IEEE, pp. 64–68.

Wei, J.-M. *et al.* (2010) 'A novel measure for evaluating classifiers', *Expert Systems with Applications*, 37(5), pp. 3799–3809.

Welti, J. *et al.* (2013) 'Recent molecular discoveries in angiogenesis and antiangiogenic therapies in cancer', *The Journal of clinical investigation*, 123(8), pp. 3190–3200.

Whitehouse, W. J. (1974) 'The quantitative morphology of anisotropic trabecular bone', *Journal of microscopy*, 101(2), pp. 153–168.

Wirjadi, O. (2007) 'Survey of 3D image segmentation methods'.

Withey, D. J. and Koles, Z. J. (2008) 'A review of medical image segmentation: methods and available software', *International Journal of Bioelectromagnetism*, 10(3), pp. 125–148.

Xu, C., Pham, D. L. and Prince, J. L. (2000) 'Image segmentation using deformable models', *Handbook of medical imaging*, 2, pp. 129–174.

Xu, H., Langer, M. and Peyrin, F. (2020) 'Segmentation of Bone Vessels in 3D Micro-CT Images Using the Monogenic Signal Phase and Watershed', in *2020 IEEE 17th International Symposium on Biomedical Imaging (ISBI)*. IEEE, pp. 741–744.

Xu, Y. *et al.* (2015) 'A method for 3D histopathology reconstruction supporting mouse microvasculature analysis', *PloS one*, 10(5), p. e0126817.

Yang, A. Y. *et al.* (2008) 'Unsupervised segmentation of natural images via lossy data compression', *Computer Vision and Image Understanding*, 110(2), pp. 212–225.

Zagorchev, L. *et al.* (2010) 'Micro computed tomography for vascular exploration', *Journal of angiogenesis research*, 2(1), p. 7.

Zaitoun, N. M. and Aqel, M. J. (2015) 'Survey on image segmentation techniques', *Procedia Computer Science*, 65, pp. 797–806.

Zeitoun, D. *et al.* (2019) 'Microcomputed tomography of the femur of diabetic rats: alterations of trabecular and cortical bone microarchitecture and vasculature—a feasibility study', *European radiology experimental*, 3(1), p. 17.

Zhang, X. *et al.* (2005) 'Periosteal progenitor cell fate in segmental cortical bone graft transplantations: implications for functional tissue engineering', *Journal of Bone and Mineral Research*, 20(12), pp. 2124–2137.

Zhang, Y. *et al.* (2008) 'Automatic thresholding of micro-CT trabecular bone images', in *2008 International Conference on BioMedical Engineering and Informatics*. IEEE, pp. 23–27.

Zhao, Y. *et al.* (2007) 'Tumor αvβ3 integrin is a therapeutic target for breast cancer bone metastases', *Cancer research*, 67(12), pp. 5821–5830.

Zhou, S. *et al.* (2019) 'High-resolution encoder–decoder networks for low-contrast medical image segmentation', *IEEE Transactions on Image Processing*, 29, pp. 461–475.

Zou, K. H. *et al.* (2004) 'Statistical validation of image segmentation quality based on a spatial overlap index1: scientific reports', *Academic radiology*, 11(2), pp. 178–189.

Zuva, T. *et al.* (2011) 'Image segmentation, available techniques, developments and open issues', *Canadian Journal on Image Processing and Computer Vision*, 2(3), pp. 20–29.

FOLIO ADMINISTRATIF

THESE DE L'UNIVERSITE DE LYON OPEREE AU SEIN DE L'INSA LYON

NOM : XU
(avec précision du nom de jeune fille, le cas échéant)

DATE de SOUTENANCE : 26/03/2021

Prénoms : Hao

TITRE : Three-dimensional quantitative analysis of bone microvasculature in synchrotron micro-CT imaging

NATURE : Doctorat

Numéro d'ordre : 2021LYSEI019

Ecole doctorale : E.E.A. (Électronique, Électrotechnique, Automatique)

Spécialité : Traitement du Signal et de l'Image

RESUME :
The three-dimensional (3D) imaging and quantitative analysis of bone microvasculature are important to describe angiogenesis involvement in bone metastatic process. Here, we propose an algorithm for the 3D segmentation of mouse bone and vessels imaged by synchrotron radiation micro-computed tomography (SR-µCT) with a contrast agent. The algorithm is based on marker-controlled watershed and the monogenic signal phase asymmetry. Markers for the watershed algorithm are generated automatically and distinguished three classes: bone, vessels and background. The marker generation uses hysteresis thresholding and morphological filters. As an alternative to standard edge detection, we exploit the monogenic signal phase asymmetry to build the control surface for the watershed. This makes the edge detection invariant to signal intensity, thus improving edge detection at bone-vessel interfaces where the contrast is relatively low.

The accuracy and robustness of the proposed method were first evaluated on a series of synthetic volumes generated to mimic the real vessel, bone and background structures. Different contrasts between the different structures, as well as different noise levels were considered. A series of multi-class synthetic volumes were segmented using the proposed method, and the overview segmentation quality was evaluated using the Matthews correlation coefficients (MCC) by comparing to the ground truth. In addition, we studied the capability of thin structure segmentation under a various levels of Gaussian noise. The simulation study indicates that the algorithm is performant in other multi-class segmentation problems.

The proposed method was applied to images of mouse model of breast cancer bone metastasis acquired using SR-µCT. The segmentation quality was evaluated using the Dice and the MCC by comparing to manual segmentation. The proposed method performs better than hysteresis thresholding as well as marker-controlled watershed using the magnitude of the gradient as control surface. To quantitatively analyze bone microstructures and vasculatures in mouse model, several parameters were extracted from the whole bone sample (BV/TV, Ct.V/TV, Me.V/TV, Ct.Th), trabecular bone in metaphysis (Tb.V/Me.Ca.V, Tb.Th, FD, SMI, Conn.D, DA), cortical porosity in diaphysis (Ct.Po.V/Ct.TV) and vessels (VV/TV, V.Th, FD, DA). Statistical analysis was performed to study the influence of anti-angiogenesis drugs on bone and vessels, in the context of bone metastases. In conclusion, metastases have developed on trabecular bone, but not yet on cortical bone at the early stage of development. In addition, we conclude that anti-angiogenesis drugs can reduce bone mass by eroding the thickness of bone, in a long-term interactions. Considering vessels in bone, results indicate that there are less, thinner and simpler vessels in the combination treatment group comparing to in other groups. This demonstrates the utility of the algorithm for the study of bone and vessels in mouse models.

MOTS-CLÉS : micro-computed tomography, watershed, monogenic signal, bone, vessel, segmentation, breast cancer bone metastases

Laboratoire (s) de recherche : Centre de Recherche en Acquisition et Traitement de l'Image pour la Santé (CREATIS), CNRS UMR 5220, INSERM U1206

Directeur de thèse: Françoise Peyrin

Président de jury : Lafage-Proust Marie Hélène

Composition du jury : David Rousseau, Claudia Redenbach, Marie Hélène Lafage-Proust, Quentin Grimal, Françoise Peyrin and Max Langer.